

Magazine of Civil Engineering

125th

ISSN
2712-8172



17(2), 2024



Magazine of Civil Engineering

ISSN 2712-8172

Online peer-reviewed open-access scientific journal in the field of Civil and Construction Engineering

Founder and Publisher: Peter the Great St. Petersburg Polytechnic University

This journal is registered by the Federal Service for Supervision of Communications, Information Technology, and Mass Media (ROSKOMNADZOR) in 2020. Certificate EI No. FS77-77906 issued February 19, 2020.

Periodicity: 8 issues per year

Publication in the journal is open and free for all authors and readers.

Indexing: Scopus, Web of Science (ESCI, RSCI), DOAJ, Compendex, Google Academia, Index Copernicus, ProQuest, Ulrich's Serials Analysis System, CNKI

Corresponding address: 29 Polytechnicheskaya st., Saint Petersburg, 195251, Russia

Chief science editor: associate member of RAS, D.S. in Engineering, Vitaly V. Sergeev

Deputy chief science editors:

D.S. in Engineering, Galina L. Kozinets

D.S. in Engineering, Sergey V. Korniyenko

Executive editor: Ekaterina A. Linnik

Translator, editor: Darya Yu. Alekseeva

DT publishing specialist:

Anastasiya A. Kononova

Contacts:

E-mail: mce@spbstu.ru

Web: <http://www.engstroy.spbstu.ru>

Date of issue: 01.04.2024

© Peter the Great St. Petersburg Polytechnic University. All rights reserved.

© Coverpicture – Ilya Smagin

Editorial board:

T. Awwad, PhD, professor, Damascus University, Syrian Arab Republic

M.I. Balzannikov, D.Sc., professor, Samara State University of Economics, Russia

A.I. Belostotsky, D.Sc., professor, StaDyO Research & Engineering Centre, Russia

A.I. Borovkov, PhD, professor, Peter the Great St. Petersburg Polytechnic University, Russia

A. Borodinecs, Dr.Sc.Ing., professor, Riga Technical University, Latvia

M. Veljkovic, PhD, professor, Delft University of Technology, The Netherlands

R.D. Garg, PhD, professor, Indian Institute of Technology Roorkee (IIT Roorkee), India

M. Garifullin, PhD, postdoctoral researcher, Tampere University, Finland

T. Gries, Dr.-Ing., professor, RWTH Aachen University, Germany

T.A. Datsyuk, D.Sc., professor, Saint-Petersburg State University of Architecture and Civil Engineering, Russia

V.V. Elistratov, D.Sc., professor, Peter the Great St. Petersburg Polytechnic University, Russia

T. Kärki, Dr.-Ing., professor, Lappeenranta University of Technology, Russia

G.L. Kozinets, D.Sc., professor, Peter the Great St. Petersburg Polytechnic University, Russia

D.V. Kozlov, D.Sc., professor, National Research Moscow State Civil Engineering University, Russia

S.V. Korniyenko, D.Sc., professor, Volgograd State Technical University, Russia

Yu.G. Lazarev, D.Sc., professor, Peter the Great St. Petersburg Polytechnic University, Russia

M.M. Muhammadiev, D.Sc., professor, Tashkent State Technical University, Republic of Uzbekistan

H. Pasternak, Dr.-Ing.habil., professor, Brandenburgische Technische Universität, Germany

F. Rögner, Dr.-Ing., professor, Technology Arts Science TH Köln, Germany

V.V. Sergeev, D.Sc., professor, Peter the Great St. Petersburg Polytechnic University, Russia

T.Z. Sultanov, D.Sc., professor, Tashkent Institute of Irrigation and Agricultural Mechanization Engineers, Republic of Uzbekistan

M.G. Tyagunov, D.Sc., professor, National Research University "Moscow Power Engineering Institute", Russia

M.P. Fedorov, D.Sc., professor, Peter the Great St. Petersburg Polytechnic University, Russia

D. Heck, Dr.-Ing., professor, Graz University of Technology, Austria

A.G. Shashkin, D.Sc., PI Georekonstruktsiya, LLC, Russia

V.B. Shtilman, D.Sc., JSC B.E. Vedeneev VNIIG, Russia

Contents

Kozhanov, D.A., Khazov, P.A., Shkoda, I.V., Likhacheva, S.Yu. Strength and stability of a pipe-concrete column of a high-rise building	12601
Petrochenko, M.V., Nedviga, P.N., Kukina, A.A., Strelets, K.I., Sherstyuk, V.V. Machine learning model for the BIM classification in IFC format	12602
Kadhim, M.Q., Hassan, H.F. Validating the predicted axial strength of FRP-reinforced concrete circular columns	12603
Lam, T.Q.K. Input parameters of three-layer steel fiber concrete beams	12604
Nguyen, T.C., Bui, A.K. The temperature nomogram to predict the maximum temperature in mass concrete	12605
Fedosov, S.V., Aleksandrova, O.V., Bulgakov, B.I., Lukyanova, N.A., Nguyen Duc Vinh, Q. Corrosion-resistant concretes for coastal underground structures	12606
Cao, P., Kozinets, G.L., Badenko, V.L., Markov, A., Zotov, D.K., Kozinets, P.V. Dynamic characteristics of a reinforced concrete frame under vibration load conditions	12607
Loganina, V.I., Fediuk, R.S., Lesovik, V.S., Klyuev, S.V., Sabitov, L.S., Lomov, M.I., Vavrenyuk, S.V., Vykhodtsev, I.A. Application of fractal analysis to assess the quality of the appearance of paint and varnish coatings	12608
Yehia, S., Shahin, R. Elastic local buckling of trapezoidal plates under linear stress gradients	12609
Isupov, S. A. Performance of TGk dowel connector plates in wooden structure joints under long-term load	12610



Research article

UDC 624.046

DOI: 10.34910/MCE.126.1



Strength and stability of a pipe-concrete column of a high-rise building

D.A. Kozhanov¹ , P.A. Khazov¹ , I.V. Shkoda^{1,2} , S.Yu. Likhacheva¹ 

¹ Nizhny Novgorod State University of Architecture and Civil Engineering, Nizhny Novgorod, Russian Federation

² Mechanical Engineering Research Institute of the RAS – Branch of the “Federal Research Center A.V. Gaponov – Grekhov Institute of Applied Physics of the Russian Academy of Sciences”, Nizhny Novgorod, Russian Federation

✉ pbk996@mail.ru

Keywords: rod model, solid-state model, strength, stability, steel-reinforced concrete, pipe concrete, normal stresses, composite material

Abstract. Reinforced concrete structures are a system consisting of monolithic reinforced concrete, a steel part and connecting elements. In this article, the stress-strain state of the structures of a high-rise building is considered. The domestic experience of research and application of steel-reinforced concrete load-bearing structures is described. The analysis of the strength and stability of the most loaded column of a high-rise building is presented. The columns of the object under study are made using tubular concrete, which is a steel shell pipe working in conjunction with concrete and design fittings. Detailed finite element modeling of each tubular concrete column is labor-intensive and not optimal from the point of view of computing resources. The use of a core model is possible in the case of determining the mechanical characteristics of a tubular concrete column as a core structure. To determine the longitudinal and bending stiffness of columns, it is proposed to use a spatial solid-state model that allows for the joint operation of all these elements. According to the calculation results, the most loaded element is determined, that is, a steel shell pipe. It is shown that the loss of stability of the column as a separate element is impossible with such a configuration of the cross section.

Funding: The work was carried out within the state assignment to IAP RAS for fundamental scientific research for 2024-2026 (topic FFUF -2024-0031, No 1023032800130-3-2.3.2).

Citation: Kozhanov, D.A., Khazov, P.A., Shkoda, I.V., Likhacheva, S.Yu. Strength and stability of a pipe-concrete column of a high-rise building. Magazine of Civil Engineering. 2024. 17(2). Article no. 12601. DOI: 10.34910/MCE.126.1

1. Introduction

Modern technologies in the field of construction are designed to ensure high reliability of buildings, reduce construction time, facilitate the development of projects in difficult conditions and make objects much more attractive through the use of individual architectural and planning solutions. When designing unique high-rise buildings, the practice of using steel-reinforced concrete structures is becoming popular. The fundamental design principle of combining functions of various elements is fully and successfully implemented in steel-reinforced concrete structures.

Steel-reinforced concrete is a composite structure that belongs to a special class of structures in modern construction. The composite form of these elements is diverse, therefore, different structural systems can be used. According to the name, it can be concluded that steel-reinforced concrete structures

are a system consisting of monolithic reinforced concrete, a steel part and connecting elements. Thus, steel-reinforced concrete is an excellent example of a composite material.

The special properties of steel-reinforced concrete structures are ensured through a joint work of steel and reinforced concrete parts. It is possible to highlight the main advantages of these composites over traditional structural materials. Compared to a reinforced concrete structure, when using steel-reinforced concrete, it is possible to reduce the building's own weight and design sections, and also to accelerate construction. The rate of development of high-rise structures made of reinforced concrete and mixed structures is ahead of the development of high-rise steel structures. The stiffness of the structures under consideration is much higher than steel structures, in addition, the consumption of steel is reduced, which has a positive effect on the cost price. Economic profitability of the steel-reinforced concrete structures is evident at the stage of installation, and subsequently – in the process of maintenance-free operation. One of the most important advantages of the mixed structures is the effective combination of different materials, which is reflected in the safety, durability and stability of high-rise objects not only in non-seismic, but also in seismic areas. Of course, there are some difficulties and disadvantages in using such constructions. In the calculation process, one should take into account the staging of work, the shift of dissimilar materials, specific influences and other factors. Accordingly, a significant amount of studies of structures is required, where two materials of different physicochemical parameters are combined, the process of making steel-reinforced concrete structures is also complicated by the need for connecting elements between steel and reinforced concrete, the active use of prestressing, and the internal static indeterminacy of structures' sections.

The first mention of pipe concrete can be considered the research of J.S. Sewell [1, 2], who filled steel pipes with concrete in order to increase their fire and corrosion resistance. At the same time, the bearing capacity of such a structure turned out to be about a quarter higher than the total of a steel pipe and a concrete core.

The first experience of using pipe-concrete structures in the Soviet Union was the Volodarsky Bridge project across the Neva River, carried out in 1936 under the supervision of engineer G. P. Perederia. To increase the bearing capacity of the arches, G P. Perederiy used for the first time the so-called "cage effect": a large-sized package of 40 pipes with a diameter of 140×5 mm was used as the upper parabolic belt of the superstructure. Before the construction of the bridge, a 1/5 life-size model of arched spans was made, which was tested with almost double the design load. The test was conducted with the participation of G.P. Perederia, V.I. Kryzhanovsky, V.K. Kachurin, A.A. Dolzhenko.

Later, G.P. Perederia, based on the experience of designing and building this facility, wrote a monograph in 1945 [3], in which he described the results of the tests and concluded about the effectiveness of using tubular fittings in bridge construction.

In 1938–1940, according to the project of Professor V.A. Rosnovsky [4, 5], a railway bridge was built across the river. Iset in Kamensk-Uralsky with the use of pipe-concrete arches. However, later a problem was identified in the operation of the pipe-concrete elements of the bridge, namely, it was found that the concrete core was detached from the steel pipe.

The main problem when designing buildings and structures using pipe concrete is the complexity of calculations. Modeling with volumetric finite elements of structures from all components of pipe concrete [6–8] leads to high complexity of the model, since the model of only one column of pipe concrete can contain several hundred thousand finite elements, as shown in the current work. Analytical models based on continuum mechanics are labor-intensive and dependent on many mechanical and geometric input parameters [9]. When using rod calculation models, the question arises about the assignment of stiffnesses, the distribution of which directly affects the final design forces. In addition, as for any composite material, the question of the correct stress distribution in the section, which has internal static indeterminacy, remains open.

Modern computer software systems allow performing calculations in linear and nonlinear formulations. But building structures must be modeled using volumetric finite elements. That is why calculation of a complete building model, as a rule, is not possible due to the lack of computing power, complexity and laboriousness of the modeling process. The solution to this problem can be the use of rod design models, the mechanical characteristics of which are assigned by means of a numerical study of individual elements that have much simpler design models.

The purpose of this study is to determine the possibility of consistently determining the mechanical characteristics of individual steel-reinforced concrete columns for the purpose of their further use in the core model of the building. To achieve this goal, it is necessary to simulate a spatial model of a tubular concrete column, determine the mechanical characteristics of the column as a rod and enter the obtained mechanical characteristics of the rod model into the Scad Office.

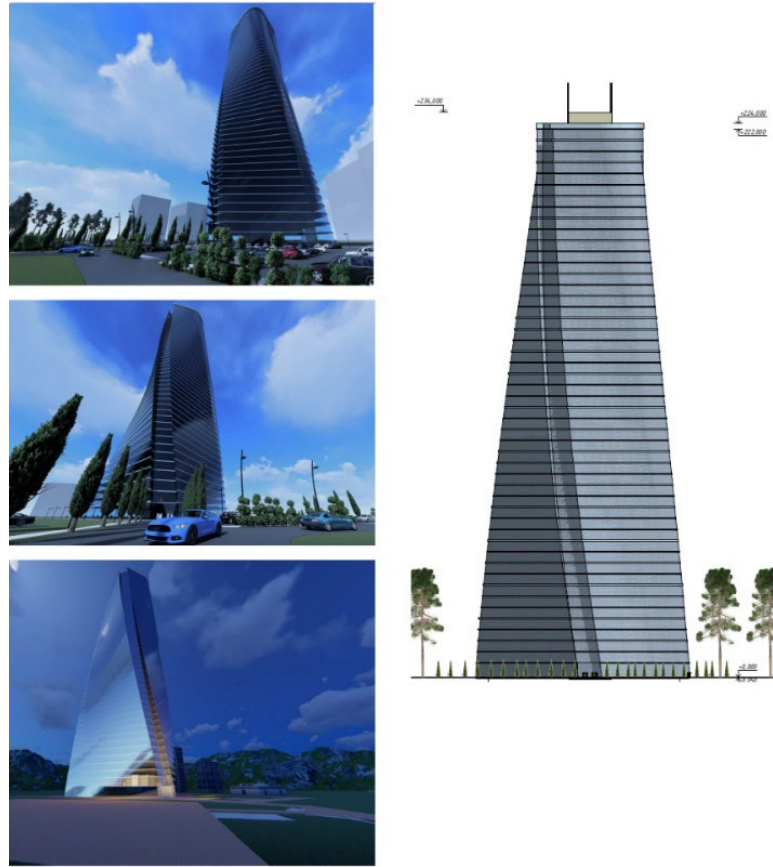


Figure 1. Projected multi-purpose high-rise building.

The main purpose of this study is to determine the stress-strain state of the structures of a high-rise building (Fig. 1).

The tasks that are solved in this paper are:

1. Creating a spatial finite element model of a high-rise building.
2. Determination of longitudinal and flexural stiffness of pipe-concrete columns by creating a solid-state model that takes into account the joint work of all elements of a pipe-concrete column.
3. Determination of normal stresses in the body of pipe-concrete columns.
4. Static calculation of a finite element model of a high-rise building to determine the most dangerous combinations of loads, taking into account the obtained equivalent rigidity.
5. Calculation of stability of the most loaded pipe concrete columns in a geometrically nonlinear formulation of the problem.

2. Materials and Methods

To perform calculations, a spatial finite element model of the building was created in the SCAD Office using rod (columns) and plate (floor slabs, stiffness core) finite elements (Fig. 2).

The columns of the object under study are made using pipe concrete (Fig. 3), which is a steel shell pipe working in conjunction with concrete and design reinforcement. To determine the longitudinal and bending stiffness of the columns, it is proposed to use a spatial solid model, which makes it possible to take into account the joint work of all the listed elements [10–23]. The model built in the ANSYS software is shown in Fig. 4.

To determine the stiffness characteristics, a cantilever bar loaded with a single concentrated moment is considered (Fig. 5). The displacement of the rod end Δ_A can be determined by the Mohr-Maxwell equation (1), the integral of which is revealed using the Vereshchagin method (2).

$$\Delta_A = \int_0^1 \frac{M_p M_i}{EJ_{eq}} ds; \quad (1)$$

$$\Delta_A = \frac{Ml^2}{2EJ_{eq}}, \quad (2)$$

where: $l = 6$ m is the rod length; M_p is the moment calculated in each section of the bar with an assigned load $M = 1$ N·m (Fig. 5); M_i is the moment calculated in each section of the bar with a single force defining the point and direction of displacement Δ_A (Fig. 5); EJ_{eq} is the equivalent bar stiffness; ds is the bar length differential.

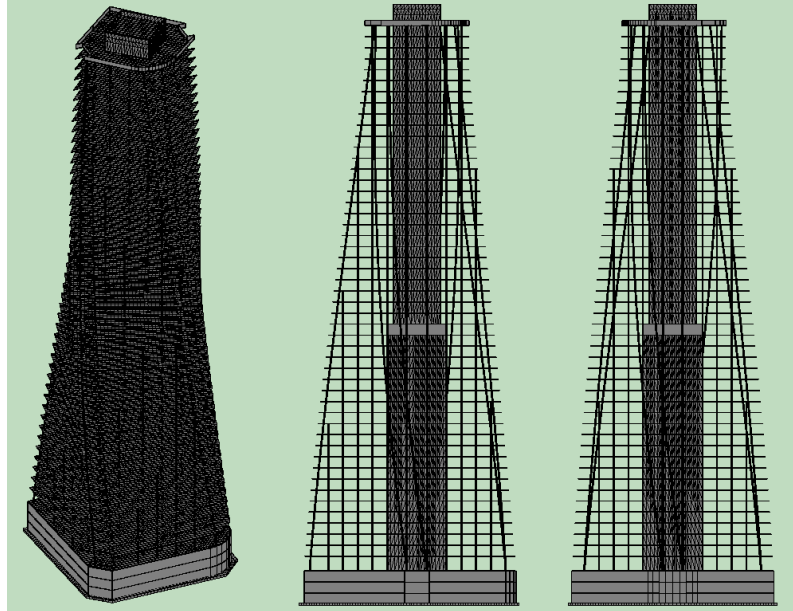


Figure 2. Spatial finite element design model of a high-rise building, built in the SCAD.

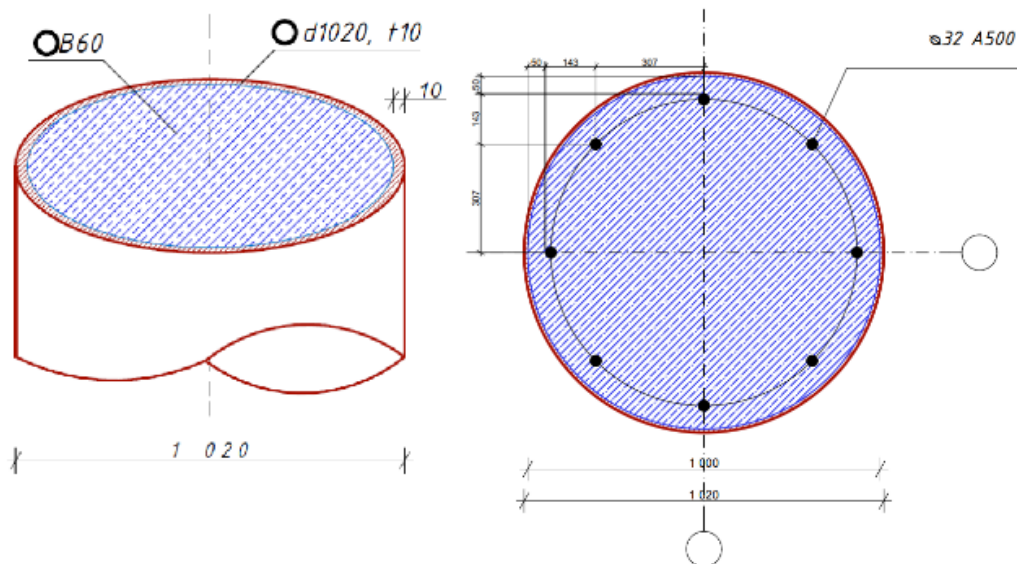


Figure 3. Steel-reinforced concrete column structure.

To determine the equivalent stiffness, the inverse problem is solved, when the displacement of point A is considered known. The displacement value is obtained from the calculation of a spatial finite element model (Fig. 5). The final equivalent stiffness is determined by the equation:

$$EJ_{eq} = \frac{Ml^2}{2\Delta_A} = 1.55 \cdot 10^6 \text{ kN} \cdot \text{m}^2. \quad (3)$$

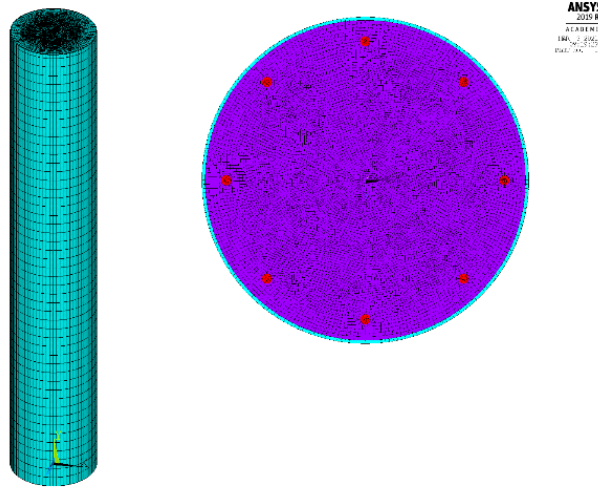


Figure 4. Spatial finite element design model of a steel-reinforced concrete column built in the ANSYS software.

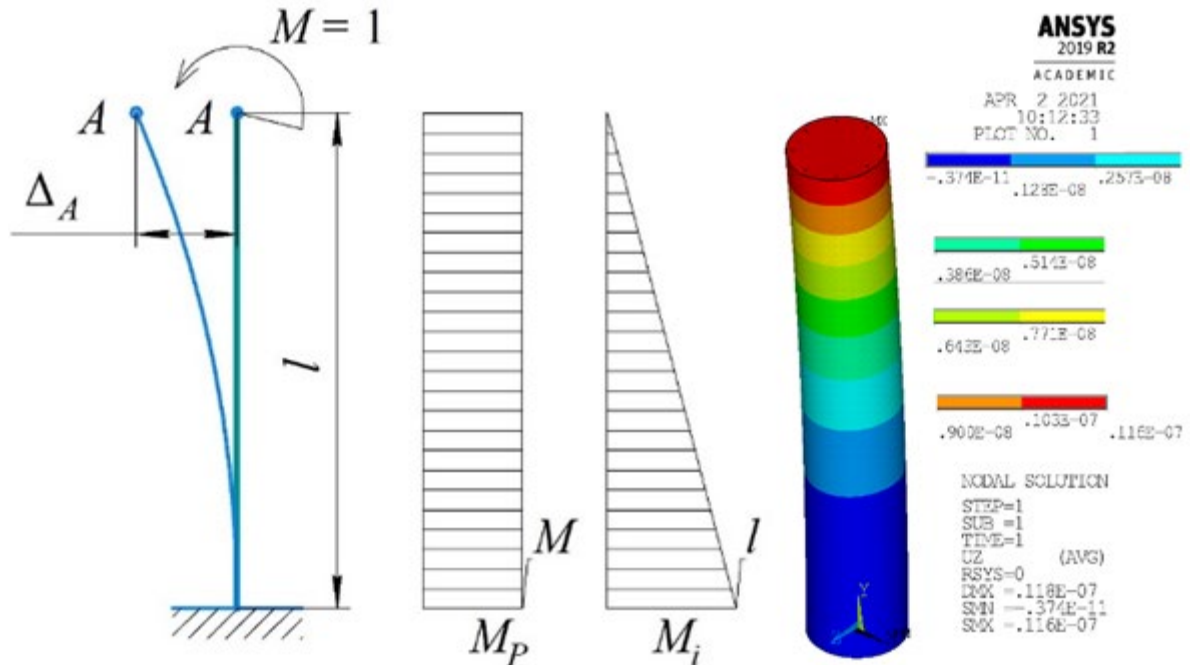


Figure 5. Determination of the bending stiffness of a column.

In this way the bending stiffness was assigned to all types of bars used in the scheme. To determine the longitudinal stiffness, a similar problem is solved, in which the model is loaded with a single longitudinal force.

Then the problem was solved related to the determination of normal stresses in the body of the column [24–31]. For this, the principle of proportionality and the principle of independence of the action of forces (superposition) were used. After assigning the stiffness characteristics to the elements of the rod spatial design model (Fig. 2), a static calculation was carried out, according to the results of which the least advantageous combinations of loadings and design forces were determined. The most dangerous were 2 columns with design forces $M = 245 \text{ kNm}$, $N = 16675 \text{ kN}$ and $M = 360 \text{ kNm}$, $N = 13035 \text{ kN}$ respectively.

The strength of the column elements is checked according to the equation:

$$\sigma_{\max} = \sigma_M^r + \sigma_N^r = \sigma_M M + \sigma_N N \leq R_y, \tag{4}$$

where:

σ'_M, σ'_N are the normal stresses caused by the calculated value of the moment and the longitudinal force, respectively;

σ_M, σ_N are the maximum normal stresses arising in a column element (shell, concrete or design reinforcement) under the action of a single moment or a single longitudinal force, respectively, determined using a solid design model (Fig. 6, 7);

M, N are the calculated values of the moment and longitudinal force, determined using a spatial bar model (Fig. 2);

R_y is the design material resistance.

To calculate the stability of the column, the calculated values of the moments M were taken, while the value of the longitudinal force was increased gradually. Such a situation can occur when a local load exceeding significantly the calculated value is applied on the floor. The problem, in this case, was solved in a geometrically nonlinear formulation using an iterative load application with control of the current deformed state. The number of steps for iterating the load application was determined automatically, but it could not be less than 50 steps and exceed 150.

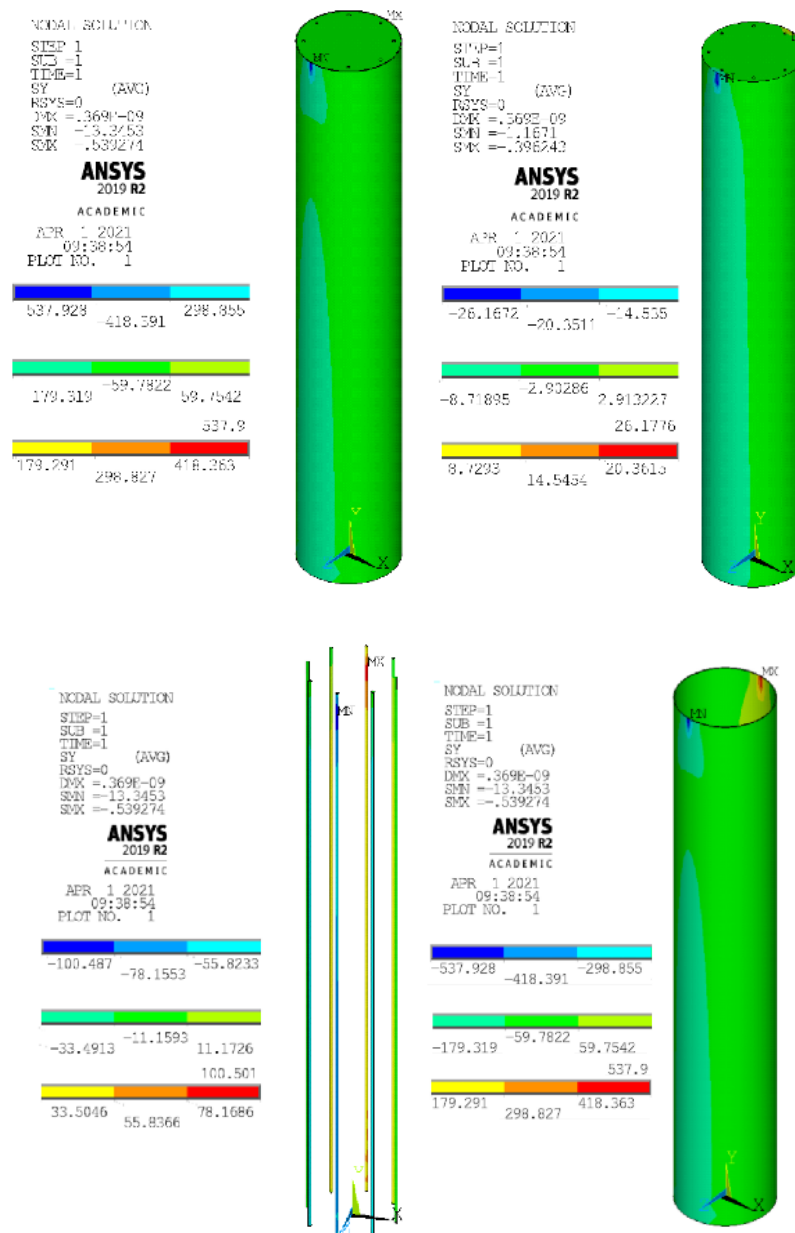


Figure 6. Normal stress (Pa) in the elements of a steel-reinforced concrete column under the action of a single moment.

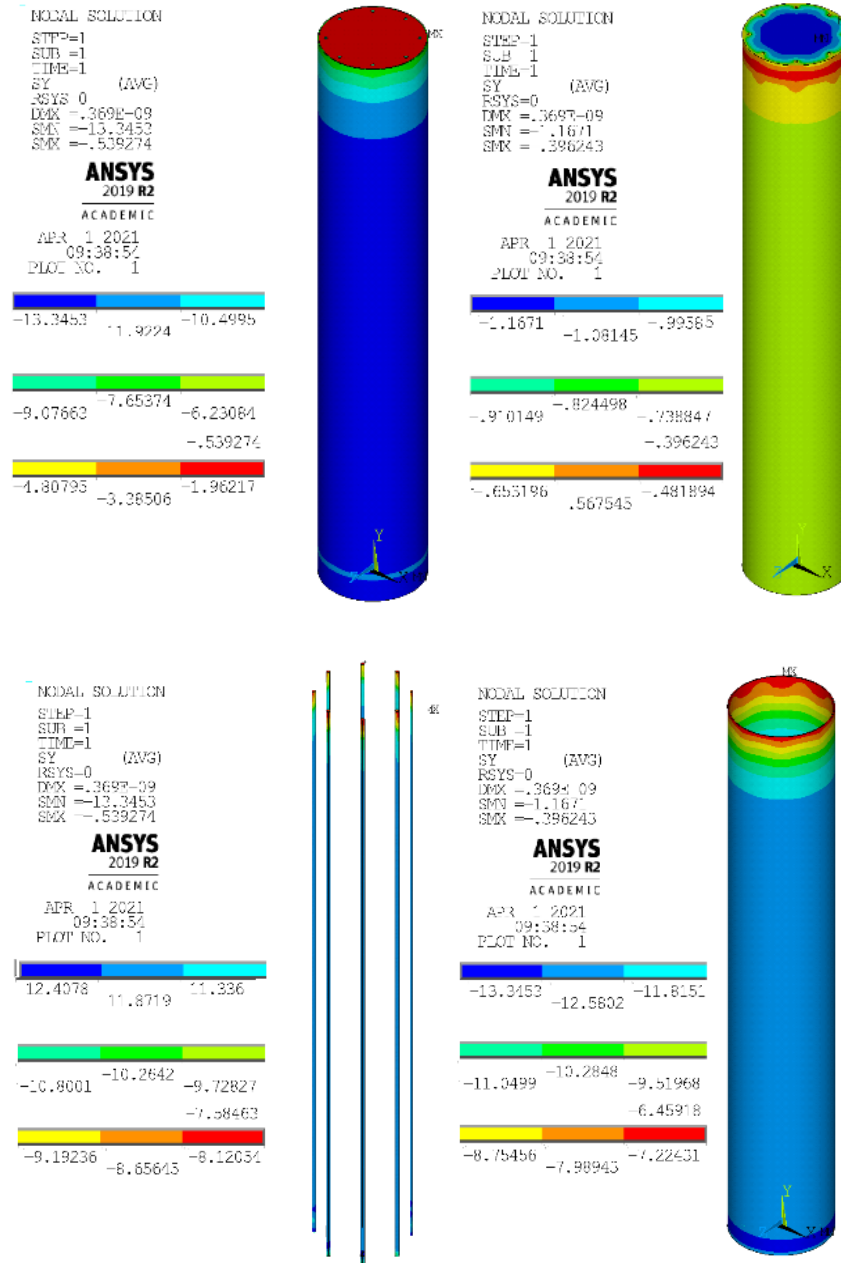


Figure 7. Normal stress (Pa) in the elements of a steel-reinforced concrete column under the action of a single longitudinal force.

To control the convergence of the solution, the ANSYS software package allows the user to track the magnitude of the current displacements and load values in the object model. If the indicators of current displacements and load values exceed the set critical values (limits), then the ANSYS software package decreases the load increment at an iteration step increasing the number of load increment steps. If the number of steps in this case exceeds the maximum set by the user, the ANSYS displays a message about the impossibility of solving the problem in the specified number of steps, which gives the right to conclude that the solution is not convergent. In this study, the divergence of the solution allows us to conclude about the loss of stability of the column.

3. Results and Discussion

The results are summarized in Table. 1. Based on the results of the performed calculation, it can be concluded that the strength of the column is ensured. At the same time, the maximum safety factor, equal to 48 % and 56 %, respectively, with combinations of forces 1 and 2, arises in the reinforcing bars, while the most loaded is the steel shell pipe, the safety factor in which is about 5 %. To rationalize the result, the adopted section can be corrected (Fig. 3), followed by the refinement of the stiffness characteristics and design forces.

According to the current regulatory documents, in order to ensure full bearing capacity, in addition to the strength, it is necessary to check the stability of the element. Issues of ensuring stability of compressed and compressed-bendable elements are of special attention [32–39], and the monograph by V.V. Katyushin [32], published in 2005, is considered one of the leading works by the scientific community in this respect.

Table 1. Strength check of column elements.

Combination of forces		Element	$\sigma_M, \text{ Pa}$	$\sigma_N, \text{ Pa}$	$\sigma_M, \text{ Pa}$ ($\cdot 10^6$)	$\sigma_N, \text{ Pa}$ ($\cdot 10^6$)	$\sigma_{\max}, \text{ Pa}$ ($\cdot 10^6$)	$R_y, \text{ Pa}$ ($\cdot 10^6$)	Reserve
$M, \text{ Nm}$	$N, \text{ kN}$								
245000	$1.668 \cdot 10^6$	Concrete	20.36	1.16	4.99	19.3	24.3	33.0	26%
		Armature	78.17	12.41	19.2	207	226.2	436	48%
		Pipe	179.32	12.58	43.9	210	253	265	5%
360000	$1.304 \cdot 10^6$	Concrete	20.36	1.16	7.33	15.1	22.8	33.0	31%
		Armature	78.17	12.41	28.1	162	190.1	436	56%
		Pipe	179.32	12.58	64.6	164	228.6	265	14%

Fig. 8 shows a diagram that visualizes the percentage of material utilization of various column elements for each of the considered stress combinations.

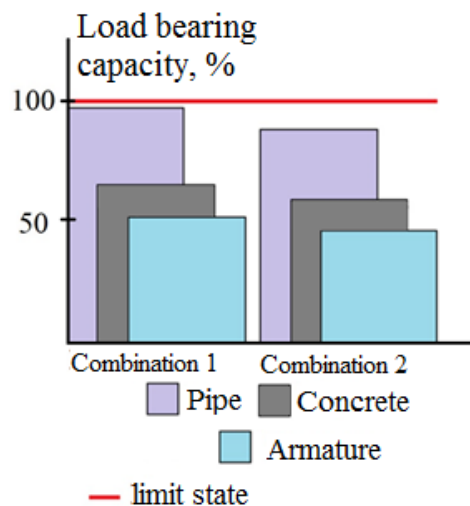


Figure 8. Chart visualizing the percentage of material utilization of various column elements.

Similar methods for determining the mechanical characteristics of individual parts, based on a spatial finite element model of these elements, are used in many problems of continuum mechanics, including the mechanics of civil structures. However, a similar method in relation to structures made of tubular concrete is not sufficiently presented in the literature.

The published works [40] present the results of field experiments on the operation of tubular concrete under axial compression, analyze the data of theoretical calculations of the maximum bearing capacity in accordance with various applicable codes of practice: EC4, NBR 8800, AISC and GB50396-2014. In many works, the greatest efficiency of tubular concrete is determined, and the issues of operation of non-centrally compressed tubular concrete elements are discussed by both domestic [41–43] and foreign [44–50] scientists. Insufficient amount of work has been devoted to the calculation of buildings and structures in general, the elements of which are tubular concrete elements.

4. Conclusions

1. The mechanical properties of the column can be obtained from the ANSYS spatial model.
2. A spatial finite element model of a high-rise multifunctional building using rod and plate finite elements was created in the SCAD Office.

3. From the calculation of the spatial finite element model, the displacements necessary for calculating the equivalent longitudinal and bending stiffness of columns are obtained.
4. A static calculation of the spatial finite element model was carried out and the most dangerous combinations of forces 1 and 2 were identified.
5. As a result of calculating the strength of a pipe-concrete column, it was revealed that the steel shell pipe is the most loaded. At the same time, reinforcing bars have a large margin of safety. This suggests that it is necessary to adjust the parameters of the section.
6. Since it was not possible to achieve the loss of stability of the column, it can be concluded that the loss of bearing capacity at given cross-sections and design characteristics of the column elements is possible only when the stresses reach values that exceed the design resistance of materials. Thus, the local stability of the column is ensured under any loads. However, it is necessary to perform a calculation of the overall stability of the entire building as a whole, which is beyond the scope of this study.
7. As a result of the performed studies of the strength and stability, it can be concluded that the bearing capacity of the studied column is provided.

References

1. Sewell, J.S. Columns for buildings. *Engineering News*. 1902. 48(17). Pp. 10–13.
2. Sewell, J.S., Thacher, E. Concrete and Concrete-Steel. *Transactions of the American Society of Civil Engineers*. 1905. 54. 240 p.
3. Perederiy, G.P. Trubchataya armatura [Tubular fittings]. Moscow: Transzheldorizdat. 1945. 105 p. (rus)
4. Rosnovsky, V.A., Lipatov, A.F. Issledovanie trub, zapolnennyh betonom [Investigation of pipes filled with concrete]. *Zheleznodorozhnoe stroitel'stvo*. 1952. 11. Pp. 27–30. (rus)
5. Rosnovsky, V.A. Trubobeton v mostostroenii [Pipe concrete in bridge construction]. Moscow: Transzheldorizdat. 1963. 110 p.
6. Habibi, A., Fanaie, N., Shahbazpanahi, S. Experimental and numerical investigation of I-beam to concrete-filled tube (CFT) column moment connections with pipe-stiffened internal diaphragm. *Journal of Constructional Steel Research*. 2023. 200. 107648. DOI: 10.1016/j.jcsr.2022.107648
7. Wang, Y., Yang, S., Han, L., Liu, Y., Xue, B., Li, J. Application research on composite support technology of concrete-filled steel tube support in high stress and large deformation soft rock roadway: A case study. *Structures*. 2024. 60. 105814. DOI: 10.1016/j.istruc.2023.105814
8. Ding, F., Lu, D., Lai, Z., Liu, X. Study on restraint coefficient of the stirrups-stiffened square concrete filled double-skin steel tube axial compression stub columns. *Structures*. 2024. 60. 105847. DOI: 10.1016/j.istruc.2023.105847
9. He R., Xu, H., Yan, D., Yi, Z., Li, H. Calculation of ultimate bearing capacity of concrete-filled double steel tubular under compression based on the unified strength theory. *Structures*. 2023. 58. 105384.
10. Gao, D., Li, W., Pang, Y., Huang, Y. Behavior analysis and strength prediction of steel fiber reinforced recycled aggregate concrete column under axial compression. *Construction and Building Materials*. 2021. 290. DOI: 10.1016/j.conbuildmat.2021.123278
11. Mao, W.J., Wang, W. Da, Zhou, K., Du, E.F. Experimental study on steel-reinforced concrete-filled steel tubular columns under the fire. *Journal of Constructional Steel Research*. 2021. 185. 106867. DOI: 10.1016/J.JCSR.2021.106867
12. Ci, J., Ahmed, M., Jia, H., Chen, S., Zhou, D., Hou, L. Testing and strength prediction of eccentrically-loaded circular concrete-filled double steel tubular stub-columns. *Journal of Constructional Steel Research*. 2021. 186. 106881. DOI: 10.1016/j.jcsr.2021.106881
13. Ramadan, A., Younis, A.A., Wong, L.S., Nehdi, M.L. Investigation of structural behavior of precast concrete pipe with single elliptical steel cage reinforcement. *Engineering Structures*. 2020. 219. Pp. 1–17. DOI: 10.1016/j.engstruct.2020.110881
14. Rong, C., Shi, Q., Wang, B. Seismic performance of angle steel frame confined concrete columns: Experiments and FEA model. *Engineering Structures*. 2021. 235. 111983. DOI: 10.1016/j.engstruct.2021.111983
15. Gao, P., Sun, D., Zhao, Y., Hong, L., Wang, Z., Chen, T. Effect of the corner radius on the axial compressive performance of large steel-reinforced concrete columns confined by carbon fibre-reinforced polymer. *Engineering Structures*. 2021. 239. DOI: 10.1016/j.engstruct.2021.112303
16. Fang, H., Chan, T.-M., Young, B. Structural performance of concrete-filled cold-formed high-strength steel octagonal tubular stub columns. *Engineering Structures*. 2021. 239. 112360. DOI: 10.1016/j.engstruct.2021.112360
17. Younis, A.A., Shehata, A., Ramadan, A., Wong, L.S., Nehdi, M.L. Modeling structural behavior of reinforced-concrete pipe with single, double and triple cage reinforcement. *Engineering Structures*. 2021. 240. 112374. DOI: 10.1016/J.ENGSTRUCT.2021.112374
18. Ramadan, A., Shehata, A., Younis, A.A., Wong, L.S., Nehdi, M.L. Modeling structural behavior of precast concrete pipe with single elliptical steel cage reinforcement. *Structures*. 2020. 27. Pp. 903–916. DOI: 10.1016/j.istruc.2020.06.037
19. Huang, L., Yu, T., Zhang, S., Wang, Z.Y. Confinement mechanism of FRP-confined concrete-encased cross-shaped steel columns. *Engineering Structures*. 276. 115349. DOI: 10.1016/j.engstruct.2022.115349
20. Sun, Y., Hu, S., Yiqun, H., Xue, X. Analytical stress model for embedded bar-wrapped cylinder concrete pressure pipe under internal load. *Thin-Walled Structures*. 2019. 149. 106540. DOI: 10.1016/j.tws.2019.106540
21. Zhang, T., Ding, F. xing, Liu, X. mei, Yu, Z. wu. Seismic behavior of terminal stirrup-confined concrete-filled elliptical steel tube columns: Experimental investigation. *Thin-Walled Structures*. 2021. 167. 108251. DOI: 10.1016/J.TWS.2021.108251
22. Tokgoz, S., Dundar, C., Karaahmetli, S., Ozel, R. Research on concrete-filled stainless steel tubular composite columns. *Structures*. 2021. 33. Pp. 703–719. DOI: 10.1016/j.istruc.2021.04.065
23. Chen, Z., Xu, R., Ning, F., Liang, Y. Compression behaviour and bearing capacity calculation of concrete filled double skin square steel columns. *Journal of Building Engineering*. 2021. 42. 103022. DOI: 10.1016/J.JOBE.2021.103022

24. Guo, Y.L., Geng, Y., Qu, L.Y. Time-dependent behaviour of circular steel tube confined reinforced concrete (STCRC) stub columns subjected to low axial load. *Engineering Structures*. 2021. 243. 112663. DOI: 10.1016/J.ENGSTRUCT.2021.112663
25. Qiyun, Q., Zhaoyuan, Y., Wanlin, C. Axial compressive behavior of stainless steel tube confined concrete column piers. *Marine Structures*. 2021. 78. 103021. DOI: 10.1016/J.MARSTRUC.2021.103021
26. Guo, Y.C., Xiao, S.H., Shi, S.W., Zeng, J.J., Wang, W.Q., Zhao, H.C. Axial compressive behavior of concrete-filled FRP-steel wire reinforced thermoplastics pipe hybrid columns. *Composite Structures*. 2020. 244. 112237. DOI: 10.1016/J.COMPSTRUCT.2020.112237
27. Li, G., Yang, Y., Yang, Z., Fang, C., Ge, H., Liu, Y. Mechanical behavior of high-strength concrete filled high-strength steel tubular stub columns stiffened with encased I-shaped CFRP profile under axial compression. *Composite Structures*. 2021. 275. 114504. DOI: 10.1016/J.COMPSTRUCT.2021.114504
28. Yan, X.F., Zhao, Y.G., Lin, S., Zhang, H. Confining stress path-based compressive strength model of axially compressed circular concrete-filled double-skin steel tubular short columns. *Thin-Walled Structures*. 2021. 165. 107949. DOI: 10.1016/J.TWS.2021.107949
29. Gao, D., Li, W., Pang, Y., Huang, Y. Behavior analysis and strength prediction of steel fiber reinforced recycled aggregate concrete column under axial compression. *Construction and Building Materials*. 2021. 290. DOI: 10.1016/j.conbuildmat.2021.123278
30. Qiyun, Q., Zhaoyuan, Y., Wanlin, C. Axial compressive behavior of stainless steel tube confined concrete column piers. *Marine Structures*. 2021. 78. 103021. DOI: 10.1016/J.MARSTRUC.2021.103021
31. Thusoo, S., Obara, T., Kono, S., Miyahara, K. Design models for steel encased high-strength precast concrete piles under axial-flexural loads. *Engineering Structures*. 2021. 228. 111465. DOI: 10.1016/J.ENGSTRUCT.2020.111465
32. Katyushin, V.V. Zdaniya s karkasami iz stalnykh ram peremennogo secheniya (ras-chyot, proektirovanie, stroitelstvo) [Buildings made of steel frames of variable cross-section (calculations, design, construction)]. Moscow: Stroyizdat, 2005. 656 p. (rus)
33. Askinazi, V.Yu. Prostranstvennaya ustoychivost elementov stalnykh ramnykh konstruksiy peremennoy zhyostkosti [Spatial stability of elements of steel frame structures of variable rigidity: abstract of the candidate of technical sciences: 05.23.01]. St. Petersburg, 2017. 26 p. (rus)
34. Nikora, N.I. Prodolny izgib sterzhney peremennoy zhyostkosti s uchyotom deformatsiy polzuchesti i temperaturnykh vozdeystviy [Longitudinal bending of rods of variable stiffness taking into account creep deformations and temperature influences: dissertation for the degree of candidate of technical sciences: 05.23.17]. Rostov-on-Don, 2016. 120 p. (rus)
35. Bogdanovich, A.U. Ustoychivost sterzhnya peremennogo ellipticheskogo secheniya pri prodolnom szhatii [Stability of a rod of variable elliptical cross-section under longitudinal compression]. *Izvestiya KGASU*. 2006. 2(6). Pp. 38–41. (rus)
36. Bogdanovich, A.U. Prodolnoe szhatie tonkostennogo sterzhnya peremennogo secheniya pri razlichnykh variantakh zakrepleniya tortsov [Longitudinal compression of a thin-walled rod of variable cross-section with various options for fixing the ends]. *Izvestiya vuzov*. Construction. 2005. 11–12(563–564). Pp. 10–16. (rus)
37. Belyaeva, S.Yu. Issledovanie nesushchey sposobnosti elementov stalnoy rami peremennogo secheniya pri oshibkakh sborki i montazha [Investigation of the bearing capacity of elements of a steel frame of variable cross-section in case of assembly and installation errors]. *Modern construction and architecture*. 2016. 1(01). Pp. 22–26. (rus)
38. Blyumin, S.L. Reshenie zadachi ustoychivosti szhato-izgibaemykh zhyostko oporytykh sterzhney peremennoy zhyostkosti [The solution of the problem of stability of compressed-bent rigidly supported rods of variable stiffness]. *Vestnik MGSU*. 2015. 5. Pp. 18–27. (rus)
39. Galkin, A.V. Zadacha ustoychivosti szhato-izgibaemykh sterzhney so stupenchatym izmeneniyem zhyostkosti [The problem of stability of compressed-bending rods with a step change in stiffness]. *Bulletin of MGSU*. 2015. 2. Pp. 38–44. (rus)
40. Nesvetaev, G.V., Rezvan I.V. Ocenka prochnosti trubobetona [Assessment of the strength of pipe concrete]. *Fundamental'nye issledovaniya*. 2011. 12-3. Pp. 580–583. (rus)
41. Skvortsov, N.F. Prochnost' staletrubobetona [Strength of steel-reinforced concrete]: diss. kand. tekhn. nauk [dissertation Candidate of Technical Sciences]. Moscow. 1953. 453 p. (rus)
42. Krishan, A.L. Prochnost' trubobetonnykh kolonn s predvaritel'no obzhatym yarom [Strength of pipe-concrete columns with pre-compressed spring] : diss. dok. tekhn. nauk [dissertation Doctors of Technical Sciences]. Magnitogorsk. 2011. 380 p. (rus)
43. Dolzhenko, A.A. Trubchataya armatura v zhelezobetone [Tubular reinforcement in reinforced concrete] : diss. kand. tekhn. nauk [dissertation Candidate of Technical Sciences]. Moscow. 1967. 413 p. (rus)
44. Abed, F. Experimental and numerical investigations of the compressive behavior of concrete filled steel tubes (CFSTs). *Journal of Constructional Steel Research*. 2013. 80. Pp. 429–439.
45. Singh, N.D., Vaghmarey, Sh. Study and Buckling Analysis of Concrete Filled Steel Tubes Columns using ANSYS. *International Research Journal of Engineering and Technology (IRJET)*. 2018. 5(12). Pp. 1259–1267.
46. Sakino, K., Xiao, Y., Tomii, M. Elastic-Plastic Behavior of Concrete Confined in Circular Steel Tube or Spiral Reinforcement. *Proc. of the 3-rd Int. Conf. on Steel-Concrete Composite Structures*. Fukuoka, Japan. 1991. Pp. 67–73.
47. Furlong, R.W. Design of steel-encased concrete beam-columns. *Proc. ASCE*. 1968. 94. Pp. 267–281.
48. Muciaccia, G., Giussani, F., Rosati, G., Mola, F. Response of self-compacting concrete filled tubes under eccentric compression. *Journal of Constructional Steel Research*. 2011. 67(5). Pp. 904–916.
49. Kedziora, S., Anwaar, M.O. Concrete-filled steel tubular (CFS) columns subjected to eccentric compressive load. *AIP Conference Proceedings*. 2019. 2060(1). 020004. DOI: 10.1063/1.5086135
50. Liu, F.Q., Gardner, L., Yang, H. Post-fire behaviour of reinforced concrete stub columns confined by circular steel tubes. *Journal of Constructional Steel Research*. 2014. 102. Pp. 82–103.

Information about authors:

Dmitry Kozhanov, PhD in Physics and Mathematics

ORCID: <https://orcid.org/0000-0002-8443-1291>

E-mail: pbk996@mail.ru

Pavel Khazov, PhD in Technical Sciences

ORCID: <https://orcid.org/0000-0003-1220-6930>

E-mail: khazov.nngasu@mail.ru

Irina Shkoda,

ORCID: <https://orcid.org/0000-0001-6759-0963>

E-mail: ShkodairinaVasil@yandex.ru

Svetlana Likhacheva, PhD in Physics and Mathematics

E-mail: razvitie@nngasu.ru

Received 29.09.2021. Approved after reviewing 30.01.2024. Accepted 05.02.2024.



Research article

UDC 69.05.04

DOI: 10.34910/MCE.126.2



Machine learning model for the BIM classification in IFC format

M.V. Petrochenko , **P.N. Nedviga**, **A.A. Kukina** , **K.I. Strelets**, **V.V. Sherstyuk**  

Peter the Great St. Petersburg Polytechnic University, St. Petersburg, Russian Federation

✉ sherstyuk2.vv@yandex.ru

Keywords: classification in construction, artificial intelligence, classifier, classification model, machine learning, neural networks, BIM technologies, BIM, IFC, Revit, civil engineering, CAD

Abstract. In the rapid development of information technology in the field of Building Information Modeling (BIM) there is a growing need for efficient classification of construction information. One of the key steps to move towards digital construction involves creating reliable systems for classifying BIM elements, providing the foundation for various use cases, from facilitating model navigation to obtaining practical outcomes such as cost estimates and materials quantities. However, the BIM classification process in practice is labor-intensive and time-consuming and leads to an increase in the cost. This study explores the application of an innovative method, based on artificial intelligence algorithms. This method automates the assignment of codes to information model components. The research investigates classification systems, machine learning models and selects the most accurate one for the classification task. It is based on metrics such as accuracy and F1-score in order to achieve an optimal balance between the efficiency and accuracy according to predefined parameters. The article presents software for automatic prediction and assignment of codes in accordance with the selected classifier, developed on selected algorithms.

Citation: Petrochenko, M.V., Nedviga, P.N., Kukina, A.A., Strelets, K.I., Sherstyuk, V.V. Machine learning model for the BIM classification in IFC format. Magazine of Civil Engineering. 2024. Article no. 12602. DOI: 10.34910/MCE.126.2

1. Introduction

In modern times, BIM (Building Information Modeling) technologies are widely used in various fields, revolutionizing the traditional processes associated with the design, construction and operation of buildings. A BIM model contains information about geometry, materials, resource consumption, work schedules, costs, and other parameters. This digital model is developed throughout the entire project lifecycle, from the conception to the operation and maintenance.

One of the key aspects that makes BIM highly significant in the construction industry is the ability to facilitate collaboration and data exchange among all the project stakeholders. Architects, engineers, builders, estimators can efficiently work together, minimizing errors and collision, while reducing time and resource wastage. BIM technologies allow for the creation of digital twins of structures, which can be used for a variety of scenarios: efficient property management, minimizing environmental impact, cost calculations for construction, operation and maintenance. Classification systems are used to solve these tasks. In order to organize the huge amount of data involved in BIM-model.

The classification of information models allows to structure and organize the huge data volumes, simplify access to information and makes it more understandable and manageable. It also enables to extract the necessary project data quickly, reducing the probability of errors during information searches and enhancing communication among project participants. Structured and classified data integrates easily into various software and systems for automating planning, management, and construction control processes, facilitating decision-making and improving efficiency.

There are various classification systems such as UniFormat, MasterFormat 2016, OmniClass, UniClass 2015, CoClass, as well as CCS and Talo classification systems. All of them are widely used in the international construction practices.

Uniformalt is a classification system commonly used for organizing information about construction projects and infrastructure. This classifier divides project data into four levels of hierarchy from a general description of the object to the detailed technical characteristics [1]. The standard is based on functional elements or components, without considering the materials and methods used for their execution. The system can be used to ensure consistency in the economic evaluation of construction projects.

MasterFormat 2016 is a classification system for organizing construction information and documentation in North America [2]. This system was developed by the Construction Specifications Institute (CSI) and Construction Specifications Canada (CSC). It provides a structure for cataloging and describing various elements and processes related to construction and renovation. MasterFormat is organized as a hierarchical structure with divisions into different sections, groups, and subgroups. Each element is assigned a unique number, making the system easy to manage and access. MasterFormat is widely used in the construction industry and serves as a standard for organizing construction documentation, including specifications, contracts and budgets.

OmniClass is a classification and categorization system for construction information designed to more efficiently organize data in the construction and engineering industry [3]. It is an integrated system, that combines both MasterFormat and Uniformalt. It allows it to cover various aspects of projects, ranging from technical specifications to financial reporting.

Uniclass 2015 is a classification system for construction information developed by the Royal Institute of British Architects (RIBA) in the UK [4]. This system is designed to simplify and standardize the description of construction projects and information within the construction industry. Uniclass 2015 is the standard classification system in the UK and widely used in the development, documentation, and management of construction projects. The system covers various disciplines, including architecture, engineering, construction, and more, making it valuable for different participants in the construction process.

CoClass is a Swedish digital classification system developed in accordance with ISO 12006-2:2015/IEC CD 81346 standards. It was originally created to reduce construction expenses related to communication issues among participants in the construction process at all stages of the object's lifecycle, from early design phases to technical maintenance, operation and demolition [5].

CCS (Common Classification System) is a Danish classification system used in Denmark for categorizing and describing construction and engineering projects [6, 7]. It is designed to simplify information exchange and improve data consistency in the construction industry. CCS is widely used in Denmark across various sectors including construction, design and project management. It serves as a standard for organizing information about construction projects.

TALO 2000 classification system is a Finnish classification system developed for organizing and structuring information in the construction and engineering industry in Finland [8, 9]. The name "TALO" means "house" in Finnish, implying that the system is used for classifying construction objects and related information. Here are some key characteristics of the Finnish classification system TALO 2000.

CIC (Construction information classifier) is the Russian national classification system for construction information, based on international standards ISO 12006 and IEC 81346. It is organized through a systematic approach, creating a structured set of disparate objects [10, 11]. All classes of construction information and their corresponding classification tables according to ISO 12006-2:2015 and fall into one of four basic categories of construction information: resource, process, result, and characteristic. Codes are assigned by combining numbers and letters.

Each of these systems provides encoding for elements of building information model based on their purpose, location, materials and other attributes. The more complex the classifier the broader its application in projects. But it may require more time for specialists to encode model elements.

Currently, information models can be classified in editable formats. This introduces certain complexities in terms of creation, coding method and subsequent handling of coded attributes for conversion into other formats without data loss. Since the information model dynamically changes during the design process, element classification typically occurs at the final modeling stage when exporting to the universal and easily processed IFC format. It is necessary for successful integration with other software, subsequent checks, filtering, use in ERP systems for further facilitating effective communication among all construction participants.

The Industry Foundation Classes (IFC) format is an open and cross-industry standard for exchanging information about construction and infrastructure objects in a computer graphics format. IFC is designed as an open standard to ensure that the building information model is available for use by all interested parties without licensing restrictions [13]. This promotes compatibility and collaboration between different programs and systems dealing with construction data.

IFC is designed to cover a wide range of industries related to design, construction, and facility management, including architecture, engineering systems, construction, asset management and others. This allows to create comprehensive models and data exchange between various specialized systems.

The format used an object-oriented approach to represent information. Each element is presented as an object with a set of properties and attributes, including both semantic descriptions (purpose, characteristics, etc.) and their geometric representations, providing the capability for visualization and analysis of construction objects in a three-dimensional environment.

The IFC format is not tied to a specific platform or program. It makes it usable in various applications, such as design software (e.g., BIM applications), construction management systems and others.

Classifying the model in the IFC format offers the possibility to encode both user-defined attributes and as part of the IFC structure, specifically within `IfcClassification`. This structure carries several advantages. Classification information embedded in the hierarchical IFC structure can be provided in two ways: through an external reference to the classification, describing `IfcClassification`, containing the classification name, edition, and resource location; or through `IfcClassification` with `IfcClassificationReference` as classification notations, facilitating the integration of the classification system structure into exchange systems.

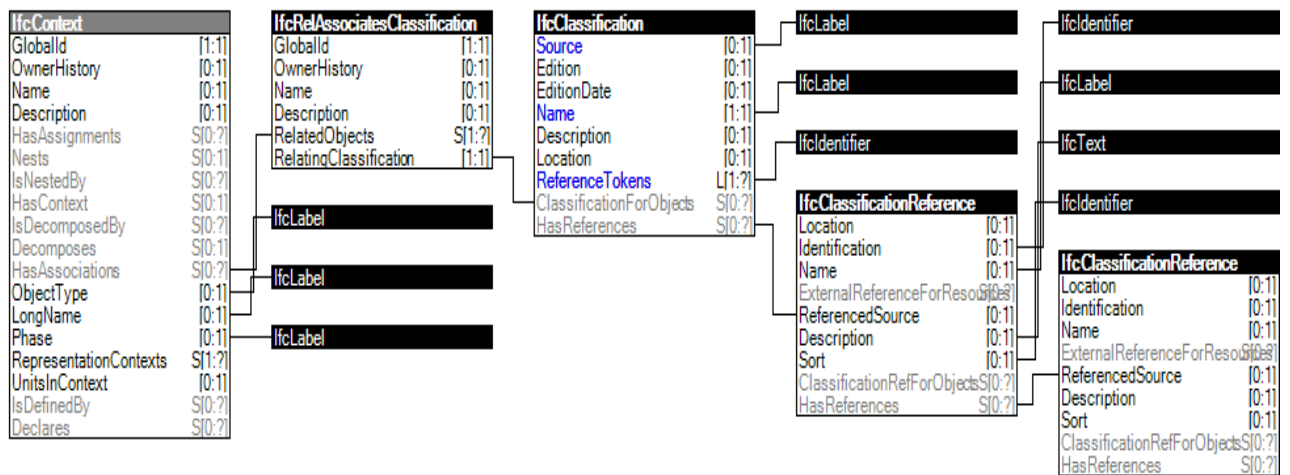


Figure 1. The structure of `IfcClassification` within BuildingSMART [14].

The interconnection of each Industry Foundation Classes (IFC) element allows the reliable and structured information transfer about construction objects, their components and classification among various software programs and systems. This promotes more efficient design, construction, operation and management of real estate. Therefore, the open format is the most suitable for the encoding process for subsequent data processing.

The purpose of this study was to find an effective machine learning model for automated classification of elements in the open cross-industry standard, Industry Foundation Classes (IFC).

2. Methods

The classification process in the formation of a building information model today can be organized manually, semi-automatically and automatically [15]. An automatic method, based on machine learning techniques was considered to solve the classification and coding tasks. Machine learning as a subfield of artificial intelligence (AI) focused on developing algorithms and models capable of learning and making predictions based on data. This technology enables to analyze the large volumes of data and to discover the hidden patterns by grouping data based on similarity without predefined categories. It also involves training models on labeled data, where both input and corresponding output data are known.

There was made decision to use neural networks, which belong to deep learning, to find a high-quality machine learning model. Neural networks utilize interconnected nodes or neurons in a layered structure, resembling the human brain.

In this research, convolutional neural networks (CNN) and recurrent neural networks (RNN) were analyzed as the primary options in the search for a suitable machine learning model for classifying elements in information models [16, 17].

Recurrent Neural Networks (RNN) are a class of deep neural networks widely used in processing sequential data such as texts and time series. There are several variants of RNNs, including standard RNNs, Long Short-Term Memory (LSTM), and Gated Recurrent Unit (GRU). For the classification task the most effective recurrent neural network was LSTM (Long Short-Term Memory), an advanced type of RNN, known for its powerful capabilities in analyzing sequential data [18].

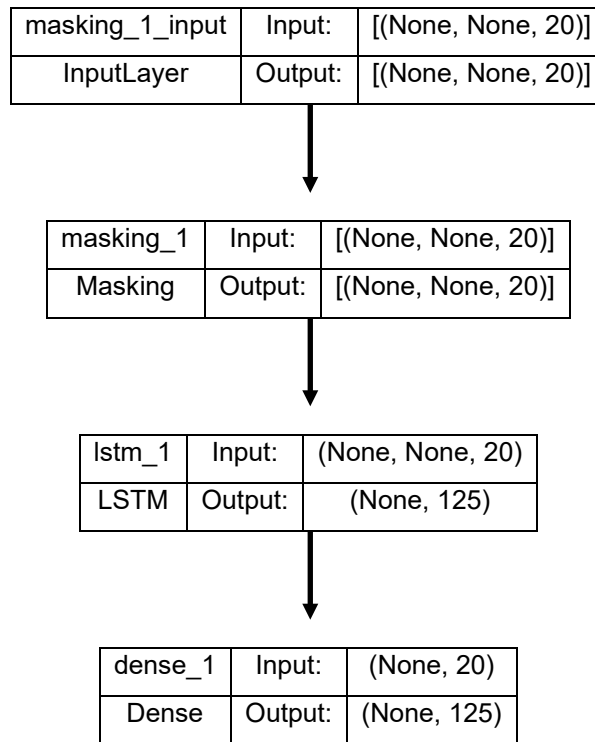


Figure 2. LSTM Architecture.

During the testing this neural network the prediction accuracy did not reach 30 % (Fig. 2). It has taken 2.5 hours to train the specified configuration. For this reason, it was hypothesized that approaches based solely on LSTM are not suitable for the considered case or, at the very least, not for the considered method of extracting information from the text. As a result, the study of recurrent networks was finished without achieving acceptable results.

The next research stage involved the consideration the various variations of Convolutional Neural Networks (CNNs). It is a class of deep neural networks, designed for processing and analyzing data related to images and videos and are also effectively used in text classification: CNN_1 and CNN_2.

CNN_1 was presented as local features with the summation of responses from different parts of the input (Fig. 3).

The implementation used keras-2.10.0 (tensorflow-2.10.0). The activation function on the final layer was 'softmax'. Activation functions were not applied on the other layers, they were linear. L1 regularization was applied on the first of the fully connected layers (default coefficient = 0.01). Class weights were not specified, as specifying them resulted in reduced accuracy due to a preference for less common classes in disputed situations. The number of epochs was set to 5.

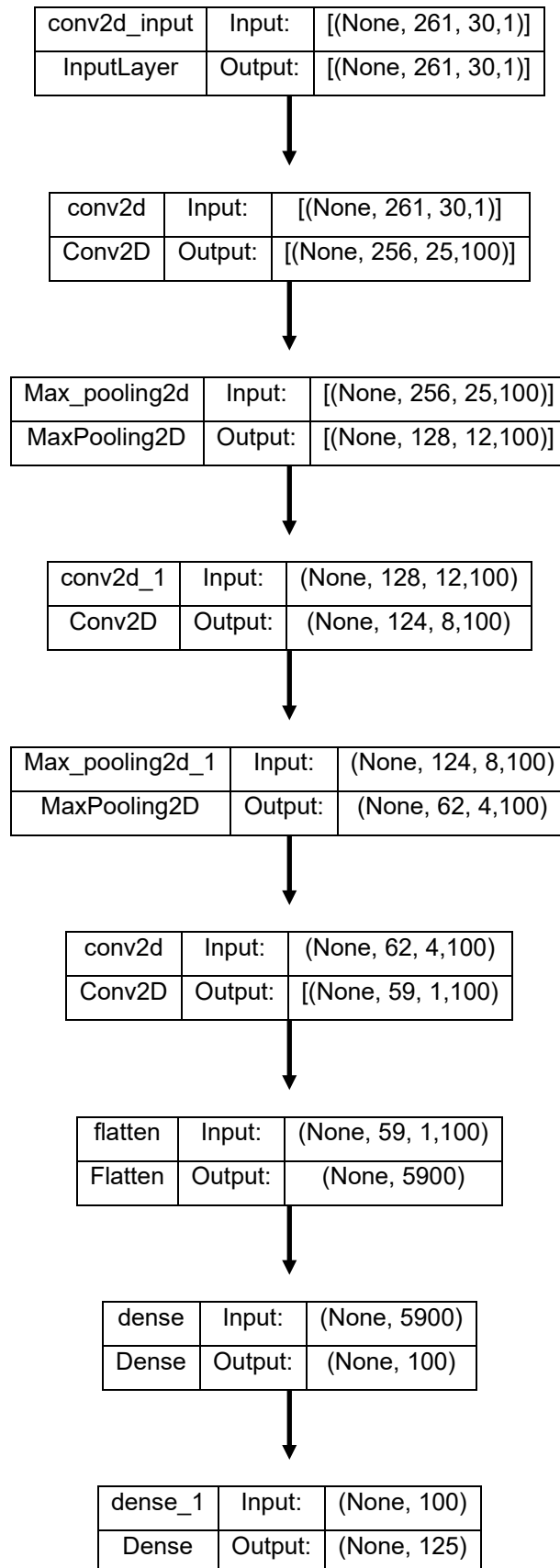


Figure 3. CNN_1 Architecture.

CNN_2 was characterized by the extraction of local features without considering responses from other positions (Fig. 4).

The implementation used keras-2.10.0 (tensorflow-2.10.0). The activation function on the final layer was 'softmax', and on the other layers, it was linear. Class weights were not specified, as specifying them resulted in reduced accuracy due to a preference for less common classes in disputed situations. The number of epochs was set to 5.

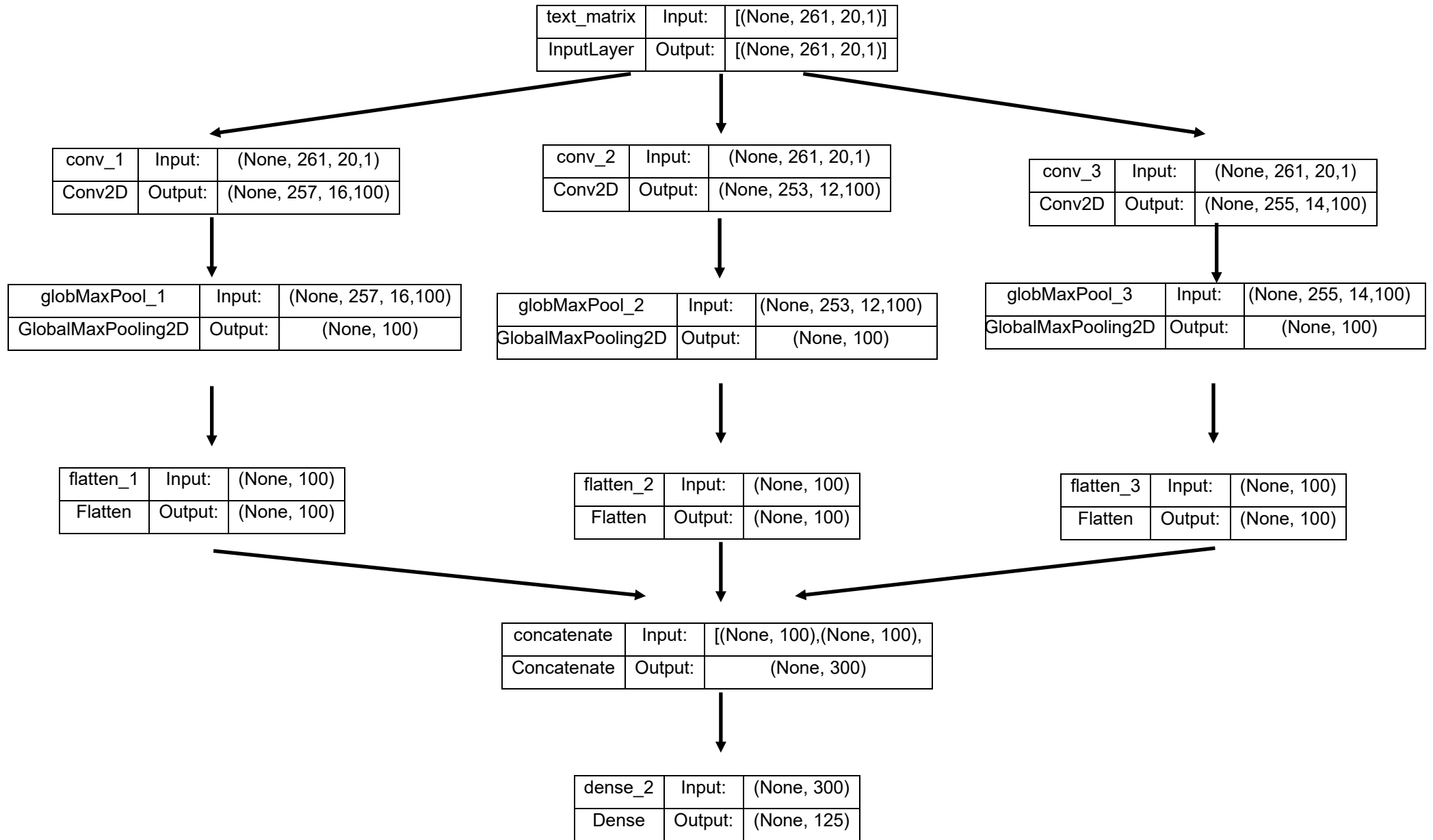


Figure 4. CNN_2 Architecture.

Both CNN configurations were trained in 10 minutes on Google Colab. The average prediction time was 1 ms per record (taking into account preprocessing of the received record).

In the next stages, machine learning models were considered, that use record correction. One of them is the Naive Bayes classifier – a statistical machine learning algorithm used for classification tasks. It is based on Bayes' theorem and makes a "naive" assumption of independence among features, which may not hold true in real data but makes the algorithm computationally efficient and easy to implement. The main idea of the algorithm is to use Bayes' theorem to estimate the probability of an object belonging to a particular class based on its features [19]:

$$P(\text{Class}|\text{Features}) = \frac{P(\text{Features}|\text{Class}) * P(\text{Class})}{P(\text{Features})},$$

where $P(\text{Class}|\text{Features})$ is the conditional probability that an object belongs to a class given the available features; $P(\text{Features}|\text{Class})$ is the conditional probability of having those features if the object indeed belongs to the given class; $P(\text{Class})$ is the prior probability of the class, i.e., the probability of an object belonging to that class without considering any features; $P(\text{Features})$ is the marginal probability of the features occurring, regardless of the class.

The algorithm made the naive assumption of feature independence. It means, that the probability of all features occurring in a class was calculated as the product of the probabilities of each feature occurring in that class. After training, the Naive Bayes classifier used probability estimates to determine the class of a new object, selecting the class with the highest probability.

During the testing, it was assumed, that the same words in the elements descriptions of different classes occurred with different probabilities. As a result, conditional probabilities were used for class prediction. An implementation of the Naive Bayes algorithm from scikit-learn v1.1.2 was used.

The next considered machine learning algorithm was the Random Forest, which builds multiple decision trees during training. Each tree was trained on a random subsample of the data (with replacement) and a subset of features, making each tree in the ensemble different [20]. For classification, each tree in the ensemble voted for the predicted class and the class with the most votes became the final prediction of the algorithm.

An implementation from scikit-learn v1.1.2 was used with 500 trees, maximum depth of 100, minimum samples per leaf set to 2, minimum samples for node splitting set to 4, bootstrap samples were used, class weights were computed inversely proportional to the class frequencies in the subsample for each tree separately ('balanced_subsample') and other parameters remained at their defaults.

Additionally, simple argmax was applied to the "vector of class probabilities." This approach was based on the idea that each word could be associated with a set of classes in which it appeared during training. Initially, each word was associated with a vector of zeros, the length of which was determined by the number of classes. Each class corresponded to a position in the vector. If a word appeared in the descriptions of elements in a particular class, a 1 was placed in the corresponding cell. Finally, vector normalization was performed using l_1 normalization. In this case, words corresponding to a smaller set of classes had higher significance.

When working with the recordings, all word vectors were summed and l_1 normalization was performed, resulting in a "vector of class probabilities" for each recording.

This approach should not be perceived as a standalone classification method due to the low likelihood of achieving good results. However, it is important to consider that, in general, this method can be used as a way to extract information from the text.

The method had an obvious drawback: two words that appeared in the same set of classes but with different probabilities were indistinguishable. Using the values in vectors corresponding to words as the proportion of class elements in which the word appeared led to a decrease in the accuracy of models built upon this approach. Less frequent classes with lower diversity tended to attract elements from more frequent classes with higher diversity.

On the next stage a random forest was applied to the "vector of class probabilities" – implemented with scikit-learn v1.1.2. The number of trees was 400, the maximum depth was 100, the minimum number of elements in a leaf was 2, the minimum number of elements for node splitting was 4, bootstrap samples were used and class weights were calculated inversely proportional to the class frequency in the subsample for each tree separately ('balanced_subsample'). Other parameters were kept at their defaults.

The CatBoost model was applied to the "vector of class probabilities" using catboost-1.1.1 with the following parameters:

- loss_function = 'MultiClass', learning_rate = 0.05, n_estimators = 2000, max_depth=7,
- auto_class_weights='Balanced', while other parameters remained at their defaults.

The use of boosting for other models was not applied, as it would lead to overfitting for strong classifiers. For example, the vectors of probabilities obtained from random forests did not generally allow distinguishing incorrectly predicted objects from those correctly predicted because they were too similar.

The training time for the considered models varied from 3 to 20 minutes, with the Bayesian algorithm being the quickest to train (due to data preprocessing) and CatBoost being the slowest. The average prediction time ranged from 1 ms for the Bayesian algorithm to 1.6 ms for CatBoost (considering data preprocessing).

3. Results and Discussion

As a result of testing the convolutional neural networks, CNN_1 showed an average F1-score of 0.9474 for class prediction, where the "FSC" code was not recognized. As a result, elements belonging to this class were not subsequently encoded.

Next, the Convolutional Neural Network CNN_2 was tested, CNN_2 showed a lower average F1-score compared to CNN_1, with an F1-score (macro) of 0.9037, resulting in an increased number of unrecognized classes including "BUA", "KNA" codes.

The results of testing Convolutional Neural Networks (CNN) were summarized in Table 1, including accuracy and F1-score (macro) values.

Table 1. Testing convolutional neural networks.

	CNN_1	CNN_2
accuracy	0.9904	0.9885
F1-score (macro)	0.9474	0.9037

During testing, the Naive Bayes classifier (complementNB) using record correction showed an F1-score (macro) of 0.8627, with a larger number of classes not being recognized compared to neural networks. Elements belonging to classes of "FSC", "NAB", "NED", "WMC" were not encoded.

After the Complement Naive Bayes the Random Forest was tested. The average F1-score (macro) during testing of the Random Forest was 0.9484, which resulted in higher prediction accuracy compared to the Naive Bayesian classifier. Only code RUA was not recognized.

When using a straightforward argmax approach on the "vector of class probabilities," the average F1-score was slightly lower than Random Forest, at 0.9249, but some classes "FSC", "NAB" went unrecognized.

Random Forest using the "probability class vector" achieved 0.9717, providing nearly perfect accuracy in predicting codes 0.9947.

CatBoost with "class probability vector" exhibited the highest F1-score among other models, reaching 0.9749 with a maximum accuracy of 0.9956.

The results of models using record correction are summarized in Table 2.

Table 2. Results of models using record correction.

	Bayesian classifier	Random Forest	Simple argmax extraction on the "vector of class probabilities"	Random Forest on the "vector of class probabilities"	CatBoost on the "vector of class probabilities"
accuracy	0.9645	0.9875	0.9723	0.9947	0.9956
F1-score (macro)	0.8627	0.9484	0.9249	0.9717	0.9749

As a result of the research, among the models that do not use record correction, the Convolutional Neural Network CNN_1 was chosen due to its higher accuracy of 0.99 and F-score of 0.95. Among the models that use record correction, CatBoost was selected with the following characteristics: accuracy of 0.9956 and F1-score of 0.9749.

The results of the research coincided with previous studies, the Convolutional Neural Networks demonstrate high accuracy in natural language processing [21], CatBoost surpasses other publicly available

implementations of quality improvement in terms of quality on various datasets among the models that use record correction [22].

For practical application, software named "Impulse" was developed, allowing the encoding of elements in formats such as rvt, tekla, and ifc based on the user's chosen classifier.

To effectively use the "Impulse" platform for automatically assigning codes to model elements based on a specific classifier, the following stages are anticipated (Figure 5):

1. Classifier selection for encoding;
2. Selection of attributes for code recording;
3. Identification of elements subject to further classification;
4. Automatic encoding;
5. Validation and correction of assigned codes;
6. Writing codes to the attributes of information model elements.

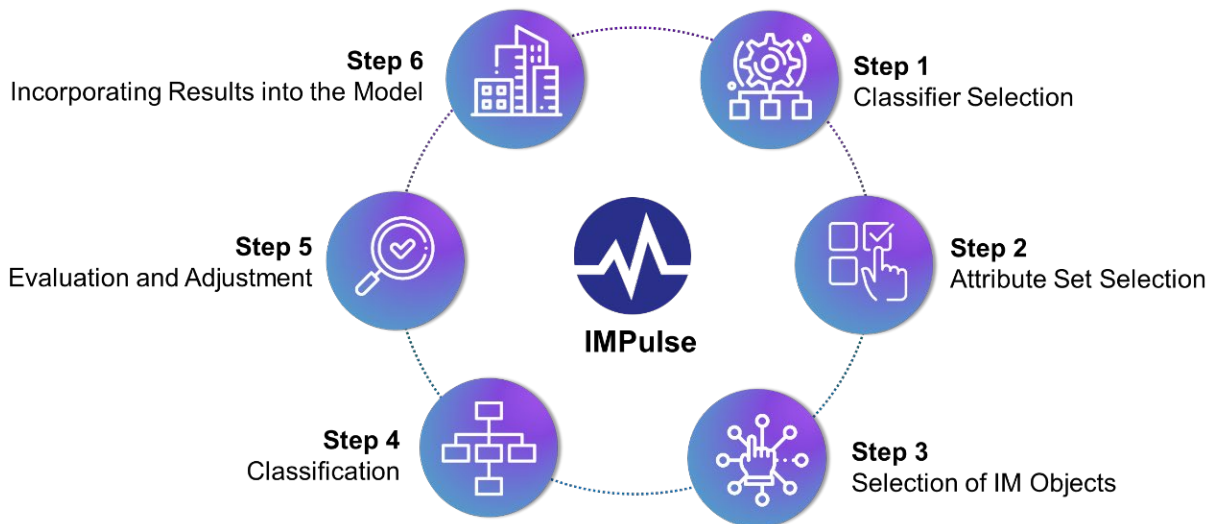


Figure 5. Workflow of the "Impulse" Application.

The algorithm of the system with a machine learning model consists of stages, depicted in Figure 6. When unclassified data appears, a specialist further trains the model by manually inputting the code into the attribute through the application or by selecting a code suggested by the system, resulting in labeled elements becoming training data for the machine learning algorithm.

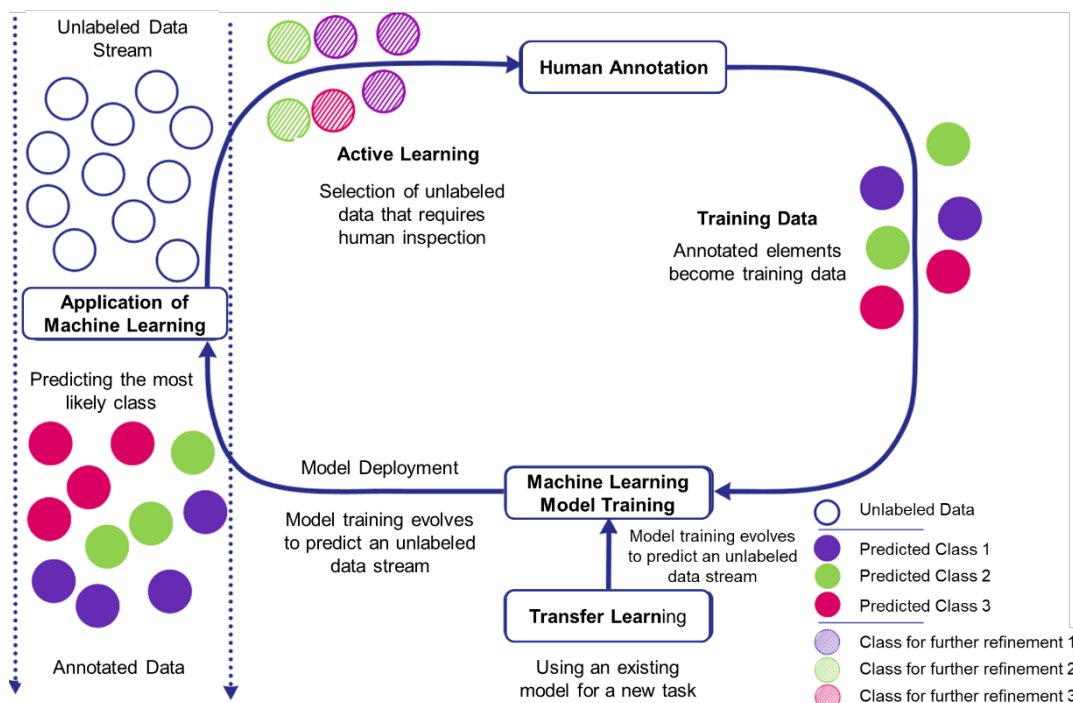


Figure 6. Architecture of the "Impulse" Software.

During the validation and adjustment of the selected code for a clear representation of the numeric characteristic, "Impulse" displays a confidence level – a metric that reflects the frequency of encoding an element with similar attributes using the predicted code (Figure 7). The confidence level allows specialists to identify and recognize incorrectly selected codes and replace them with the correct ones by retraining the model.

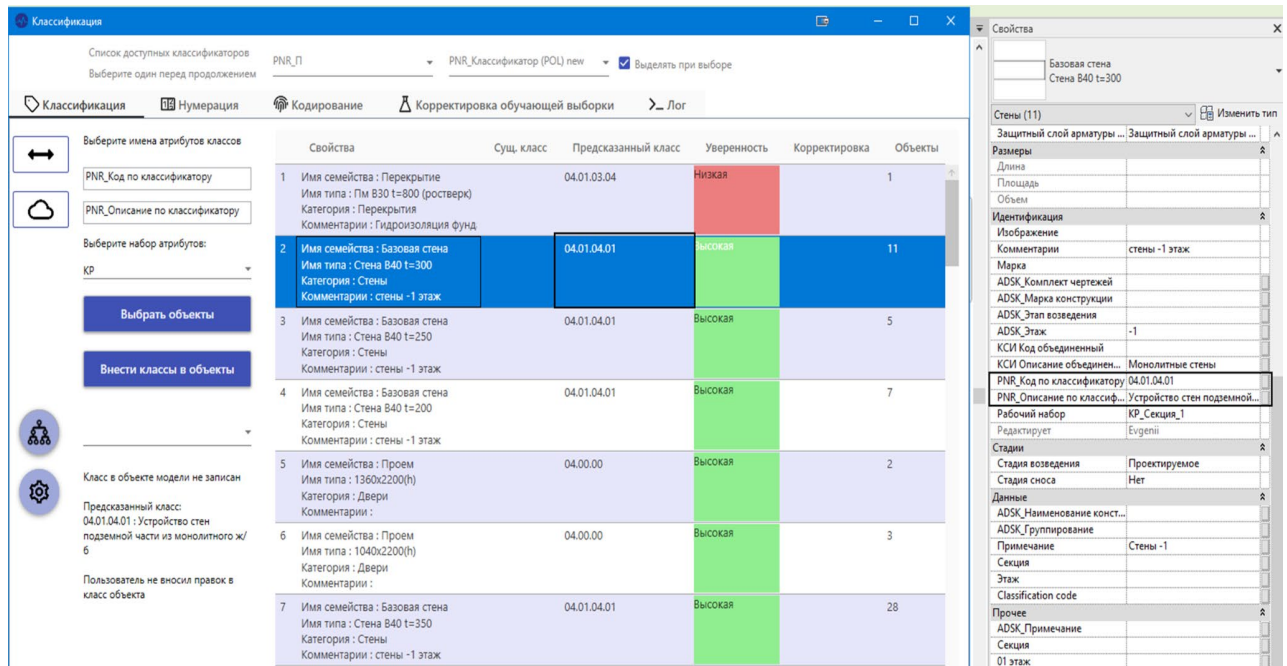


Figure 7. User Interface of the "Impulse" Software.

Code recording can be done in both user-defined attributes and in the root IFC classification class, enabling navigation from code to all elements with the same code and vice versa (Figure 8).

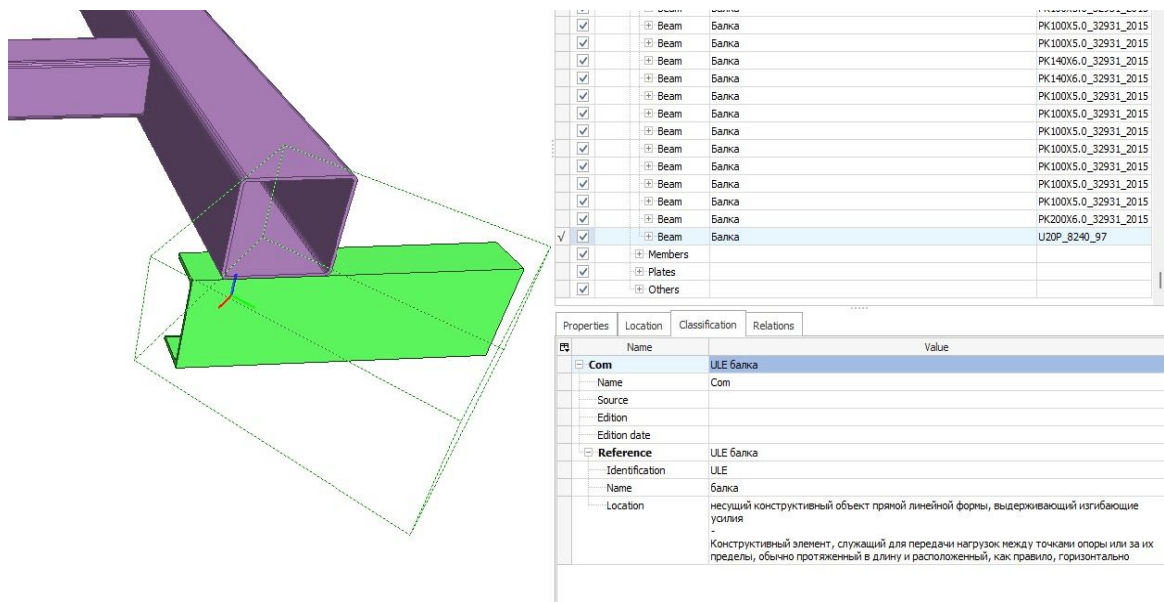


Figure 8. Code Recording Using the "Impulse" Software.

There was conducted a building information models (BIM) classification of civil and industrial objects with a specific number of elements in each model to test the "Impulse" software, based on machine learning models. The steps were following:

- training the machine learning model on a sample group of elements;
- classification the selected group of elements, validation and correction the codes obtained;
- encoding the remaining elements or the next group of the information model.

There was made an element-by-element classification to compare the time spent on encoding BIM elements using the "Impulse" tool and the manual method. The results were summarized in Table 3.

Analyzing the obtained results, the automated classification process showed a reduction in time compared to manual coding by an average factor of 2.54.

Table 3. Comparison of "Impulse" Automated Classification and Manual Classification.

№ of Information Model	Stage	Work in "Impulse" Software				Time Spent on Manual Classification, min	
		Total Number of Groups, pcs.	Number of Incorrectly Predicted Elements, pcs.	Accuracy, %	Time Spent on Stage, min.		Total Time Spent on Automatic Classification, min.
1	Stage 1 (Training)	255	-	-	17	66	136
	Stage 2 (Validation and Retraining)	255	66	74.1	15		
	Stage 3 (Validation and Retraining)	255	157	38.4	14		
	Stage 4 (Validation and Retraining)	255	96	62.4	12		
	Stage 5 (Validation)	255	22	91.4	8		
2	Stage 1 (Training)	884	-	-	45	111	175
	Stage 2 (Validation and Retraining)	884	26	97.1	36		
	Stage 3 (Validation and Retraining)	884	27	96.9	19		
	Stage 4 (Validation)	884	11	98.8	11		
3	Stage 1 (Training)	86	-	-	4	9	24
	Stage 2 (Validation and Retraining)	86	8	90.7	3		
	Stage 3 (Validation)	86	0	100.0	2		
4	Stage 1 (Training)	155	-	-	9	24	56
	Stage 2 (Validation and Retraining)	155	5	96.8	5		
	Stage 3 (Validation and Retraining)	155	6	96.1	4		
	Stage 4 (Validation and Retraining)	155	18	88.4	4		
	Stage 5 (Validation)	155	9	94.2	2		
5	Stage 1 (Training)	443	-	-	23	63	136
	Stage 2 (Validation and Retraining)	443	53	88.0	20		
	Stage 3 (Validation and Retraining)	443	49	88.9	13		
	Stage 4 (Validation)	443	19	95.7	7		

№ of Information Model	Work in "Impulse" Software						Time Spent on Manual Classification, min
	Stage	Total Number of Groups, pcs.	Number of Incorrectly Predicted Elements, pcs.	Accuracy, %	Time Spent on Stage, min.	Total Time Spent on Automatic Classification, min.	
6	Stage 1 (Training)	68	-		4	8	25
	Stage 2 (Validation)	68	0	100.0	2		
7	Stage 1 (Automatic Classification and Validation)	201	112	44.3	14	26	74
	Stage 2 (Validation)	201	2	99.0	7		
	Stage 3 (Model Update after Refinement and Validation)	186	2	98.9	5		
8	Stage (Automatic Classification and Validation)	372	277	25.5	10	10	34
9	Stage (Automatic Classification and Validation)	248	150	39.5	5	5	17

4. Conclusions

The conducted research resulted in a numerical comparative analysis of classification models: models without data correction - convolutional neural networks and models with data correction – Naive Bayes classifier, Random Forest, simple argmax extraction on the "class probability vector," random forest on the "class probability vector", and CatBoost on the "class probability vector".

As a result, the following machine learning models were chosen as effective for automated classification of elements in Information Models within the open cross-industry standard Industry Foundation Classes (IFC): CNN_1, which exhibited the highest accuracy and F-score, equal to 0.99 and 0.95, and CatBoost, with an accuracy of 0.9956 and an F1-score of 0.9749. The obtained research results exceed the accuracy of the forecasts in comparison with the results of other authors on the classification of elements of BIM models.

Software "Impulse" was developed for the practical implementation of these models. It is based on the selected algorithms and tested on civil and industrial purpose Information Models. The developed application has significantly reduced the classification time by an average of 2.54 times, improving the coding accuracy and reducing labor costs. It is recommended to use "Impulse" as a tool for automatic classification of Building Information Models for the substantial optimization the classification timelines and overall efficiency.

References

1. CSI, CSC, UniFormatTM: A Uniform Classification of Construction Systems and Assemblies, 2010.
2. CSI, CSC, MasterFormat® 2018 Edition: Master List of Numbers and Titles for the Construction Industry, 2018.
3. CSI, OmniClassTM: A Strategy for Classifying the Built Environment. Introduction and User's Guide, first ed., 2006
4. Crawford, M., Cann, J., O'Leary, R. Uniclass: Unified Classification for the Construction Industry, first ed. RIBA Publications Ltd, London, 1997.
5. Svensk Byggtjänst, A.B., "CoClass – Nya Generationen BSAB Klassifikation Och tillämpning, 2016. (in Swedish)
6. Pupeikis, D., Navickas, A.A., Klumbyte, E., Seduikyte, L. Comparative study of construction information classification systems: CCI versus Uniclass 2015. *Buildings*. 2022. 12(5). 656. DOI: 10.3390/buildings12050656
7. ICIS, Comparison of OmniClass, Uniclass, Cuneco and CoClass with Reference to ISO 12006-2 and ISO 81346-12, 2018. Zurich.
8. Knopp-Trendafilova, A., Suomi, J., Tauriainen, M. Link between a structural model of buildings and classification systems in construction, in: K. Belloni, Kojima Jun, I. Pinto-Seppä (Eds.). *Proceedings of the 1st International Conference on Improving Construction and Use through Integrated Design Solutions*. CIB IDS 2009, 2009. 259. Pp. 285–301.
9. Rakennustieto Oy, The Finnish Construction 2000 Classification System, 2016.
10. Volkodav, V.A., Volkodav, I.A. Development of the structure and composition of a building information classifier towards the application of BIM technologies. *Vestnik MGSU*. 2020. 15(6). Pp. 867–906. DOI: 10.22227/1997-0935.2020.6.867-906
11. Timchenko, V.S., Volkodav, V.A., Volkodav, I.A., Timchenko, O.V., Osipov, N.A. Development of classification tables "Process management", "Design processes" and "Information" of the classifier of construction information for creating and maintaining information models of capital construction objects. *Vestnik MGSU*. 2021. 16(7). Pp. 926–954. DOI: 10.22227/1997-0935.2021.7.926-954
12. Qiu, Q., Zhou, X., Zhao, J., Yang, Y., Tian, Sh., Wang, J., Liu, J., Liu, H. From sketch BIM to design BIM: An element identification approach using Industry Foundation Classes and object recognition. *Building and Environment*. 2021. 188. 107423. DOI: 10.1016/j.buildenv.2020.107423
13. Park, S.I., Lee, S.-H., Almasi, A., Song, J.-H. Extended IFC-based strong form meshfree collocation analysis of a bridge structure. *Automation in Construction*. 2020. 119. 103364. DOI: 10.1016/j.autcon.2020.103364
14. BuildingSMART International, 2020. <https://standards.buildingsmart.org/IFC/RELEASE/IFC4/FINAL/HTML/link/project-classification-information.htm> (Accessed 14 September 2023).
15. Petrochenko, M.V., Nedviga, P.N., Kukina, A.A., Sherstyuk, V.V. Classification of information models in BIM using artificial intelligence algorithms. *Vestnik MGSU*. 2022. 17(11). DOI: 10.22227/1997-0935.2022.11
16. Huang, Sh.-Yu., An, W.-J., Zhang, D.-Sh, Zhou, N.R. Image classification and adversarial robustness analysis based on hybrid quantum-classical convolutional neural network. *Optics Communications*. 2023. 533. 129287. DOI: 10.1016/j.optcom.2023.129287
17. Babalhavaeji, A., Radmanesh, M., Jalili, M., Gonzalez, S.A. Photovoltaic generation forecasting using convolutional and recurrent neural networks. *Energy Reports*. 2023. 9. Suppl. 12. Pp. 119–123. DOI: 10.1016/j.egy.2023.09.149
18. Ahmad, M.W., Mourshed, M., Rezgui, Ya. Tree-based ensemble methods for predicting PV power generation and their comparison with support vector regression. *Energy*. 2018. 164. Pp. 465–474. DOI: 10.1016/j.energy.2018.08.207
19. Diab, D.M., El Hindi, K.M. Using differential evolution for fine tuning naïve Bayesian classifiers and its application for text classification. *Applied Soft Computing*. 2017. 54. Pp. 183–199. DOI: 10.1016/j.asoc.2016.12.043
20. Sun, Zh., Wang, G., Li, P., Wang, H., Zhang, M., Liang, X. An improved random forest based on the classification accuracy and correlation measurement of decision trees. *Expert Systems with Applications*. 2024. 237. Part B. 121549. DOI: 10.1016/j.eswa.2023.121549
21. Kane, B., Rossi, F., Guinaudeau, O., Chiesa, V., Quénel, I., Chau, S., Joint intent detection and slot filling via CNN-LSTM-CRF. 2020 6th IEEE Congress on Information Science and Technology. *CiSt*, 2020. Pp. 342–347. DOI: 10.1109/CiSt49399.2021.9357183
22. Song, Ch.M. Data construction methodology for convolution neural network based daily runoff prediction and assessment of its applicability. *Journal of Hydrology*. 2022. Vol. 605. 127324. DOI: 10.1016/j.jhydrol.2021.127324

Information about authors:

Marina Petrochenko, PhD in Technical Sciences

ORCID: <https://orcid.org/0000-0002-4865-5319>

E-mail: mpetroch@mail.ru

Pavel Nedviga,

E-mail: pavel.nedviga@gmail.com

Anna Kukina,

ORCID: <https://orcid.org/0000-0003-4271-7408>

E-mail: kukina_aa@spbstu.ru

Kseniya Strelets, PhD in Technical Sciences

E-mail: kstrelets@mail.ru

Valeriya Sherstyuk,

ORCID: <https://orcid.org/0000-0002-5644-5629>

E-mail: sherstyuk2.vv@yandex.ru

Received 24.10.2023. Approved after reviewing 29.12.2023. Accepted 29.12.2023.



Research article

UDC 69.04

DOI: 10.34910/MCE.126.3



Validating the predicted axial strength of FRP-reinforced concrete circular columns

M.Q. Kadhim , H.F. Hassan 

College of Engineering, Mustansiriyah University, Baghdad, Iraq

✉ mohamedq1992@uomustansiriyah.edu.iq

Keywords: fiber reinforced polymers, axial load, circular columns, spirals, hoops, experimental load

Abstract. Over the last three decades, researchers have significantly contributed to advancing fiber-reinforced polymer (FRP) bars to address corrosion issues in conventional steel reinforcement bars embedded in components of reinforced concrete structures. This research aimed to establish an ideal allowable axial compression load for concrete columns reinforced with FRP using data from previous studies. This article compares and explains the contrasts of several of the most popular FRP codes (ACI, CSA, and JSCE) with one equation proposed in previous research using empirical information gleaned from the literature review. The models' statistical analysis compares theoretical and practical loads, Young's modulus, concrete strength, longitudinal reinforcement ratio, and transverse reinforcement ratio for hoops and spirals. Estimating the effect of FRP longitudinal bars on the applied load carried by FRP-reinforced concrete columns can be done with the help of an empirical equation that uses the compressive strength of concrete to estimate the axial stress of FRP longitudinal bars in concrete columns. Results from the CSA and the ACI were almost similar, and both were superior to those from the JSCE in terms of being ideal, consistent, and safe. The results for modulus of elasticity, concrete compressive strength, and transverse reinforcement ratio for spiral reinforcement were more stable, according to the CSA. In contrast, according to the ACI, results for longitudinal and transverse reinforcement ratios of hoop reinforcement were more stable and secure. Lastly, the previously proposed equation is the best way to determine the transverse reinforcement ratio for hoop reinforcement and the compressive strength of concrete from all codes. In conclusion, the previously proposed equation is the most effective for calculating the transverse reinforcement ratio for hoop reinforcement and compressive strength.

Citation: Kadhim, M.Q., Hassan, H.F. Validating the predicted axial strength of FRP-reinforced concrete circular columns. Magazine of Civil Engineering. 2024. 17(2). Article no. 10.34910/MCE.126.3. DOI: 10.34910/MCE.126.3

1. Introduction

The primary function of a reinforced concrete column is to sustain axial loads with or without bending moments. Due to the corrosion of steel bars, the axial load-carrying capacity of steel bar-reinforced concrete columns decreases over the concrete structures' service life, especially in coastal regions or harsh environments. The cost of rehabilitating and repairing deteriorated concrete structures is significantly high [1]. The literature review found that FRP composites can be used in various civil/structural applications. The FRP composites have various structural forms that can be classified into two main classes: 1) external reinforcement (FRP jacketing) and 2) internal reinforcement (FRP reinforcing bars). There are four common varieties of FRP: aramid (AFRP), basalt (BFRP), glass (GFRP), and carbon (CFRP) fibers, all encased in the polymer [2, 3]. FRP composites, including FRP bars, possess many advantageous characteristics, such as resistance to harsh environmental conditions, lightweight, and high tensile strength [4, 5]. Hence, FRP bars have the potential to replace steel bars and overcome the deterioration of concrete structures associated with the corrosion of steel reinforcement. However, using FRP bars as reinforcement in

compression members is still not recommended. This is because the FRP bar's ultimate compressive strength is considerably lower than its ultimate tensile strength [6]. De Luca et al. [7] investigated five square concrete columns subjected to axial load. They concluded that GFRP bars could be used in columns, but their contribution could be ignored when calculating nominal capacity. Moreover, they found that GFRP hoops did not grow longitudinal bars' ultimate capacity but reduced their bend. Kobayashi and Fujisaki [8] conducted experiments with bars made of AFRP, CFRP, and GFRP. The compressive strengths of CFRP, AFRP, and GFRP reinforcement bars were 30–50 %, 10 %, and 30–40 % of their tensile strength, respectively. Deitz et al. [9] conducted compression tests on 45 GFRP bars (15-mm diameter with unbraced lengths varying from 50 to 380 mm). Based on the experiments' outcomes, the average ultimate compressive strength was nearly 50% of the average ultimate tensile strength. However, the compression modulus was about the same as that of tension. Alsayed et al. [10] tested fifteen 450×250×1200 mm concrete columns under concentric axial loads to determine the effect of replacing longitudinal and transverse steel reinforcing bars with an equivalent amount of GFRP reinforcement. GFRP reinforcing bars reduced column axial capacity by 13 %. GFRP hoops reduced axial capacity by 10%, regardless of the longitudinal bar type. Up to 80% of the column's ultimate capacity, replacing steel hoops with GFRP hoops did not affect load deformation. Tobbi et al. [11] and Afifi et al. [12] reported that GFRP and CFRP longitudinal bars can contribute up to 10% and 13%, respectively, to the axial load-carrying capacity of the concrete columns. Hadhood et al. [13] conducted an experimental investigation on the concentric and eccentric behavior of full-scale circular high-strength concrete (HSC) columns reinforced with GFRP bars and spirals. A total of 10 columns were tested under monotonic loading with different eccentricities. The test variables were the eccentricity-to-diameter ratio and the longitudinal-reinforcement ratio. Compression failure in the concrete controlled the ultimate capacity of specimens tested under small eccentric loads. However, a flexural-tension failure initiated in specimens tested under high eccentric loading resulted from excessive axial and lateral deformations and cracks on the tension side until a secondary compression and stability failure occurred due to the concrete's strain limitations. Longitudinal GFRP bars contributed about 5% of the axial load capacity of GFRP-HSC columns. Hadi et al. [14] conducted a study on the use of GFRP bars in HSC. It was observed that the GFRP bar-reinforced HSC specimens sustained a similar axial load under concentric axial compression compared to their steel counterparts, but the efficiency of GFRP bar-reinforced HSC specimens in sustaining axial loads decreased with an increase in the axial load eccentricity. Direct replacement of steel reinforcement with the same amount of GFRP reinforcement in HSC specimens resulted in about 30% less ductility under a concentric axial load. In CAN/CSA S806-12 [15] or ACI 440.1R-15 [16], no theoretical equation was proposed to predict the maximum axial load capacity of FRP bar-reinforced concrete columns. This is because of the variances in the reported ultimate compressive strength of the FRP bars and their contribution as longitudinal reinforcement in concrete columns. However, previous research gave many theoretical equations for predicting the maximum axial loads that FRP bar-reinforced concrete columns could carry. The issue of utilizing FRP as a substitute for traditional reinforcing steel in compression members has yet to be evaluated through available equations and whether these equations can be used for design purposes. As we mentioned, there are available equations, but they have yet to be evaluated through many models. Thus, in this research, we will evaluate the most prominent four equations to determine the validity of their use for design purposes based on a wide range of experimental data collected from previous studies. This statistical analysis predicted the maximum axial load capacity of concrete columns reinforced longitudinally with FRP bars and studied other factors based on many codes and one significant suggested equation from earlier studies.

Table 1. Experimental data of FRP bar reinforced concrete columns taken from available previous research studies.

No.	The specimen reference	Specimen cross-section			FRP longitudinal reinforcement				FRP transverse reinforcement		f'_c (MPa)
		Specimen	Column shape	Diameters (mm)	Type	ρ_{fl} (%)	f_{fu} (MPa)	E_f (MPa)	Type	ρ_{ft} (%)	
1	Pantelides et al. [17]	#13GLCT L	Circular	254	GFRP bars	1.60	740	43300	GFRP spirals	1.70	36
2		#14GLCT L	Circular	254	GFRP bars	1.60	740	43300	GFRP spirals	1.70	36
3	Afifi et al. [12]	C6V-3H80	Circular	300	CFRP bars	1.00	1899	140000	CFRP spirals	1.50	42.90
4		C10V-3H80	Circular	300	CFRP bars	1.70	1899	140000	CFRP spirals	1.50	42.90
5		C14V-3H80	Circular	300	CFRP bars	2.40	1899	140000	CFRP spirals	1.50	42.90
6		C10V-2H80	Circular	300	CFRP bars	1.70	1899	140000	CFRP spirals	0.70	42.90
7		C10V-4H80	Circular	300	CFRP bars	1.70	1899	140000	CFRP spirals	2.70	42.90

No.	The specimen reference	Specimen cross-section			FRP longitudinal reinforcement			FRP transverse reinforcement		f'_c (MPa)	
		Specimen	Column shape	Diameters (mm)	Type	ρ_{fl} (%)	f_{fu} (MPa)	E_f (MPa)	Type		ρ_{ft} (%)
8		C10V-3H40	Circular	300	CFRP bars	1.70	1899	140000	CFRP spirals	3.00	42.90
9		C10V-3H120	Circular	300	CFRP bars	1.70	1899	140000	CFRP spirals	1.00	42.90
10		C10V-2H35	Circular	300	CFRP bars	1.70	1899	140000	CFRP spirals	1.50	42.90
11		C10V-4H145	Circular	300	CFRP bars	1.70	1899	140000	CFRP spirals	1.50	42.90
12		G8V-3H80	Circular	300	GFRP bars	2.20	934	55400	GFRP spirals	1.50	42.90
13		G4V-3H80	Circular	300	GFRP bars	1.10	934	55400	GFRP spirals	1.50	42.90
14		G12V-3H80	Circular	300	GFRP bars	3.20	934	55400	GFRP spirals	1.50	42.90
15		G8V-2H80	Circular	300	GFRP bars	2.20	934	55400	GFRP spirals	0.70	42.90
16	Affi et al. [18]	G8V-4H80	Circular	300	GFRP bars	2.20	934	55400	GFRP spirals	2.70	42.90
17		G8V-3H40	Circular	300	GFRP bars	2.20	934	55400	GFRP spirals	3.00	42.90
18		G8V-3H120	Circular	300	GFRP bars	2.20	934	55400	GFRP spirals	1.00	42.90
19		G8V-2H35	Circular	300	GFRP bars	2.20	934	55400	GFRP spirals	1.50	42.90
20		G8V-4H145	Circular	300	GFRP bars	2.20	934	55400	GFRP spirals	1.50	42.90
21		G2S	Circular	300	GFRP bars	2.24	934	55400	GFRP spirals	0.70	42.90
22		G3S	Circular	300	GFRP bars	2.24	934	55400	GFRP spirals	1.50	42.90
23		G4S	Circular	300	GFRP bars	2.24	934	55400	GFRP spirals	2.70	42.90
24		G3H200	Circular	300	GFRP bars	2.24	934	55400	GFRP hoops	1.50	42.90
25		G3H400	Circular	300	GFRP bars	2.24	934	55400	GFRP hoops	1.50	42.90
26		G3H600	Circular	300	GFRP bars	2.24	934	55400	GFRP hoops	1.50	42.90
27	Mohamed et al. [19]	C2S	Circular	300	CFRP bars	1.79	1899	140000	CFRP spirals	0.70	42.90
28		C3S	Circular	300	CFRP bars	1.79	1899	140000	CFRP spirals	1.50	42.90
29		C4S	Circular	300	CFRP bars	1.79	1899	140000	CFRP spirals	2.70	42.90
30		C3H200	Circular	300	CFRP bars	1.79	1899	140000	CFRP hoops	1.50	42.90
31		C3H400	Circular	300	CFRP bars	1.79	1899	140000	CFRP hoops	1.50	42.90
32		C3H600	Circular	300	CFRP bars	1.79	1899	140000	CFRP hoops	1.50	42.90
33		G6-G60	Circular	205	GFRP bars	2.30	1600	66000	GFRP spirals	2.97	37
34		G6-G30	Circular	205	GFRP bars	2.30	1600	66000	GFRP spirals	5.94	37
35	Karim et al. [20]	00-G60	Circular	205	-	0.00	0.00	0.00	GFRP spirals	2.97	37
36		00-G30	Circular	205	-	0.00	0.00	0.00	GFRP spirals	5.94	37
37		C-8-00	Circular	250	GFRP bars	2.43	1184	62600	-	-	38
38		GGC-8-H50	Circular	250	GFRP bars	2.43	1184	62600	GFRP hoops	3.13	38
39	Maranan et al. [21]	GGC-8-H100	Circular	250	GFRP bars	2.43	1184	62600	GFRP hoops	1.57	38
40		GGC-8-H200	Circular	250	GFRP bars	2.43	1184	62600	GFRP hoops	0.78	38
41		GGC-8-S50	Circular	250	GFRP bars	2.43	1184	62600	GFRP spirals	3.13	38

No.	The specimen reference	Specimen cross-section			FRP longitudinal reinforcement			FRP transverse reinforcement		f'_c (MPa)	
		Specimen	Column shape	Diameters (mm)	Type	ρ_{fl} (%)	f_{fu} (MPa)	E_f (MPa)	Type		ρ_{ft} (%)
42		GGC-8-S100	Circular	250	GFRP bars	2.43	1184	62600	GFRP spirals	1.57	38
43		GGC-16-H100	Circular	250	GFRP bars	2.43	1184	62600	GFRP hoops	1.57	38
44		GGC-16-S100	Circular	250	GFRP bars	2.43	1184	62600	GFRP spirals	1.57	38
45	Hadi et al. [14]	G60E0	Circular	210	GFRP bars	2.19	1190	52000	GFRP spirals	2.94	85
46		G30E0	Circular	210	GFRP bars	2.19	1190	52000	GFRP spirals	5.88	85
47	Hadhood et al. [22]	C1-I	Circular	305	GFRP bars	2.18	1289	54900	GFRP spirals	1.44	35
48		C1-II	Circular	305	GFRP bars	3.27	1289	54900	GFRP spirals	1.44	35
49	Abdelazim et al. [23]	C1	Circular	305	GFRP bars	2.19	1449	61800	GFRP spirals	1.17	46.60
50		C2	Circular	305	GFRP bars	2.19	1449	61800	GFRP spirals	1.17	46.60
51		C3	Circular	305	GFRP bars	2.19	1449	61800	GFRP spirals	1.17	46.60
52		C4	Circular	305	GFRP bars	2.19	1449	61800	GFRP spirals	1.17	46.60
53		C5	Circular	305	GFRP bars	2.19	1449	61800	GFRP spirals	1.17	46.60
54	Raza et al. [24]	GH75-C	Circular	250	GFRP bars	1.57	794	50000	GFRP hoops	1.42	37.66
55		GH150-C	Circular	250	GFRP bars	1.57	794	50000	GFRP hoops	0.71	37.66
56		GS38-C	Circular	250	GFRP bars	1.57	794	50000	GFRP spirals	2.84	37.66
57		GS75-C	Circular	250	GFRP bars	1.57	794	50000	GFRP spirals	1.42	37.66
58	El-Gamal and Alshareedah [25]	G1 (6G12-G75)	Circular	230	GFRP bars	1.63	1113	62300	GFRP spirals	2.20	25.40
59		G6 (6G12-G75)	Circular	230	GFRP bars	1.63	1250	61400	GFRP spirals	2.20	25.40
60		G2 (8G12-G75)	Circular	230	GFRP bars	2.17	1113	62300	GFRP spirals	2.20	25.40
61		G3 (8G16-G75)	Circular	230	GFRP bars	3.87	1102	61200	GFRP spirals	2.20	25.40
62		G4 (6G12-G100)	Circular	230	GFRP bars	1.63	1113	62300	GFRP spirals	1.65	25.40
63	G5 (6G12-G50)	Circular	230	GFRP bars	1.63	1113	62300	GFRP spirals	3.30	25.40	
64	Elchalakani et al. [26]	G3-120-C	Circular	215	GFRP bars	0.55	930	59000	GFRP spirals	0.94	34
65		G4-120-C	Circular	215	GFRP bars	0.73	930	59000	GFRP spirals	0.94	34
66		G5-120-C	Circular	215	GFRP bars	0.92	930	59000	GFRP spirals	0.94	34
67		G4-40-C	Circular	215	GFRP bars	0.73	930	59000	GFRP spirals	2.75	34
68		G4-80-C	Circular	215	GFRP bars	0.73	930	59000	GFRP spirals	1.39	34
69	Elhamaymy et al. [27]	GCP-80S	Circular	304	GFRP bars	2.18	1389	52500	GFRP spirals	1.50	40
70		GCP-80S-22	Circular	304	GFRP bars	2.18	1389	52500	GFRP spirals	1.50	40
71		GCP-80S-60	Circular	304	GFRP bars	2.18	1389	52500	GFRP spirals	1.50	40
72		GCP-40S	Circular	304	GFRP bars	2.18	1389	52500	GFRP spirals	3.00	40
73		GCP-40S-22	Circular	304	GFRP bars	2.18	1389	52500	GFRP spirals	3.00	40
74		GCP-40S-60	Circular	304	GFRP bars	2.18	1389	52500	GFRP spirals	3.00	40
75		GCP-120S	Circular	304	GFRP bars	2.18	1389	52500	GFRP spirals	1.00	40

No.	The specimen reference	Specimen cross-section			FRP longitudinal reinforcement			FRP transverse reinforcement		f'_c (MPa)	
		Specimen	Column shape	Diameters (mm)	Type	ρ_{fl} (%)	f_{fu} (MPa)	E_f (MPa)	Type		ρ_{ft} (%)
76		GCP-120S-22	Circular	304	GFRP bars	2.18	1389	52500	GFRP spirals	1.00	40
77		GCP-120S-60	Circular	304	GFRP bars	2.18	1389	52500	GFRP spirals	1.00	40
78		GCP-80-O	Circular	304	GFRP bars	2.18	1389	52500	GFRP hoops	1.50	40
79		GCP-80-O-22	Circular	304	GFRP bars	2.18	1389	52500	GFRP hoops	1.50	40
80		GCP-80-O-60	Circular	304	GFRP bars	2.18	1389	52500	GFRP hoops	1.50	40
81	Bakouregui et al. [28]	G-8-0	Circular	305	GFRP bars	2.20	1289	54900	GFRP spirals	1.44	52
82		B-8-0	Circular	305	BFRP bars	2.20	1724	64800	GFRP spirals	1.44	52
83	Gouda et al. [29]	SC-6G-80	Circular	305	GFRP bars	1.63	1289	54900	GFRP spirals	0.95	34.70
84		SC-8G-80	Circular	305	GFRP bars	2.18	1289	54900	GFRP spirals	0.95	34.70
85		SC-12G-80	Circular	305	GFRP bars	3.27	1289	54900	GFRP spirals	0.95	34.70
86	Tang et al. [30]	fh-f-2	Circular	150	BFRP bars	5.50	1100	50000	BFRP spirals	7.30	65
87		fh-f-4	Circular	150	BFRP bars	5.50	1100	50000	BFRP spirals	3.70	53
88		fh-f-8	Circular	150	BFRP bars	5.50	1100	50000	BFRP spirals	1.80	42
89		fl-f-2	Circular	150	BFRP bars	3.10	1250	50000	BFRP spirals	7.30	55
90		fl-f-4	Circular	150	BFRP bars	3.10	1250	50000	BFRP spirals	3.70	43
91		fl-f-8	Circular	150	BFRP bars	3.10	1250	50000	BFRP spirals	1.80	35

f_{fu} is the ultimate tensile strength of FRP bars.

E_f is the modulus of elasticity of FRP bars.

f'_c is the compressive strength of the concrete.

2. Methods

A collection of 91 FRP RC columns that failed under axial compression was made to study their behavior in axial compression and evaluate the design codes and previously proposed equation [12, 14, 17–30]. Specimens had long and short columns. Data from many studies were clearly reported. However, other calculations used individual parameters to determine parameter values separately. The column results were unaffected. The compression design parameters are summarized in Table 2. The column diameter D was 150–305 mm. Diameter cores D_c range from 104 to 237.2 mm. Column lengths L varied from 300 mm to 2,500 mm. During the test day, the concrete cylinder strength, f'_c , was between 25.4 and 85 MPa. The gross area, A_g was found to be in the range from 17671.46 to 73061.66 mm² where it was reported. The longitudinal reinforcement ratio ($\rho_{fl} = n \times A_b / A_g$), where n is the number of longitudinal reinforcements, A_b is the area of the FRP bar, and A_g is the gross sectional area, was between 0.00 and 5.5 %. The transverse reinforcement ratio ($\rho_{ft} = 4 \times A_{ft} / D_c \times s$), where A_{ft} is the area of the FRP bar of transverse reinforcement, D_c is the diameter of the core, and s is the spacing between hoops of reinforcement or the pitch of the spiral reinforcement) ranged from 0.00 to 7.3 %. The longitudinal reinforcement's elasticity modulus, E_{fl} , varied from 0 to 140 GPa. The transverse reinforcement's elasticity modulus, E_{ft} , varied from 0 to 140 GPa. The longitudinal reinforcement's tensile strength, f_{fil} ,

wide-ranging 0 toward 1,899 MPa. Also, the transverse reinforcement's tensile strength is a wide range, f_{ft} , varied from 0 toward 1,899 MPa.

Table 2. Compression design parameters for columns used in the database.

Number of columns	Database				
	91				
Properties	Min	Max	SD	Avg	COV (%)
D (mm)	150.00	305.00	46.65	268.25	17.39
D_c (mm)	104.00	237.20	40.21	203.69	19.74
A_g (mm ²)	17671.46	73061.66	17790.53	58207.06	30.56
R (mm)	75.00	152.50	23.32	134.13	17.39
L (mm)	300.00	2500.00	403.79	1245.85	32.41
L/R	4.00	16.39	2.55	9.16	27.86
ρ_{ft} (%)	0.00	5.50	0.89	2.12	41.85
f_{ful} (MPa)	0.00	1899.00	393.26	1253.60	31.37
E_{ft} (MPa)	0.00	140000.00	33215.50	68729.67	48.33
ρ_{ft} (%)	0.00	7.30	1.34	1.98	67.76
f_{ful} (MPa)	0.00	1899.00	336.65	1227.52	27.42
E_{ft} (MPa)	0.00	140000.00	27859.66	66413.19	41.95
f'_c (MPa)	25.40	85.00	9.11	41.08	22.18

Table 3. Comparison between the experimental and theoretical axial load-carrying capacity of FRP bar-reinforced concrete columns available in the previous research studies.

No.	The study	Specimen	$P_{exp.}^a$	$P_o / P_{exp.}^b$				
				Eq. (5)	Eq. (5)	Eq. (2.1 or 2.2)	Eq. (3)	
				ACI 318-19 [31] c	CSA A23.3-19 [32] c	JSCE 1997 [33]	Tobbi et al. [11] d	
1	Pantelides et al. [17]	#13GLCTL	1975	0.83	0.83	0.60	0.88	
2		#14GLCTL	1788	0.91	0.92	0.67	0.97	
3	Affi et al. [12]	C6V-3H80	2905	0.99	1.01	0.68	1.05	
4		C10V-3H80	3013	1.02	1.05	0.66	1.12	
5		C14V-3H80	3107	1.05	1.09	0.64	1.19	
6		C10V-2H80	2948	1.04	1.07	0.67	1.14	
7		C10V-4H80	3147	0.97	1.00	0.63	1.07	
8		C10V-3H40	3070	1.00	1.03	0.65	1.10	
9		C10V-3H120	2981	1.03	1.06	0.67	1.13	
10		C10V-2H35	3148	0.97	1.00	0.63	1.07	
11		C10V-4H145	2941	1.04	1.07	0.67	1.15	
12		Affi et al. [18]	G8V-3H80	2920	0.95	0.97	0.68	1.04
13			G4V-3H80	2826	0.95	0.96	0.70	0.99
14	G12V-3H80		2998	0.96	0.98	0.66	1.09	
15	G8V-2H80		2857	0.97	0.99	0.69	1.06	
16	G8V-4H80		3019	0.92	0.94	0.66	1.01	
17	G8V-3H40		2964	0.94	0.95	0.67	1.03	
18	G8V-3H120		2804	0.99	1.01	0.71	1.08	
19	G8V-2H35		2951	0.94	0.96	0.67	1.03	
20	G8V-4H145		2865	0.97	0.99	0.69	1.06	
21			G2S	2857	0.97	0.99	0.69	1.06

No.	The study	Specimen	$P_{exp.}^a$	$P_o / P_{exp.}^b$			
				Eq. (5)	Eq. (5)	Eq. (2.1 or 2.2)	Eq. (3)
				ACI 318-19 [31] c	CSA A23.3-19 [32] c	JSCE 1997 [33]	Tobbi et al. [11] d
22	Mohamed et al. [19]	G3S	2920	0.95	0.97	0.68	1.04
23		G4S	3019	0.92	0.94	0.66	1.01
24		G3H200	2840	0.98	1.00	0.70	1.07
25		G3H400	2871	0.97	0.98	0.69	1.06
26		G3H600	2935	0.95	0.96	0.68	1.04
27		C2S	2948	1.04	1.07	0.67	1.14
28		C3S	3013	1.02	1.05	0.66	1.12
29		C4S	3147	0.97	1.00	0.63	1.07
30		C3H200	2869	1.07	1.10	0.69	1.18
31		C3H400	2960	1.03	1.06	0.67	1.14
32		C3H600	3008	1.02	1.05	0.66	1.12
33		Karim et al. [20]	G6-G60	1425	0.82	0.83	0.56
34	G6-G30		2041	0.57	0.58	0.39	0.71
35	00-G60		940	1.10	1.10	0.85	1.10
36	00-G30		1343	0.77	0.77	0.59	0.77
37	Maranan et al. [21]	GGC-8-00	1772	1.00	1.02	0.69	1.15
38		GGC-8-H50	1791	0.99	1.01	0.68	1.14
39		GGC-8-H100	1981	0.89	0.91	0.62	1.03
40		GGC-8-H200	1988	0.89	0.91	0.61	1.03
41		GGC-8-S50	1838	0.96	0.98	0.66	1.11
42		GGC-8-S100	2063	0.86	0.88	0.59	0.99
43		GGC-16-H100	1624	1.09	1.11	0.75	1.26
44		GGC-16-S100	1208	1.47	1.50	1.01	1.69
45	Hadi et al. [14]	G60E0	2721	0.95	0.96	0.71	1.05
46		G30E0	2593	1.00	1.01	0.74	1.10
47	Hadhood et al. [22]	C1-I	2608	0.92	0.93	0.64	1.09
48		C1-II	2670	0.93	0.96	0.63	1.19
49	Abdelazim et al. [23]	C1	3535	0.88	0.90	0.63	1.03
50		C2	3490	0.90	0.91	0.64	1.04
51		C3	3453	0.91	0.92	0.64	1.05
52		C4	3359	0.93	0.95	0.66	1.08
53		C5	3331	0.94	0.95	0.67	1.09
54	Raza et al. [24]	GH75-C	2290.51	0.73	0.73	0.53	0.77
55		GH150-C	1965.8	0.84	0.85	0.61	0.89
56		GS38-C	2678.1	0.62	0.63	0.45	0.66
57		GS75-C	2403.54	0.69	0.70	0.50	0.73
58	El-Gamal and AlShareedah [25]	G1 (6G12-G75)	1202	0.84	0.86	0.57	0.95
59		G6 (6G12-G75)	1166	0.86	0.88	0.59	1.01
60		G2 (8G12-G75)	1536	0.68	0.70	0.45	0.80
61		G3 (8G16-G75)	1457	0.79	0.83	0.47	1.02
62		G4 (6G12-G100)	1065	0.95	0.97	0.65	1.08
63	G5 (6G12-G50)	1585	0.64	0.65	0.44	0.72	
64	Elchalakani et al. [26]	G3-120-C	943	1.15	1.16	0.86	1.19
65		G4-120-C	1031	1.06	1.07	0.78	1.11
66		G5-120-C	1286	0.86	0.87	0.63	0.91
67		G4-40-C	1223	0.90	0.90	0.66	0.93
68		G4-80-C	1088	1.01	1.02	0.74	1.05
69	Elhamaymy et al. [27]	GCP-80S	2850	0.93	0.95	0.67	1.12
70		GCP-80S-22	3200	0.83	0.85	0.59	1.00
71		GCP-80S-60	3350	0.80	0.81	0.57	0.95
72		GCP-40S	2900	0.92	0.93	0.65	1.10

No.	The study	Specimen	$P_{exp.}^a$	$P_o / P_{exp.}^b$			
				Eq. (5)	Eq. (5)	Eq. (2.1 or 2.2)	Eq. (3)
				ACI 318-19 [31] c	CSA A23.3-19 [32] c	JSCE 1997 [33]	Tobbi et al. [11] d
73		GCP-40S-22	3100	0.86	0.87	0.61	1.03
74		GCP-40S-60	3450	0.77	0.78	0.55	0.92
75		GCP-120S	2800	0.95	0.97	0.68	1.14
76		GCP-120S-22	3000	0.89	0.90	0.63	1.06
77		GCP-120S-60	3250	0.82	0.83	0.58	0.98
78		GCP-80-O	2700	0.99	1.00	0.70	1.18
79		GCP-80-O-22	3100	0.86	0.87	0.61	1.03
80		GCP-80-O-60	3300	0.81	0.82	0.58	0.97
81	Bakouregui et al. [28]	G-8-0	3530	0.97	0.98	0.70	1.10
82		B-8-0	3530	0.98	1.00	0.70	1.17
83	Gouda et al. [29]	SC-6G-80	2550	0.91	0.92	0.65	1.04
84		SC-8G-80	2700	0.88	0.89	0.61	1.05
85		SC-12G-80	2890	0.86	0.88	0.57	1.09
86		fh-f-2	1589.63	0.67	0.69	0.47	0.81
87		fh-f-4	1317.76	0.68	0.70	0.46	0.85
88		fh-f-8	908.05	0.82	0.84	0.53	1.07
89	Tang et al. [30]	fl-f-2	1127.35	0.78	0.79	0.56	0.92
90		fl-f-4	824.88	0.86	0.87	0.60	1.05
91		fl-f-8	616.12	0.96	0.98	0.66	1.21
	Mean			0.92	0.94	0.64	1.04
	SD			0.125	0.128	0.089	0.136
	COV (%)			13.66	13.74	13.87	13.08
	MAPE			10.798	10.122	35.618	10.334

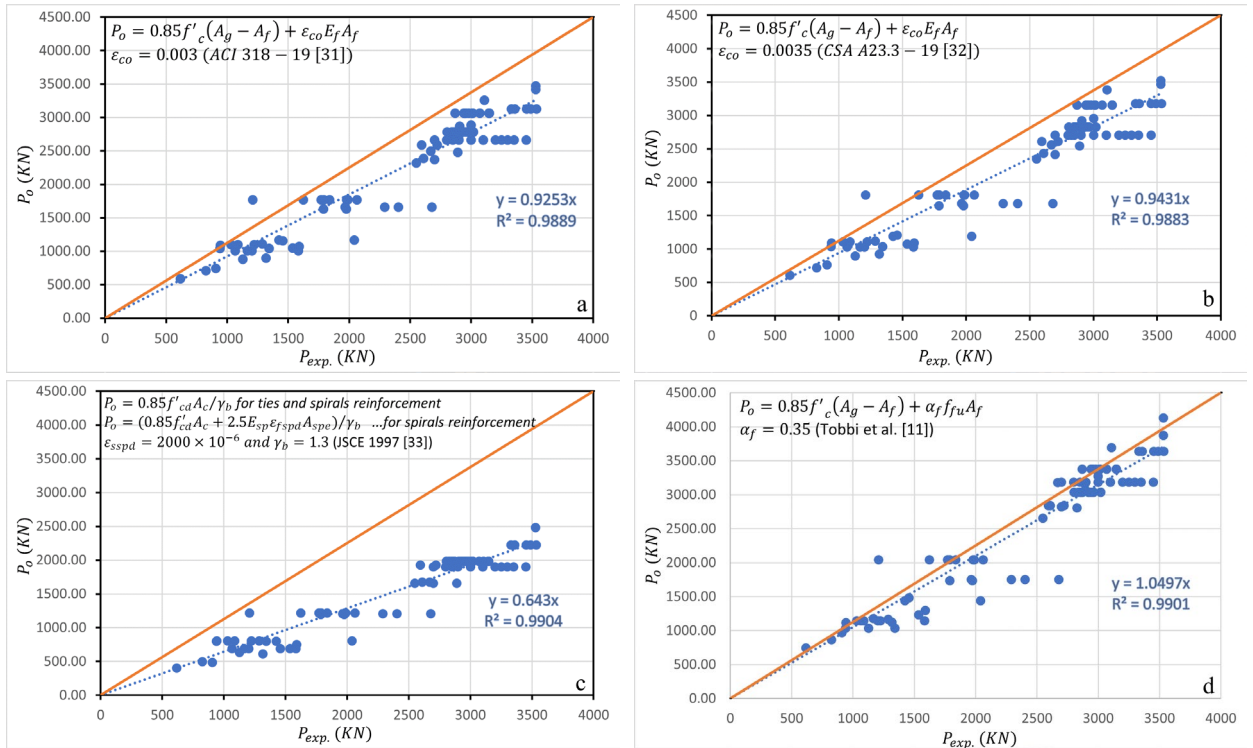


Figure 1. Experimental versus predicted axial load carrying capacity of FRP bar reinforced concrete columns obtained using: a) Eq. (5) ($\epsilon_{co} = 0.003$); b) Eq. (5) ($\epsilon_{co} = 0.0035$); c) Eq. (2.1 or 2.2) ($\gamma_b = 1.3$); and d) Eq. (3) ($\alpha_f = 0.35$).

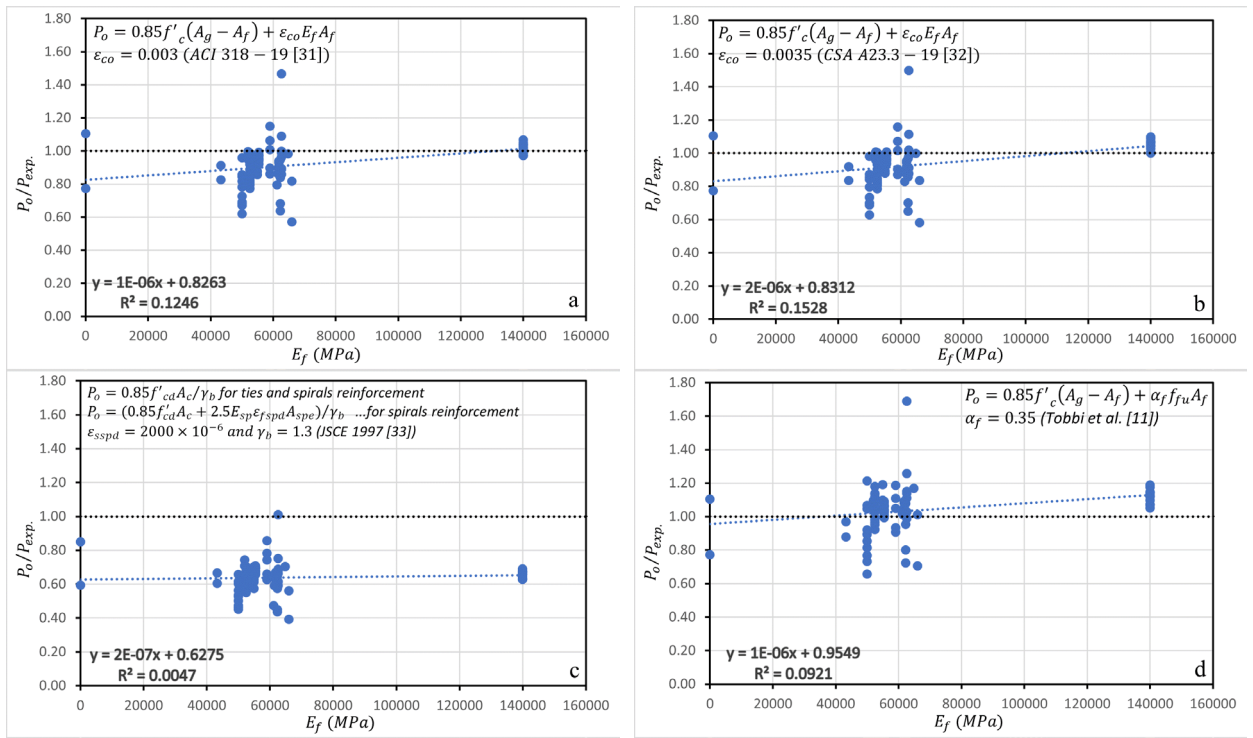


Figure 2. The relationship between P_o / P_{exp} of the FRP-bar reinforced concrete column and the modulus of elasticity of the reinforcement E_f . The following equations were used to calculate P_o : a) Eq. (5) ($\epsilon_{co} = 0.003$), b) Eq. (5), c) Eq. (2.1 or 2.2) ($\gamma_b = 1.3$), and d) Eq. (3) ($\alpha_f = 0.35$).

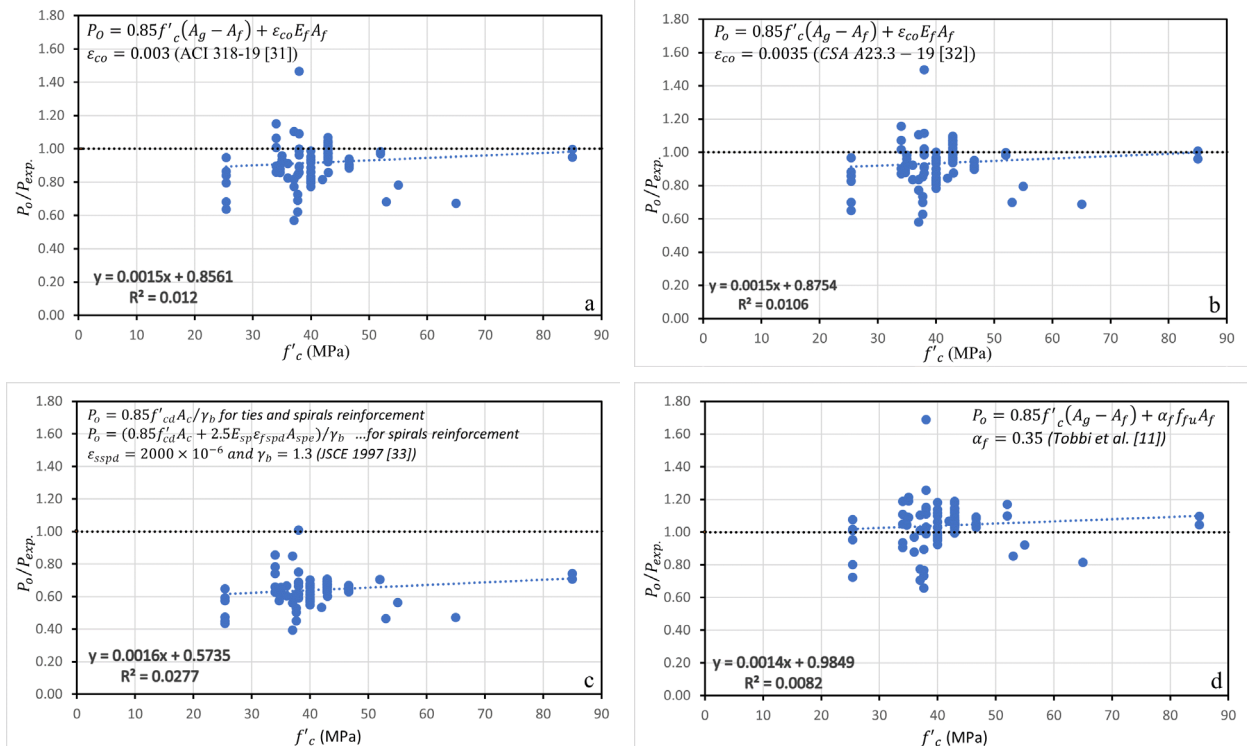


Figure 3. The relationship between P_o / P_{exp} of the FRP bar reinforced concrete column and the compressive strength of the concrete f'_c . Note: P_o were calculated using: a) Eq. (5) ($\epsilon_{co} = 0.003$); b) Eq. (5) ($\epsilon_{co} = 0.0035$); c) Eq. (2.1 or 2.2) ($\gamma_b = 1.3$); and d) Eq. (3) ($\alpha_f = 0.35$).

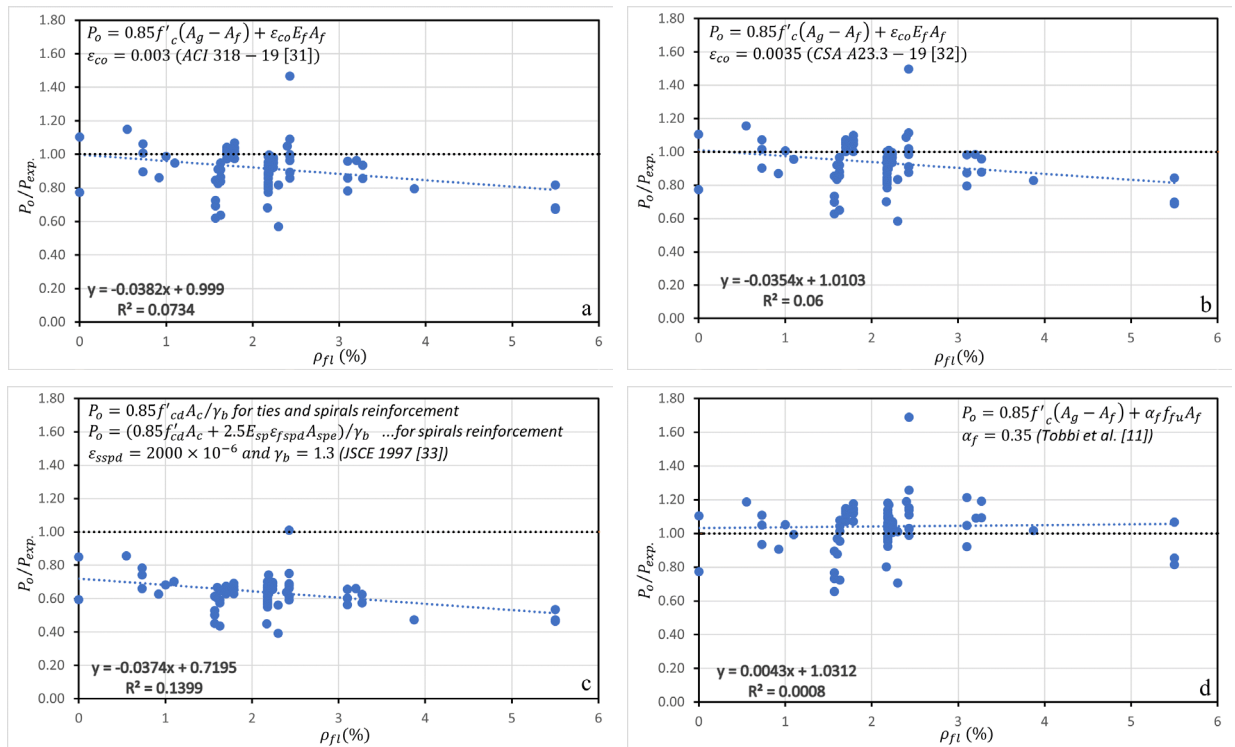


Figure 4. The relationship between P_o / P_{exp} of the FRP bar reinforced concrete column and the longitudinal reinforcement ratio ρ_{ft} . Note: P_o were found by using: a) Eq. (5) ($\epsilon_{co} = 0.003$), b) Eq. (5) ($\epsilon_{co} = 0.0035$), c) Eq. (2.1 or 2.2) ($\gamma_b = 1.3$), and d) Eq. (3) ($\alpha_f = 0.35$).

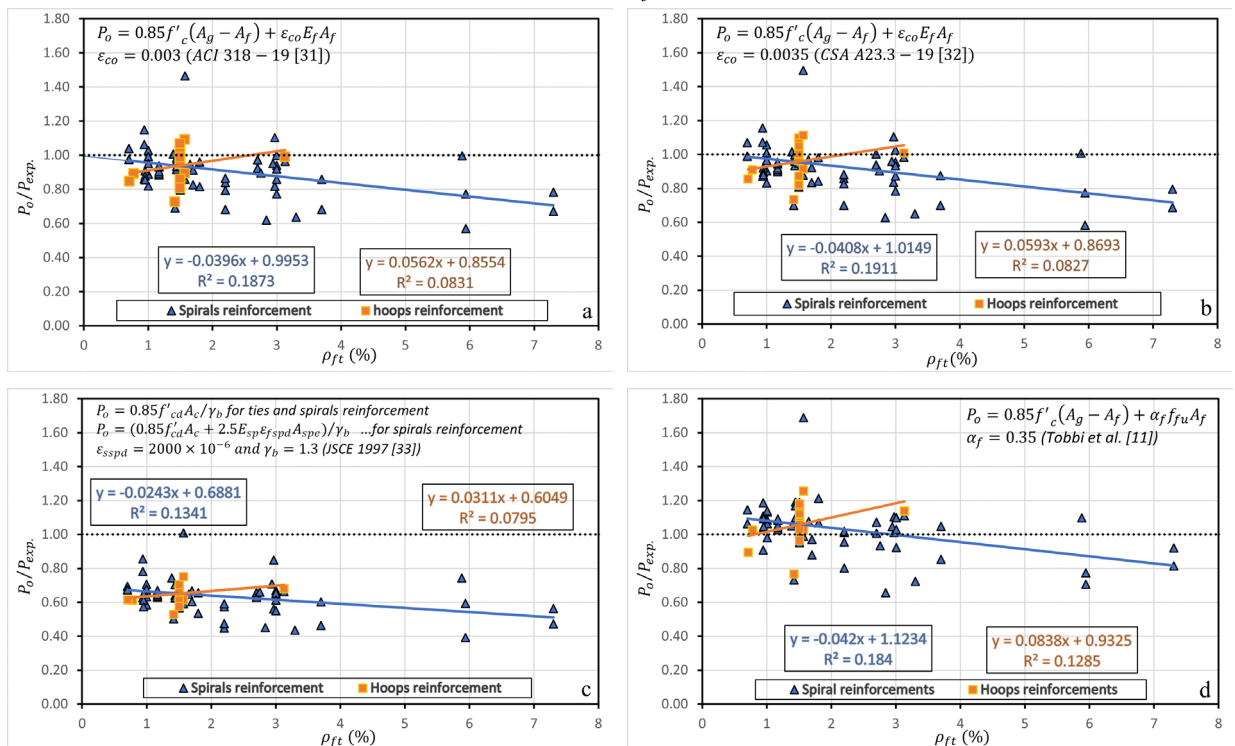


Figure 5. The relationship between P_o / P_{exp} and the transverse reinforcement ratio ρ_{ft} of the FRP bar reinforced concrete column. Note: P_o was calculated by using the equations: a) Eq. (5) ($\epsilon_{co} = 0.003$), b) Eq. (5) ($\epsilon_{co} = 0.0035$), c) Eq. (2.1 or 2.2) ($\gamma_b = 1.3$), and d) Eq. (3) ($\alpha_f = 0.35$).

3. Results and Discussion

3.1. Maximum axial load carrying capacity of reinforced concrete columns

This statistical study looks at theoretical equations to find the maximum axial load-carrying capacity of FRP bar-reinforced concrete columns under pure compression stresses. The previously proposed equations for the maximum axial load-carrying capacity of FRP bar-reinforced concrete columns can be used in future compound structure design codes. This research doesn't address the effect of combined axial and flexural loads on the behavior of FRP bar-reinforced concrete columns. Previous research studies used several equations to predict the maximum axial load-carrying capacity of FRP bar-reinforced concrete columns. It is critical to remember that the concrete's contribution to the analytically computed axial load-carrying capacity of FRP-bar reinforced concrete columns, remains similar in all of the proposed equations. In simpler terms, the differences in analytically derived P_o values for FRP bar-reinforced concrete columns are primarily due to the different concepts adopted in different equations for calculating the longitudinal bar contribution ($P_{bar,FRP}$). As was mentioned above, the FRP bar's compressive strength is considerably lower than its tensile strength and the behavior of the FRP bar under compressive loads differs significantly. Therefore, ACI 440.1R-06 [34] suggests that FRP bars shouldn't be used to reinforce concrete columns longitudinally, and ACI 440.1R-15 [16] makes no recommendations about this. The CAN/CSA S806-12 [15] and JSCE 1997 [33] allow FRP bars to be used to reinforce concrete columns in a main direction. However, CAN/CSA S806-12 and JSCE 1997 [15, 33] say that the contribution of the FRP longitudinal bars should be ignored when estimating the maximum axial load-carrying capacity of FRP bar-reinforced concrete columns. Using the recommendations in CAN/CSA S806-12 and JSCE 1997 [15, 33], Eq. (1) and Eq. (2) can be used to predict the maximum axial load-carrying capacity of FRP bar-reinforced concrete columns.

$$P_o = 0.85 f'_c (A_g - A_f); \quad (1)$$

$$P_o = 0.85 f'_c A_c / \gamma_b; \quad (2.1)$$

$$P_o = (0.85 f'_c A_e + 2.5 E_{sp} \varepsilon_{fspd} A_{spe}) / \gamma_b, \quad (2.2)$$

where A_f is the total cross-sectional area of FRP longitudinal bars, A_c is the cross-sectional area of concrete (mm²), A_e is the cross-sectional area of concrete surrounded by spiral reinforcement, A_{spe} is the equivalent cross-sectional area of spiral reinforcement ($= \Pi d_{sp} A_{sp} / s$), d_{sp} is the diameter of the concrete section surrounded by spiral reinforcement, A_{sp} is the cross-sectional area of spiral reinforcement, E_{sp} is the young's modulus of spiral reinforcement (E_{fu}), ε_{fspd} is the design value for the strain of spiral reinforcement in the ultimate limit state, which is usually taken to be 2000×10^{-6} , γ_b is the member factor, which is generally taken to be 1.3, s is the pitch of spiral reinforcement. Note that JSCE 1997 [33] stated that when the members are subjected to axial compression force, the upper limit of axial compression capacity P_o will be calculated using Eq. (2.1) while hoops are used and either Eq. (2.1) or Eq. (2.2) whatever provides the biggest result, when spiral reinforcement is used. But a lot of research has shown that ignoring the contribution of FRP longitudinal bars in compression, as in Eq. (1–2.2), could cause a big difference between the analytically calculated axial load-carrying capacity of FRP bar reinforced concrete columns and the experimentally obtained value [12, 35, 36]. Consequently, two approaches were considered to compute the contribution of FRP longitudinal bars in the maximum axial load-carrying capacity of FRP bar-reinforced concrete columns. In the first approach, the axial load sustained by FRP longitudinal bars is calculated using the tensile strength of the FRP bars, $\alpha_f f_{fu} A_f$ (Equation (3)). In the second approach, the axial load sustained by FRP longitudinal bars is calculated using the axial strain in the FRP bars and the stiffness of the FRP bars, $\varepsilon_f E_f A_f$ (Eq. (4)).

$$P_o = 0.85 f'_c (A_g - A_f) + \alpha_f f_{fu} A_f; \quad (3)$$

$$P_o = 0.85 f'_c (A_g - A_f) + \varepsilon_f E_f A_f. \quad (4)$$

In Eq. (3), the α_f is a reduction factor that represents the ratio between the strength of the FRP bar under compression and the strength of the FRP bar under tension. Different values for α_f were recommended in the previous studies. Alsayed et al. [10] suggested taking α_f equal to 0.6. Later, Tobbi et al. [11] recommended taking α_f equal to 0.35 based on experimental observations reported in Kobayashi and Fujisaki [8]. Moreover, α_f was recommended to be taken equal to 0.35 in Afifi et al. [18] for GFRP bar-reinforced circular concrete columns. Nevertheless, for CFRP bar-reinforced circular concrete columns, Afifi et al. [12] recommended taking α_f equal to 0.25. In Eq. (4), different values were also suggested for the axial strain in the FRP longitudinal bars, α_f , at the maximum axial load-carrying capacity of the concrete columns. Mohamed et al. [19] suggested taking ε_f equal to 0.002, explaining that this value ($\varepsilon_f = 0.002$) represents the axial strain in the FRP longitudinal bars at the initiation of the micro-cracks in the plastic stage of the concrete. Nevertheless, Hadi et al. [36] recommended taking ε_f equal to 0.003, which represents the ultimate strain of the concrete, ε_{cu} . It is obvious that different research studies proposed different equations based on a limited number of experimental data. Therefore, there is no consensus in the previous research studies on a unified equation for predicting the maximum axial load-carrying capacity of FRP bar-reinforced concrete columns, which may also be attributed to the variances in the response of the FRP bars under axial compression. In this study, the axial load sustained by FRP longitudinal bars, $P_{bar,FRP}$, was predicted based on the stiffness (modulus of elasticity) of the FRP bars because the modulus of elasticity of FRP bars in compression is approximately similar to the modulus of elasticity of FRP bars in tension [7, 9]. Therefore, simply changing the value of the reduction factor α_f in Eq. (3) might not provide reasonable predictions for the maximum axial load-carrying capacity of FRP bar-reinforced concrete columns. The axial strain in the FRP longitudinal bars ε_f at the maximum axial load-carrying capacity of the concrete columns was considered to be equal to the concrete axial strain at peak stress ε_{co} . The concept adopted in this study is consistent with the assumption which states that the axial strain in the concrete and the axial strain in longitudinal FRP reinforcing bars are equal at any concentric axial load. Consequently, the maximum axial load-carrying capacity of FRP bar-reinforced concrete columns can be predicted using Eq. (5):

$$P_o = 0.85f'_c(A_g - A_f) + \varepsilon_{co}E_fA_f. \quad (5)$$

3.2. Evaluation of the proposed and codes equations

3.2.1. Overall performance

In this study, the three code equations were assessed with a proposed equation from a previous study through the analysis of a large set of available experimental data (Table 1). This study examined the equation proposed by Tobbi et al. [8]. Hadi et al. [36] recommended assuming ε_f equal to ε_{cu} . The equation proposed by Hadi et al. [36] was also assessed. First, by taking ε_{cu} equal to 0.003 as defined in the ACI 318-19 [31] standard. Then, by taking ε_{cu} equal to 0.0035 as defined in the CSA A23.3-19 standard [32]. Table 3 presents the ratios between the analytically predicted and the experimentally obtained axial load carrying capacity ($P_o/P_{exp.}$) for the experimentally tested specimens in Table 1. The analytically predicted axial load carrying capacity, P_o , was calculated by either using Eq. (3) by taking α_f equal to 0.35, as recommended by Tobbi et al. [11], or using Eq. (5), in which the value of ε_{co} was taken equal to ε_{cu} (0.003 or 0.0035, as defined in the ACI 318-19 [31] and CSA A23.3-19 [32], or using Eq. (2.1 and 2.2) from the JSCE 1997 [33], which depends mostly on the type of transverse reinforcement (hoops or spirals). The most optimal line for each equation is also shown alongside the experimental and theoretical axial load. The same number shows perfect performance. The equation with fewer scatters and better performance is one where the most optimal line and the plotted data are closer to the perfect line. Four

relationships (f'_c , ρ_{fl} , E_f , and ρ_{ft}) are displayed to illustrate the ratio between the experimental axial load and the theoretical axial load using the selected equations for each tested column. In Table 3, four different mathematical measurements (Mean value (μ), Standard Deviation (SD), Coefficient of Variation (COV), and the Mean Absolute Percent Error (MAPE)) were used to evaluate the accuracy, consistency, and safety of the equations available according to three codes (ACI 318-19 [31], CSA A23.3-19 [32], and JSCE 1997 [33]) and according to only one proposed in one previous study (Tobbi et al. [11]). Among the unique values, the Mean value (μ) is the midpoint between the wide range of P_o . More precise results can be expected when the mean is closer to unity. The dispersion (variation) in P_o values was measured using the SD. For FRP bar-reinforced concrete specimens, a high SD indicates that the predicted axial load-carrying capacities fall within a wider range of values (less precisely) and a lower value SD indicates the opposite. The COV was then used to evaluate the dispersion of P_o values relative to the mean value as a percentage. As the COV decreases, performance becomes more stable and less variable from the mean. The MAPE is used to compare the accuracy of different equations used to determine the maximum axial load-carrying capacities of FRP-bar reinforced concrete columns. If the MAPE is small, then the equation should yield precise results. The most optimal line's slope indicates how consistently the performance meets or exceeds predictions for the chosen parameter. Table 3 shows a comparison of the experimental axial load-carrying capacity of FRP-bar-reinforced concrete columns to the theoretical value. It was noticed that Eq. (5), in which the contribution of the FRP bars is calculated based on their stiffness, is a more precise and safe way to predict P_o than Eq. (3), in which the contribution of the FRP bars is calculated based on their tensile strength. Eq. (5) is a safer and more reliable way to predict P_o than (2.1, 2.2), which uses transverse reinforcement. Possible explanations for this include the fact that despite significant differences between their tensile and compressive strengths, FRP bars have a modulus of elasticity that is nearly identical in tension and compression. Table 3 presents the SD and COV, which are 0.136 and 13.08, respectively, when P_o is calculated using Eq. (5), the equation proposed by Tobbi et al. [11]. This permits more consistent results. However, the lowest MAPE of 10.798 in predicting P_o was achieved by taking the concrete axial strain at peak stress $\varepsilon_{co} = 0.003$ in the computation of $P_{bar,FRP}$. By taking ε_{co} equal to 0.0035 when computing $P_{bar,FRP}$, predictions for P_o/P_{exp} with = 0.94, which is very close to unity and rather secure, but with high SD and COV of 0.128 and 13.74, respectively, were obtained (Fig. 1). As can be seen in Fig. 1, the SD and COV are 0.089 and 13.87, respectively, when using the Eq. (2.1, 2.2) that is available in JSCE is used to calculate $P_{bar,FRP}$, resulting in higher discrepant values of P_o . Thus, Eq. (5) which is available in CSA provides more realistic predictions than do those of other codes (ACI, JSCE). The axial load-carrying capacity of FRP bar-reinforced concrete columns was taken from previous studies and compared to the axial load-carrying capacity calculated using ACI 318-19 [31] and CSA A23.3-19 [32], respectively in Fig. 1. The JSCE's 1997 [33] equation and Tobbi et al.'s equation [11], were assessed. The slope of the trend line is 0.92 for the ACI, 0.94 for the CSA, 0.64 for the JSCE, and 1.04 for Tobbi. In addition, the axial load was calculated by using CSA and Tobbi equations, and that is more in line with the axial load measured experimentally. ACI, CSA, JSCE, and Tobbi each found a COV for axial load experimental versus a theoretical axial load of 13.66, 13.74, 13.87, and 13.08, respectively. The ACI and JSCE are less precise than the CSA. Finally, when comparing the Tobbi equation to the others that were considered, it was found to be the most precise in predicting the axial load-carrying capacity. Lastly, the performance tests on concrete compression design practices (Table 3) showed that the proposed equation by Tobbi et al. [11] with suitable safety factors had better optimization, followed by the CSA A23.3-19 [32] guidelines, the ACI 318-19 [31] code, and the JSCE 1997 guidelines [33]. The statistical tests yielded consistent results for the SD, COV, MAPE, and mean. The Tobbi et al. [11] design equation and the CSA A23.3-19 [32] guidelines did better than the ACI 318-19 [31] code, which had some extreme values because they had fewer conservative values. The JSCE 1997 [33] was not safe and had more conservative points than the other design methods because 97 % of their predictions were dangerous or extremely dangerous. Tobbi et al. [11], CSA A23.3-19 [32], and ACI 318-19 [31] showed better assessment because the P_o/P_{exp} was less conservative by 9, 19, and 23 %, respectively.

3.2.2. Young's modulus

For solids only, the stress (tension or compression) ratio to strain is known as Young's modulus or the main modulus of elasticity. This linear relationship between stress and strain expresses the extent of

flexibility of the material and explains how the material behaves under the influence of forces. This factor has a major effect on the axial load-carrying capacity of FRP-RC columns. The P_o/P_{exp} vs the E and the most optimal line trendlines from the database are shown in Fig. 2. As Young's modulus increases, so does the P_o/P_{exp} . The most optimal lines for the ACI, CSA, JSCE, and Tobbi have an inclination of 1E-6, 2E-6, 2E-7, and 1E-6, respectively. Therefore, CSA provides greater consistency in terms of E value in terms of safety compared to ACI, JSCE, and Tobbi. The CSA equation can be inferred to be more reliable for FRP types than any of the chosen equations.

3.2.3. Concrete strength

One measure of a material's or structure's durability is its compressive strength, or how well it carries up under compression stresses. The axial load-carrying capacity of FRP-RC columns is significantly impacted by this factor. The P_o/P_{exp} vs f'_c and the most optimal line trendline using the proposed and selected equations are shown in Fig. 3. The P_o calculated using Eq. (3) by taking α_f equal to 0.35 as recommended by Tobbi et al. [11], using Eq. (5) by taking ε_{co} equal to 0.003 as defined in the ACI 318-19 [31] and equal to 0.0035 as defined in the CSA A23.3-19 [32] or calculated using the Eq. (2.1, 2.2) as recommended in JSCE 1997 [33] are shown in Fig. 3. The axial load-carrying capacity for the majority of the FRP bar-reinforced NSC and HSC columns provided in Table 1 is well predicted using an assumption of α_f equal to 0.35 (Eq. (3)), as suggested by Tobbi et al. [11], as illustrated in Fig. 3a. The performance indicator P_o/P_{exp} tends to rise as f'_c gets higher. The slope of the line that provides the best match has an inclination of 1.5E-3 for the ACI, 1.5E-3 for the CSA, 1.6E-3 for the JSCE, and 1.4E-3 for the Tobbi. In terms of f'_c safety, the CSA is more reliable than the ACI and the JSCE. The Tobbi also exhibits the greatest degree of consistency with respect to f'_c of any of the chosen equations.

3.2.4. The longitudinal reinforcement ratios

The longitudinal reinforcement ratio, ρ_{fl} , is calculated by dividing the area of the longitudinal reinforcement by the cross-sectional area of the column. It is a significant factor affecting the axial load-carrying capacity of FRP-RC columns. The fluctuation in P_o/P_{exp} with longitudinal reinforcement ratio, according to the database, is shown in Fig. 4. As the reinforcement ratio rises, it can be seen that the P_o/P_{exp} has a decreasing trend. In addition, the slope of the most optimal line for the ACI, CSA, JSCE, and Tobbi is -38.2E-3, -35.4E-3, -37.4E-3, and +4.3E-3, respectively. Compared to CSA, JSCE, and Tobbi, ACI points are less crowded and closer to the perfect horizontal line. Consequently, ACI safety is more consistent concerning the ρ_{fl} value than CSA, JSCE, and Tobbi. It may be inferred that the ACI equation is more consistent for the FRP type than it is for the other equations considered.

3.2.5. Transverse reinforcement ratio

3.2.5.1. Spiral reinforcement ratio

The P_o/P_{exp} vs ρ_{ft} and the most optimal line trendline are shown in Fig. 5. The slope of the most optimal lines is -39.6E-3, -40.8E-3, -24.3E-3, and -4.2E-2 for the ACI, CSA, JSCE, and Tobbi, in that order. As ρ_{ft} increases, P_o/P_{exp} decreases. This suggests that the performance of spiral reinforcement improves when the distances are increased but within the applicable limits. In addition, the ACI is more consistent regarding ρ_{ft} safety than the Tobbi and JSCE. Finally, the CSA equation is more consistent concerning with respect to ρ_{ft} than any of the selected equations.

5.5.2. Hoops reinforcement ratio

The P_o/P_{exp} vs ρ_{ft} and the most optimal line trendline are shown in Fig. 5. For the ACI, CSA, JSCE, and Tobbi, the slope of the most optimal line is 56.2E-3, 59.3E-3, 31.1E-3, and 83.8E-2, respectively. Generally, there is a clear increase in P_o/P_{exp} with each increase in the ρ_{ft} . This indicates that hoop

reinforcement gives better performance when the spacings are smaller but within the applicable limits. In addition, the safety of the ACI is more consistent concerning the ρ_{ft} than that of the CSA and JSCE.

Furthermore, the Tobbi outperforms the codes in terms of ρ_{ft} consistency. Finally, the behavior of the most optimal line trendlines for spiral reinforcement is clear that it is the opposite of the behavior of the perfect line for hoops reinforcement. Also, the ACI and the CSA provide better results than the JSCE in general, although Tobbi provides perfect results better than all other codes at least in the hoops reinforcement, and the results are close For the ACI and CSA in spirals reinforcement.

4. Conclusions

An extensive experimental database comprising 91 circular FRP-reinforced concrete columns was utilized to investigate the interrelation of geometry and details of circular FRP-reinforced concrete columns. The axial load-carrying capacity of the experimental database was determined using selected design codes and guidelines with one equation proposed in earlier research, the CSA design code exhibited superior precision compared to JSCE and ACI but less compared with Tobbi. The mean safety factors for JSCE, ACI, CSA, and Tobbi were found to be 0.64, 0.93, 0.94, and 1.04, respectively. JSCE showed less consistency and a significantly more conservative behavior compared to ACI, CSA, and Tobbi while ignoring the contribution of longitudinal bars and ultimate axial strain, which leads to an increase in implementation costs. Key distinctions between FRP-reinforced concrete columns and conventional steel-reinforced concrete columns were considered, such as varying FRP types (Young's modulus: 0–140 GPa), compressive failure due to concrete crushing without yielding FRP reinforcements, and increased deformation experienced by FRP-reinforced concrete columns. To validate the accuracy of the codes and the previously proposed equation, the experimental axial load-carrying capacity was compared with the predicted axial load-carrying capacity using equations for a large experimental database of reinforced concrete circular columns with FRP reinforcements. Tobbi's equation showed good agreement with experimental loads compared to other equations, which can be a good conclusion due to the remarkable complexity in the behavior of FRP bars and the big difference in the behavior of these bars in compression and tension. The analysis investigated the effects of concrete strength, FRP Young's modulus, longitudinal reinforcement ratio, and transverse reinforcement ratio on the results. These results showed the P_o/P_{exp} .

of FRP-reinforced concrete columns increases with an increase in the value of the FRP Young's modulus, the longitudinal reinforcement ratio, and the concrete strength, respectively; and Tobbi's equation adequately accounted for the concrete strength and the hoops reinforcement effect. When the type is hoops, P_o/P_{exp} increases as the ρ_{ft} increases, but when the type is spiral, P_o/P_{exp} decreases as the ρ_{ft} increases. Finally, Tobbi's equation has the lowest COV compared with all code's equations and the best average nearing unity. However, MAPE for Tobbi is greater than CSA but less than JSCE and ACI, which require more experimental testing and more exact test measurements.

References

1. Sheikh, M.N., Légeron, F. Performance based seismic assessment of bridges designed according to canadian highway bridge design code. Canadian Journal of Civil Engineering. 2014. 41(9). Pp. 777–787. DOI: 10.1139/cjce-2013-0025
2. Zaman, A., Gutub, S.A., Wafa, M.A. A review on FRP composites applications and durability concerns in the construction sector. Journal of Reinforced Plastics and Composites. 2013. 32(24). Pp. 1966–1988. DOI: 10.1177/0731684413492868
3. Mukhopadhyay, T., Dey, T.K., Chowdhury, R., Chakrabarti, A., Adhikari, S. Optimum design of FRP bridge deck: an efficient RS-HDMR based approach. Structural and Multidisciplinary Optimization. 2015. 52(3). Pp. 459–77. DOI: 10.1007/s00158-015-1251-y
4. Li, X., Lu, J., Ding, D.D., Wang, W. Axial strength of FRP-confined rectangular RC columns with different cross-sectional aspect ratios. Magazine of Concrete Research. 2017. 69(19). Pp. 1011–1026. DOI: 10.1680/jmacr.17.00036
5. Karsh, P.K., Mukhopadhyay, T., Dey, S. Spatial vulnerability analysis for the first ply failure strength of composite laminates including effect of delamination. Composite Structures. 2018. 184. Pp. 554–567. DOI: 10.1016/j.compstruct.2017.09.078
6. American Concrete Institute (ACI) Committee 440. Report on Fiber-Reinforced Polymer (FRP) Reinforcement for Concrete Structures. ACI 440R-07. 2007. 100.
7. De Luca, A., Matta, F., Nanni, A. Behavior of full-scale glass fiber-reinforced polymer reinforced concrete columns under axial load. ACI Structural Journal. 2010. 107(5). Pp. 589–596.
8. Kobayashi, K., Fujisaki, T. 32 compressive behavior of FRP reinforcement in non-prestressed concrete members. Non-Metallic (FRP) Reinforcement for Concrete Structures: Proceedings of the Second International RILEM Symposium. First edition. Ghent E & FN Spon, an imprint of Chapman and Hall. 1995. 29. Pp. 267–274.
9. Deitz, D.H., Harik, I.E., Gesund, H. Physical properties of glass fiber reinforced polymer rebars in compression. Journal of Composites for Construction. 2003. 7 (4). Pp. 363–366. DOI: 10.1061/(ASCE)1090-0268(2003)7:4(363)
10. Alsayed, S.H., Al-Salloum, Y.A., Almusallam, T.H., Amjad, M.A. Concrete columns reinforced by glass fiber reinforced polymer rods. ACI Special Publication. 1999. 188. 103–112. DOI: 10.14359/5614

11. Tobbi, H., Farghaly, A.S., Benmokrane, B. Concrete columns reinforced longitudinally and transversally with glass fiber-reinforced polymer bars. *ACI Structural Journal*. 2012. 109(4). Pp. 551–558.
12. Afifi, M.Z., Mohamed, H.M., Benmokrane, B. Strength and axial behavior of circular concrete columns reinforced with CFRP bars and spirals. *Journal of Composites for Construction*. 2014. 18(2). 04013035. DOI: 10.1061/(ASCE)CC.1943-5614.0000430
13. Hadhood, A., Mohamed, H.M., Benmokrane, B. Experimental study of circular high-strength concrete columns reinforced with gfrp bars and spirals under concentric and eccentric loading. *Journal of Composites for Construction*. 2017. 21(2). 04016078. DOI: 10.1061/(ASCE)CC.1943-5614.0000734
14. Hadi, M.N., Hasan, H.A., Sheikh, M.N. Experimental investigation of circular high-strength concrete columns reinforced with glass fiber-reinforced polymer bars and helices under different loading conditions. *Journal of Composites for Construction*. 2017. 21(4). 04017005.
15. CAN/CSA S806-12. CSA (Canadian Standards Association). Design and construction of building structures with fibre-reinforced polymers (CAN/CSA S806-12). CAN/CSA S806-12. 2012. (Reaffirmed).
16. ACI440.1R-15. Guide for the design and construction of structural concrete reinforced with fiber-reinforced polymer (FRP) bars. American Concrete Institute. 2015.
17. Pantelides, C.P., Gibbons, M.E., Reaveley, L.D. Axial load behavior of concrete columns confined with GFRP spirals. *Journal of Composites for Construction*. 2013. 17(3). Pp. 305–313.
18. Afifi, M.Z., Mohamed, H.M., Benmokrane, B. Axial capacity of circular concrete columns reinforced with GFRP bars and spirals. *Journal of Composites for Construction*. 2014. 18(1). 04013017. DOI: 10.1061/(ASCE)CC.1943-5614.0000438
19. Mohamed, H.M., Afifi, M.Z., Benmokrane, B. Performance evaluation of concrete columns reinforced longitudinally with FRP bars and confined with FRP hoops and spirals under axial load. *Journal of Bridge Engineering*. 2014. 19(7). 04014020. DOI: 10.1061/(ASCE)BE.1943-5592.0000590
20. Karim, H., Noel-Gough, B., Sheikh, M.N., Hadi, M.N. Strength and ductility behavior of circular concrete columns reinforced with GFRP bars and helices. In: FRPRCS-12/APFIS-2015 – Joint Conference of the 12th International Symposium on Fiber Reinforced Polymers for Reinforced Concrete Structures, FRPRCS 2015 and the 5th Asia-Pacific Conference on Fiber Reinforced Polymers in Structures, APFIS 2015. 2015.
21. Maranan, G.B., Manalo, A.C., Benmokrane, B., Karunasena, W., Mendis, P. Behavior of concentrically loaded geopolymer-concrete circular columns reinforced longitudinally and laterally with GFRP bars. *Engineering Structures*. 2016. 117. Pp. 422–436. DOI: 10.1016/j.engstruct.2016.03.036
22. Hadhood, A., Mohamed, H.M., Benmokrane, B. Failure envelope of circular concrete columns reinforced with glass fiber-reinforced polymer bars and spirals. *ACI Structural Journal*. 2017. 114(6). Pp. 1417–1428. DOI: 10.14359/51689498
23. Abdelazim, W., Mohamed, H.M., Benmokrane, B. Effect of slenderness ratio on the performance of concrete columns reinforced with GFRP bars and spirals. *Proceedings, Annual Conference – Canadian Society for Civil Engineering*. 2019.
24. Raza, A., Khan, Q.U.Z. Experimental and theoretical study of GFRP hoops and spirals in hybrid fiber reinforced concrete short columns. *Materials and Structures*. 2020. 53(6). 139. DOI: 10.1617/s11527-020-01575-9
25. El-Gamal, S., Al-Shareedah, O. Behavior of axially loaded low strength concrete columns reinforced with GFRP bars and spirals. *Engineering Structures*. 2020. 216. 110732. DOI: 10.1016/j.engstruct.2020.110732
26. Elchalakani, M., Dong, M., Karrech, A., Mohamed Ali, M.S., Huo, J.S. Circular concrete columns and beams reinforced with gfrp bars and spirals under axial, eccentric, and flexural loading. *Journal of Composites for Construction*. 2020. 24(3). 04020008. DOI: 10.1061/(ASCE)CC.1943-5614.0001008
27. Elhamaymy, A., Mohamed, H.M., Benmokrane, B. Durability assessment and behavior under axial load of circular GFRP-RC piles conditioned in severe simulated marine environment. *Engineering Structures*. 2021. 249. 113376. DOI: 10.1016/j.engstruct.2021.113376
28. Bakouregui, A.S., Mohamed, H.M., Yahia, A., Benmokrane, B. Axial load–moment interaction diagram of full-scale circular LWSCC columns reinforced with BFRP and GFRP bars and spirals: experimental and theoretical investigations. *Engineering Structures*. 2021. 242. 112538. DOI: 10.1016/j.engstruct.2021.112538
29. Gouda, M.G., Mohamed, H.M., Manalo, A.C., Benmokrane, B. Behavior of hollow glass fiber-reinforced polymer-reinforced concrete columns under axial load: experimental and theoretical investigation. *ACI Structural Journal*. 2022. 119(6). Pp. 289–302. DOI: 10.14359/51736117
30. Tang, Y., Sun, Z., Wei, Y., Zou, X. Compressive behavior and design method of BFRP bars constrained with a BFRP spiral with different spacings in concrete members. *Engineering Structures*. 2022. 268. 114757. DOI: 10.1016/j.engstruct.2022.114757
31. ACI (American Concrete Institute). Building Code Requirements for Structural Concrete (ACI 318-19) Commentary on Building Code Requirements for Structural Concrete (ACI 318R-19) IN-LB. 2019.
32. CSA (Canadian Standards Association). Design of concrete structures. CAN/CSA A23.3:19.
33. Japan Society of Civil Engineers (JSCE). Recommendation for Design and Construction of Concrete Structures Using Continuous Fiber Reinforcing Materials. Concrete Engineering Series 23, Research Committee on Continuous Fiber Reinforcing Materials. 1997; 23.
34. ACI (American Concrete Institute). Guide for the design and construction of structural concrete reinforced with FRP bars, ACI 440.1R-06 ACI (American Concrete Institute). Farmington Hills, MI. 2006.
35. Tobbi, H., Farghaly, A.S., Benmokrane, B. Behavior of concentrically loaded fiber-reinforced polymer reinforced concrete columns with varying reinforcement types and ratios. *ACI Structural Journal*. 2014. 111(2). Pp. 375–86. DOI: 10.14359/51686528
36. Hadi, M.N., Karim, H., Sheikh, M.N. Experimental investigations on circular concrete columns reinforced with GFRP bars and helices under different loading conditions. *Journal of Composites for Construction*. 2016. 20(4). 04016009. DOI: 10.1061/(ASCE)CC.1943-5614.0000670

Information about authors:

Mohamed Qassim Kadhim, Master of Structural Engineering

ORCID: <https://orcid.org/0009-0007-0037-6453>

E-mail: mohamedq1992@uomustansiriyah.edu.iq

Hassan Falah Hassan, PhD

ORCID: <https://orcid.org/0000-0003-4610-0560>

E-mail: hassanfalah@uomustansiriyah.edu.iq

Received 15.02.2023. Approved after reviewing 19.10.2023. Accepted 22.10.2023.



Research article

UDC 691.3

DOI: 10.34910/MCE.126.4



Input parameters of three-layer steel fiber concrete beams

T.Q.K. Lam 

Mien Tay Construction University, Vinh Long city, Vietnam

 lamthanhquangkhai@gmail.com

Keywords: reinforced concrete, fiber reinforced concrete, stress-strain, numerical simulation, multilayered beam, bending beam

Abstract. Many researchers have shown interest in the study of bending concrete beams. One method involves using multilayer concrete beams with a layer of steel fiber concrete. This technique aims to improve the beams' capability for supporting load and to minimize the occurrence of cracks, particularly in areas subjected to high compressive and tensile stress. The primary goal is to reduce the stress in these beams. An advantage of using three-layer steel fiber reinforced concrete beams is the ability to repair damaged beams by adding another layer of concrete on top or below the existing concrete layer. Modifying the input parameters during the three-layer beam design process significantly impacts the overall effectiveness of the beams. In this study ANSYS simulation and nonlinear material analysis was used. The objective of the study was to investigate the behavior of three-layer bending concrete beams subjected to two concentrated loads. Specifically, the study examined the impact of varying the content of steel fiber in the concrete, as well as the effects of slirrup at the ends of the beams. Furthermore, the study explored the influence of changes in the quantity and size of steel bars in the places of tensile strength, along with the effect of varying the steel fiber concrete layer's thickness. The research results on three-layer beams were used to create diagrams that depicted the relationship between load and vertical displacement, load and stress in the compressive area, and load and stress in the tensile zone. These diagrams also helped to determine the initiation and progression of cracks in three-layer beams, starting from the application of load until the utter damaging of beams. Ultimately, this information allowed to identify the specific load level that had caused the cracking and the damaging of beams.

Citation: Lam, T.Q.K. Input parameters of three-layer steel fiber concrete beams. Magazine of Civil Engineering. 2024. 17(2). Article no. 12604. DOI: 10.34910/MCE.126.4

1. Introduction

In research on new concrete materials, various types of concrete were investigated, such as high-strength concrete, inorganic concrete, organic concrete and steel fiber (SF) reinforced concrete. These materials were added to enhance the bearing capacity of concrete, improve its characteristics and reduce the occurrence of cracks in concrete beams. In order to create multilayer reinforced concrete (RC) beams, the process involves repairing damaged RC beams (RCB) by adding a new layer of concrete either above, below, or both above and below the existing concrete. To successfully repair damaged RCBs, it is crucial to thoroughly examine the input parameters, particularly in the case of three-layer steel fiber RCB. Numerous researchers have used nanosilica in their studies on SFRC. Their aim is to enhance the tensile strength and plasticity of nano concrete containing SFs. Consequently, these researchers have examined the impact of nanosilica on high-performance concrete that incorporates SF [1, 2].

Numerous studies have been conducted on the use of thin multilayer shells to repair damaged shell roofs. These studies have focused on various aspects, such as investigating the formation and development of cracks in the shell through experimental and ANSYS numerical simulation methods. Furthermore, studies have been carried out to establish relationships between load, vertical displacement (VD), and stress when evaluating the thickness of the SF concrete layer (SFCL) in the compressible shell

[3–5]. Numerous studies have been conducted on SF RCBs. These studies have focused on investigating the cracking and stress-strain states of RCB by modifying the SF content in the concrete. For example, different SF contents, such as $\mu=0\%$, $\mu=2\%$, $\mu=4\%$, and so on, have been examined in the studies [6], [7]. Several researchers have conducted studies on delaminated composite beams, focusing on various aspects, such as bending analysis, cracking propagation, and bending of composite beams [8, 9].

Iskhakov and his colleagues conducted a study on multilayer RCBs [10]. They had analyzed beams made of high strength concrete (HSC) in the compression zone and normal strength concrete (NSC) in the tensile zone. The research presented and examined the issues associated with different types of beams. Each layer was prescribed with an appropriate depth. The compatibility conditions between HSC and NSC layers were established. The premise was based on the assumption that the shear deformations on the layer borders in a section had been equal, particularly in the section with maximal depth of compression zone. A rigorous definition of HSC was given for the first time, achieved by careful analysis and comparison of deformability and strength characteristics of different classes of concrete. The application fields of two-layer concrete beams, including specific static schemes and load conditions, was made known. The main disadvantage of HSCs is their low ductility. To overcome this, fibers were incorporated into the HSC layer. Iskhakov's study examined the impact of different fiber volume ratios on structural ductility.

An evaluation was conducted on the strength of reinforced concrete beams made of high-performance concrete and fiber reinforced concrete through a bending test. An evaluation was conducted to assess the efficiency of utilizing steel fiber in bending structures. The significance of calculating the fiber content for such elements, similar to that of reinforcing steel bars for typical RC beams, was highlighted [11–12].

The experimental study [13] focused on two-layer beams made of steel fibered high strength concrete (SFHSC) in the compression zone and NSC in the tensile zone. Calculating the fiber content for two-layer beams was essential corresponding to the required ductility level of an RC element. This research was focused on testing full scale two-layer beam. The purpose of this work was to show the efficiency of two-layer bending element during the whole loading process, including collapse, and to experimentally verify the data related to interaction of concrete layers in two-layer beams. After the NSC layer was hardened, the SFHSC layer was cast to examine the influence of separate casting technology, which is more convenient for two-layer beam production in real construction.

The same authors performed tests on models of full-scale statically determinate two-layer beams in another study [14]. These beams were also constructed using SFHSC in the compression zone and NSC in the tensile zone. The current study represented the next phase of these investigations, focused on testing a continuous two-span two-layer beam with an optimal steel/fiber ratio, similar to the previous phases. The objective of this study was to examine the behavior of the continuous two-layer beam in both the span and above the middle support. Additionally it was investigated how the continuous two-layer beam responded to both positive and negative bending moments. This study was part of a series of investigation on two-layer beams [15]. In this series, a two-layer beam concept was designed, SFHSC was tested, as were the materials for simple supported and continuous two-span two-layer beams. The focus of the current research was testing full-scale prestressed simple supported two-layer beams. The objective of this study was to examine the behavior of prestressed two-layer beams at four-point bending and to compare it with the behavior of nonprestressed beams. No de-bonding has been observed between the SFHSC and the NSC layers in the tested beams up to the ultimate limit state. This indicated that there had been a proper interaction between the layers. The results suggested that further investigation of prestressed two-layer beam had been recommended for full-scale RC elements with longer spans (9–12 m). This research also highlighted the potential practical application of prestressed two-layer beam as effective and economical bending solution.

In structural analysis, the concept of concrete stiffness is important since it indicates the performance of beam elements in resisting deflection due to the working loads. In the study [16], the behavior of the graded concrete beam was continually examined. The bending moment-curvature relationship of the graded concrete beam was performed numerically to understand the level of ductility and the failure mode in relation to the conventional beam. A singly reinforced graded concrete beam was modelled using a non-linear simulation program Strand7. The result of the analysis was then evaluated in accordance with the Eurocode. The graded concrete beam "was expected to show a reliable behavior of bending moment – curvature so that it was possible for advanced application as structural element".

Numerical studies of these structures' stress-strain state under different types of loading are required in order to efficiently build multilayer structures out of concrete with different physico-mechanical characteristics. In the article [17] was analyzed the effect of concrete and cross section materials for the stress-strain state of three-layer RC with light weight concrete in the internal layer and heavy concrete in the external layers. The study showed that differences in the external layer's height and material had a substantial impact on the stress and deformation state of the three-layer beam under the different loads.

Rational specifications for the geometric cross section and materials used in various structural solutions for multilayer RC constructions were determined through scientific results. The research on three-layer beams [18] investigated the impact of geometrical parameters of the cross section, as well as the strength and deformability of the materials used in the stress-strain state and finite element analysis. This study focused specifically on the effect of these factors on the three-layer RCB with composite reinforcement. In addition, the study [19] examined the design parameters of RCB that impacted their bearing capacity. A separate study on multilayer RCB are presented in the References section of this article [20–26].

Further research should be conducted on multilayer beams, with a specific focus on three-layer SFRCB. These beams consist of upper and lower layers made of SF concrete, while the middle layer is made of normal concrete. The inclusion of concrete SF layers in the tensile zone and compressive area of the beams has the potential to improve their bearing capacity and minimize cracks in the bending beams. Therefore, it is important to explore and expand upon the study of these multilayer beams. In this paper, the author used ANSYS numerical simulations to examine the input parameters involved in the design of three-layer SFRCBs. These parameters have an impact on the bearing capacity of the beams, as well as on the formation and progression of cracks. The study focused specifically on factors such as the content of SF in concrete, the spacing of the shear steel stirrups at the ends of the beams, the number of tensile steel bars, and the thickness of the concrete layer of SF. The author constructed a diagram of how cracks in three-layer beams started and spread. The relationships between load and tensile stress (L-TS), load and compressive stress (L-CS), and load and vertical displacement (L-VD) are shown in the diagram. The author worked with ANSYS software to create simulation of RCB work, which allowed to calculate the stress at which the beam began to fail and become damaged.

2. Materials and Methods

2.1. Design Model of Beams

The research involved studying a three-layer beam made of steel fiber reinforced concrete (SFRC). The beam had a layer of SFRC on both the upper and lower layers, while the middle layer was made of normal concrete (NC). The dimensions of the beam were 15×30×220 cm. The SFCL was of grade B30, while the NC layer at the center of the beam was of grade B20.

Figure 1 shows the design of the three-layer RCB model.

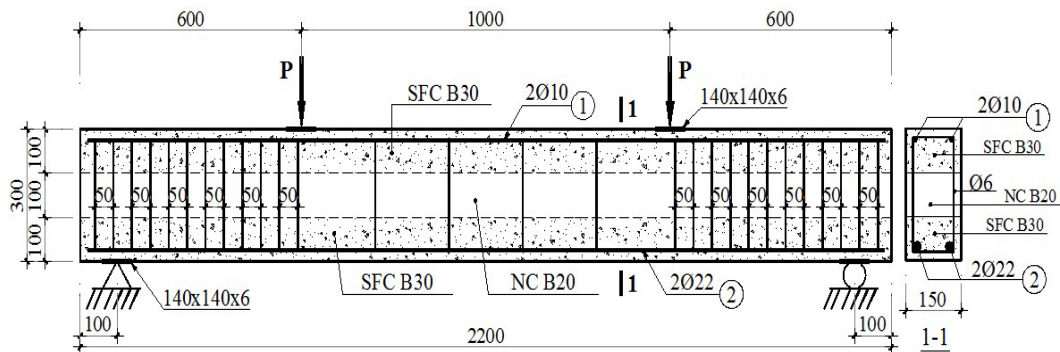


Figure 1. The design of the three-layer reinforced concrete beam model.

2.2. Finite element model for the three-layer reinforced concrete beams

Choosing the right model of SF dispersed in concrete is a crucial decision. The following models were used: smeared model, embedded model, and discrete model. The smeared model was used to represent the dispersion of SFs in concrete in this study.

Currently, there are two main models that are used to represent cracks in concrete: discrete model and smeared model. In this study, the focus was on examining the relationship between load and displacement. We were primarily interested in understanding this behavior and its correlation, without placing significant emphasis on factors such as crack shape or local stress. Therefore, the smeared model had been chosen to study cracks in concrete.

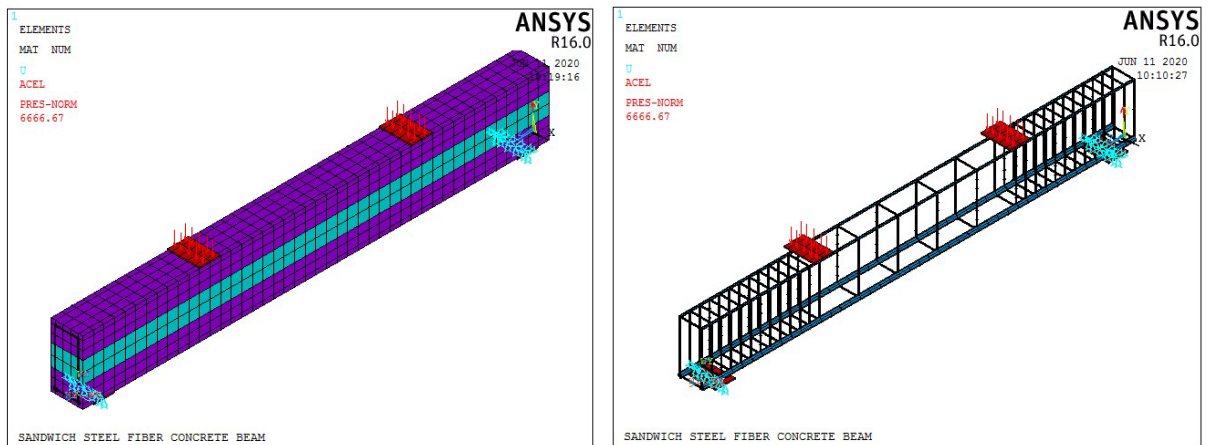
The modelling of reinforcement bars can be achieved by using the BEAM188 element, which consists of two nodes. Finite element modelling in beams is a technique used to analyze the structural behavior of beams. The SOLID65 element is a specialized simulation element that can accurately model concrete materials. It is capable of simulating the behavior of reinforcement in concrete, including phenomena such

as cracking and compression. Additionally, it allows to define nonlinear material properties. This element is three-dimensional and consists of eight buttons.

The mesh shapes in ANSYS were divided by 3D blocks because of the simple beam structure. Additionally, the element size was optimized for better performance. To input the parameters for the SOLID65 concrete element in ANSYS, we needed to specify eight essential parameters:

- 1) the shear force transmission coefficient when the crack is opened,
- 2) the shear force transmission coefficient when the crack is closed,
- 3) the cracking stress in tension,
- 4) the compressive stress,
- 5) the reduction coefficient for weakening due to cracking in tension,
- 6) the modulus,
- 7) Poisson's coefficient,
- 8) the stress-strain relationship.

Figure 2 shows the three-layer beam model in ANSYS.



a) three-layer beam model

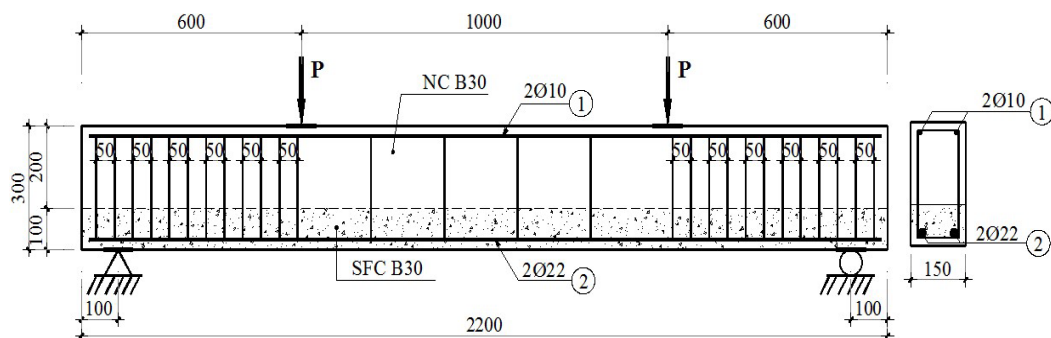
b) steel bar model, borders conditions and loads

Figure 2. Model of three-layer beams.

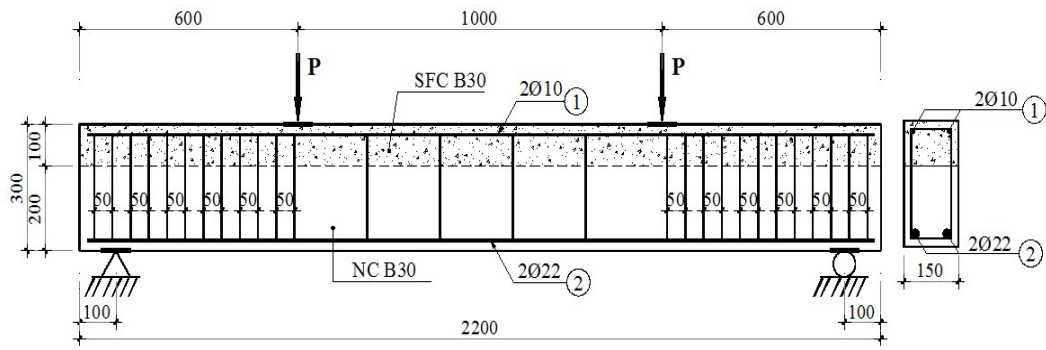
3. Results and Discussion

The author compared the accuracy of the two-layer beam testing method with the three-layer beam (TLB) model constructed in ANSYS. The two-layer beam was constructed to be the same size as the TLB, since there were no experimental results available for the TLBs to serve as a basis for the beam survey.

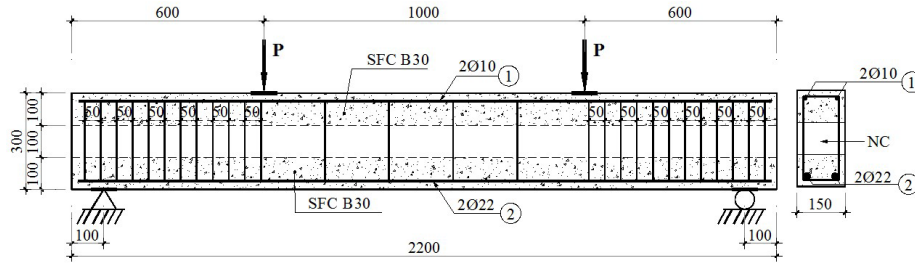
The design model in Figure 3 shows two-layer and three-layer RCBs.



a) The steel fiber layer is located at the bottom.



b) The steel fiber layer is located on top.



c) A three-layer SFRF beam.

Figure 3. Model of two-layer and three-layer reinforced concrete beams

Figure 4 shows the process of concreting beams in layers.



Figure 4. Concreting beams in layers.

Figure 5 shows the test beams.



Figure 5. Test beams on the experimental pedestal.

Figure 6 shows the measuring devices.

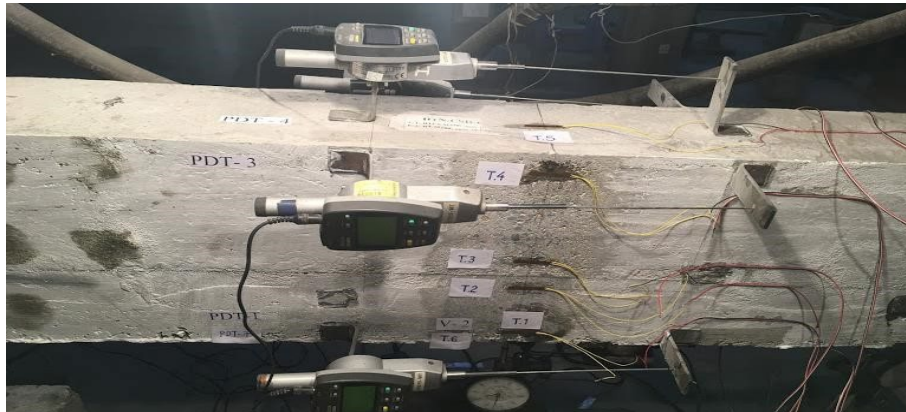


Figure 6. The beams had measuring devices on them.

The formation and development of cracks are shown in Figure 7.



Figure 7. Formation and development of cracks in test beams.

The L-VD relationship in the middle of RCB is shown in Figure 8.

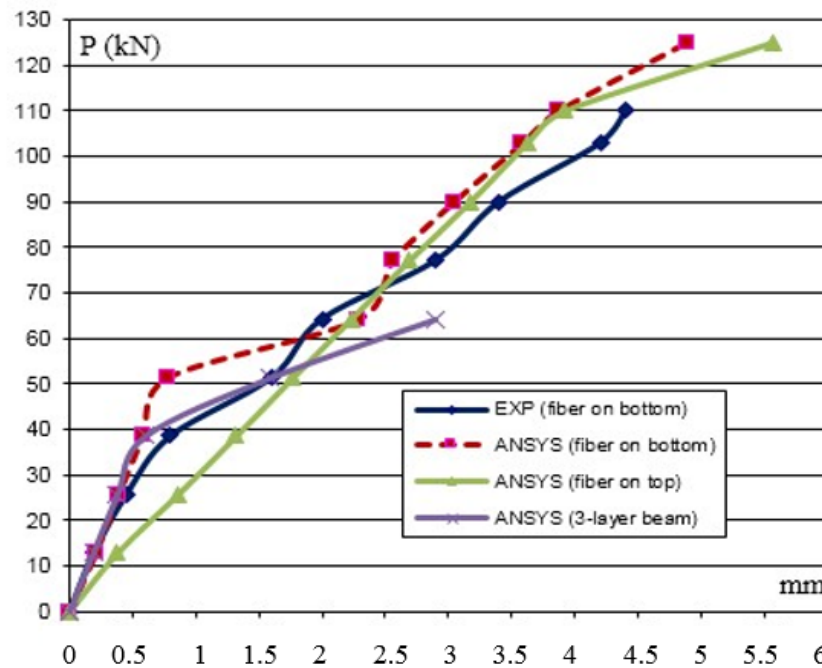
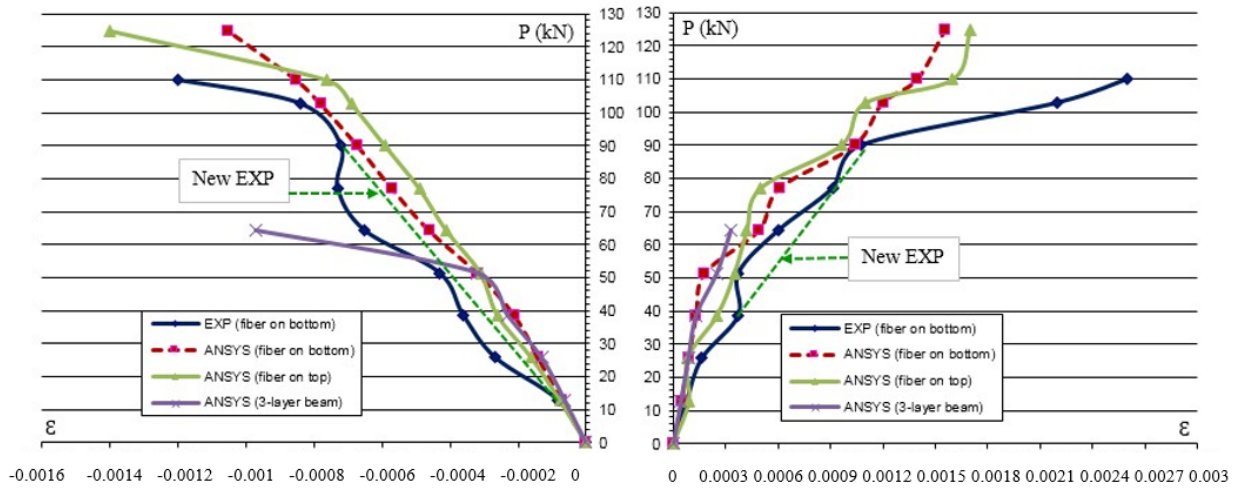


Figure 8. vertical displacement at the middle of reinforced concrete beams

The relationship between load and compressive deformation (L-CD), as well as the relationship between load and tensile deformation in the middle of RCB, are shown in Figure 9.



a) Load - compressive deformation relationship b) Load - tensile deformation relationship

Figure 9. Load - deformation relationships of reinforced concrete beams.

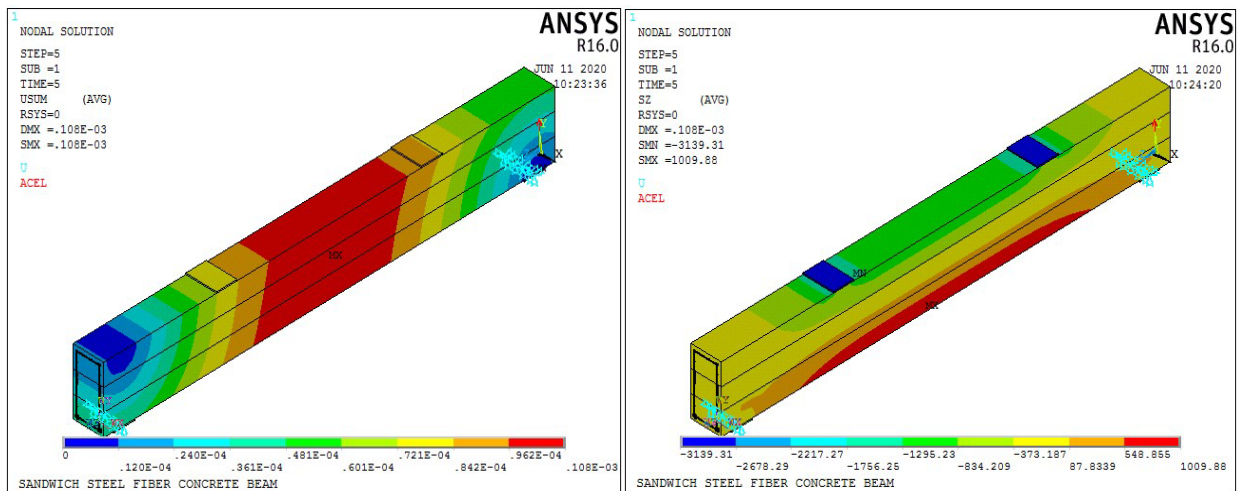
Comment: After comparing the results of test beams and simulations in ANSYS for the survey, it was proven that the program had been designed correctly. It can be used effectively to change input parameters. The input parameters that affect the stress-strain state and VD in SFRC beam are following:

- the content of SF in concrete,
- the spacing of the shear steel stirrups at the ends of RCB,
- the number of TS bars,
- the diameter of TS bars and the thickness of the SF concrete layer.

3.1. Investigation of the effects of changes in SF content on the properties of concrete

The concrete SF content was adjusted to 2 % and 4 % from its initial 0 %. Stirrups, with a diameter of $\phi 6a50$, were placed at the ends of the beam. In the middle of the beam stirrups with a diameter of $\phi 6a200$ were used. TS bars with a diameter of $2\phi 22$ were used, while compression steel bars with a diameter of $2\phi 10$ were used. The thickness of the SF concrete layers, both at the bottom and at the top, was set at $H1 = H2 = 10$ cm. Furthermore, a NC layer with a thickness of $H3 = 10$ cm was placed in the middle of the beam. It is important to note that the numerical simulation analysis in ANSYS considered non-linear materials.

Figure 10 shows VD and the stress color spectrum.



a) Color spectrum of vertical displacement

b) Color spectrum of stresses

Figure 10. Color spectrum of VD and stresses values on the beam.

Comment: In Figure 10a the middle of the beam has the biggest VD; as it gets closer to the supports, the value decreases. Tensile stress is centered on the bottom of the beam, with the maximum value occurring in the middle of the beam, as indicated by the color spectrum of the prestresses in Figure 10b. On the other hand, the compressive stress is located in the upper part of a beam and is affected by the force applied by two concentrated forces. This demonstrates that the beam's actual operating conditions are accurately simulated by ANSYS.

The beams begin to crack when there is a change in the SF content in the concrete, as shown in Figure 11.

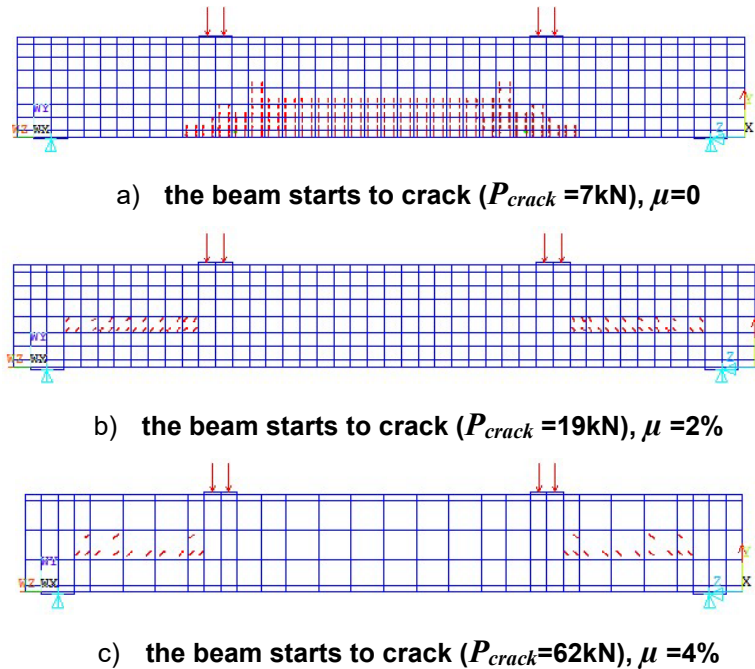
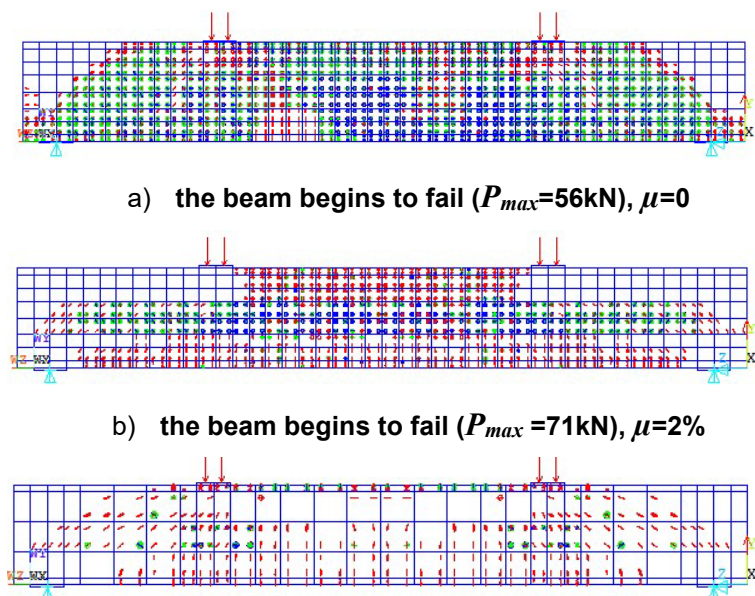


Figure 11. The beginning of beam cracking in the ANSYS.

Comment: In Figure 11a the three layers consist of NC. As a result, cracks initially appear in the part with the highest tensile stress, which is located at the bottom of the beam. These cracks then progress towards the compressive area. In Figures 11b and 11c the lower layer consists of SFRC, which has a higher intensity compared to the NC layer in the middle. As a result, the cracks initially appear in the middle layer of the beam. By increasing the SF content in concrete from 2 % to 4 %, load-induced cracking increased from 19kN to 62kN. This happens because the concrete layer in the tensile zone consists of SF concrete, resulting in fewer cracks and a higher bearing capacity of the beam.

The beams begin to fail when there is a change in the SF content in the concrete, as shown in Figure 12.



c) the beam begins to fail ($P_{max}=122\text{kN}$), $\mu=4\%$

Figure 12. Beginning of beam failure in ANSYS.

Comment: In Figure 12a it was observed that RCB without any SF content began to show signs of damage at a load level of 56kN. Cracks were observed in the RCB. However, when the SF content was increased to 2 %, the destructive load of the beams also increased to 71kN. Furthermore, the presence of SFs resulted in a decrease in the number of cracks compared to beams without any SF content. By increasing the content of SFs to 4 %, the bearing capacity of the beam is further enhanced, reaching 122kN. Furthermore, the presence of SFs in concrete has significantly reduced the appearance of cracks in the beam. This demonstrates that the inclusion of SFs not only minimizes cracks, but also increases the beam's ability to withstand force.

The L-CS, L-TS and L-VD relationships are shown in Figure 13.

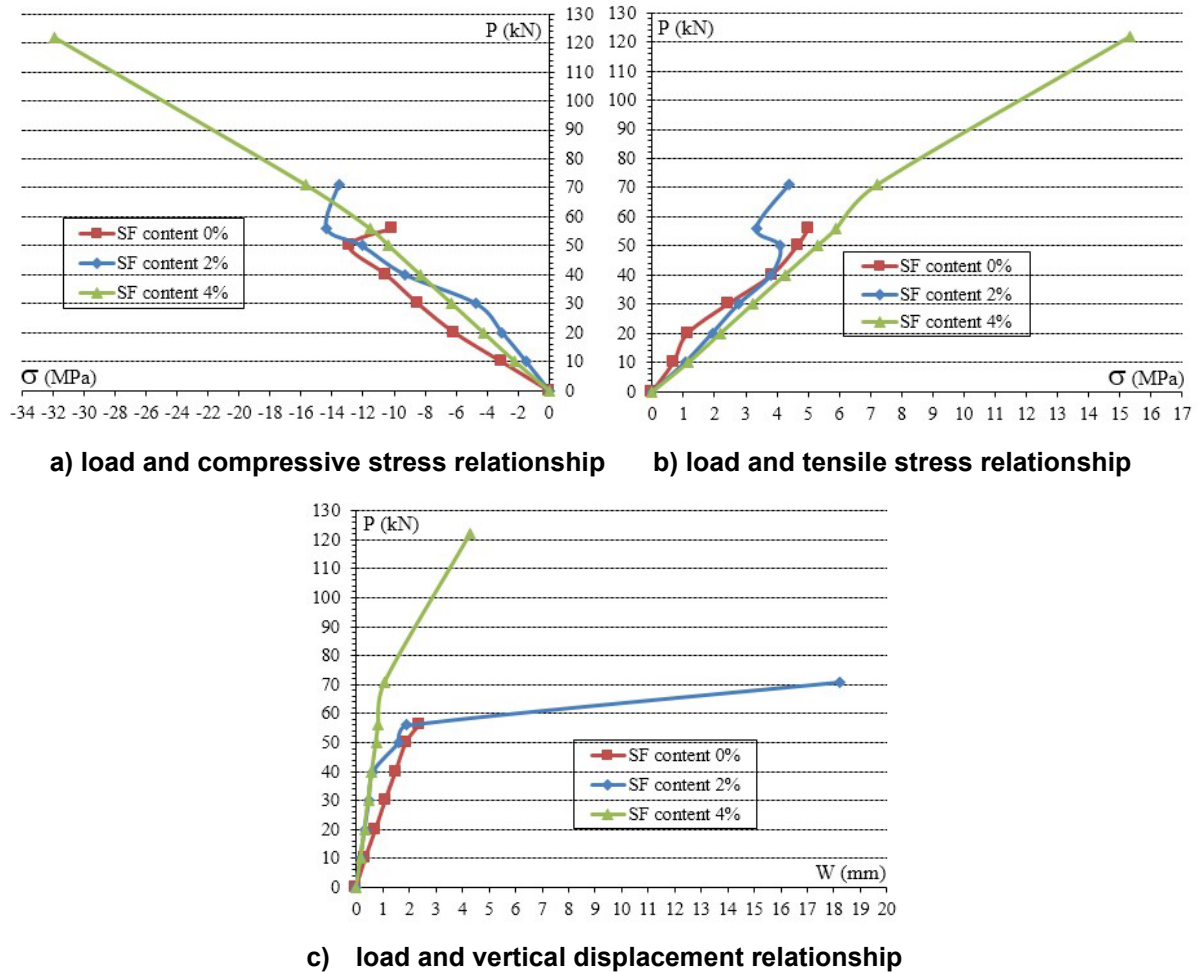


Figure 13. load and compressive stress, load and tensile stress and load and vertical displacement Relationships in the Beam, where SF content refers to the SF content present in concrete.

Comment: In Figure 13a it can be observed that normal RCB with SF content of 0 % shows the minimum compressive strain value. On the other hand, Figure 13b shows that beams with SF content of 4 % have the highest tensile strain. The VD of normal RCB is greater than that of other beams. When concrete contains 0 % and 2 % SFs, VDs are approximately equal under loads ranging from 0 to 56kN. However, once the limit is exceeded, the stress levels show significant variation.

3.2. Investigation of the effects of changes in shear steel stirrup spacing at the ends of the beam

RCB had a SF content of 2 %. The spacing of the stirrups has been changed from $\phi 6a50$ to $\phi 6a100$. TS bar had a diameter of $2\phi 22$, while the compression steel bars had a diameter of $2\phi 10$. The thickness of the SF concrete layers was $H1 = H2 = 10$ cm, and the thickness of the NC layer was $H3 = 10$ cm. The ANSYS numerical simulation analysis considered non-linear materials as shown in Figure 14.

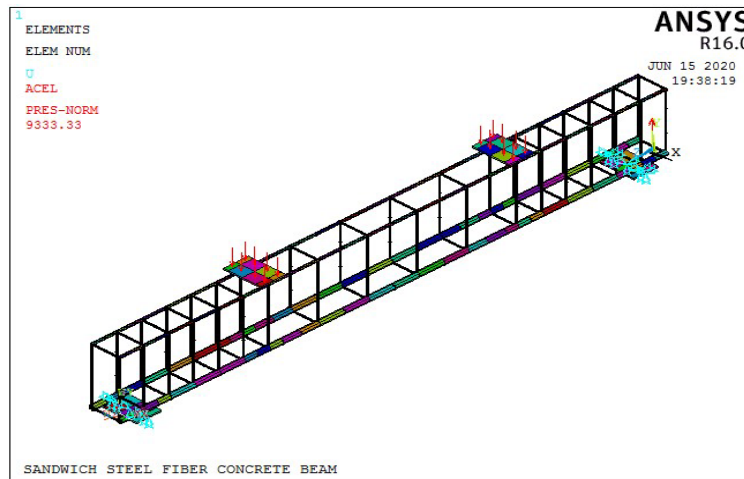


Figure 14. Shear steel stirrup spacings are changed.

The beams began to crack and fail when the stirrups at the ends of the beam had changed, as shown in Figure 15.

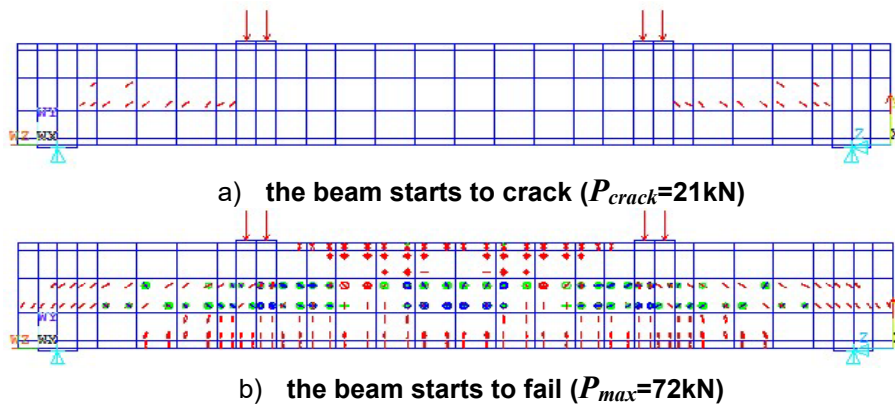
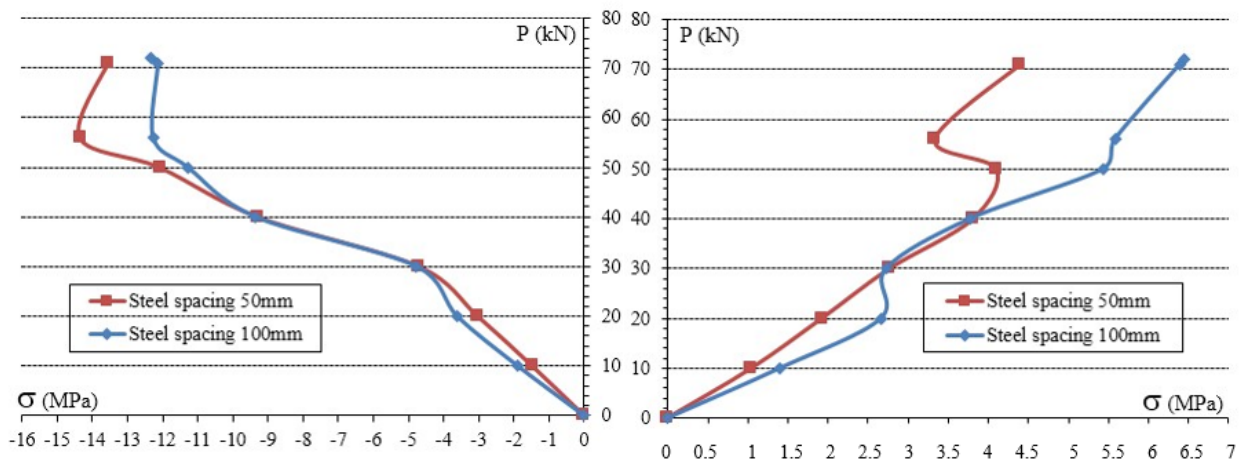


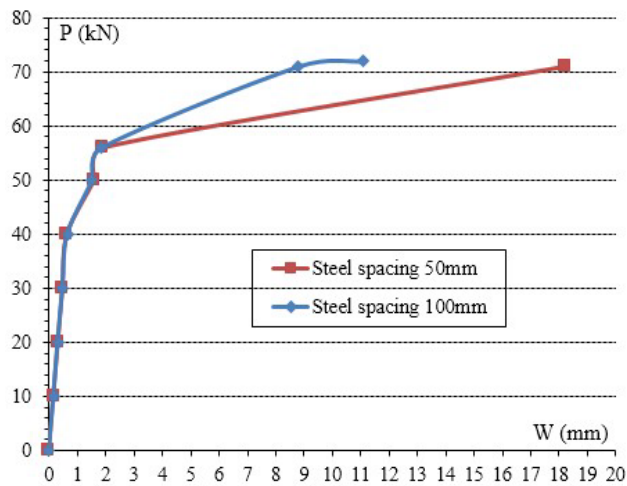
Figure 15. Beams start to crack and fail when shear steel stirrup spacing is changed.

Comment: In Figure 11b the beam shows cracking at a load of 19 kN, when the shear steel stirrup spacing at the ends of the beam is 50 mm. When the shear steel stirrup spacing is increased to 100 mm, the beam experiences cracking at a higher load of 21 kN. Furthermore, the beam begins to show signs of damage when the shear steel stirrup spacing is 50 mm, with a load of 71 kN. Lastly, when the shear steel stirrup spacing is 100 mm, the beam begins to show signs of damage at a load of 72kN. However, the number of cracks in the beams decreased significantly at the shear steel stirrup spacing 100 mm. This is due to the shear steel stirrup spacing being too thick and the steel content in concrete exceeding the allowed content value of steel in concrete.

The L-CS, L-TS and L-VD relationships are shown in Figure 16.



a) load and compressive stress relationship b) load and tensile stress relationship



c) load and vertical displacement relationship

Figure 16. load and compressive stress, load and tensile stress and load and vertical displacement relationships.

Comment: In Figures 16a and 16b, as the load increases from 0 kN to 40 kN, both compressive and tensile stresses experience minimal changes. However, beyond 40 kN, these stress values begin to vary. It should be noted that the steel stirrup spacing is 100 mm, which is smaller compared to the shear steel stirrup spacing of 50 mm. Additionally, the tensile stress in the former is greater than that in the latter. The shear steel stirrups are placed at a spacing of 100 mm, which is reduced to 50 mm in situations where there is VD.

3.3. Investigation of the effects of changes in TS bars number on the beam

The RCB had a SF content of 2 %. The spacing of the stirrups was $\phi 6a100$. TS bars had been changed from $2\phi 22$ to $3\phi 22$. The thickness of the SF concrete layers was $H1 = H2 = 10$ cm and the thickness of the NC layer was $H3 = 10$ cm. The ANSYS numerical simulation analysis shown in Figure 17 took into account non-linear materials.

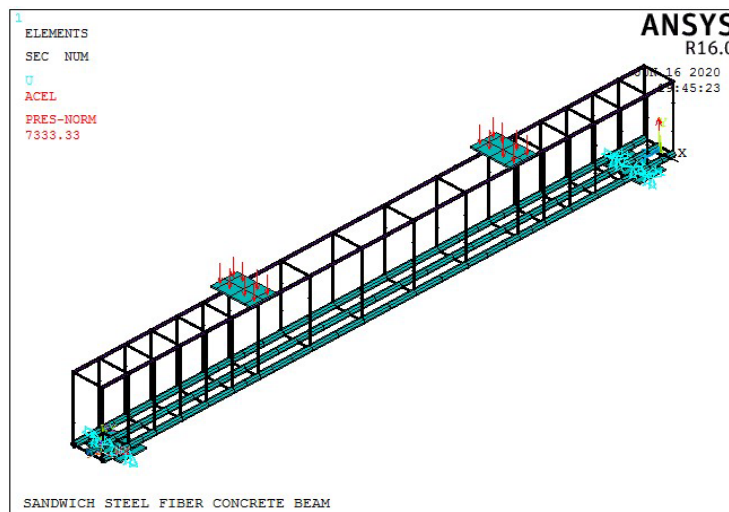
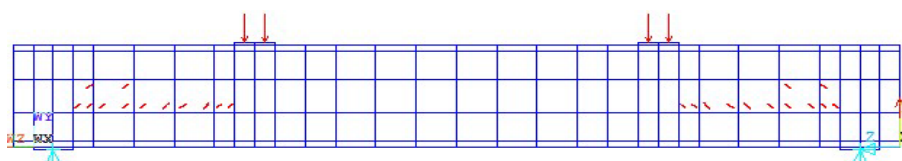
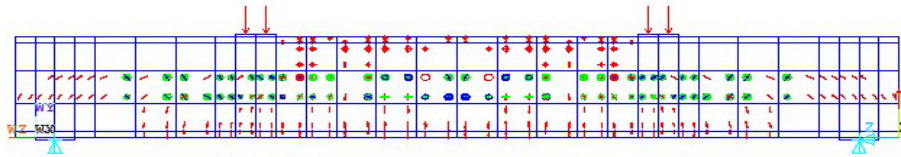


Figure 17. The beam with tensile stress bars number changes.

The beams began to crack and get damaged when the number of TS bar changes, as shown in Figure 18.



a) the beam starts to crack ($P_{crack}=22kN$), $3\phi 22$

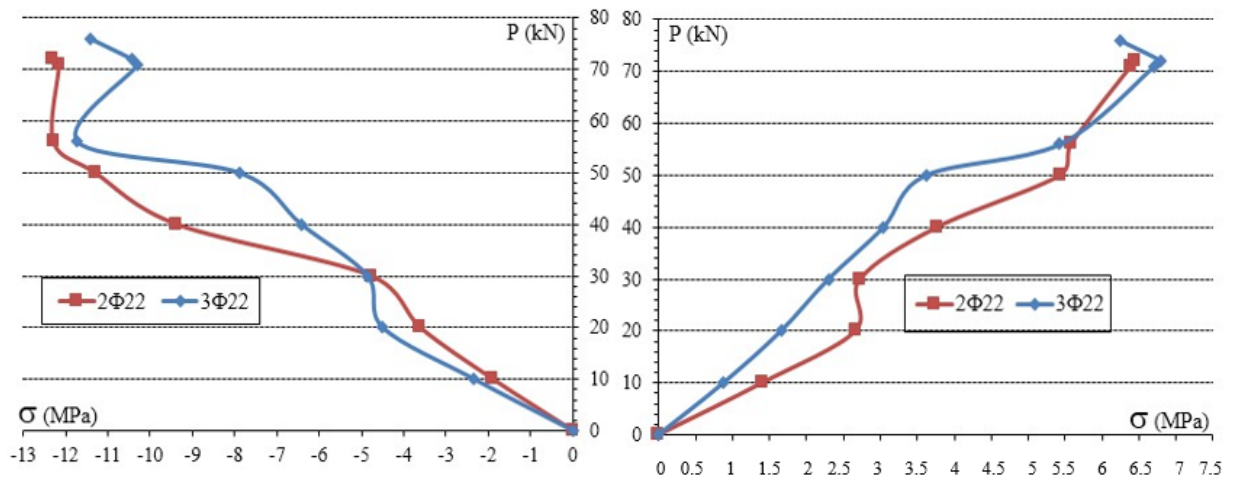


b) the beam starts to fail ($P_{max}=76kN$), $3\phi22$

Figure 18. Beams start to crack and fail when the tensile stress bars number is changed.

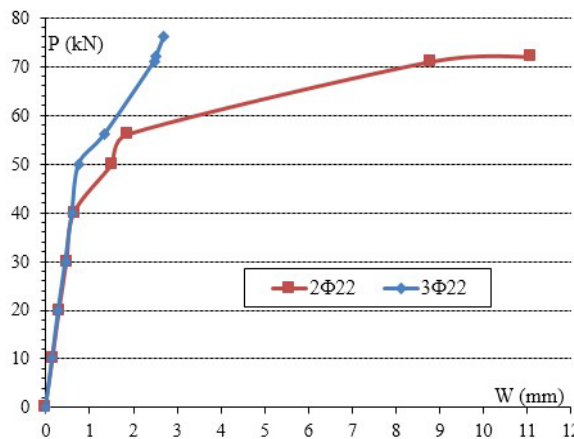
Comment: The beam begin to crack and fail when the number of tensile bars increased to $3\phi22$, compared to when there were only $2\phi22$ tensile bars. The beams in Figure 15a starts to crack at a load of 21 kN. On the other hand, the beams in Figure 18a begin to crack at a load of 22 kN, with an increase of 1 kN afterward. When the beam starts to fail, it occurs at 72 kN for $2\phi22$ beams and at 76 kN for $3\phi22$ beams. However, despite an increase in the TS bars number in the beam, the crack does not show significant changes (as is observed in Figures 8a and 18a). It is worth noting, that the beam only starts to crack in the NC layer located in the middle of the beam.

The L-CS, L-TS and L-VD relationships are shown in Figure 19.



a) load and compressive stress relationship

b) load and tensile stress relationship



c) load and vertical displacement relationship

Figure 19. Load and compressive stress, load and tensile stress and load and vertical displacement relationships.

Comment: In Figure 19a, as the load increases from 0 to 30 kN in compressive stress, the compressive stress between $2\phi22$ and $3\phi22$ remains relatively stable. However, once the load exceeds 30 kN, there is a significant increase in compressive stress, reaching 3 MPa. Tensile stress undergoes a slight change of only 1 MPa in the middle of the beam, as shown in Figure 19b. When the RCB reach a VD of 40 kN, they begin to show changes as the value of $2\phi22$ increases. Additionally, it is worth noting, that

3 ϕ 22 differs significantly from 2 ϕ 22. This demonstrates the effectiveness of increasing the quantity of TS bars in the tensile zone.

3.4. Investigation of the effects of changes in the TS bars diameter

The RCB had a SF content of 2%. The spacing of the stirrups was ϕ 6a100. The TSB consist of 2 ϕ 22, 2 ϕ 16, and 2 ϕ 30 bars. The thickness of the SF concrete layers was H1 = H2 = 10 cm and the thickness of the NC layer was H3=10cm. The ANSYS numerical simulation analysis took into account the nonlinear behavior of the materials.

The beams began to crack and fail when the diameter of the TSB had been changed, as shown in Figure 20.

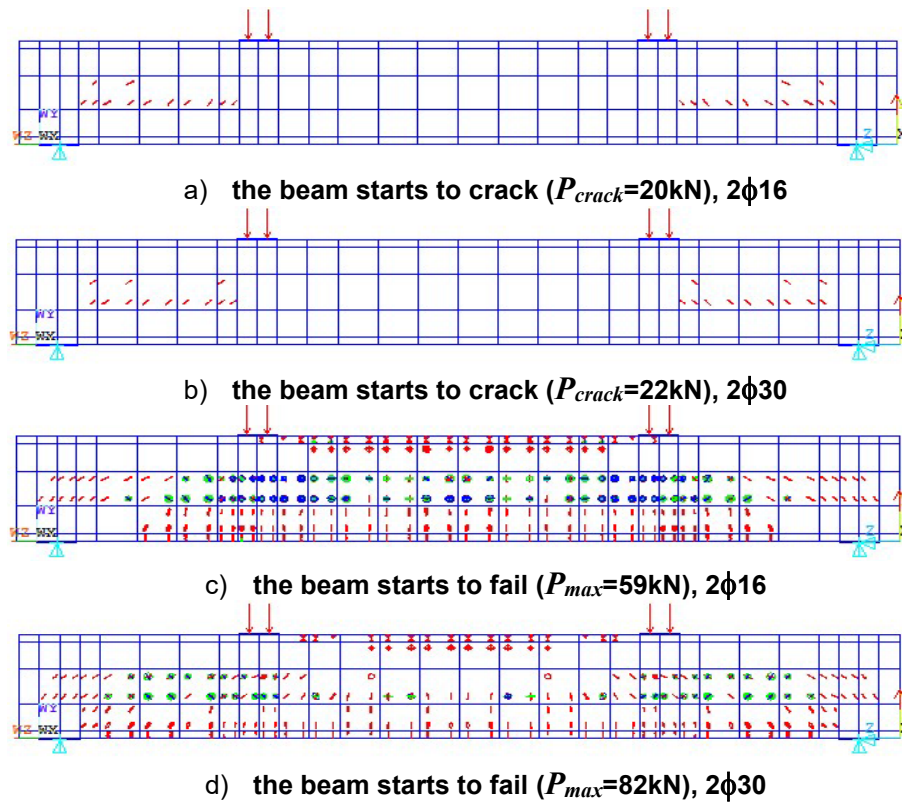
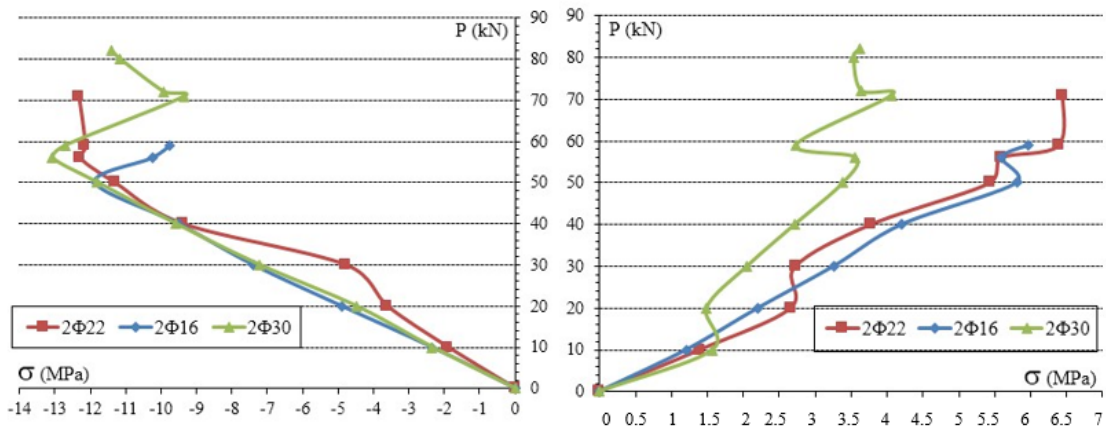


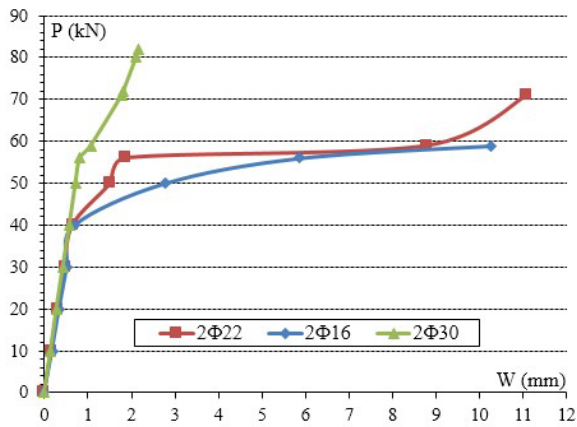
Figure 20. Beams start to crack and fail when diameter of TSB had been changed.

Comment: The cracks in Figures 20a and 20b initially appear in the NC layer. Cracking occurs when the load is applied and the diameter of the TS bar remains relatively unchanged. The limit of the damaged beams varies significantly. Specifically, 2 ϕ 16 beams have a limit of 59 kN, 2 ϕ 22 beams have a limit of 72 kN, and 2 ϕ 30 beams have a limit of 82 kN. The bearing capacity increases to 23 kN between 2 ϕ 16 and 2 ϕ 30, however, there is not a significant change in the number of cracks.

The L-CS, L-TS and L-VD relationships are shown in Figure 21.



a) load and compressive stress relationship b) load and tensile stress relationship



c) load and vertical displacement relationship

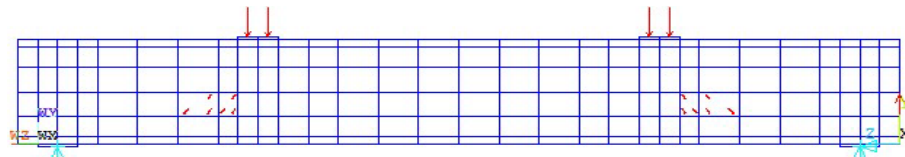
Figure 21. load and compressive stress, load and tensile stress and load and vertical displacement relationships.

Comment: When the diameter of the TS bars is changed, the stresses in the compression zone show minimal changes (as shown in Figure 21a) for the tensile stress of $2\phi 16$ and $2\phi 22$. However, for the tensile stress of $2\phi 30$, there is variation, with a difference of 3 MPa in the tensile stress (as shown in Figure 21b). In the same way, the VD in the beams also varies when the load exceeds 40 kN. During this period, beams of $2\phi 16$ and $2\phi 22$ show a higher displacement value compared to beams of $2\phi 30$.

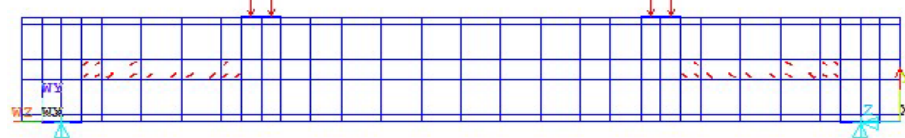
3.5. Investigation of the effect of changes in SF concrete layer that has the same thickness

The RCB had a SF content of 2 %, the spacing of the stirrups was $\phi 6a100$. The beam also contained $2\phi 22$ TS bars and $2\phi 10$ compression steel bars. The thickness of the concrete layers of SFs was currently $H1 = H2 = H = 10$ cm, but had been changed to $H1 = H2 = H = 8$ cm and $H1 = H2 = H = 12$ cm. The ANSYS numerical simulation analysis took into account the nonlinear behavior of the materials.

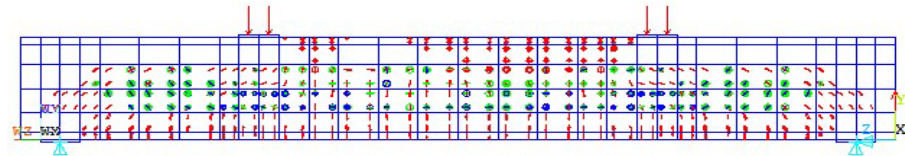
The beams began to crack and fail when there was a change in the thickness of the SF concrete layer, as shown in Figure 22.



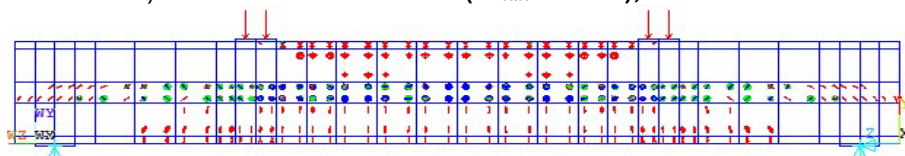
a) the beam starts to crack ($P_{crack}=17kN$), $H1=H2=8cm$



b) the beam starts to crack ($P_{crack}=21kN$), $H1=H2=12cm$



c) the beam starts to fail ($P_{max} = 62kN$), $H1 = H2 = 8$ cm



d) the beam starts to fail ($P_{max}=78kN$), $H1=H2=12$ cm

Figure 22. Beams start to crack and fail when the thickness of SFCL changes.

Comment: Increasing the thickness of SF concrete layers from 8 to 12 cm results in the improvement of the beam's bearing capacity from 17 to 21 kN. Furthermore, cracks begin to appear in the RCB. In the same way, the bearing capacity of the beams increased from 62 kN to 78 kN during failing. Additionally, there is a significant decrease in the number of cracks observed in the RCB. It is worth noting, that in both cases, the NC layer of the beam showed cracking, as shown in Figure 22.

The L-CS, L-TS and L-VD relationships are shown in Figure 23.

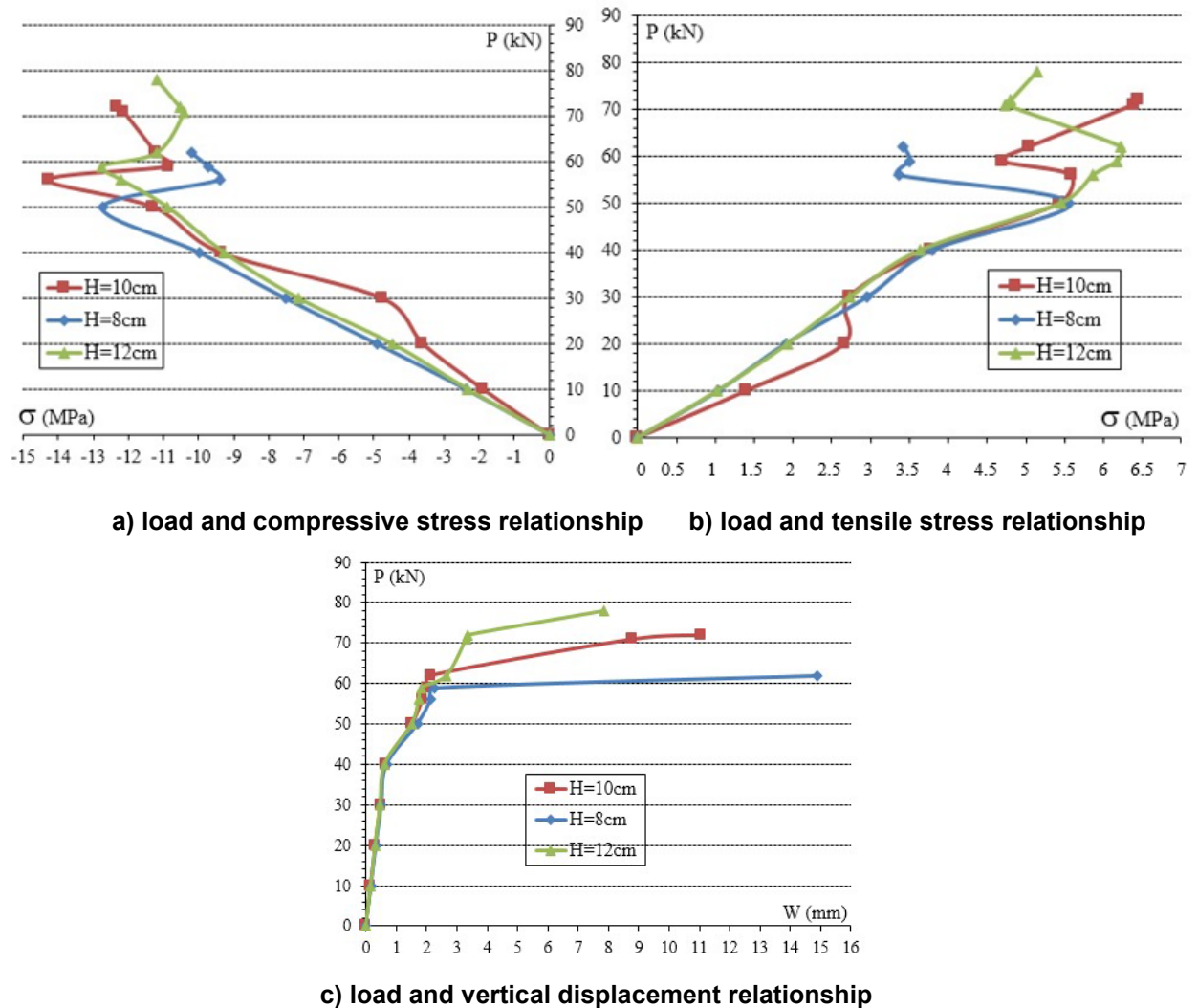


Figure 23. Load and compressive stress, load and tensile stress and load and vertical displacement relationships.

3.6. Comment: In Figure 23, when the thickness of the SF concrete layer is changed without modifying the size of the RCB, the compressive stress, tensile stress and VD in the middle of the beam remain unchanged while the load is varied from 0 kN to 50 kN. The beams undergo a change when the load exceeds this value.

The stresses and VDs of beams with a small thickness of SF concrete layer ($H1 = H2 = H = 8$ cm) undergo changes. Investigation of the effects of changes in the thickness of a SF concrete layer

The RCB had a SF content of 2 %. The spacing of the stirrups was $\phi 6a100$. The thickness of the SF concrete layers was $H1 = H2 = H = 10$ cm, but it could be changed to $H1 = 8$ cm and $H2 = 12$ cm or $H1 = 12$ cm and $H2 = 8$ cm. The ANSYS numerical simulation analysis took into account the nonlinear behavior of the materials.

The thickness of the SF concrete layer at the bottom was marked as H1, while the thickness of the SF concrete layer at the top was marked as H2.

The beams began to crack and fail when there was a change in the thickness of the SF concrete layer, as shown in Figure 24.

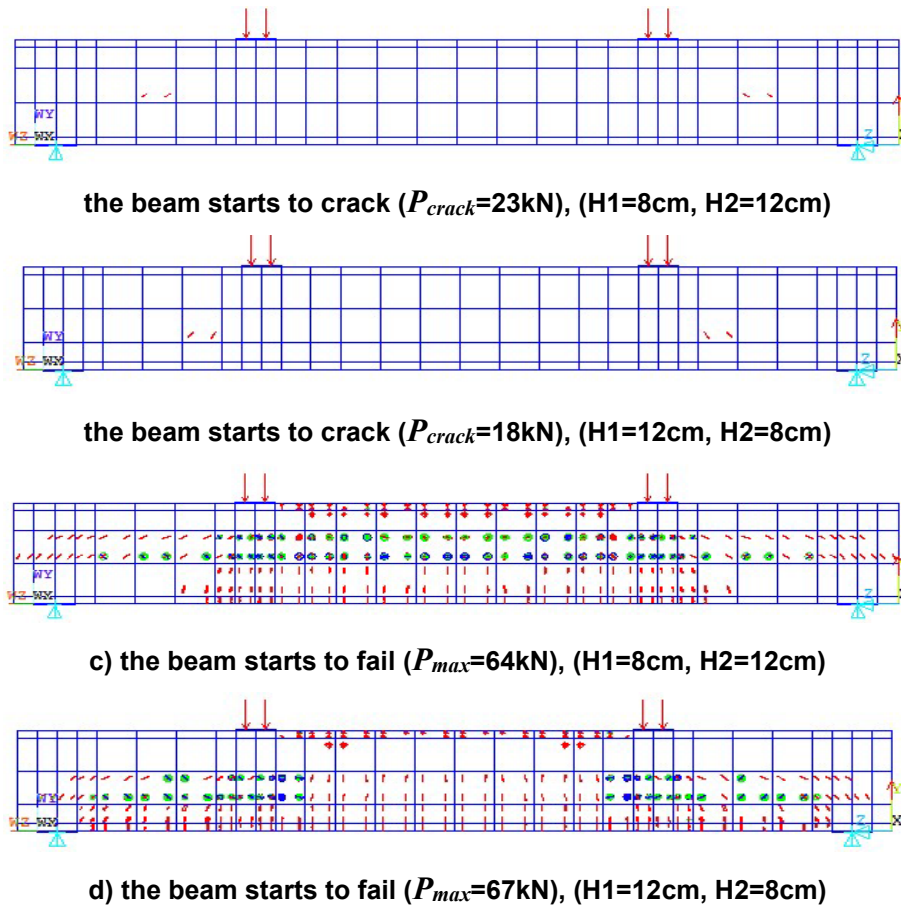
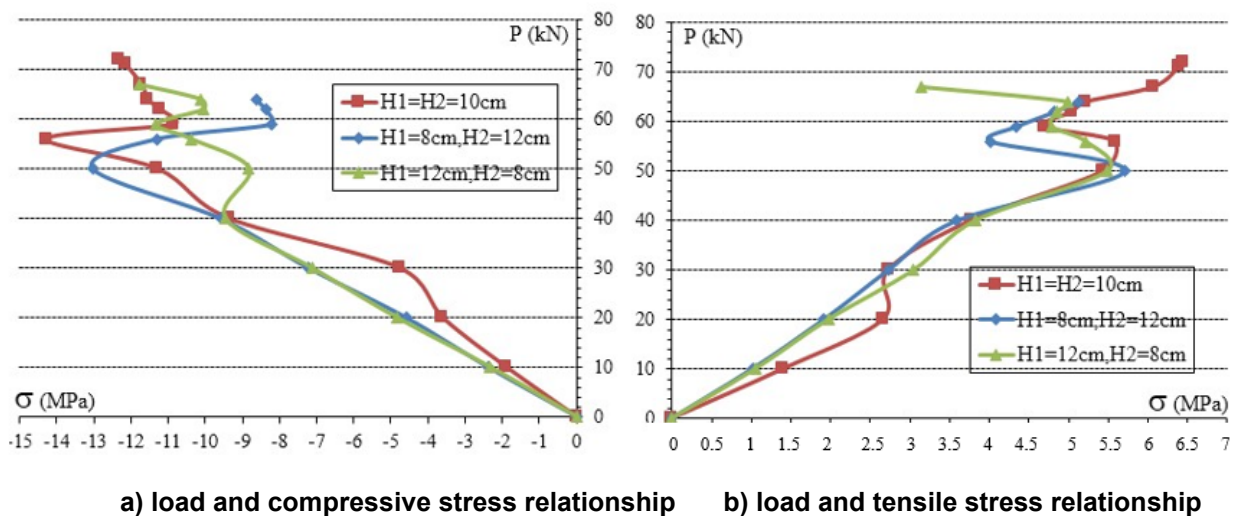
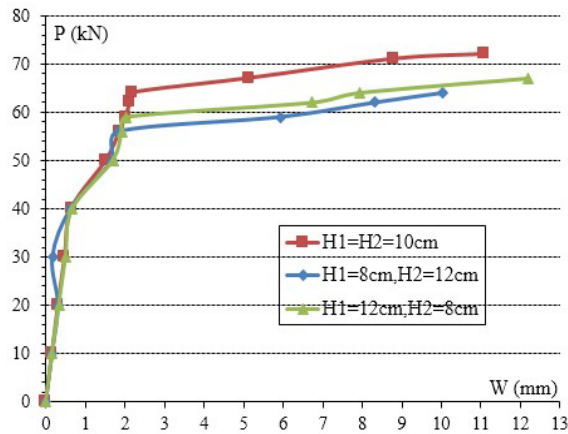


Figure 24. Beams start to crack and fail when thickness of SFCL changes.

Comment: In Figure 24 the top SF concrete layer is thicker than the bottom SF concrete layer. Specifically, the thickness of the top layer (H1) is 8 cm, while the thickness of the bottom layer (H2) is 12 cm. As a result of this configuration, the bearing capacity of the beam increases from 18 kN to 23 kN, when the thicknesses are reversed (H1 = 12 cm, H2 = 8 cm). However, it is important to note that this change in configuration also leads to the formation of cracks in the beam. When the beam is gradually damaged, there is a corresponding change observed. The thickness of the SF concrete layer at the bottom becomes greater than the thickness of the SF concrete layer at the top. This increase in thickness leads to an improvement in bearing capacity, which increases from 64 kN to 67 kN. These findings suggest that increasing the thickness of the SFCL improves its performance.

The L-CS, L-TS and L-VD relationships are shown in Figure 25.





c) load and vertical displacement relationship

Figure 25. Load and compressive stress, load and tensile stress and load and vertical displacement relationships.

Comment: In Figure 25, it can be observed that the change in thickness of various layers of SF concrete does not result in significant changes in the values of compressive stress, tensile stress, and VD. However, it is observed that when the heights of H1 and H2 are both 10 cm, the beam shows a higher bearing capacity compared to other types. This is followed by beams with heights of H1 = 12 cm and H2 = 8 cm, and finally beams with heights of H1 = 8 cm and H2 = 12 cm.

According to this, another experimental study of two-layer RCB [13–14] demonstrates that the cracks observed in the test RCB share similar characteristics in terms of shape, formation, and development of the crack. This is shown in Figures 26 and 27. This study uses ANSYS numerical simulation [18] to investigate crack formation and development in three-layer RCB, as shown in Figure 28.

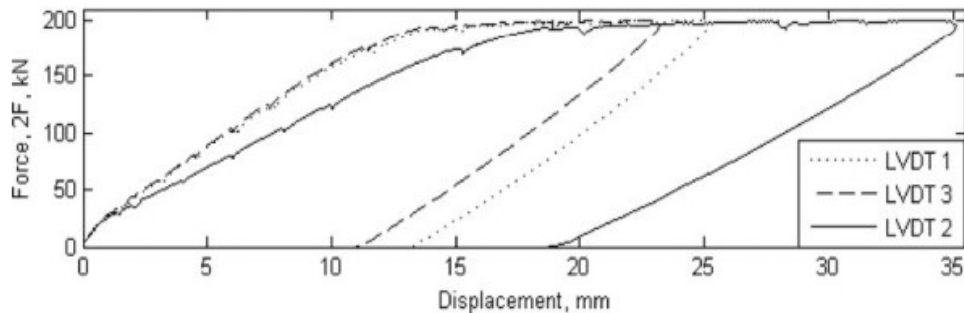


Figure 26. Beam deflections [13].

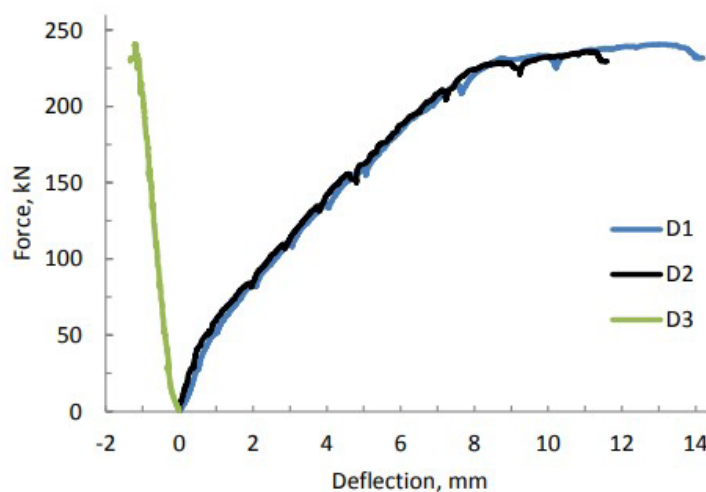


Figure 27. Load Deflection curves in the middle of the spans (D1 and D2) and the mid support uplift (D3) [14].

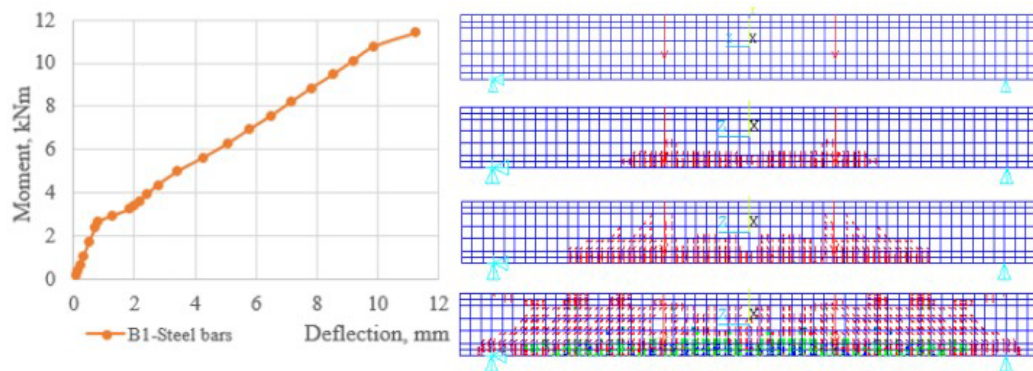


Figure 28. Moment deflection curve and crack pattern [18].

4. Conclusions

Based on the results of the study, we came to the following conclusions:

1. The addition of SFs to concrete resulted in a significant reduction in the number of cracks. When the SF content in the concrete was increased to 4 %, the beam began to experience damage, at a load value that was at least twice as high as the load value for other SF contents.
2. The effectiveness of the beam performance was enhanced by extending the distance between the shear steel bars to 100 mm. The reason for this was that the steel content in the concrete had exceeded the permitted limits.
3. Increasing the number of TS bars and their diameter significantly improved the bearing capacity of the beams, thereby reducing the occurrence of cracks. In this case, the increase in both the number and diameter of the steel bars in the tensile zone had a significant impact on the tensile stress.
4. There was minimal change in the stress value and VD when altering the thickness of the SF concrete layers.
5. The survey conducted on the input parameters of three-layer SF RCB revealed that these parameters had a significant impact on the stress-strain state of the beam. This survey can help modify the parameters needed to restrict or improve specific values that are more appropriate for the design of three-layer SF RCBs.

References

1. Ngo, V.T., Lam, T.Q.K., Do, T.M.D., Nguyen, T.C. Nano concrete aggregation with steel fibers: A problem to enhance the tensile strength of concrete. E3S Web of Conferences. 2019. 135. 03001. DOI: 10.1051/e3sconf/201913503001.
2. Ngo, V.T., Lam, T.Q.K., Do, T.M.D., Nguyen, T.C. Increased plasticity of nano concrete with steel fibers. Magazine of Civil Engineering. 2020. 93(1). Pp. 27–34. DOI: 10.18720/MCE.93.3.
3. Lam, T.Q.K., Do, T.M.D. Stress-strain in multi-layer reinforced concrete doubly curved shell roof. International Journal of Innovative Technology and Exploring Engineering (IJITEE). 2019. 8(4S2). Pp. 419–424.
4. Lam, T.Q.K., Do, T.M.D. Effect of each shell thickness on deformation stress and the ability for causing the cracks in the multilayer doubly curved shell roof. International Journal of Innovative Technology and Exploring Engineering (IJITEE). 2019. 8(6C2). Pp. 215–220.
5. Chepurmenko, A.S. Stress-strain state of three-layered shallow shells under conditions of nonlinear creep. Magazine of Civil Engineering. 2017. 76(8). Pp. 156–168. DOI: 10.18720/MCE.76.14.
6. Lam, T.Q.K., Do, T.M.D., Ngo, V.T., Nguyen, T.C., Huynh, T.P. Numerical simulation and experiment on steel fiber concrete beams. Journal of Physics: Conference Series. 2019. 1425. 012007. DOI: 10.1088/1742-6596/1425/1/012007.
7. Altun, F., Köse, M., Yılmaz, C., Arı, K., Durmuş, A. Experimental investigation of reinforced concrete beams with and without steel fiber under explosive loading. Indian Journal of Engineering & Materials Sciences. 2008. 14. Pp. 419–426.
8. Atlihan, G. Buckling analysis of delaminated composite beams. Indian Journal of Engineering & Materials Sciences. 2013. 20. Pp. 276–282.
9. Soto, A., Tehrani, F.M. An Investigation of Crack Propagation in Steel Fiber-Reinforced Composite Beams. Periodica Polytechnica Civil Engineering. 2018. 62(4). Pp. 956–962. DOI: 10.3311/PPci.10910.
10. Iskhakov, I., Ribakov, Y. A design method for two-layer beams consisting of normal and fibered high strength concrete. Materials & Design. 2007. 28(5). Pp. 1672–1677. DOI: 10.1016/j.matdes.2006.03.017.
11. Travush, V.I., Konin, D.V., Krylov, A.S. Strength of reinforced concrete beams of high-performance concrete and fiber reinforced concrete. Magazine of Civil Engineering. 2018. 77(1). Pp. 90–100. DOI: 10.18720/MCE.77.8.
12. Iskhakov, I., Ribakov, Y. Two-Layer Beams from Normal and Fibered High Strength Concrete. Conference: Modern Methods and Advances in Structural Engineering and Construction. 2011. DOI: 10.3850/978-981-08-7920-4_S3-M029-cd.
13. Iskhakov, I., Ribakov, Y., Holschemacher, K., Mueller, T. Experimental Investigation of Full Scale Two-Layer Reinforced Concrete Beams. Mechanics of Advanced Materials and Structures. 2014. 21. Pp. 273–283. DOI: 10.1080/15376494.2012.680673.

14. Iskhakov, I., Ribakov, Y., Holschemacher, K. Experimental investigation of continuous two-layer reinforced concrete beams. *Structural Concrete*. 2017. 18(1). Pp. 205–215. DOI: 10.1002/suco.201600027.
15. Iskhakov, I., Ribakov, Y., Holschemacher, K., Kaeseberg, S. Experimental investigation of prestressed two layer reinforced concrete beams. *Structural Concrete*. 2021. 22(1). Pp. 238–249. DOI: 10.1002/suco.201900328.
16. Pratama M.M.A., Suhud, R.K., Puspitasari, P., Kusuma, F.I., Putra, A.B.N.R. Finite element analysis of the bending moment-curvature of the double-layered graded concrete beam. *IOP Conf. Series: Materials Science and Engineering*. 2019. 494. 012064. DOI: 10.1088/1757-899X/494/1/012064.
17. Vu, D.T., Korol, E.A. Influence of geometrical parameters of the cross section, strength and deformability of the materials used on stress-strain state of three-layered reinforced concrete. *IOP Conf. Series: Materials Science and Engineering*. 2019. 661. 012121. DOI: 10.1088/1757-899X/661/1/012121.
18. Vu, D.T., Korol, E., Kustikova, Yu., Nguyen, H.H. Finite element analysis of three-layer concrete beam with composite reinforcement. *E3S Web of Conferences*. 2019. 97 02023. DOI: 10.1051/e3sconf/20199702023.
19. Do, T.M.D., Lam, T.Q.K. Design parameters of steel fiber concrete beams. *Magazine of Civil Engineering*. 2021. 102(2). 10207. DOI: 10.34910/MCE.102.7.
20. Olmedo, F.I., Valivonis, J., Cobo, A. Experimental study of multilayer beams of lightweight concrete and normal concrete. *Procedia Engineering*. 2017. 172. Pp. 808–815. DOI: 10.1016/j.proeng.2017.02.128.
21. Ranjbaran, F., Rezayfar, O., Mirzababai, R. Experimental investigation of steel fiber-reinforced concrete beams under cyclic loading. *International Journal of Advanced Structural Engineering*. 2018. 10. Pp. 49–60. DOI: 10.1007/s40091-018-0177-1.
22. Muselemov, Kh.M., Bulgakov, A.I., Muselemov, Dz.U. Stress-Strain State of an Unsymmetrical Three-Layer Beam. *Modern Trends in Construction, Urban and Territorial Planning*. 2023. 2(4). Pp. 27–33. DOI: 10.23947/2949-1835-2023-2-4-27-33.
23. Do, T.M.D., Lam, T.Q.K. Cracks in single-layer and multi-layer concrete beams. *Transportation Research Procedia*. 2022. 63. Pp. 2589–2600. DOI: 10.1016/j.trpro.2022.06.298.
24. Su, C., Liu, D., Cao, S., et al. Analysis of static and dynamic flexural and tensile failure modes of double-layer concrete composite beams [J]. *Journal of Southwest Jiaotong University*. 2017. 52(4). Pp. 731–737. DOI: 10.3969/j.issn.0258-2724.2017.04.011.
25. Najm, H.B. Flexural Behavior of Two-layers Reinforced Concrete Beams. *Polytechnic Journal*. 2022. 12(2). Pp. 180-192. DOI: 10.25156/ptj.v12n2y2022.pp180-192.
26. TrustGod, J.A., Blessing, B.T. Optimum Depth of a Lower Concrete Grade at the Tension Zone in a Two-Layer Reinforced Concrete Beam. *Nigerian Journal of Technological Development*. 2023. 20(1). Pp. 1–8. DOI: 10.4314/njtd.v20i1.1197.

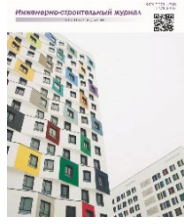
Information about author:

Thanh Quang Khai Lam, PhD

ORCID: <https://orcid.org/0000-0003-3142-428X>

Email: lamthanhquangkhai@gmail.com

Received 01.08.2020. Approved after reviewing 08.10.2021. Accepted 09.10.2023.



Research article

UDC 666.97

DOI: 10.34910/MCE.126.5



The temperature nomogram to predict the maximum temperature in mass concrete

T.C. Nguyen¹ , A.K. Bui²  

¹ Le Quy Don Technical University, Ha Noi, Vietnam

² Ho Chi Minh City Open University, Ho Chi Minh City, Vietnam

 kiet.ba@ou.edu.vn

Keywords: mass concrete, thermal analysis, thermal crack, temperature nomogram, finite element simulation

Abstract. At an early age, the problem of cracking in concrete structures in general and large block structures in particular often appears. Many factors affect the formation of cracks in mass concrete structures. One of the factors considered is thermal cracking. Temperature is the most important factor to consider while constructing mass concrete. The temperature is affected by cement hydration and other factors, which leads to the production of thermal cracks at an early age. Tensile stresses that are greater than the concrete's tensile strength are typically the cause of cracking in mass concrete. These tensile stresses are more frequently caused by constraints against volumetric change, though they can also result from loads placed on the structure. Therefore, the prediction of temperature fields in massive concrete structures has been a significant challenge. This study presents a temperature nomogram by using numerical methods to quickly determine the maximum temperature in concrete structures with various characteristics, such as cement content and the initial temperature of concrete mixtures. The research results are meaningful for construction management agencies to use temperature diagrams to predict the maximum temperature in large concrete structures without the need to model the mass concrete. Besides, a nomogram can be used to predict the maximum temperature in mass concrete structures in order to prevent thermal cracks during construction and thereafter.

Funding: The authors would like to gratefully acknowledge the financial support of the Ministry of Education and Training of Vietnam for the Research Project, under the Contract no. B2022-MBS-08.

Citation: Nguyen, T.C., Bui, A.K. The temperature nomogram to predict the maximum temperature in mass concrete. Magazine of Civil Engineering. 2024. 17(2). Article no. 12605. DOI: 10.34910/MCE.126.5

1. Introduction

Mass concrete has different definitions and requirements depending on each country. However, the minimum size is the most important consideration in determining the mass concrete construction properties. According to ACI 116R-90 [1], mass concrete is defined as a concrete block of sufficient size that requires methods to deal with heat generation due to cement hydration and the concomitant volume transformation to prevent cracking. ACI 301-10 defines mass concrete as a concrete structure with a minimum size of 4 feet (1.3 m) [2]. The process of heat transfer from the concrete block's interior to the surrounding environment is influenced by the surface area of the mass. To evaluate that influence, the study [3, 4] considered the ratio of surface area to volume of concrete to affect the temperature field inside the mass concrete [3, 4]. Additionally, it is necessary to take measures to prevent the thermal crack formation at an early age not only for large-sized structures but also for small-sized structures that use a high cement content or high-heat cement. According to TCXDVN 9341:2012: "Mass concrete – Construction and acceptance", conventional reinforced concrete and concrete constructions with the smallest side greater

than 2 m can be called mass block concrete [5]. Mass concrete structures include dams, mass block foundations, pile caps, earth retaining walls, tunnel walls, bridge piers, etc. [5].

In Vietnam, during concrete structure construction, cracks often appear on the surface of the structural members at an early age for a variety of reasons. One of them, considered as the main reason, is due to heat generation of the hydration process. The formation of cracks impacts the expectancy, loading capacity, waterproofing ability, as well as aesthetics of the structures. Many domestic and international studies have discussed the process of heat generation and thermal stresses in large pouring blocks in order to propose technical solutions for controlling thermal cracking. However, the process of assessing, calculating, and evaluating the distribution of temperature fields and thermal stress fields determining the formation of thermal cracks in mass concrete blocks has still not been completed. As a result, more researches are required because many materials and technological factors influencing the problem of thermal analysis in mass concrete structures need more consideration, such as component size, concrete mix composition (cement content and type, cement substitutes used), initial concrete mix temperature, ambient temperature, construction progress, curing conditions, etc. [6].

As a result of this research, the development of a nomogram to predict the maximum temperature helps in the prevention of thermal cracks in mass concrete structures with changing material and technological parameters. The above study results are very useful in the design and construction of mass concrete blocks. The study extends to building theory and practice by preventing the formation of thermal cracks in mass concrete structures at an early stage.

In addition, the creation of a nomogram based on the conditions of materials and construction techniques will effectively and quickly support the processes of design and construction in the preliminary determination of the maximum temperature in mass concrete structures.

2. Materials and Methods

2.1. Research subjects

Consider a 8 m (length) \times 6 m (width) \times 3 m (height) cubic concrete block with geometric dimensions of a 3D numerical analysis model placed on a 16 \times 12 \times 3 m foundation as presented in Fig. 1. The physical properties of concrete and the foundation are presented in Table 1.

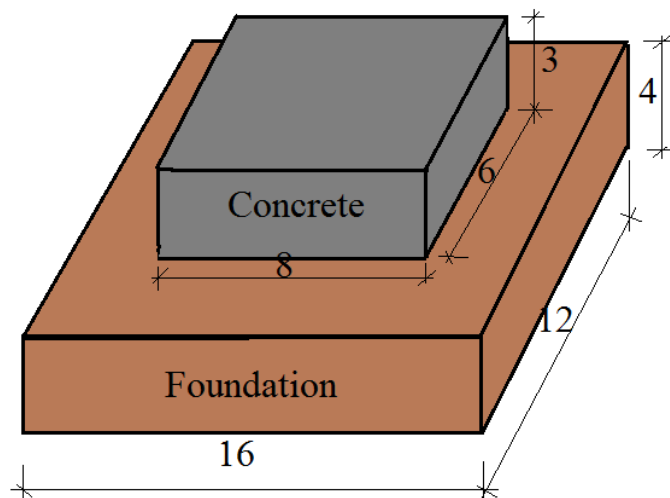


Figure 1. Dimensions of concrete block and foundation, unit: m.

In the process of forming the temperature field in the mass concrete structures, there are many factors influencing temperature distribution in the mass concrete structures, such as material composition, construction technique, and environmental temperature. Material factors should be mentioned, such as the cement content per 1 m³, the type of cement, and the initial temperature of the concrete mix. Factors in construction technique include division of placing block sizes, construction procedure between placed concrete blocks, the use of cooling pipe systems (if any), and surface insulation. These factors causing major impact on the temperature in mass concrete structures constitute the scope of this study, which takes into account many scenarios of materials and building techniques [7–9].

Mass concrete structures in Vietnam are typically constructed using concrete grades between M150 and M400. When using concrete compressive strength grade varying from M150 to M400 corresponding to the cement content used in the mixture varying from 120 kg/m³ to 450 kg/m³. Furthermore, the average ambient temperature in Vietnam normally ranges from 15°C to 30°C, so the initial temperature of the

concrete mixture fluctuates within that range. However, under certain conditions, the concrete mixture can be cooled down to 10°C to prevent thermal cracking [5]. Therefore, in the study, two material factors such as cement content and initial temperature of the concrete mixture are considered as follows:

$X_1(C)$ is cement content varies from 120 to 450, kg/m³;

$X_2(t_{pl})$ is initial temperature of concrete mix from 10 to 30, °C;

Construction technique factors are considered with two construction cases, as follows:

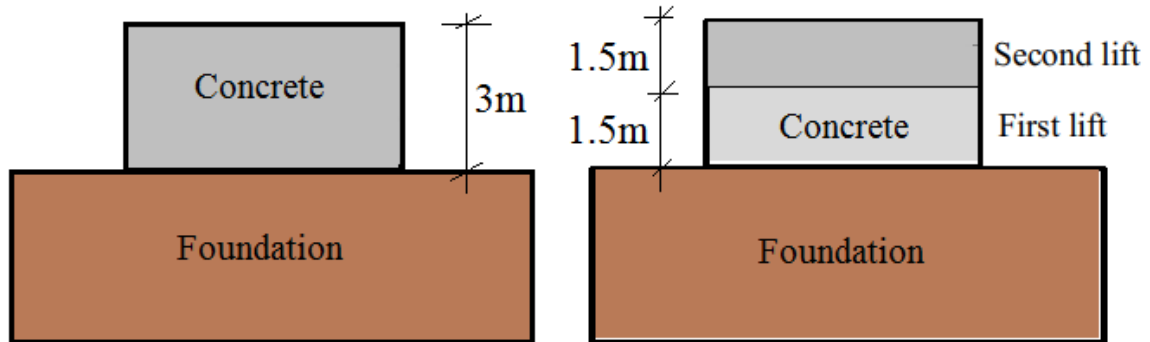


**Figure 2. Cases of pouring concrete:
Case 1: Concrete placing without block division;
Case 2: Concrete placing with two 1.5 m thick lifts
and construction schedule of 5 days for each lift.**

Table 1. Physical properties of materials used in the analysis.

Characteristics	Units	Concrete	Foundation
Specific heat	kcal/kg.°C	0.26	0.21
Density of the material	kg/m ³	2400	2600
The coefficient of thermal conductivity	kcal/m.h.°C	2.49	1.81
The coefficient of convective heat transfer: concrete – air	kcal/m ² .h.°C	12	12
The coefficient of convective heat transfer with wooden formwork	kcal/m ² .h.°C	8	–
Ambient temperature	°C	30	25
Modulus of elasticity	kG/cm ²	2.5×10^5	1.0×10^4
The coefficient of linear expansion	1/°C	13.0×10^{-6}	1.0×10^{-5}
Poisson's ratio		0.20	0.30

Convection is the process of transferring heat through the mass motion of a fluid, like air or water, where the heated fluid is moved away from the heat source while transferring heat along with it. Convection is influenced by the type of formwork, setting time, curing procedures, and wind speed. The convection coefficients between the concrete surface – air and the formwork – air, which are 12 kcal/m².h.°C and 8 kcal/m².h.°C, respectively, are considered in the study based on the local climate condition in Vietnam.

The value of elasticity modulus of the soil can be selected being based on the local conditions. In the study, the value of elasticity modulus of the soil ($E = 10000$ kg/cm²) is selected being based on the sandy soil foundation in a local region in the Northern part of Vietnam.

The ambient temperature is a factor varying versus time. The average annual temperature of the air and the foundation is different. According to the depth of soil layers, their temperature gradually decreases. In this study, the average temperature of the air is taken at 30 °C and the ground at 25 °C, suitable for Vietnam's summer climate [5].

The adiabatic temperature equals the temperature at the center of a mass concrete structure. Depending on the content of the concrete mixture and the initial temperature of the concrete mixture, the temperature rise process and the curve form may change. The adiabatic temperature rise curve is defined as mentioned in Equation (1) [10–12]:

$$T(t) = K(1 - e^{-\alpha t}), \quad (1)$$

where T is the amount of adiabatic temperature rise at time (°C); α is the coefficient of temperature rise (reaction rate); K is the final amount of adiabatic temperature rise acquired by test (°C); t is time (day);

K and α are experience values depending on the expected quantity of cement in 1 m³ concrete, type of cement, and casting temperature. These values can found in the Korean standard and are presented in Table 2 [11].

Table 2. Coefficients for estimating adiabatic temperature.

Type of cement	Placing temperature, (°C)	$T(t) = K(1 - e^{-\alpha t})$			
		$K(C) = aC + b$		$\alpha(C) = gC + h$	
		a	b	g	h
Fly ash cement	10	0.15	- 3.0	0.0007	0.141
	20	0.12	8.0	0.0028	- 0.143
	30	0.11	11.0	0.003	0.059

where C is cement content in 1 m³ of concrete; a , b , g and h are coefficients determined from experiment.

2.2. Methods

2.2.1. Creating a regression equation for the maximum temperature in mass concrete using an experimental planning technique

Assume that Equation (2) represents the approximate polynomial function reflecting the survey region [13]:

$$Y_i = b_0 + b_1X_1 + b_2X_2 + b_{12}X_1X_2 \quad (2)$$

Equation (3) calculates the number of experiments required (N) to discover the coefficients of the regression equation:

$$N = 2^k + 1, \quad (3)$$

where k is the number of basic parameters; 1 is experiments in the center; therefore, $N = 2^3 + 1 = 9$; b_{ij} is coefficients to be determined.

2.2.2. The Finite Element Method (FEM) is used to calculate the temperature field in mass concrete

When solving the problem of unstable heat transfer with an internal source, the finite element method is given by the reduced matrix equation as follows [14–16]:

$$[K]\{T\} + [C]\left\{\frac{\partial T}{\partial \tau}\right\} = [Q], \quad (4)$$

With the problem of unstable heat transfer, it is necessary to transient analyze with time steps $\Delta\tau$ as follows:

$$\left\{\frac{\partial T}{\partial \tau}\right\} = \frac{1}{\Delta\tau} [\{T(\tau_n) - T(\tau_{n-1})\}]. \quad (5)$$

Equation (4) can be rewritten as:

$$[K]\{T\} + \frac{[C]}{\Delta\tau} [\{T(\tau_n) - T(\tau_{n-1})\}] = [Q], \quad (6)$$

where $[K]$ is the matrix of thermal conductivity coefficient; $[C]$ is specific heat matrix; $[Q]$ is matrix of heat generated; $\Delta\tau = \Delta\tau_n - \Delta\tau_{n-1}$ is step of computation time.

The finite element method, which is one of the most powerful and reliable methods, is frequently used in studying temperature distribution of mass concrete. It divides elements, and their features are represented at nodes [17, 18].

Currently, there are many FEM based software solutions for structural problems in general and heat transfer problems in concrete in particular, such as Ansys, Abaqus, Midas Civil, etc. The above software is widely used in universities, research institutes, or companies around the world with high reliability [19–21].

2.2.3. Criteria for evaluating thermal cracking

Each country has adopted different criteria in controlling the formation of thermal cracks based on the characteristics of construction technique as well as local climatic conditions. Each standard represents characteristics that are specific to the climate and construction technique in each of these countries. The temperature difference ΔT between the concrete surface and the core of the mass concrete structure is frequently controlled by placing concrete, as a general rule. Regardless of the construction area or concrete type, the allowable temperature difference is typically around 20 °C [17].

The criterion for temperature difference, according to several Russian standard texts, is dependent on the concreting technique and the location of the structure in issue [18]. The difference temperature ΔT in the contact area (concrete and foundation) should not exceed (16–18) °C when pouring concrete with long blocks and (20–27) °C when using for construction according to column cutting, according to Standard SP 357.1325800.2017 [22]. A structural area having a height of 0.2 times the height of a mass concrete structure is known as the contact area. The temperature differential between the core and plate surfaces ΔT should not exceed (20–25) °C for concrete in the free zone (above the contact zone from the substrate surface) [13].

According to Vietnamese standard TCXDVN 9341:2012: “Mass concrete - Code of practice of construction and acceptance”, two factors are controlled to prevent the occurrence of cracks in mass concrete structures. The first, the temperature difference between its center and surface (ΔT), should be less than 20 °C. And the second, the temperature gradient (M_T), should not exceed 50 °C/m [10].

In Table 3, a criterion for the prevention of thermal crack formation in the construction of Chinese gravity dams and arch dams is described, with the allowable temperature difference between the center and surface of the concrete block depending on its size [23]. In particular, the size of the poured block affects the temperature difference in mass concrete. For example, if the length of the pouring block $L < 16$ m and the height of the pouring block is in the range (0–0.1) L , the temperature difference in mass concrete should not exceed (25–26) °C [23].

Table 3. Permissible temperature gradient T (°C) according to Chinese design standards.

Concrete block height	Length of concrete block L (m)				
	< 16 m	17–20 m	21–30 m	31–40 m	> 40 m
(0–0.1) L	26–25	24–22	22–19	19–16	16–14
(0.1–0.4) L	33–31	31–28	28–26	24–20	20–18

According to the evaluation of thermal crack formation according to CIRIA C600 (UK), the maximum temperature differential between the center and the surface of the concrete block (ΔT_{\max}) is defined by Equation (7) [24]:

$$\Delta T_{\max} = \frac{3.7\varepsilon}{\alpha}, \quad (7)$$

where ε is final tensile strength of early concrete; α is coefficient of thermal expansion of concrete.

Substituting the known approximations $\alpha = 13.10^{-6}$ and $\varepsilon = 70.10^{-6}$ into expression (7), the value of the maximum allowable difference $\Delta T_{\max} = 19.9$ °C \approx 20 °C is adopted. Hence, it is required that the temperature difference between the center and the surface of the concrete block should not exceed 20 °C during construction process.

Criteria for evaluating resistance to thermal cracking are presented in the Russian Standard SP 41.13330.2012 (proposed by GS P.I. Vasiliev) [25]:

$$\sigma(\tau) \leq \gamma_{b3} \gamma_{b6} \varepsilon_{lim} \varphi(\tau) E_b(\tau), \quad (8)$$

where $\sigma(\tau)$ is thermal stress at time τ ; $\gamma_{b6} = 1.15$ is working conditions for large block concrete structures; γ_{b3} is the coefficient of the mass concrete structure's working condition, taking into consideration the effect of the deformation gradient on the section on the concrete's tensile strength; ε_{lim} is ultimate tensile strength of concrete; $\varphi(\tau)$ is the coefficient depending on the age of concrete; $E(\tau)$ is elastic modulus of concrete at age τ .

The crack index is used to evaluate the formation of thermal cracks in concrete structures, and it is determined by Equation (9) [26]:

$$I_{cr} = \frac{f_t(\tau)}{f_{sp}(\tau)}, \quad (9)$$

where I_{cr} is crack index; $f_t(\tau)$ is tensile strength of concrete at age τ ; $f_{sp}(\tau)$ is maximum tensile stress induced during cement hydration at a time τ .

The cracking possibility was estimated by the value of the thermal cracking index based on the criteria values presented in Table 4 [26, 27]:

Table 4. Evaluation of cracking according to the Japanese cracking index.

Criteria	Cracking index (I _{cr})
To prevent cracks	$I_{cr} \geq 1.5$
To limit cracks	$1.2 \leq I_{cr} \leq 1.5$
To limit harmful cracks	$0.7 \leq I_{cr} \leq 1.2$

3. Results and Discussion

3.1. Developed mathematical model to predict the maximum temperature of a concrete block

In previous studies, Caltrans (State of California Department of Transportation) proposed a nomogram to predict temperature in the mass concrete considering the four most significant factors affecting temperature, such as cement content, element size, the initial temperature of the placing concrete, and the surrounding air temperature. However, the assumption of cement type used as that of type 2 may limit the actual application in other countries, such as Vietnam. Besides, construction technique showing the schedule of placing concrete blocks has not been mentioned [28].

For the present study, the maximum temperature in the concrete block is determined by using the finite element method; it is presented in Table 5 for two construction cases (one lift and two lifts) as an example of considering the construction conditions.

Table 5. Matrix of numerical experimental plans with consideration of technology and materials factors.

#	x_1	x_2	Value		Case 1	Case 2
			$x_1, \text{kg/m}^3$	$x_2, ^\circ\text{C}$	T_{max}	T_{max}
1	-1	-1	120	10	27.91	26.00
2	1	-1	450	10	66.51	58.33
3	-1	1	120	30	49.11	45.33
4	1	1	450	30	87.50	75.78
5*	0	0	285	20	57.99	50.96

The mathematical model to determine the maximum temperature in a mass concrete structure is shown by Equations (10) and (11):

Case 1: without division of concrete pouring

$$T_{\max} = 57.76 + 19.25x_1 + 10.55x_2 - 0.05x_1x_2. \quad (10)$$

Case 2: concrete blocks are poured in 2 lifts

$$T_{\max} = 51.36 + 15.70x_1 + 9.20x_2 - 0.47x_1x_2. \quad (11)$$

From the maximum temperature regression function obtained with two construction options, we can make the following comments:

1. The maximum temperature of the concrete building is influenced by both the cement concentration (x_1) and the initial temperature of the concrete mix (x_2).
2. When changing the cement content from 120 kg/m³ to 450 kg/m³, the maximum temperature in the concrete structure changes the value of 38.5 °C for the construction without division of concrete pouring, 31.4 °C for concrete blocks poured in 2 lifts.
3. When the initial temperature of the concrete mix is changed from 10 °C to 30 °C, the maximum temperature change for both construction techniques is roughly 20 °C. That is, if the initial temperature of the concrete mixture is increased by 1 °C, the maximum temperature of the concrete mixture increases by 1 °C. The above linear rule is perfectly consistent with earlier research.
4. When constructing two lifts, the rest time between lifts is enough for some heat to escape to the outside due to the hydration of cement. Based on Equations (10), (11), it can be seen that the maximum temperature in Case 2 is reduced by 11.3 °C compared to Case 1 having the same input parameters of the material.

From the results obtained in Table 5, the author considered Equations (10) and (11) as the most reasonable construction conditions to assess the risk of forming thermal cracks.

3.2. Establishing a nomogram to predict the maximum temperature in mass concrete construction

From the maximum temperature regression function obtained above, there are now many methods to establish mathematical nomograms to represent the correlation between the unknowns (x_1 and x_2) with the maximum temperature, such as Matlab, Maple, or the theory of establishing nomograms. The basis for building a plane nomogram is based on the Equation (12):

$$f_1 + f_2 = f_3. \quad (12)$$

The value f_1 is built into the grid of coordinates (x, y) with:

$$x = 0; \quad y = m(f_1 - a). \quad (13)$$

The value f_2 is built into the grid of coordinates (x, y) with:

$$x = H; \quad y = n(f_2 - b). \quad (14)$$

The f_3 value is built into the grid of coordinates (x, y) with:

$$x = \frac{mH}{m+n}; \quad y = \frac{mn}{m+n}(f_3 - a - b), \quad (15)$$

where m, n, H, a, b are arbitrary parameters.

We obtain a nomogram for each construction method (Case 1 or Case 2) by applying the theory of building a nomogram. We chose the values of m, n, H, a, b of the two building options so that the ratio on the nomogram of x_1 (cement content) and the initial temperature of the concrete mix (x_2) are identical proportions because the input material is the same. Fig. 3 shows a nomogram for determining the maximum temperature in a mass concrete structure for various construction materials and technologies.

Based on the obtained maximum temperature nomogram, we can quickly determine the maximum temperature in mass concrete structures with different concrete mixes and construction technologies. This helps to preliminarily select such input parameters as cement content, initial temperature of the concrete mix, or special construction methods. According to many current regulations, the maximum temperature in mass concrete members should not exceed 70 °C to ensure the best strength development and no enstrigite delay. Based on the above temperature nomogram, it is possible to reverse the cement content, initial

temperature, construction conditions with unfavorable case $T_{\max} = 70\text{ }^{\circ}\text{C}$. In case of a structure that requires a large amount of cement, the amount of heat generated can be greater than the adverse temperature of $70\text{ }^{\circ}\text{C}$, thus, it is necessary to take measures to reduce the maximum temperature, such as using a cooling pipe system.

How to use the nomogram. Connecting the cement content (kg/m^3) value in the X_1 axis to the initial temperature value of the concrete mix in the X_2 axis, crossing the maximum temperature axis at 1 point, the maximum temperature value is the value at the cutoff position. When building a concrete block without division of concrete pouring, check the maximum temperature in the mass concrete on the left of the nomogram; when building a concrete block with 2 lifts, check the maximum temperature in the mass concrete on the right of the nomogram.

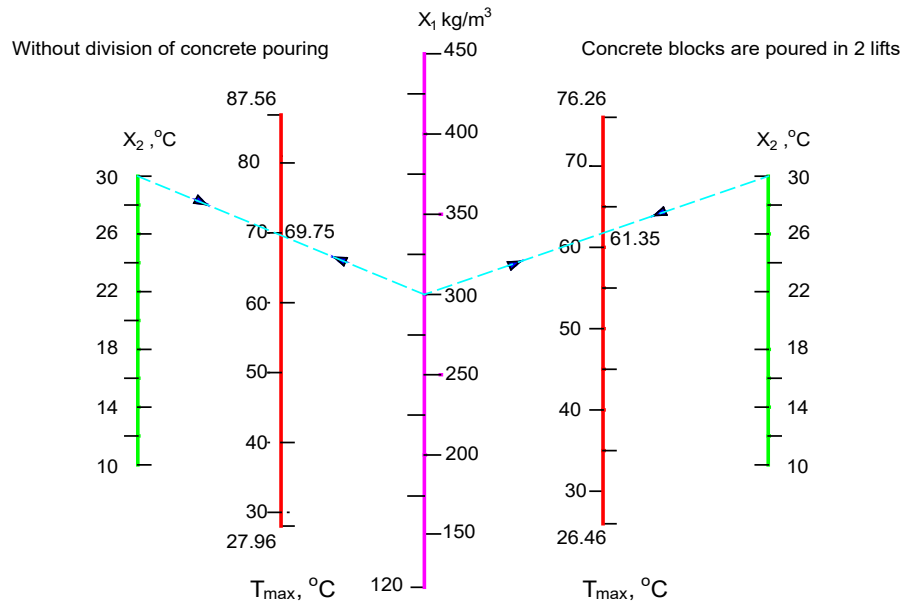


Figure 3. Nomogram for predicting the maximum temperature in concrete structures with different construction materials and technologies.

Example of using the nomogram. Assuming the cement content of $300\text{ kg}/\text{m}^3$, the initial temperature of the concrete mixture is $30\text{ }^{\circ}\text{C}$, we can completely determine the maximum temperature in the concrete structure without division of concrete pouring as $69.75\text{ }^{\circ}\text{C}$ (on the left of the nomogram) and $61.35\text{ }^{\circ}\text{C}$ (on the right of the nomogram).

3.3. Verifying the correctness of the obtained maximum temperature nomogram

To verify the obtained temperature nomogram, we use the finite element method to model the large concrete structure. The obtained results are compared with the temperature obtained from the temperature nomogram.

Consider a concrete block of sufficiently large dimensions (dimensions greater than 2 m). The cement content is $300\text{ kg}/\text{m}^3$, the initial temperature of the concrete mix is $25\text{ }^{\circ}\text{C}$. Concrete block is constructed without division of the poured block. Using the left branch temperature nomogram with $x_1 = 300\text{ kg}/\text{m}^3$, and $x_2 = 25\text{ }^{\circ}\text{C}$, we get the maximum temperature of $64\text{ }^{\circ}\text{C}$, as presented in Fig. 4.

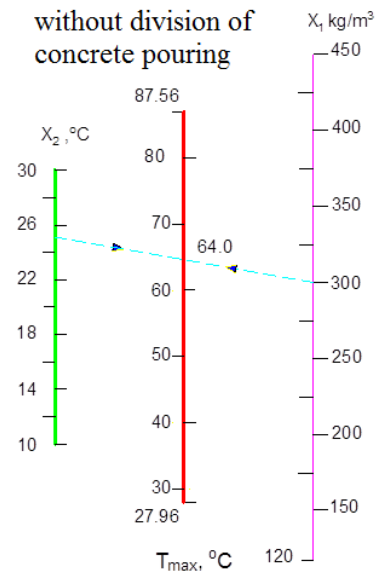


Figure 4. Verification of the maximum temperature in large concrete blocks with $x_1 = 300 \text{ kg/m}^3$, $x_2 = 25 \text{ °C}$ when building concrete blocks without division of concrete pouring (left branch of the nomogram).

The maximum temperature in the mass concrete structure from the finite element method is presented in Fig. 5.

Fig. 5 shows that the maximum temperature in the mass concrete structure reached 64.81 °C after 96 hours of pouring. The results from the finite element method model in the above case are consistent with the results obtained from the temperature nomogram and the error of $(64.81 - 64) / 64.81 = 1.25 \%$. This above error is quite small when compared with a maximum prediction error of $\pm 6.8 \text{ °C}$ for a 90 % confidence level between actual application and the established prediction nomogram proposed by Silva and Vít Smilauer [29]. Thus, the maximum temperature result obtained from the nomogram is reliable.

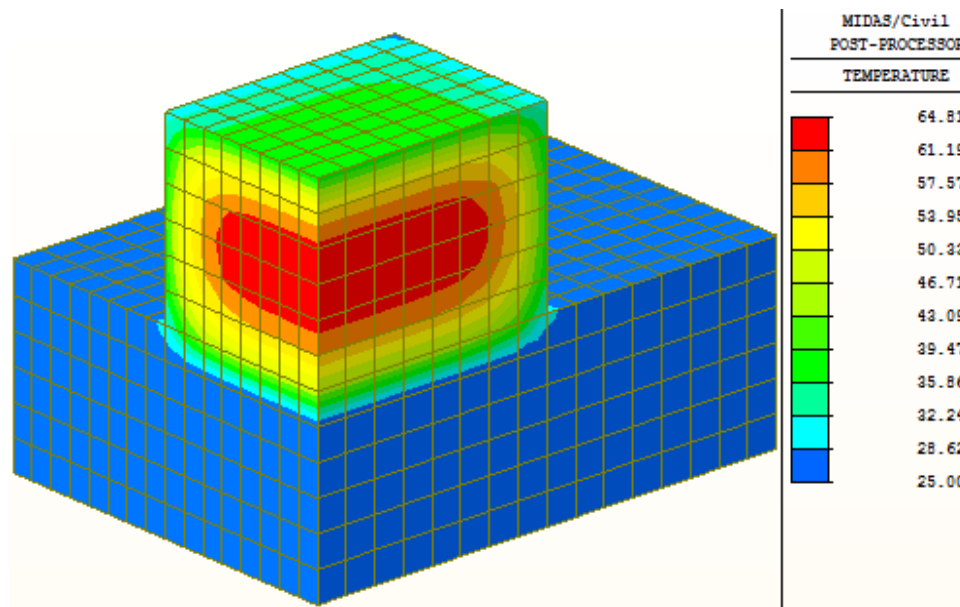


Figure 5. Maximum temperature in mass concrete members at the age of 96 hours after pouring (according to finite element method).

4. Conclusions

Based on the obtained results from the study, the following conclusions can be drawn:

1. The temperature in mass concrete structures is most affected by such factors as concrete mix and construction technique. The nomogram to predict the maximum temperature in the mass concrete structures, based on the mathematical functions of the maximum temperature acquired depending on the material and construction method, is established. The advantage of the maximum temperature nomogram

is that it allows engineers to quickly determine the maximum temperature with variations in cement content, the initial temperature of the concrete mix, and building conditions.

2. Instead of using the finite element method, the obtained math is of great practical value to quickly determine the maximum temperature in mass concrete. Following that, proper construction methods for preventing the formation of thermal cracks in mass concrete structures are proposed.

References

1. ACI 116R-90. Cement and Concrete Terminology. American Concrete Institute. 2000. 58 p.
2. ACI 301-10. Specifications for Structural Concrete. American Concrete Institute. 2010. 81 p.
3. Saeed, M.K., Rahman, M.K., Alfawzan, M., Basha, S., Dahish, H.A. Recycling of date kernel powder (DKP) in mass concrete for mitigating heat generation and risk of cracking at an early age. *Construction and Building Materials*. 2023. 376. Article no 131033. DOI: 10.1016/j.conbuildmat.2023.131033
4. Nguyen, C.T., Aniskin, N.A. Temperature regime during the construction massive concrete with pipe cooling. *Magazine of Civil Engineering*. 2019. 5(89). Pp. 156–166. DOI: 10.18720/MCE.89.13
5. TCXDVN 9341:2012. Mass concrete – code of practice of construction and acceptance. Hanoi. 2012. 85 p.
6. Mardmomen, S., Chen, H-L. Prediction of the early age thermal behavior of mass concrete containing SCMs using ANSYS. *Journal of Thermal Analysis and Calorimetry*. 2023. 148. Pp. 7899–7917. DOI: 10.1007/s10973-023-12243-9
7. Chen, Sh.-h., Su, P., Shahrour, I. Composite element algorithm for the thermal analysis of mass concrete: Simulation of cooling pipes. *International Journal of Numerical Methods for Heat & Fluid Flow*. 2011. 21(4). Pp. 434–447. DOI: 10.1108/09615531111123100
8. Xiaoda, Li, Zhipeng, Yu, Kexin, Ch., Chunlin, D., Fang, Yu. Investigation of temperature development and cracking control strategies of mass concrete: A field monitoring case study. *Case Studies in Construction Materials*. 2023. Article no 18.e02144. DOI: 10.1016/j.cscm.2023.e02144
9. Mansour, D.M., Ebid, A.M. Predicting thermal behavior of mass concrete elements using 3D finite difference model. *Asian Journal of Civil Engineering*. 2024. 25. Pp. 1601–1611. DOI: 10.1007/s42107-023-00864-2
10. Matos, P.R. de, Junckes, R., Graeff E., Prudêncio Jr., L.R. Effectiveness of fly ash in reducing the hydration heat release of mass concrete. *Journal of Building Engineering*. 2020. 28. Article no 101063. DOI: 10.1016/j.jobbe.2019.101063
11. Korean Concrete Institute. Thermal crack control of mass concrete, concrete practices Manual. Korean. 2010. 70 p.
12. Kuryłowicz-Cudowska, A. Experimental and Numerical Investigations of the Effect of Curing Conditions on the Temperature Rise of Concrete. *International Journal of Civil Engineering*. 2024. DOI: 10.1007/s40999-024-00966-1
13. Aniskin, N.A., Nguyen, T.C. Temperature regime of massive concrete dams in the zone of contact with the base. *Materials Science and Engineering*. 2018. 365(4). DOI: 10.1088/1757-899X/365/4/042083
14. Singh, M.P., Sen, S., Pathak H., Dogra, A.B. Early age cracking relevant to mass concrete dam structures during the construction schedule. *Construction and Building Materials*. 2024. 411. Article no 134739. DOI: 10.1016/j.conbuildmat.2023.134739
15. Zhao, Y., Li, G., Fan, C., Pang, W., Wang, Y. Effect of Thermal Parameters on Hydration Heat Temperature and Thermal Stress of Mass Concrete. *Advances in Materials Science and Engineering*. 2021. Article no 5541181. DOI: 10.1155/2021/5541181
16. Bushmanova, A.V., Kharchenko, D.K., Semenov, K.S., Barabanshchikov, Yu.G., Korovina, V.K., Dernakova, A.V. Thermal cracking resistance in massive steel-reinforced concrete structures. *Magazine of Civil Engineering*. 2018. 3. Pp. 45–53. DOI: 10.18720/MCE.79.5
17. Liu, W. C., Cao, W. L., Yan, H. Q., Ye, T., Wang, J. Experimental and Numerical Studies of Controlling Thermal Cracks in Mass Concrete Foundation by Circulating Water. *Applied Sciences*. 2016. 6(4). Article no 110. DOI: 10.3390/app6040110
18. Bushmanova, A.V., Videnkov, N.V., Semenov, K.V., Barabanshchikov, Yu.G., Dernakova, A.V., Korovina, V.K. The thermo-stressed state in massive concrete structures. *Magazine of Civil Engineering*. 2017. 71(3). Pp. 51–60. DOI: 10.18720/MCE.71.6
19. Rahimi A., Noorzaei J. Thermal and structural analysis of roller compacted concrete (R.C.C) dams by finite element code. *Australian Journal of Basic and Applied Sciences*. 2011. 5(12). Pp. 2761–2767.
20. Struchkova, A.Y., Barabanshchikov, Yu.G., Semenov, K.S., Shaibakova, A.A. Heat dissipation of cement and calculation of crack resistance of concrete massifs. *Magazine of Civil Engineering*. 2017. 78(2). Pp. 128–135. DOI: 10.18720/MCE.78.10
21. Ghasabeh, M., Göktepe S. Phase-field modeling of thermal cracking in hardening mass concrete. *Engineering Fracture Mechanics*. 2023. 289. Article no 109398. DOI: 10.1016/j.engfracmech.2023.109398
22. SP 357.1325800.2017. Concrete construction of hydraulic structures. Rules of works and acceptance of works. Ministry of construction and housing and communal services of the Russian Federation. 2016. 77 p.
23. Bofang, Z. Thermal stresses and temperature control of mass concrete. Elsevier Inc. 2014. 497 p.
24. Bamforth, P.B. Early-age thermal crack control in concrete. CIRIA C660. London. 2007. 113 p.
25. SP 41.13330.2012. Concrete and reinforced concrete hydraulic structures of the Russian Federation. 2012.
26. Japan Concrete Institute. Guidelines for Control of Cracking of Mass Concrete. Japan. 2016. 302 p.
27. Xin, J., Liu, Y., Zhang, G. et al. Comparison of thermal cracking potential evaluation criteria for mass concrete structures. *Mater Struct*. 2021. 54. Article no 243. DOI: 10.1617/s11527-021-01840-5
28. Caltrans. Bridge Design Memos. Mass Concrete Prediction Nomogram. California Department of Transportation. Sacramento. CA. 2021.
29. Da Silva, W.R.L., Šmilauer, V. Nomogram for Maximum Temperature of Mass Concrete. *Concrete International*. 2015. 37(5). Pp. 30–36.

Information about authors:

Trong Chuc Nguyen,

ORCID: <https://orcid.org/0000-0001-9723-5161>

E-mail: ntchuc.mta198@gmail.com

Anh Kiet Bui, PhD

ORCID: <https://orcid.org/0000-0002-8906-2886>

E-mail: kiet.ba@ou.edu.vn

Received 14.04.2022. Approved after reviewing 17.01.2023. Accepted 07.02.2023.



Research article

UDC 691.32

DOI: 10.34910/MCE.126.6



Corrosion-resistant concretes for coastal underground structures

S.V. Fedosov¹ , O.V. Aleksandrova¹ , B.I. Bulgakov¹ , N.A. Lukyanova¹  ,
Q. Nguyen Duc Vinh² 

¹ Moscow State University of Civil Engineering (National Research University), Moscow, Russian Federation

² Institute of Engineering and Technology – Hue University, Hue City, Vietnam

✉ galcevanadezda@mail.ru

Keywords: underground concrete structures, concrete corrosion, active mineral additives, mathematical modelling, concrete-soil-liquid, strength, corrosion resistance and durability of concrete structures, diffusion of Ca²⁺ ions

Abstract. Introduction. The underground structures of the coastal zone in Vietnam are periodically flooded with seawater, which causes corrosion of concrete. Therefore, the aim of the study is to increase the corrosion resistance of coastal underground concrete structures by modifying the structure of concrete with a complex of mineral additives obtained mainly from local raw materials, including micro- and nanosilicon, fly ash from thermal power plants and finely ground white quartz sand. In addition, it requires development of a mathematical model describing the processes of mass transfer in conditions of liquid corrosion of concrete underground structures in coastal zone, to assess their durability. Methods. The development of concrete mixtures, the study of their properties and properties of concrete, were carried out in accordance with the requirements of current Russian and Vietnamese standards. Results and Discussion. The results of experimental studies confirmed the possibility of using local raw materials to create modifying additives and obtain corrosion-resistant concretes with high performance. It was found that with an increase in the content of white quartz sand in the concrete mixture, the compressive strength of concrete increased rapidly at an early age of hardening up to 7 days, after which its growth rate gradually decreased. Replacing 60 % of river sand with white quartz sand provided the highest compressive strength, axial tension and flexural tension of concrete, which can be explained by the fact that white quartz sand is finer than river sand, and this increases the density of the concrete structure. In addition, an increase in the density of concrete can be explained by a decrease in water absorption and an increase in resistance to sulfate corrosion with an increase in the content of white quartz sand in the concrete mixture instead of river sand, as well as with the introduction of 1–1.5 % nanosilicon. Conclusions. For the construction of underground structures in the coastal zone of Vietnam, we developed corrosion-resistant concrete compositions based on local raw materials with high strength characteristics and low water absorption. A mathematical model is proposed to solve the problem of determining the mass transfer of Ca²⁺ ions in the system "concrete structure – moist soil – coastal area" to control the processes of mass transfer during the corrosive destruction of concrete underground structures in coastal zones periodically flooded with seawater, in order to predict their operational durability.

Citation: Fedosov, S.V., Aleksandrova, O.V., Bulgakov, B.I., Lukyanova, N.A., Nguyen Duc Vinh, Q. Corrosion-resistant concretes for coastal underground structures. Magazine of Civil Engineering. 2024. 17(2). Article no. 12606. DOI: 10.34910/MCE.126.6

1. Introduction

Exposure of the concrete structure to aggressive soil layers with dry-wet cycles [1], repeated temperature and humidity changes, etc., causes serious damage to the structure and leads to reduced durability and service life of underground structures [2–5]. Therefore, the object of the study was corrosion-resistant concrete for coastal underground structures.

1.1. Factors affecting the durability of concrete in underground construction

The durability of concrete in underground structures is influenced by environmental factors, design and construction factors.

The design factors mainly include design form of the concrete structure, the thickness of the protective layer, and the strength of the concrete [6], while the construction factors mainly include method and construction process [7]. Environmental difficulties of underground construction are also a significant factor affecting the durability of concrete and its susceptibility to erosion and groundwater penetration. Concrete, which is constantly influenced by groundwater pressure, passes free water through itself, which can lead to the formation of cracks and the destruction of concrete structures [8]. The result of this process can be the biological decomposition and erosion of concrete material, the enrichment of the soil with minerals and the development of microorganisms that can actively multiply on the surface of concrete and contribute to its destruction. In difficult operating conditions, when exposed to factors such as soil pressure and groundwater pressure, concrete undergoes significant compression or stretching, and an increase in stress significantly reduces its durability. In a complex stressed environment with such factors as soil pressure and seepage pressure, concrete will experience severe compression or tensile stress, an increase in stress will lead to a decrease in durability. The ions Cl^- or SO_4^{2-} in moist soil accelerate the erosion of concrete and form an electrochemical erosion environment [9]. During the construction of various underground structures, one of the primary missions is to guarantee the durability and reliability of concrete structures [10], as well as the resistance to subterranean and aggressive water, which, in turn, should be taken into an account when developing concrete compositions.

1.2. Coastal groundwater systems

Coastal regions are interface zones between land and ocean, which are affected by both marine and terrestrial processes [11]. The coastal area is quite an ill-defined concept, for which various definitions were proposed [12]. For example, it can be understood as a contiguous and hydro-logically connected land area along the coast and below 10 m above sea level [13].

Underground water in coastal aquifers is usually a mixture of fresh and seawater. Since the salinity of seawater is higher than compared to recharge of freshwater of groundwater sources, small amounts of seawater can prevail in chemical composition [14, 15]. Adding one percent of seawater to freshwater with 0.1 g/l of chloride increases the chloride concentration by nearly three times; supplementing five percent of seawater content increases the salinity of the source fresh water to more than 1 g/l [16]. Superimposed on mixing effects are the changes in the composition of groundwater in coastal aquifer systems due to chemical processes. Rising sea levels can impact coastal aquifer systems in several ways [17]. The boundary between seawater and fresh groundwater is pushed further inland, which leads to an increase in the seawater penetration. There is further migration of seawater upstream along river channels in coastal estuaries, which then affects the salinity of adjacent groundwater [18, 19].

The durability of concrete directly affects the service-life of underground concrete structures [20]. With the speeding up pace of urban construction and the scale of urbanization, the development of urban underground space in Vietnam became one of the important ways for the sustainable development of urban infrastructure [21]. However, underground concrete structures are exposed to the groundwater, which affects the characteristics of the concrete structure, such as impermeability and corrosion resistance [22]. Currently, at the early stages of underground construction in an underground humid environment, serious problems related to durability have arisen, which leads to subsequent repairs that will require a lot of labor and material resources. Understanding the mechanism of concrete quality degradation as a result of exposure to aggressive environmental factors [23] is important to design the composition of corrosion-resistant concrete for underground structures in coastal areas, which was the main purpose of this study [24].

To achieve this goal, it is necessary to solve the following two main tasks:

- to improve the physical and mechanical properties and corrosion resistance of concrete intended for the construction of underground structures in the coastal zone periodically flooded with

Table 4. Properties of mineral additives.

Properties / Mineral additives	Specific surface, m ² /kg	Density, kg/m ³	Particle size, μm
Finely ground quartz powder	~ 250	2670	5–95
Silica fume	15000 – 30000	2150	< 0.1
Fly ash (Class F)	~ 9600	2410	1–8
Nano – SiO ₂	139000	2330	(10–50)10 ⁻³

Chemical admixture: polycarboxylate superplasticizer (SP) Sika® ViscoCrete®-151 with density of 1.075–1.095 kg/l and pH value of 4.0±6.0 conforming to TCVN 8826 and GOST 24211 standards.

2.2. Research methods

2.2.1. Design of concrete mix compositions

The concrete mixes were developed using existing composition design methods, namely, TCVN 10306 and GOST 27006 standards. At the beginning of the experiment, the composition of concrete mixture for concrete with the average strength of 80 MPa was obtained without considering the addition of any mineral and chemical admixtures and was treated as a basic mix proportion. The control concrete mixture composition (admixture-free) is presented in Table 5.

Table 5. Concrete mixture proportions.

Materials	Quantity material	Absolute volume, m ³	Mix proportion
Water, kg/m ³	156	156/10 ³	0.284
Cement, kg/m ³	550	550/3.15=174.6/10 ³	1
Crushed rock aggregate, kg/m ³	1088	1088/2.68=405.97/10 ³	1.98
Natural river sand, kg/m ³	654	654/2.65 = 247/10 ³	1.19
Entrained air, %	2	20/10 ³	-
Superplasticizer Sika®ViscoCrete® -151, l/m ³	9.9	9.9/1.075=9.2/10 ³	0.018
Sum total		1000/10 ³	4.472

2.2.2. Ultrasonic pulse velocity method

The 100×100×100 mm cubic samples were tested using ultrasonic pulse velocity (UPV) on the 28th day of curing according to TCVN 9357 and GOST 17624-2021 standards.

Ultrasonic velocity was measured in a direct way, through cubic samples and between two parallel sides. The pulse velocity measuring device uses a transmitting transducer to send a compression wave into the concrete and a receiving transducer at a distance of L , which receives a pulse sent through the concrete from another point. The display of the device shows the time T required for the pulse to pass through the concrete. Ultrasound velocity (V), m/s, is calculated by the formula:

$$V = \frac{L}{T} \cdot 10^{-3},$$

where T is the actual time passage of the ultrasonic pulse through medium, s; L is the distance between the centers of the transducer installation zones (sounding base), mm.

The test method for pulse velocity passing through concrete was standard. The device used to determine the ultrasonic pulse velocity is the TICO concrete ultrasonic detector was developed by Proceq in Zurich, Switzerland. The device can calculate and evaluate the functions of concrete homogeneity, crack depth, modulus of elasticity, and concrete strength [25].

2.2.3. Workability of concrete mix

The workability of concrete mix was determined in conformity with TCVN 3106 and GOST 10181 standards. The workability of concrete mixes is checked and evaluated by filling capacity and resistance of segregation. TCVN 12209 and GOST R 57812 standards pose the main requirements for the flowability of concrete mixtures: 550 mm ≤ SF ≤ 750 mm; 3 s ≤ T500 ≤ 25 s; 0 ≤ PA ≤ 50 mm; 0 mm ≤ Δh ≤ 25 mm.

2.2.4. Determination resistance to leaching corrosion of concrete samples

The corrosion resistance of concrete in aggressive environments was assessed according to TCVN 9346:2012 and Russian State Standard GOST 31384-2017. Three control and three main samples for each aggressive environment from each concrete composition on cube samples of 150×150×150 mm or 100×100×100 mm in size were assessed at the age of 28 days of normal hardening.

2.3. Chemical composition of groundwater in coastal regions of South Vietnam

Over the past two decades, like any part of the world, Southeast Asia has witnessed climate change with increasing numbers of extreme heat waves, tropical storms with, heavier rains of increasingly terrible and unpredictable intensity. The major impacts of climate change leading to many environmental changes have had a severe impact on the lower Mekong basin: it is one of the most vulnerable regions to climate change, which faces land subsidence, saltwater intrusion, extreme drought, riverbank and coastal erosion and sea level rise. Across the Greater Mekong region, temperatures have risen by 0.5 to 1.5 °C in the past 50 years and continue to rise. By the end of the century, higher sea levels in the Mekong Delta may inundate about 1.4 million ha threatening the region's coastal communities.

Salinization of surface waters. Various sources contribute to the salinization of surface waters. The penetration of seawater into rivers, the migration wedge of saltwater to land due to differences in density, are the main sources of salinity in the mouths of rivers with open water. Thus, in these regions, the salinity of surface waters is closely related to salt deposition and its distribution in shallow groundwater [26]. The study area is located in the upper and lower reaches of the rivers along the Hậu River (Bassac River) and Mekong River of southern Vietnam given in the study by H. Sato et al. [27]. The characteristics of ionic compositions and analytical data of dissolved ions are given Fig. 1 showing a statistical analysis of the chemical characteristics of shallow groundwater samples.

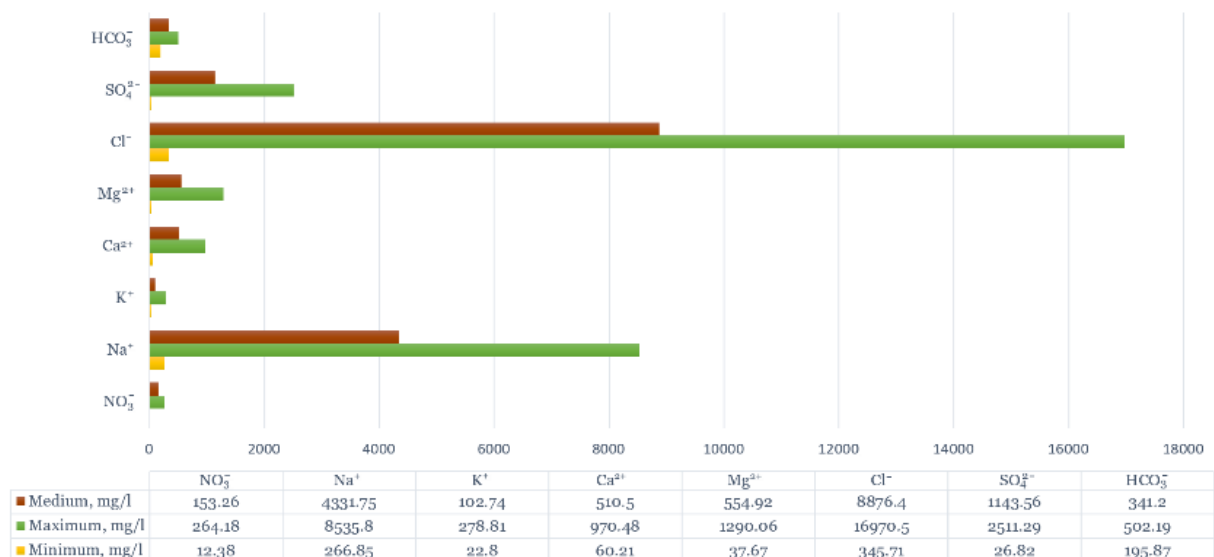


Figure 1. Chemical characteristics of shallow groundwater.

2.4. Mathematical model

In order to predict the corrosion resistance of concrete structures, it is necessary to develop a mathematical model describing the processes of diffusion-kinetic penetration of aggressive seawater salts of coastal zones into soil bases and enclosing structures. The evaluation of the effect of different service conditions on the durability of reinforced concrete structures in underground engineering of coastal regions is to be made by using mathematical modeling and numerical experiments based on them. Several mathematical models of predicting concrete corrosion process in different corrosion environments have been developed and applied in practice. For example, the mathematical models by S.V. Fedosov and a few others [28].

The effectiveness of computational methods using a new mathematical model for predicting the corrosion process of concrete and reinforcement in underground structures has been demonstrated through the results obtained for each specific work. The results obtained from both models theoretical and experimental give equivalent values. The obtained mathematical relation help to solve the inverse problem with using available experimental data, it is possible to predict the numerical value of free Ca(OH)₂ by thickness of the structure. Below is a mathematical model of mass transfer for the processes of liquid corrosion of cement concretes, taking into account the influence of the coastal region soil. The "concrete

structure – moist soil – seawater area" system can be represented by two plates of non-limiting contacts. Each plate is characterized by its dimensions (a concrete wall of thickness δ_1 , on the right side, was in contact with a moist soil layer of thickness δ_2 and the soil is in contact with saline water) and properties (Fig. 2).

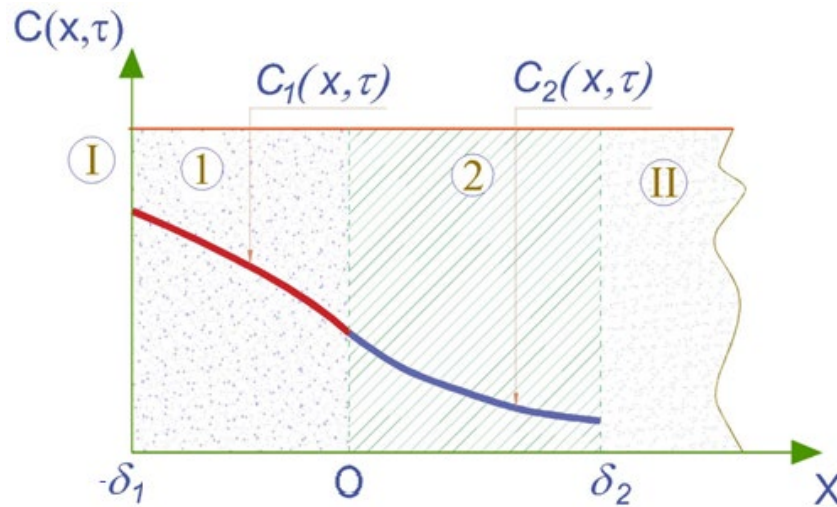


Figure 2. Mass transfer model: I is indoor environment, II is marine water area; 1 is concrete structure, 2 is moist soil; δ_1 is thickness of structure, δ_2 is the size of soil.

A mathematical model of mass transfer in an unlimited two-layer plate can be represented as a system of partial differential equations with combined boundary conditions of the second kind at the external boundaries of the system and of the fourth kind at the boundary of concrete with soil. The mathematical model of non-stationary mass transfer processes in the "reinforced concrete – soil – coastal water" system should be a solution of two boundary problems of mass conductivity with nonlinear boundary conditions in the concrete structure and coastal soil massif.

A feature of these problems will be the use of boundary conditions of the combined type: second kind on the inner surface of the reinforced concrete structure; second to third kind on the border of the soil with the water area, and fourth kind on the border of the structure and the soil.

There are mathematical expressions describing these boundary value problems in a dimensionless form below.

- Mass conduction differential equations:

$$\frac{\partial Z_1(\bar{x}, Fo_m)}{\partial Fo_m} = \frac{\partial^2 Z_1(\bar{x}, Fo_m)}{\partial \bar{x}^2}, \quad Fo_m > 0; \quad -1 \leq \bar{x} \leq 0; \quad (1)$$

$$\frac{\partial Z_2(\bar{x}, Fo_m)}{\partial Fo_m} = \frac{\partial^2 Z_2(\bar{x}, Fo_m)}{\partial \bar{x}^2} \cdot K_k, \quad Fo_m > 0; \quad 0 \leq \bar{x} \leq K_\delta. \quad (2)$$

- Initial conditions that determine the fields of mass transfer potentials at the time taken as the initial ($Fo_m = 0$),

$$Z_1(\bar{x}, Fo_m) \Big|_{Fo_m=0} = Z_{1,0}(\bar{x}); \quad (3)$$

$$Z_2(\bar{x}, Fo_m) \Big|_{Fo_m=0} = Z_{2,0}(\bar{x}). \quad (4)$$

The following designations are adopted here:

$$\bar{x} = \frac{x}{\delta_1}, \quad Fo_m = \frac{k_1 \tau}{\delta_1^2}; \quad (5)$$

$$Z_1(\bar{x}, Fo_m) = \frac{C_{1,0} - C_1(x, \tau)}{C_{1,0}}, \quad Z_2(\bar{x}, Fo_m) = \frac{C_{2,0} - C_2(x, \tau)}{C_{2,0}}; \quad (6)$$

$$K_{\delta} = \frac{\delta_2}{\delta_1}, K_k = \frac{k_2}{k_1}, \quad (7)$$

where $C_1(x, \tau)$ is concentration of "free" Ca(OH)_2 determined by CaO content in concrete at time (τ) evaluated at an arbitrary point of co-ordinate (x), $\text{kg CaO} \cdot \text{kg}^{-1}$ of concrete; $C_2(x, \tau)$ is concentration of "free" Ca(OH)_2 determined by CaO content in the soil layer at time (τ) at an arbitrary point of co-ordinate (x), $\text{kg CaO} \cdot \text{kg}^{-1}$ of solid; $k_{1,2}$ are mass conductivity coefficients, m^2/s ; δ_1 is thickness of concrete structure, m ; δ_2 is thickness of soil layer, m .

- Boundary conditions of the second on the inner surface of a reinforced concrete structure:

$$\frac{\partial Z_1(|-1|, Fo_m)}{\partial \bar{x}} = 0. \quad (8)$$

- Boundary conditions of the fourth kind at the point of contact of two solid bodies:

$$Z_1(\bar{x}, Fo_m)|_{\bar{x}=0} = Z_2(\bar{x}, Fo_m)|_{\bar{x}=0}; \quad (9)$$

$$\frac{\partial Z_1(\bar{x}, Fo_m)}{\partial \bar{x}} \Big|_{\bar{x}=0} = N \frac{\partial Z_2(\bar{x}, Fo_m)}{\partial \bar{x}} \Big|_{\bar{x}=0}, \quad (10)$$

where $N = \frac{\rho_2}{\rho_1} \cdot \frac{k_2}{k_1} \cdot \frac{1}{m}$ is a coefficient that takes into account the characteristics of phases.

- Boundary conditions of the second kind at the boundary of the soil massif and the coastal water area:

$$\frac{\partial Z_2(K_{\delta}, Fo_m)}{\partial \bar{x}} = Ki_H^*, \quad (11)$$

where $Ki_H^* = \frac{\rho_H \cdot \rho_1 \cdot m \cdot K_{\delta}}{\delta_2 \cdot \rho_2 \cdot k_2 \cdot C_0}$ is Kirpichev criterion for mass transfer.

The solution of these boundary value problems was obtained by the method of Laplace integral transformations [28].

The general solution of the mass conductivity problems describing the dynamics of concentration fields has the form [29]:

$$\begin{aligned} Z_1(\bar{x}, Fo_m) = & \\ = \frac{1}{1 + NK_k K_{\delta}} & \left\{ 1 - NK_{\delta} + Ki_H^* \left[Fo_m + \frac{(1 - \bar{x})^2}{2} + \varphi(K_k, N, K_{\delta}) \right] \right\} + 2 \sum_{m=1}^{\infty} \frac{1}{\mu_m^2 \Psi_1 / (\mu_m)} \cdot \\ & \cdot \left\{ \mu_m \sin \mu_m \left[\cos(\mu_m \bar{x}) \cos(\mu_m \sqrt{K_k} K_{\delta}) - \sqrt{K_k} K_{\delta} \sin(\mu_m \bar{x}) \sin(\mu_m \sqrt{K_k} K_{\delta}) \right] - \right. \\ & \left. - \frac{N}{\sqrt{K_k}} \cos(\mu_m (1 + \bar{x})) \right\} \exp(-\mu_m^2 Fo_m); \end{aligned} \quad (12)$$

$$\begin{aligned}
Z_2(\bar{x}, Fo_m) &= \frac{1}{1 + NK_k K_\delta} \cdot \\
&\cdot \left\{ 1 - NK_\delta + Ki_H^* [\bar{x} - Fo_m K_k K_\delta] + NK_i H^* \left(\varphi(K_k, N, K_\delta) - \frac{1 + K_k \bar{x}^2}{2} \right) \right\} - \\
&- 2 \sum_{m=1}^{\infty} \frac{\sin(\mu_m \sqrt{K_k} \cdot K_\delta)}{\mu_m^3 \sqrt{K_k} \Psi_1'(\mu_m)} \left\{ \mu_m \sin \mu_m \cos [\mu_m \sqrt{K_k} (K_\delta - \bar{x})] - \right. \\
&- \frac{\mu_m}{\sqrt{K_k}} \sin(\mu_m \sqrt{K_k} K_\delta) \left[N \cos \mu_m \cos(\mu_m \sqrt{K_k} \bar{x}) + \frac{1}{\sqrt{K_k}} \sin \mu_m \sin(\mu_m \sqrt{K_k} \bar{x}) \right] + \\
&+ Ki_H^* \left[N \cos \mu_m \cos(\mu_m \sqrt{K_k} \bar{x}) + \frac{1}{\sqrt{K_k}} \sin \mu_m \sin(\mu_m \sqrt{K_k} \bar{x}) \right] \left. \right\} \exp(-\mu_m^2 K_k Fo_m),
\end{aligned} \tag{13}$$

where μ_m is roots of the characteristic equation,

$$\operatorname{tg} \mu_m = N \sqrt{K_k} \operatorname{tg}(\mu_m \sqrt{K_k} K_\delta); \tag{14}$$

$$\varphi(K_k, N, K_\delta) = \frac{1 + K_k K_\delta (3K_\delta + 3N + NK_k K_\delta^2)}{6(1 + NK_k K_\delta)}; \tag{15}$$

$$J = \int_0^1 Z_{1,0}(\xi) \cos[\mu_m (1 - \xi)] d\xi. \tag{16}$$

The interpretation of the values of the obtained equations is given in [29]. Fig. 3 illustrates the dependence of dimensionless concentrations on the Kirpichev mass transfer criterion [30]. With increasing (ρ) of the Kirpichev mass transfer criterion, large gradients (α) of concentrations appear.

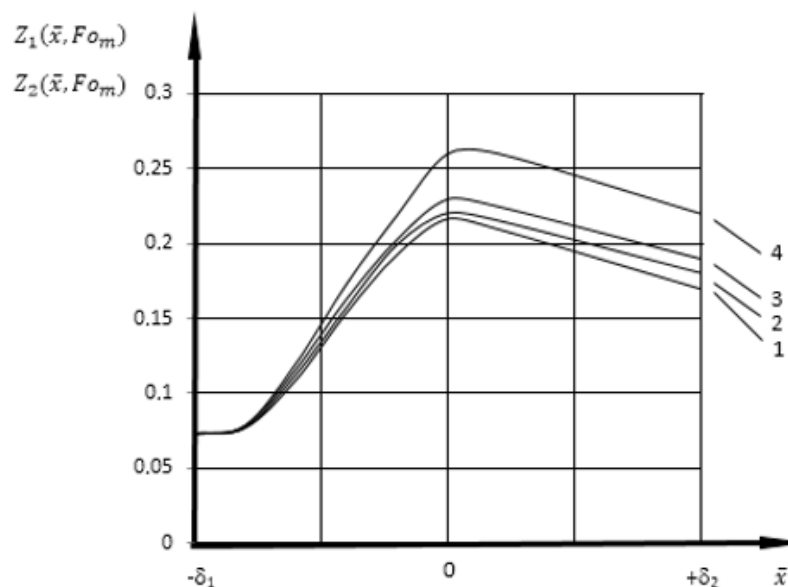


Figure 3. Diagram of dimensionless concentrations in the thickness of concrete and soil at $K_k = 1$; $K_\delta = 0.1$; $Fo_m = 1$ with different values of Ki_H^* : 1 – 0.5; 2 – 1; 3 – 1.5; 4 – 2.

The successful design of concrete composition with high anticorrosive properties is possible if the effect of aggressive environmental factors during the operation of concrete and reinforced concrete products and structures is taken into account.

3. Result and Discussion

3.1. Technological properties of concrete mixtures

Seven compositions of concrete mixes were prepared: a control mixture (100 % river quartz sand) and six mixtures containing white quartz sand in various proportions. Fine aggregate (river sand) was replaced by white quartz sand by weight. The proportion of the replaced fine aggregate varied from 40 % to 100 % in increments of 20 %. The influence of white quartz sand on the mechanical properties, corrosion resistance of concrete and reinforcing steel in concrete was investigated. The compositions of concrete mixtures are presented in Table 6.

Table 6. Compositions of concrete mixtures, kg/m³.

Mixture No.	Cementitious materials (B), kg/m ³					Concrete aggregate, kg/m ³				Water	SP	(W+SP)/B	
	Cement	SF	FA	Nano SiO ₂	Coarse aggregate	Fine aggregate							
						Rs	Qs	Qp					
kg	kg	kg	%	kg	kg	kg	%	Kg	kg	kg	l	–	
5aS0	357.5	27.5	165	–	–	1088	592.3	–	–	104.5	127.6	9.9	0.25
5aS1	352.0	27.5	165	1.0	5.5	1088	592.3	–	–	104.5	127.6	9.9	0.25
Q40	357.5	27.5	165	–	–	1088	355.4	40	236.9	104.5	127.6	9.9	0.25
Q60	357.5	27.5	165	–	–	1088	236.9	60	355.4	104.5	127.6	9.9	0.25
Q80	357.5	27.5	165	–	–	1088	118.5	80	473.8	104.5	127.6	9.9	0.25
Q100	357.5	27.5	165	–	–	1088	–	100	592.3	104.5	127.6	9.9	0.25
QS1.0	352.0	27.5	165	1.0	5.5	1088	–	100	592.3	104.5	127.6	9.9	0.25
QS1.5	349.3	27.5	165	1.5	8.25	1088	–	100	592.3	104.5	127.6	9.9	0.25

Mixture designations: No. 5aS0 is the control mixture in which natural river sands (with content 100 % by weight of fine aggregate) were used as a fine aggregate. Mixtures No. Q40, No. Q60, No. Q80, and No. Q100 contain white quartz sand in the amount of 40, 60, 80 and 100 % by weight of natural river sand, respectively; No. QS1.0 and No. QS1.5 – mixtures contain 100 % white quartz sand and nano-SiO₂ content of 1 and 1.5 %, respectively.

After curing, the cubes were used to determine the total compressive load taken by concrete at different ages including 3, 7, 14, 28, 365, and 450 days of age. Compression testing machine Matest model C089-17N with the capacity of 3000 kN was used for compressive tests of all specimens. Cylinders and beams were tested on a testing machine up to 600 kN, at the age of 28 days to determine the splitting tensile and flexural strength of concrete. The results of the tests for the spreading of the concrete mixture are shown in Table 7, the tests of concrete mixtures are shown in Fig. 4.

Table 7. Results of tests for the spreading of concrete mixtures.

Mixture No.	Spreading diameter, SF	Time, T ₅₀₀	J-Shaped ring		Separation
			ΔH	SF _J	
			mm	mm	
5aS0	560	8.0	22	500	No
Q40	620	7.5	17	580	No
Q60	690	6.0	15	700	No
Q80	730	5.0	14	695	No
Q100	760	3,7	13	730	No
QS1.0	740	4.5	14	705	No
QS1.5	700	5.0	16	660	No

According to the observations during the experiment and results obtained from tests in Table 7 following conclusions can be drawn: 1) segregation was not observed in any of the studied concrete

mixtures; 2) the spreading diameter (slump flow) of the No. Q100 mixture is 760 mm, relegate to Class SF2, high flowability according to TCVN 12209 standard; 3) the result of T500 time (a measure of viscosity) of the No. Q100 mixture is 3.7 s, in the range of 3 to 25 s, which meets the requirements; 4) the result of ΔH (inside and outside) is 13 mm of the No. Q100 mixture in the range is 0 to 25 mm, which meets the requirements; 5) the passing ability result of the No. Q100 mixture is $PA = SF - SF_J = 30$ mm, which corresponds to Class PA1 meeting the requirements.

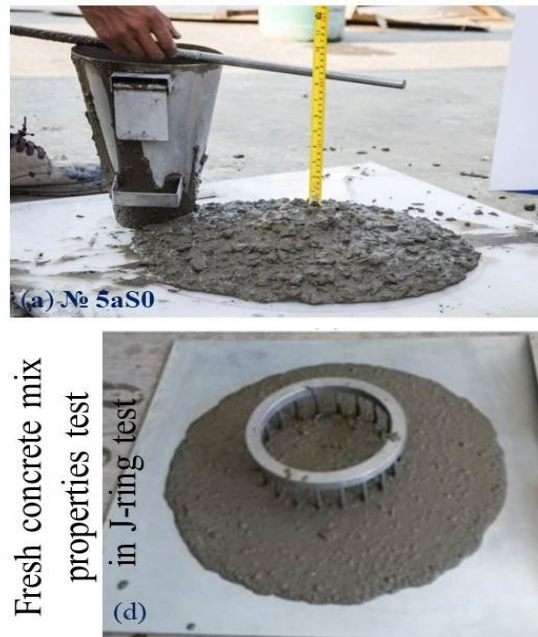


Figure 4. Tests for the workability of concrete mixtures: (a) Slump cone test or spreading (slump flow) test for concrete; (d) Limited spread measurement test.

3.2. Determination of mechanical characteristics of concrete

For concretes obtained as a result of hardening of the investigated concrete mixtures, compressive strength was determined at the age of 3, 7, 28, 356, and 450 days and the tensile strength in the axial direction, the bending strength at the age of 28 days according to GOST 10180 standard. The obtained test results are presented in Fig. 5 and 6.

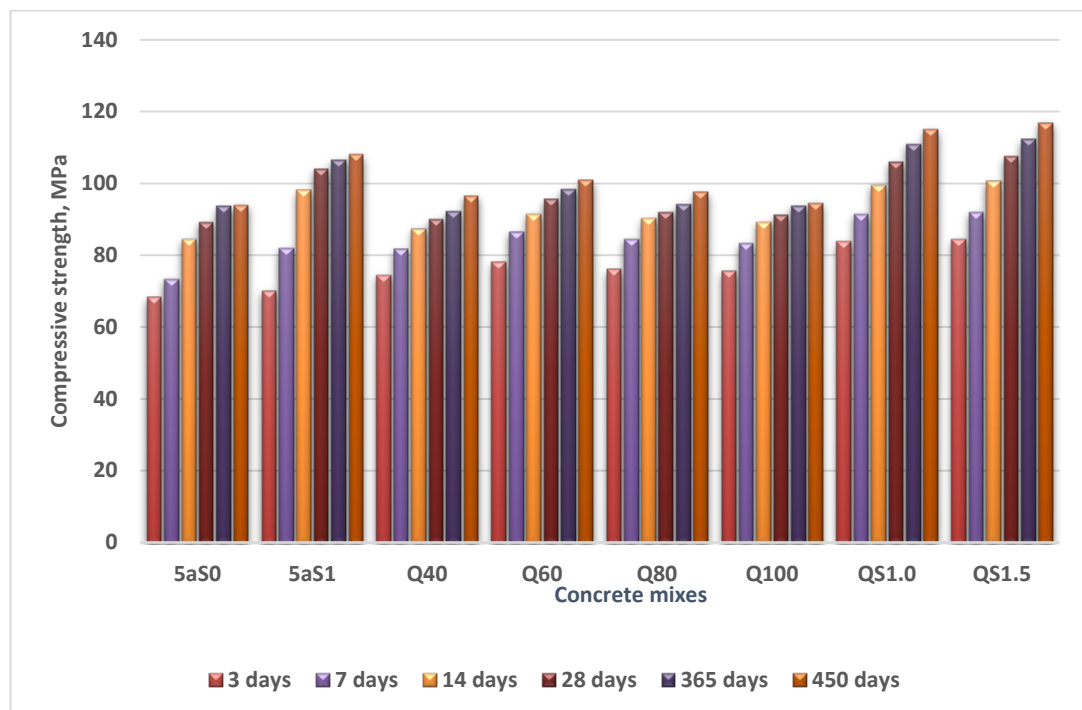


Figure 5. Change in the compressive strength of concrete at different curing ages.

The main purpose of the study was to utilize white quartz sand as an alternative for natural river sand in concrete production, and not to enhance the strength characteristics of concrete. However, the received experimental results showed that when white quartz sand was used as a fine aggregate instead of river sand in the concrete mixture, an increase in strength was observed at all substitution ratios. Fig. 5 shows that with an increase in the amount of white quartz sand in concrete, compressive strength develops rapidly at an early age, namely from 3 to 7 days and it's growth is gradually slowing down at a later age.

In addition, concrete samples containing white quartz sand showed higher compressive strength than the No. 5aS0 control sample during all hardening periods. In these results, at the age of 3 days, compressive strength of the concrete containing white sand in the amount of 40, 60, 80, and 100 % (by weight of river sand) reached the compressive strength values of 74.5, 78.2, 76.0, and 75.5 MPa, respectively. These values exceed the compressive strength of the control sample (No. 5aS0) with a value of 68.2 MPa. With an amount of white quartz sand equal to 60 %, concrete compressive strength has the highest values at different curing ages. The results show that 60 % replacement of river sand by white quartz sand provided optimal strength. No. Q60 mixtures showed higher compressive strength compared to mixtures No. 5aS0 (control mixture), No. Q40, No. Q80, and No. Q100 with the values of 7.2 %, 6.1 %, 3.8 %, and 4.7 %, respectively, and this difference in strength is comparatively high. The increase in compressive strength of concrete mixtures containing white quartz sand compared to the control mixture (river sand) is explained by the fact that white sand is finer than river sand, which leads to an improvement in the particle packing density of the concrete mix.

Compared to No. 5aS0 reference mixture, the No. Q100 mixture containing 100 % white quartz sand showed 9.7 %, 12.0 %, 5.2 %, 2.3 %, 0.2 %, and 0.5 % higher compressive strength at the age of 3, 7, 14, 28, 356 and 450 days, respectively. This can be explained by the fact that certain properties of river sand, such as porous structure and uneven intensity, differences in the physicochemical properties of fine aggregate particles in its composition, and high water absorption lead to water demand for concrete mixes, which causes a reduction in concrete strength. Another possible factor is the presence of impurities, such as clay content, organic impurities, small plant waste, silt, as well as unequal strength and structure of aggregate particles from river sand, which creates air voids in concrete. This reduces the specific density of the material, as result a significant decrease in concrete strength.

Split-tensile and flexural strength at the age of 28 days. In Fig. 6 were summarized the results obtained by tests of tensile and flexural strength for various concrete compositions at the age of 28 days. The change in split-tensile and flexural strength of concrete containing white quartz sand was similar to one in compressive strength. Compared to the No. 5aS0 reference sample, the No. Q60 mixtures showed higher split-tensile and flexural strength values of 7.26 MPa and 9.78 MPa, respectively. The average results of the three 100×200 mm cylinders that were used to test split tensile strength are shown in Fig. 6. The 28-day split tensile strength showed a decrease of 0.55 %, 0.97 %, and 1.66 % corresponding to mixtures No. Q40, No. Q80, and No. Q100, and an increase of 0.6 % for the mixture No. Q60 compared to reference mixture No. 5aS0 (tensile strength value is 7.22 MPa).

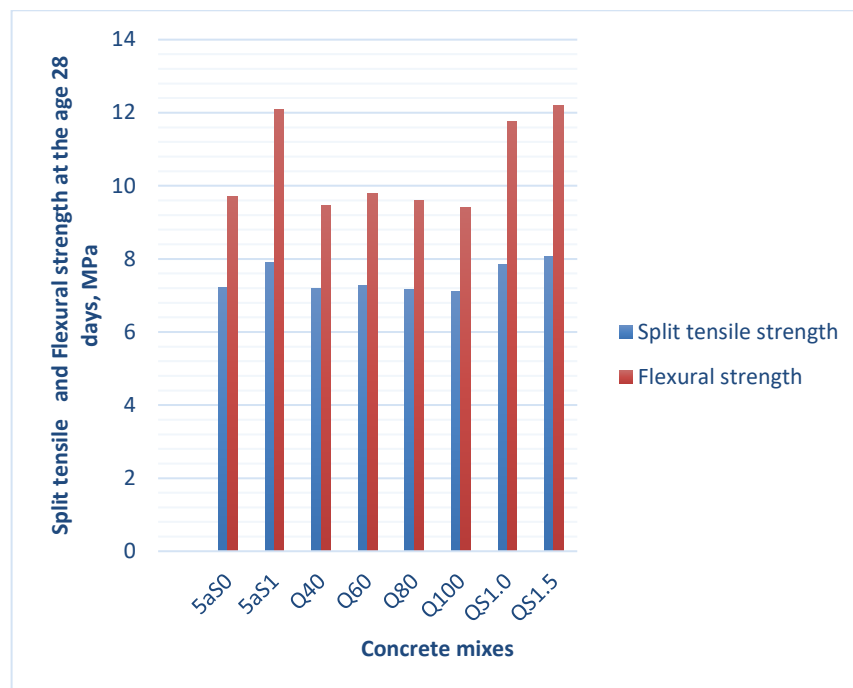


Figure 6. Split tensile strength and flexural strength of concrete at the age of 28 days.

The results of the flexural strength tests are presented in Fig. 6, the 28-day flexural strength showed a decrease of 2.68 %, 1.13 %, and 2.16 % for mixtures No. Q40, No. Q80, and No. Q100 and an increase of 0.72 % for mixtures No. Q60 compared to reference mixture No. 5aS0 (tensile strength value is 9.71 MPa). The optimal composition for replacing natural river sand with white quartz sand is of Q60 mixes composition, which showed the greatest strength at the age of 28 days.

Water absorption was determined according to TCVN 3113 and GOST 12730.3 standards. Tests were carried out on cube samples measuring 100x100x100 mm. The samples were tested after 28 days of curing. The average value of three samples was indicated as water absorption for each concrete mixture. The test results are presented in Fig. 7.

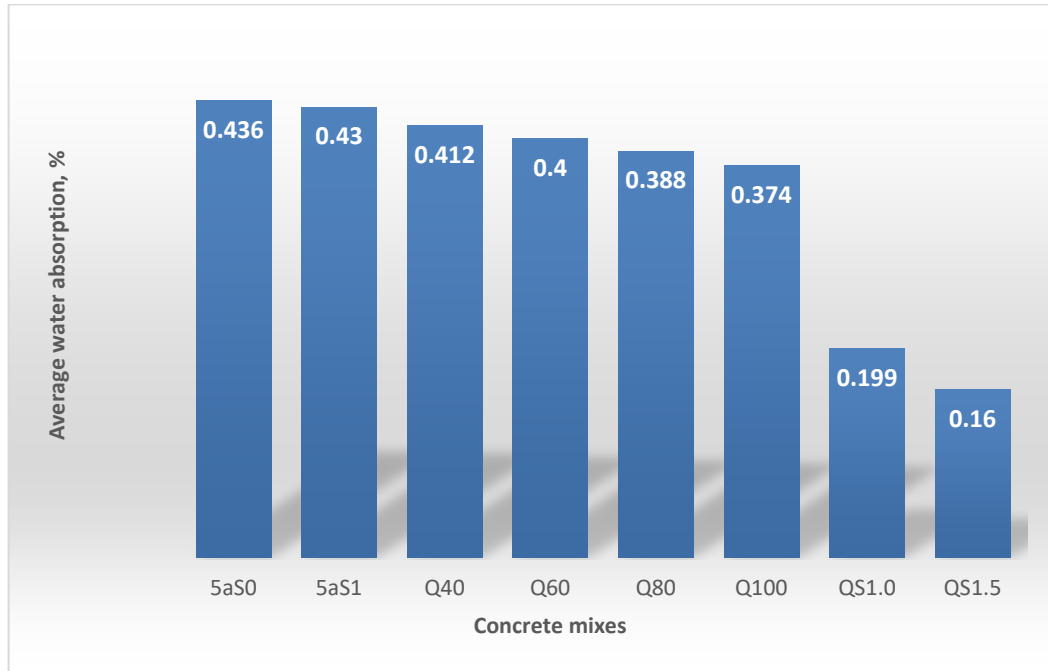


Figure 7. Effect of white quartz sand and Nano-SiO₂ on water absorption of concrete.

The water absorption rate of the concrete reduced as the white quartz sand content in concrete mixtures increased. The decrease in water absorption may be due to the fineness modulus of white quartz sand. The fineness modulus of white quartz sand ($M_k < 2.2$) is smaller than that of river sand ($M_k = 3.0$), which leads to a decrease in the total porosity of concrete, thereby increasing the density and strength. The result is a reduction in water absorption of the concrete.

3.3. Investigation of corrosion resistance of concrete exposed to sodium sulfate (Na₂SO₄) attack

To test the sulfate corrosion resistance, seven groups (three samples for each group) of concrete samples (100x100x100 mm cubes) with different white quartz sand contents were prepared. Cube samples were immersed in a 10 % Na₂SO₄ solution, the duration of immersion in sulfate solution was extended to 450 days. The sulfate resistance of concrete mixtures was evaluated by measuring the compressive strength and ultrasonic pulse velocity test of immersed cubes samples at the age of 450 days. The results of testing concrete samples of developed compositions placed in 10 % Na₂SO₄ solution for a period of 450 days for tests on weight loss and compressive strength are presented in Fig. 8.

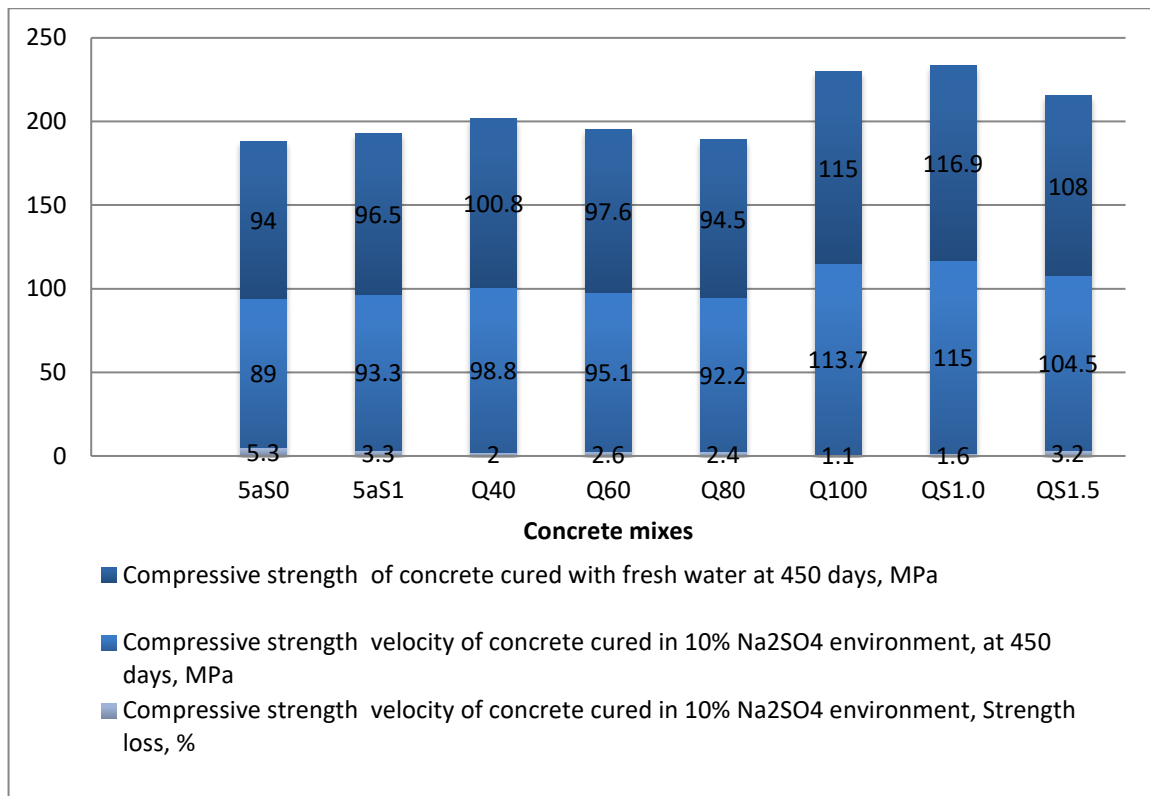


Figure 8. Compressive strength of hardened concrete in various environments.

The test results showed that the presence of white quartz sand augments the sulfate resistance of concrete, and this effect raises with an increase in the amount of white quartz sand instead of river sand. At the age of 450 days, strength tests sample No. 5aS0 showed a reduction in compressive strength by 5.3% due to sulfate corrosion. Mixtures containing white quartz sand showed a low reduction in compressive strength compared to the reference samples, namely, No. Q40, No. Q60, No. Q80, and No. Q100 showed a decrease in compressive strength by 3.3 %, 2.0 %, 2.6 %, and 2.4 %, respectively. In fact, the control sample No. 5aS0 (containing river sand) showed strength reduction of up to 5.3 %, higher than compared to the remaining samples.

It can be noted that the presence of Nano-SiO₂ increases the sulfate resistance of concrete mixture containing 100 % white quartz sand from 1.0 % (No. QS1.0) to 0.9 % (No. QS1.5) compared to the reference sample No. Q100; while compressive strength in the presence of nano-SiO₂ with 1 % content in the concrete mixture containing 100 % river sand (No. 5aS1 mixtures) went by 3.2 % at the age of 450 days.

From the above it follows that adding nano-silica (SiO₂) into concrete mixture intensifies the durability of concretes exposed to external sulfates attack (sulfate corrosion). Sulfate corrosion causes significant expansion and weight loss at the later stage of development, which exposes concrete structures to great danger, especially monolithic concrete structures. Sulfate diffusion in concrete without nano-SiO₂ content occurs at a faster rate, compared to concrete containing nano-SiO₂ in an amount of 1 % by weight of cement, due to the faster development of cracks in concrete.

The results of the conducted experimental studies on the possibility of using local raw materials to create modifying additives, through the use of which it is possible to obtain concretes with high performance and corrosion resistance in contact with an aqueous medium, are consistent with the results of other researchers [31–38].

4. Conclusions

1. We developed compositions of corrosion-resistant concrete with high strength characteristics and low water absorption for underground structures in coastal zone.
2. The developed physical and mathematical model displays the mass transfer of Ca²⁺ ions in the “concrete structure – moist soil – seawater area” system, which makes it possible to control mass transfer processes in order to counteract the corrosion of concrete in coastal underground structures periodically flooded with seawater, and thereby predict their operational durability.

References

- Gong, J., Jian Cao, Y. Effects of sulfate attack and dry-wet circulation on creep of fly-ash slag concrete. *Construction and Building Materials*. 2016. 125. Pp. 12–20. DOI: 10.1016/j.conbuildmat.2016.08.023
- Li, C., Qing, C., Wang, R., Wu, M., Jiang, Z. Corrosion assessment of reinforced concrete structures exposed to chloride environments in underground tunnels: Theoretical insights and practical data interpretations. *Cement and Concrete Composites*. 2020. 103652. DOI: 10.1016/j.cemconcomp.2020.103652
- Alexander, M., Beushausen, H. Durability, service life prediction, and modelling for reinforced concrete structures – Review and critique. *Cement and Concrete Research*. 2019. 122. Pp. 17–29. DOI: 10.1016/j.cemconres.2019.04.018
- Wenjun, Z., Raoul, F. Corrosion of the reinforcement and its influence on the residual structural performance of a 26-year-old corroded RC beam. *Construction and Building Materials*. 2014. 51(31). Pp. 461–472. DOI: 10.1016/j.conbuildmat.2013.11.015
- Wenjun, Z., Raoul, F., Coronelli, D., Cleland, D. Effect of corrosion of reinforcement on the mechanical behaviour of highly corroded RC beams. *Engineering Structures*. 2013. 56. Pp. 544–554. DOI: 10.1016/j.engstruct.2013.04.017
- Bonić, Z., Čurčić, G.T., Trivunić, M., Davidović, N., Vatin, N. Some methods of protection of concrete and reinforcement of reinforced-concrete foundations exposed to environmental impacts. *Procedia Engineering*. 2015. 117. Pp. 419–430. DOI: 10.1016/j.proeng.2015.08.189
- Zhao, Y., Jin, W. Damage analysis and cracking model of reinforced concrete structures with rebar corrosion. *Steel Corrosion-Induced Concrete Cracking*. 2016. Pp. 55–77. DOI: 10.1016/b978-0-12-809197-5.00004-9
- Aleksandrova, O.V., Quang, N.D., Bulgakov, V.I., Lukyanova, S.V., Petropavlovskaya, V.B. The Effect of Mineral Admixtures and Fine Aggregates on the Characteristics of High-Strength Fiber-Reinforced Concrete. *Materials*. 2022. 15. 8851. DOI: 10.3390/ma15248851
- Lu, B.T., Luo, J.L. Synergism of electrochemical and mechanical factors in erosion-corrosion. *The Journal of Physical Chemistry B*. 2006. 110 (9). Pp. 4217–4231. DOI: 10.1021/jp051985f
- Zhang, H. Durability reliability analysis for corroding concrete structures under uncertainty. *Mechanical Systems and Signal Processing*. 2018. 101. Pp. 26–37. DOI: 10.1016/j.ymssp.2017.08.027
- Rahman, M.A., Zhao, Q., Wiederhold, H. Coastal groundwater systems: mapping chloride distribution from borehole and geophysical data. *Grundwasser-Zeitschrift der Fachsektion Hydrogeologie*. 2021. 26. Pp. 191–206. DOI: 10.1007/s00767-021-00475-1
- Crossland, C.J., Kremer, H.H., Lindeboom, H., Crossland, J.I.M., Le Tissier, M.D. Coastal fluxes in the anthropocene: The land-ocean interactions in the coastal zone project of the international geosphere-biosphere programme. Springer Science and Business Media, Berlin, 2005. 253 p.
- McGranahan, G., Balk, D., Anderson, B. The rising tide: assessing the risks of climate change and human settlements in low elevation coastal zones. *Environment and Urbanization*. 2007. 19 (1). Pp. 17–37. DOI: 10.1177/0956247807076960
- Taniguchi, M., Dulai, H., Burnett et al, K.M. Submarine groundwater discharge: Updates on its measurement techniques, geophysical drivers, magnitudes, and effects. *Frontiers in Environmental Science*. 2019. 75 p. DOI: 10.3389/fenvs.2019.00141
- Purwoarminta, A., Moosdorf, N., Delinon, R. M. Investigation of groundwater-seawater interactions: A review. *IOP Conference Series: Earth and Environmental Science*. 2018. 118. 012017. DOI: 10.1088/1755-1315/118/1/012017
- Bear, J., Cheng, A.H.-D., Sorek, S., Ouazar, D., Herrebra, I., eds. *Geochemical investigation. Seawater intrusion in coastal aquifers – concepts, methods and practices*. Kluwer Academic Publishers. Springer Science & Business Media. 1999. 627 p.
- Barlow, P.M. *Ground water in freshwater-saltwater environments of the atlantic coast*. US Department of the Interior, USGS, Reston, VA, 2003. 113 p. DOI: 10.3133/cir1262
- Xiao, H., Tang, Y., Li, H., Zhang, L., Ngo-Duc, T., Chen, D., Tang, Q. Saltwater intrusion into groundwater systems in the Mekong Delta and links to global change. *Advances in Climate Change Research*. 2021. 12(3). Pp. 342–352. DOI: 10.1016/j.accre.2021.04.005
- Tran, D.A., Tsujimura, M., Vo, L.P., Nguyen, V.T., Kambuku, D., Dang, T.D. Hydrogeochemical characteristics of a multi-layered coastal aquifer system in the Mekong Delta, Vietnam. *Environmental Geochemistry and Health*. 2019. 42(2). Pp. 661–680. DOI: 10.1007/s10653-019-00400-9
- In, K.J., Jiang, Y.R., Jung, S.H., Lee, M.K., Yoo, S.W., Oh, B.H. Durability of concrete under combined exposure conditions of chlorides and sulfates. *Key Engineering Materials*. 2016. 711. Pp. 319–326. DOI: 10.4028/www.scientific.net/KEM.711.319
- Hai, D.L. Urban underground space planning. *Vietnam Architecture Magazine. Construction Newspaper*. 2021.
- Aggarwal, P. *Self-Compacting Concrete: Materials, Properties and Applications Carbonation and corrosion of SCC*. Woodhead Publishing Series in Civil and Structural Engineering. 2020. Pp. 147–193. DOI: 10.1016/B978-0-12-817369-5.00007-6
- Alonso, M.C., Villar, K., Qvaeschning, D., Irico, S., Pérez, G. Investigation on the Combined Interaction of Sulphate and Acidic Attack on Concretes Exposed to Aggressive Environments. In: Menéndez, E., Baroghel-Bouny, V. (eds) *External Sulphate Attack – Field Aspects and Lab Tests*. RILEM Bookseries. 2020. 21. Springer, Cham. DOI: 10.1007/978-3-030-20331-3_3
- Yang, W., Baji, H., Li, C.Q. Time-dependent reliability method for service life prediction of reinforced concrete shield metro tunnels. *Structure and Infrastructure Engineering*. 2017. 08. Pp. 1095–1107. DOI: 10.1080/15732479.2017.1401094
- Ngo, L.T.Q., Wang, Y.R., Chen, Y.M. Applying Adaptive Neural Fuzzy Inference System to Improve Concrete Strength Estimation in Ultrasonic Pulse Velocity Tests. *Advances in Civil Engineering*. 2018. 2451915. DOI: 10.1155/2018/2451915
- Nguyen, L.D., Nguyen, T.V.K., Nguyen, D.V., Tran, A.T., Nguyen, H.T., Heidbüchel, I., Merz, B., Apel, H. Groundwater dynamics in the Vietnamese Mekong Delta: Trends, memory effects, and response times. *Journal of Hydrology: Regional*. 2021. 33. 100746. DOI: 10.1016/j.ejrh.2020.100746
- Sato, H., Shibasaki, N., Lap, N.V., Oanh, T.T.K., Lan, N.T.M. Characteristics on distribution of chemical composition in groundwater along the Mekong and Bassac (Hậu) river, Vietnam. *Vietnam Journal of Earth Sciences*. 2019. 41 (3). Pp. 272–288. DOI: 10.15625/0866-7187/41/3/13969
- Fedosov, S.V., Rumyancheva, V.E., Kas'yanenko, N.S. Mathematical modeling of mass transfer in the processes of concrete corrosion of the second type. *Stroitel'nye materialy*. 2008. 7. Pp. 35–39.
- Fedosov, S.V., Aleksandrova, O.V., Fedoseev, V.N., Loginova, S.A., Nguyen, D.V.Q. Physico-mechanical foundations of theoretical and engineering investigation on the development to corrosion-resistant materials in buried structures of coastal zones.

- «XXX Russian-Polish-Slovak Seminar Theoretical Foundation of Civil Engineering». Solid State. 2022. 329. Pp. 209–261. DOI: 10.4028/p-tkq4eg
30. Sorochinsky, V.F. The influence of convective drying on the change of Kirpichev mass-exchange criterion. Journal of Physics: Conference Series. 2019. 1399. 022012. DOI: 10.1088/1742-6596/1399/2/022012
 31. Sinsiri, T.T., Jaturapitakkul, P.C., Kiattikomol, K. Effect of finenesses of fly ash on expansion of mortars in magnesium sulfate. Science Asia. 2006. 32. Pp. 63–69.
 32. Aghabaglou, A.M., Inan, G., Sezer, K. Ramyar Comparison of fly ash, silica fume and metakaolin from mechanical properties and durability performance of mortar mixtures view point. Construction and Building Materials. 2014. 70. Pp. 17–25.
 33. Mohamed, A.M., Influence of nano materials on flexural behavior and compressive strength of concrete. HBRC Journal. 2016. 12(2). Pp. 212–225. DOI: 10.1016/j.hbrj.2014.11.006
 34. Said, A.M., Zeidan, M.S., Bassuoni, M., Tian, Y. Properties of concrete incorporating nano-silica. Construction and Building Materials. 2012. 36. Pp. 838–844.
 35. Hou, P., Qian, J., Cheng, X., Shah, S.P. Effects of the pozzolanic reactivity of nano-SiO₂ on cement-based materials. Cement and Concrete Composites. 2015. 55. Pp. 250–258.
 36. Sahoo, S., Das, B.B., Rath, A.K., Kar, B.B. Acid, alkali and chloride resistance of high-volume fly ash concrete. Indian Journal of Science and Technology. 2015. 8(19). 72266. DOI: 10.17485/ijst/2015/v8i19/72266
 37. Sounthararajan, V.M., Srinivasan, K., Sivakumar, A. Micro filler effects of silica-fume on the setting and hardened properties of concrete. Research Journal of Applied Sciences, Engineering and Technology. 2013. 6(14). Pp. 2649–2654.
 38. Mostafa, J., Alireza, P., Omid, F.H., Davoud, J. Comparative study on effects of Class F fly ash, nano silica and silica fume on properties of high performance self-compacting concrete. Construction and Building Materials. 2015. 94. Pp. 90–104.

Contacts:

Sergey Fedosov, Doctor of Technical Sciences

ORCID: <https://orcid.org/0000-0001-6117-7529>

E-mail: fedosovsv@mgsu.ru

Olga Aleksandrova, PhD Technical Sciences

ORCID: <https://orcid.org/0000-0003-1791-8515>

E-mail: aleks_olvl@mail.ru

Boris Bulgakov, PhD Technical Sciences

ORCID: <https://orcid.org/0000-0002-4737-8524>

E-mail: fakultetst@mail.ru

Nadezhda Lukyanova, PhD Technical Sciences

ORCID: <https://orcid.org/0000-0001-7950-3003>

E-mail: galcevanadezda@mail.ru

Quang Nguyen Duc Vinh, PhD Technical Sciences

ORCID: <https://orcid.org/0000-0001-5840-5279>

E-mail: ndvquang@hueuni.edu.vn

Received 24.10.2022. Approved after reviewing 20.02.2024. Accepted 13.03.2024.



Research article

UDC 69.04

DOI: 10.34910/MCE.126.7



Dynamic characteristics of a reinforced concrete frame under vibration load conditions

P. Cao¹ ✉, G.L. Kozinets², V.L. Badenko² , A. Markov¹, D.K. Zotov², P.V. Kozinets²

¹ Jilin University, Changchun city, Jilin Province, China

² Peter the Great St. Petersburg Polytechnic University, St. Petersburg, Russian Federation

✉ jlucpl@jlu.edu.cn

Keywords: reinforced concrete frame, load-bearing columns, soil foundation, natural frequencies, vibration modes, finite element method, structural strengthening, vibration, accelerogram, equipment

Abstract. The object of the research is the reinforced concrete frame of an industrial building. A review of publications on methods of dynamic calculation of reinforced concrete structures is presented. Computational studies were carried out using the finite element method. The initial data for the calculation are the physical characteristics of the material of concrete, steel and base, the geometric parameters of the reinforced concrete frame obtained as a result of laser scanning. The resulting point cloud was combined with a mathematical model built based on design documentation. Based on a cloud of terrestrial laser scanning points, the computational model was refined. A comparison was made between the actual and design dimensions of columns and nodes. Discrepancies in the geometric dimensions of columns, nodes and connections were determined. The strength and stability of the reinforced concrete frame were not included in the methodology, but were used to determine the geometric dimensions of the structure, which are the initial data for the research. To determine the natural frequencies and vibration modes of the reinforced concrete frame, dynamic calculations of the equipment-frame-based system were performed. The equipment is presented in the form of distributed point masses on the marks of the frame consoles. An analysis of vibrations of the frame, based on which the structure was strengthened, is presented. The dynamic load from equipment operation is specified based on the measurements of vibration values in the longitudinal direction of the frame. The resonance zone during equipment operation was determined. Based on the results of the dynamic calculation, the frame structure was strengthened to prevent resonance phenomena. Test calculations and measurements showed the efficiency of the proposed method. The first translational (in the longitudinal direction) natural frequency increased from 3.609 Hz to 6.4258 Hz.

Citation: Cao, P., Kozinets, G.L., Badenko, V.L., Markov, A., Zotov, D.K., Kozinets, P.V. Dynamic characteristics of a reinforced concrete frame under vibration load conditions. Magazine of Civil Engineering. 2024. 17(2). Article no. 12607. DOI: 10.34910/MCE.126.7

1. Introduction

Columns of a reinforced concrete frame of an industrial structure are often used as foundation supports for placing equipment on them. Reinforced concrete columns are the main load-bearing elements of the frame, and the load on the columns is distributed unevenly due to operation-related equipment vibration. A feature of the dynamics of this system is that the reinforced concrete frame is modeled together with the base and equipment, which is installed at the marks of the column consoles. At the same time, the vibration effect from the operation of the equipment causes vibrations of the structure.

The study was carried out based on a numerical model of a reinforced concrete frame together with the foundation and equipment (Fig. 1). The equipment is presented in the form of distributed point masses on the marks of the frame consoles.

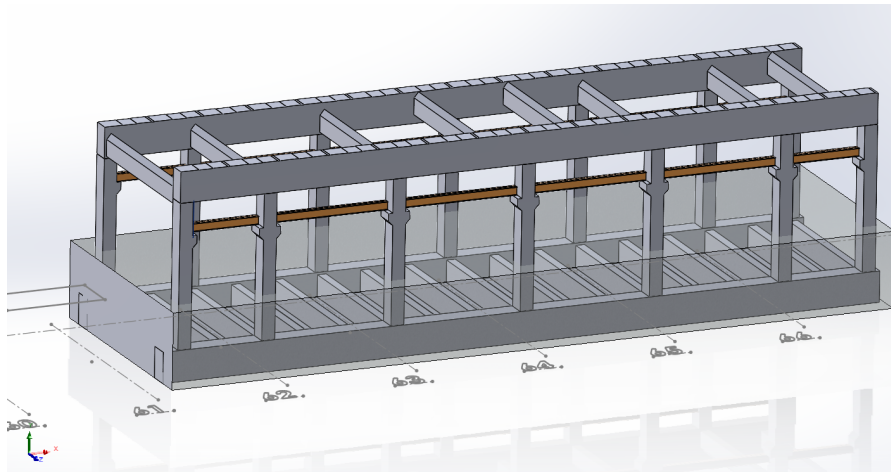


Figure 1. Three-dimensional geometric model of a reinforced concrete frame with a base.

Carrying out a dynamic calculation of a reinforced concrete frame with a base involves analyzing vibration modes and determining the predominant (resonant) frequency during equipment operation. Thus, in article [1], sets of records of accelerograms obtained at certain points of a real reinforced concrete four-story building structure subjected to forced vibrations are presented. The design has vertical indentations from the central axis, which gives it a natural eccentricity in one direction. The tests were carried out to study the torsional moment of a structure subjected to forced vibrations. A mechanical eccentric exciter was used for testing. The exciter was attached to the roof slab in two places, and the resulting force varied in position, magnitude, direction, and frequency. During testing, the only vertical loads applied to the building structure were the self-weight loads of the columns, beams, and slabs. There were no additional vertical dead or dynamic loads. Given the design characteristics and test results, the generated data can be used for several purposes such as building torsion and design verification. The simplicity of the building allows the tests to be accurately reproduced analytically, since there is no interference with non-structural elements or live loads.

In article [2], a new method for reinforcing multilayer (4-layer) vibration insulation of industrial buildings is presented. A new reinforcement method using a shear wall with short supports is also proposed. In addition, an engineering example of a multi-layer industrial building with high vibration is presented. A three-dimensional finite element model of a multi-layer industrial building was created and field vibration tests were carried out. The test results showed that the large vibration of the industrial building was caused by the resonance between the machines and the sandwich industrial building. Finally, the multi-layer industrial building was strengthened with a new reinforcement method, and after reinforcement, a vibration experiment was carried out. The results show that the new reinforcement method has a good effect. The strength and stiffness of the sandwich industrial building were improved, the natural frequency of the industrial building in one direction increased from 2.45 Hz to 5.87 Hz, and in the other direction increased from 2.94 Hz to 7.83 Hz. At the same time, the frequencies of the equipment and the frequencies of the multi-layer industrial building were not in the resonant range, and the vibration characteristics of the multi-layer industrial building were improved. The study can serve as a source of recommendations for reinforcement of a multi-layer industrial building with a similar structural configuration.

In article [3], studies were carried out on the use of forced vibration testing and finite element model verification to assess existing damage in a four-story reinforced concrete structure. The so-called "Four Seasons Building" located in Sherman Oaks, California is examined. It was damaged in the 1994 Northridge earthquake. Using mobile testing equipment, accelerations as well as deformations at selected locations were measured during forced vibration tests using linear and eccentric vibrator devices. This data was used to update the finite element model of the structure. The updated model correlates well with the observed distribution of damage throughout the building and allows us to quantify its magnitude.

In the article [4], a new indicator is proposed for detecting damage in reinforced concrete (RC) beams based on the transient characteristics of nonlinear vibration. Two reinforced concrete beams were studied, one of which was reinforced with external sheets of fiber-reinforced polymer. Both beams were loaded statically and dynamically to relate the dynamic behavior of the beams to the deformations. A model is developed to simulate the general behavior of cracked concrete elements using a softening Duffing generator. Numerical results and test data show that the index increases rapidly with increasing damage

and is very sensitive to cracking even under service loads. The indicator is directly related to transient processes along the crack surface and does not require a baseline for practical use. The experimental test results also show that the fundamental natural frequency of the reinforced beam suddenly decreases when cracks occur and then remains almost constant, while the natural frequency of the unstrengthened beam continuously decreases as the beam undergoes concrete cracking and reinforcement yielding.

The article [5] presents the results of studies of vibration of buildings with reinforced concrete frames based on vibration measurements and numerical analysis. Vibrations were measured at roof level for 29 selected buildings ranging in height from one to six storeys. Using Nakamura's technique [6], horizontal and vertical spectral ratio curves were obtained in two orthogonal plotting directions. Period estimates ranged from 44 % to 91 % of the elastic periods suggested by local regulations. Preliminary period-altitude relationships have been proposed using regression analysis of the measured periods. Due to the lack of structural details, the vibration periods of only 15 buildings were estimated using linear modal analysis of 3D computer models, including the influence of masonry concrete infills. Considering the cracking of structural reinforced concrete elements, the vibration period increased by 40–50 % compared to the elastic value. The analytical period values showed large differences with both measured and calculated values.

In article [7], two models were tested on a vibration stand. One of the models is a conventional reinforced concrete megaframe structure, and the other is a multi-functional vibration-absorbing reinforced concrete megaframe structure, in which laminated rubber supports are placed between the main and small frames. During the test, two seismic motions are used (El Centro wave [8] and Taft wave [9]). This paper presents the dynamic characteristics, seismic responses, and failure mechanism of these two models at different peak acceleration levels for each of the earthquake motions. The test results show that the seismic behavior of the multifunctional vibration-absorbing reinforced concrete megaframe structure is significantly better than that of the conventional reinforced concrete megaframe structure.

Article [10] investigated the influence of the time-varying modulus of elasticity of concrete, pouring of structural elements, assembly of a temporary frame fastening system and impacts from operating construction equipment on the dynamic behavior of a reinforced concrete frame structure during construction. Dynamic tests of an eight-story reinforced concrete frame structure at the full-scale stages of construction of the sixth floor were carried out by external vibration. Natural frequencies, corresponding mode shapes and attenuation coefficient were determined by processing the power spectrum of the test signal data in the frequency domain. Changes in frequencies, vibration modes and damping coefficients at different stages of construction are presented. The results show that the natural frequencies and modal damping coefficients reach a maximum during the fresh concrete pouring stage, especially for higher modes. Modal damping coefficients at each stage of construction are less than 5 % of the coefficients during operation.

Many articles and books are devoted to methods for numerical solution of problems of dynamics of structures [11–25]. Among the famous scientists who studied seismic resistance and dynamic characteristics of structures, it is necessary to note the works of Ya.N. Eisenberg, A.N. Birbraera, S.P. Tymoshenko.

The relevance of the research topic is determined by the safety of the frame working together with the equipment. Vibrations from equipment operation often result in resonance phenomena, which can lead to sudden structural failure. This task is especially relevant for frames and equipment during long-term operation.

The objective of the study is to determine the natural frequencies and analyze the vibration modes of a reinforced concrete frame, as well as proposals for increasing the rigidity of the frame, ensuring the absence of resonances during equipment operation.

2. *Materials and methods*

A method for dynamically calculating vibration loads for equipment standing at the marks of frame columns is presented. The strength and stability of the reinforced concrete frame is not included in the methodology but was carried out when determining the geometric dimensions of the structure, which were used as initial data for this work.

To calculate the reinforced concrete frame, a final elemental “frame-base” model was built. The “frame-base” model was divided into three-dimensional 4-node tetrahedron elements connected to each other at nodes. Coordinate system: OX axis – along the frame, OZ axis – across the frame, OY axis vertically upward (Fig. 1).

Computational studies were carried out within the framework of the spatial formulation of the problem using the Finite Element Method (FEM). FEM and its application in structural calculations are presented in works. The construction of the calculation model was carried out based on the geometric and physical

parameters of the reinforced concrete frame and foundation. The calculation model of the frame is presented in Fig. 2.

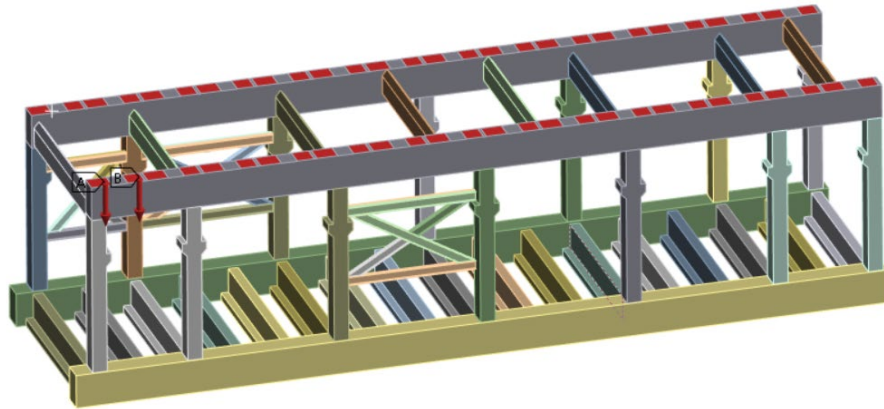


Figure 2. Computational finite element model of the frame.

The initial data for the calculation are the physical characteristics of the concrete, steel and foundation materials obtained because of engineering surveys and frame strength calculations. For dynamic calculations, an accelerogram of vibration impact in the OX direction (along the frame), obtained from the measurement results, was used.

The main stages of the method are as follows

1. Construction of a mathematical dynamic model "frame-base", including geometric construction, division into finite elements, setting the properties of materials, setting boundary conditions.
2. Model verification based on terrestrial laser scanning.
3. Dynamic calculation of the original structure based on the original accelerogram. Determination of natural frequencies and vibration modes of the frame
4. Strengthening the structure to increase dynamic rigidity.
5. Dynamic calculation of the reinforced frame structure based on the newly measured accelerogram.

3. Results and Discussion

Stage 1

Fig. 2 shows the finite element calculation model of the frame, together with the foundation.

Description of boundary conditions:

- The nodes on the lower edge of the foundation are secured against movement and rotation along all axes.
- The nodes on the vertical faces of the foundation are secured against movement in the direction perpendicular to each face.

Physical characteristics of materials

The frame is made of structural concrete – B22.5.

The characteristics of concrete are accepted:

- Concrete density $p_b = 2.4\text{t/m}^3$.
- Calculated resistance of concrete in compression R_b and tension R_{bt} for limit states of the first group:
- $R_b = 11.5\text{ MPa}$;
- $R_{bt} = 0.9\text{ MPa}$;
- Transverse concrete deformation coefficient (Poisson's ratio) for slab structures $\nu = 0.20$.

Additional longitudinal I-beams are made of steel C245:

- Steel density $p_s = 7.85\text{t/m}^3$.
- $R_s = 280\text{ MPa} = 280,000\text{ kPa}$.

- Poisson's ratio of steel $\nu = 0.30$.
- Modulus of elasticity of steel in compression and tension $E_s = 2.1 \times 10^5$ MPa.

Stage 2

At stage 2, the model was verified using terrestrial laser scanning. Based on the results of registration of 12 stations (119,256,031 points), 24 connections were created. The locations of the stations are shown in Fig. 3.

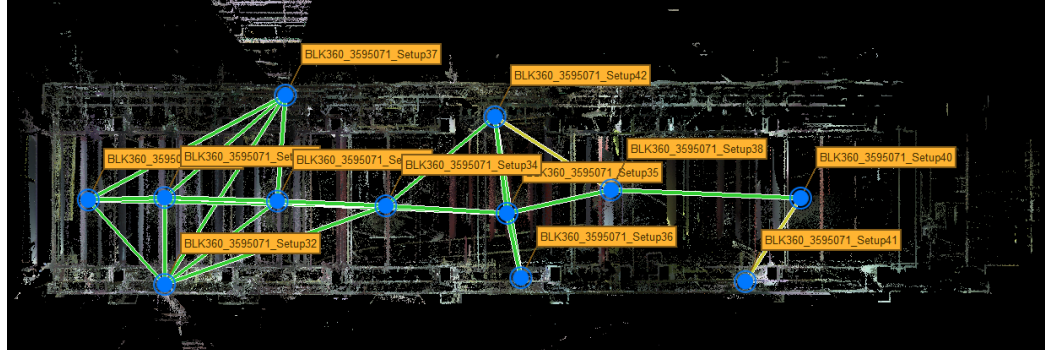


Figure 3. Location of laser scanning stations and links.

The total error was 7 mm (primarily due to the Setup41 station, located in a hard-to-reach place with an overlap of 18 %), and the average overlap was 46 %. Registration is carried out in a local coordinate system. The resulting point cloud was combined with a model built based on design documentation. Based on a cloud of terrestrial laser scanning points, the calculation model was refined. A comparison was made of the design dimensions of the assembly with the values obtained as a result of laser scanning. The actual dimensions of some units are slightly larger than the design ones. The calculation model was built based on the results of actual measurements.

Stage 3

At the third stage, the calculation of the natural frequencies and vibration modes of the structure with the base was carried out.

The calculation obtained the first 15 natural frequencies from 3.609 to 11.237 Hz. The first translational natural waveform with a frequency of 3.609 Hz is shown in Fig. 4.

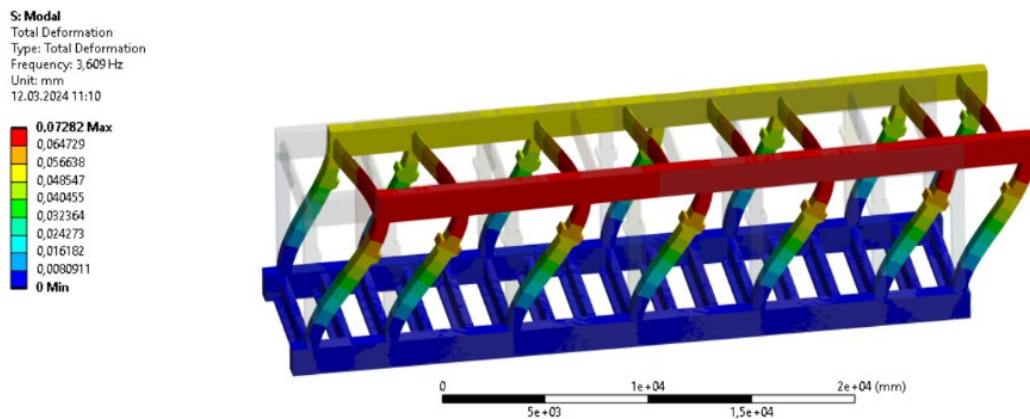
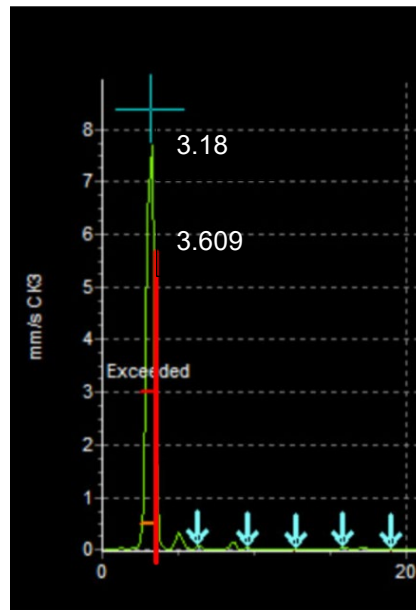


Figure 4. The first translational natural vibration mode of the frame is 3.609 Hz.

The disturbing frequency is 3.18 Hz. The corresponding accelerogram is shown in Fig. 6.



**Figure 5. Accelerogram for the original model.
The disturbing frequency is 3.18 Hz along the X axis.**

When vibration is applied to equipment with a disturbing peak frequency of 3.18 Hz, the phenomenon of partial resonance occurs when the lower boundary of the disturbance coincides with the first translational frequency of the frame, which is 3.609 Hz. To get out of the state of resonance, the structure was strengthened to increase its rigidity.

Stage 4

As reinforcement, 3 vertical connections between the columns were chosen, 2 on one side and 1 on the other side. Mechanical reinforcement option is shown in Fig. 6.

The strengthening of the structure turned out to be asymmetrical due to the presence of technological elements in the operating frame. Thus, the reinforcement is performed using cross connections in the openings between the columns where there are no technological elements.

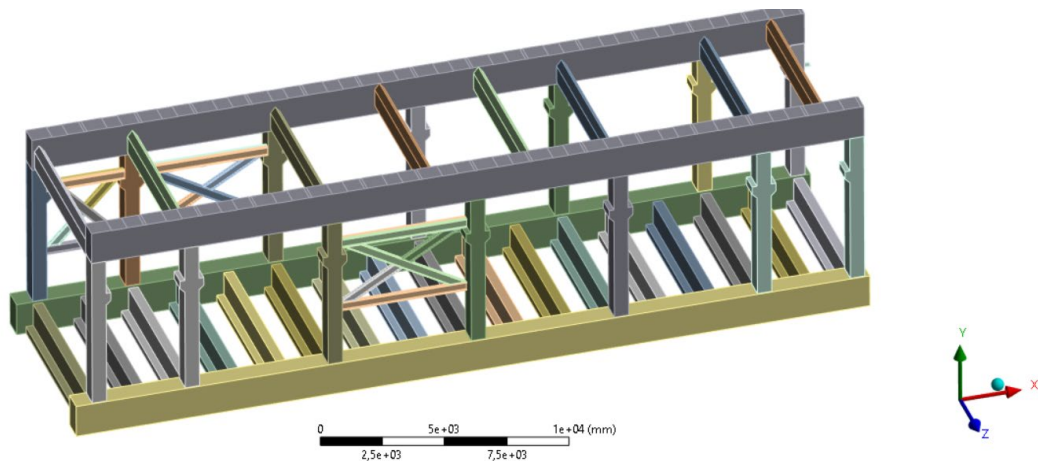


Figure 6. Strengthening structures.

The first translational natural frequency, considering the strengthening of the structure, is 6.4258 Hz, the corresponding vibration shape is presented in Fig. 7.

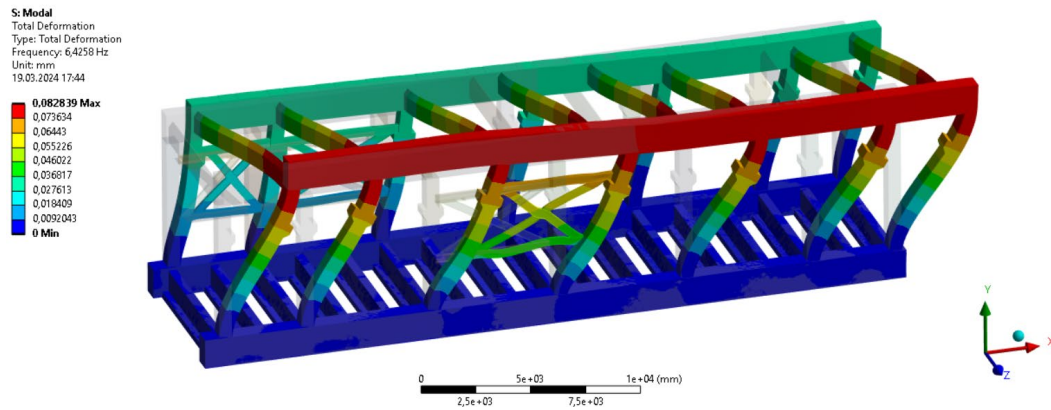


Figure 7. The first translational form of natural vibrations, considering the reinforcement of the frame, frequency 6.4258 Hz.

After strengthening the structure, vibrations from the operation of the equipment were measured. The new accelerogram is presented in Fig. 8.

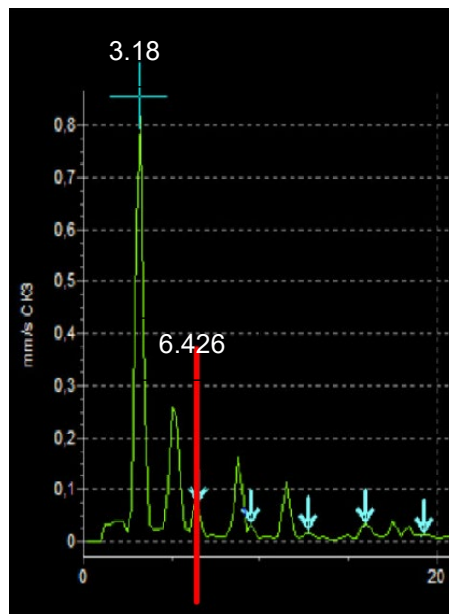


Figure 8. Accelerogram of the reinforced structure. The first translational form of natural vibrations, considering the reinforcement of the frame, frequency 6.462 Hz.

The disturbing resonant frequency is 3.18 Hz. The first natural translational frequency of the frame is 6.4258 Hz. Thus, the resonance phenomena of the reinforced concrete frame, considering the amplification during equipment operation, are completely excluded.

The obtained research results are compared with similar calculations in [2]. When the rigidity of a structure increases in a certain direction, a significant increase in the frequency of translational vibrations occurs, which removes the structure from resonance with the operating equipment.

4. Conclusions

1. As a result of modal analysis, 15 natural frequencies and vibration modes from 3.609 to 11.237 Hz were obtained. In this case, the first translational mode of vibration with a frequency of 3.609 Hz causes the phenomenon of partial resonance with a disturbing peak frequency of 3.18 Hz.
2. Dynamic calculations were performed based on the calculated accelerogram of the translational impact obtained during field measurements of equipment vibrations.
3. The phenomenon of resonance was studied; design solutions were made to strengthen the reinforced concrete frame, leading to exit from the zone of resonance phenomena. The frequency of the disturbing influences did not change and amounted to 3.18 Hz, while the first translational form of oscillation was obtained with a frequency of 6.4258 Hz.

References

1. De-la-Colina, J., Valdés-González, J. Forced-vibration tests of a reinforced concrete four-story building structure. *Journal of Structural Engineering*. 2021. 147(7). DOI: 10.1061/(ASCE)ST.1943-541X.0003011
2. Xie, K., Wang, H., Zhou, J., Luo, X., Yue, M. Experimental study on a new reinforcement method for multilayer industrial building's vibration. *Advances in Civil Engineering*. 2019. Pp. 1–10. DOI: 10.1155/2019/2651915
3. Yu, E., Skolnik, D., Wallace, J., Taciroglu, E. On forced vibration testing for quantifying damage in building structures. *Structural Engineering Research Frontiers*. 2007. Pp. 1–16. DOI: 10.1061/40944(249)75
4. Chen, G., Yang, X., Ying, X., Nanni, A. Damage detection of concrete beams using nonlinear features of forced vibration. *Structural Health Monitoring*. 2006. 5(2). Pp. 125–141. DOI: 10.1177/1475921706057985
5. Al-Nimry, H., Resheidat, M., Al-Jamal, M. Ambient vibration testing of low and medium rise infilled RC frame buildings in Jordan. *Soil Dynamics and Earthquake Engineering*. 2014. 51. Pp. 21–29.
6. Nakamura, Y. What is the Nakamura method? *Seismological Research Letters* 90.4 (2019). Pp. 1437–1443. DOI: 10.1785/0220180376
7. Lan, Z., Tian, Y., Fang, L., Liang, S., Wang, X. An experimental study on seismic responses of multifunctional vibration-absorption reinforced concrete megaframe structures. *Earthquake Engineering & Structural Dynamics*. 2004. 33(1). Pp. 1–14.
8. Zou, Z., Lei, D., Jiang, G., Luo, B., Chang, S., Hou, C. Experimental Study of Bridge Foundation Reinforced with Front and back rows of anti-slide piles on gravel soil slope under El Centro waves. *Applied Sciences*. 2020. 10(9). 3108.
9. Yang, M.G., Chen, Z.Q., Hua, X.G. An experimental study on using MR damper to mitigate longitudinal seismic response of a suspension bridge. *Soil Dynamics and Earthquake Engineering*. 2011. 31(8). Pp. 1171–1181. DOI: 10.1016/j.soildyn.2011.04.006
10. Tian, M.G., Yi, W.J. Dynamic behavior of reinforced concrete frame structure during construction. *Journal of Central South University of Technology (English Edition)*. 2008. 15(3). Pp. 418–422. DOI: 10.1007/s1177100800788
11. Rybakov, V., Jos, V., Raimova, I., Kudryavtsev, K. Modal analysis of frameless arches made of thin-walled steel profiles. *IOP Conference Series: Materials Science and Engineering*. 2020. 883(1). 012197. DOI: 10.1088/1757-899X/883/1/012197
12. Chepurnenko, A., Efimenko, E., Mailyan, D., Zazyev, B. The location of supports under the monolithic reinforced concrete slabs optimization. *Magazine of Civil Engineering*. 2021. 104(4). 10404. DOI: 10.34910/MCE.104.4
13. Kozinetc, G.L., Kozinetc, P.V. The calculation of the dynamic characteristics of the spillway of the dam. *Magazine of Civil Engineering*. 2022. 113(5). 11312. DOI: 10.34910/MCE.113.12
14. Badenko, V., Volgin, D., Lytkin, S. Deformation monitoring using laser scanned point clouds and BIM. *MATEC Web of Conferences*. 2018. 245(177). 01002. DOI: 10.1051/mateconf/201824501002
15. Ayzenberg, YA.M., Kodysh, E.N., Nikitin, I.K., Smirnov, V.I., Trekin, N.N. (2012). *Seysmostoykiye mnogoetazhnyye zdaniya s zhelezobetonnyim karkasom* [Earthquake-resistant multi-storey buildings with reinforced concrete frames]. Moscow: Izdatel'stvo ASB, 2012. 264 p. (rus)
16. Verret, D., LeBoeuf, D. Dynamic characteristics assessment of the Denis-Perron dam (SM-3) based on ambient noise measurements. *Earthquake Engineering & Structural Dynamics*. 2022. 51(3). Pp. 569–587. DOI: 10.1002/eqe.3580
17. Arbain, A., Mazlan, A., Zhafran, A., Hafiz, M., Radzi, M. Vibration Analysis of Kenyir Dam Power Station Structure Using a Real Scale 3D Model. *Civil And Environmental Engineering Reports*. 2019. 30(3). Pp. 48–59. DOI: 10.2478/ceer-2019-0023
18. Pereira, S., Magalhães, F., Gomes, J.P., Cunha, Á., Lemos, J.V. Dynamic monitoring of a concrete arch dam during the first filling of the reservoir. *Engineering Structures*. 2018. 174. Pp. 548–560.
19. Gordan, B., Raja, M., Jahed Armaghani, D., Adnan, A. Review on Dynamic Behaviour of Earth Dam and Embankment During an Earthquake. *Geotechnical and Geological Engineering*. 2022. 40. Pp. 1–31. DOI: 10.1007/s10706-021-01919-4
20. Jianyun, C., Jia, Q., Xu, Q., Fan, S., Liu, P. The PDEM-based time-varying dynamic reliability analysis method for a concrete dam subjected to earthquake. *Structures*. 2021. 33. Pp. 2964–2973. DOI: 10.1016/j.istruc.2021.06.036
21. Boulanger, R.W. Nonlinear dynamic analyses of Austrian dam in the 1989 Loma Prieta earthquake. *Journal of Geotechnical and Geoenvironmental Engineering*. 2019. 145(11). 05019011. DOI: 10.1061/(ASCE)GT.1943-5606.0002156
22. Savich, A.I., Bronshteyn, V.I., Groshev, M.Ye., Gaziyev, E.G., Il'in, M.M., Rechitskiy, V.I., Rechitskiy, V.V. *Sticheskiye i dinamicheskiye povedeniye Sayano-Shushenskoy arochno-gravitatsionnoy plotiny* [Static and dynamic behavior of the Sayano-Shushenskaya arch-gravity dam]. *Gidrotekhnicheskoye stroitel'stvo*. 2013. 3. Pp. 2–13.
23. Regni, M., Arezzo, D., Carbonari, S., Gara, F., Zonta, D. Effect of environmental conditions on the modal response of a 10-story reinforced concrete tower. *Shock and Vibration*. 2018. 9476146. DOI: 10.1155/2018/9476146
24. Arslan, M.E., Durmuş, A. Modal testing and finite element model calibration of in-filled reinforced concrete frames. *Journal of Vibration and control*. 2014. 20(13). Pp. 1946–1959. DOI: 10.1177/1077546313480545
25. Pereira, S., Magalhães, F., Gomes, J.P., Cunha, Á., Lemos, J.V. Dynamic monitoring of a concrete arch dam during the first filling of the reservoir. *Engineering Structures*. 2018. 174. Pp. 548–560. DOI: 10.1007/s13349-021-00536-2

Information about authors:

Pinlu Cao, Doctor of Science

E-mail: jluopl@jlu.edu.cn

Galina Kozinetc, Doctor in Technical Sciences

E-mail: kozinets_gl@spbstu.ru

Vladimir Badenko, Doctor in Technical Sciences

ORCID: <https://orcid.org/0000-0002-3054-1786>

E-mail: vbadenko@gmail.com

Alexey Markov, Doctor of Science
E-mail: am100@inbox.ru

Dmitry Zotov,
E-mail: zotovdk@gmail.com

Pavel Kozinets,
E-mail: pavelstrenger@gmail.com

Received 20.12.2023. Approved after reviewing 28.02.2024. Accepted 01.03.2024.



Research article

UDC 691

DOI: 10.34910/MCE.126.8



Application of fractal analysis to assess the quality of the appearance of paint and varnish coatings

V.I. Loganina¹ , R.S. Fediuk^{2,3}  , V.S. Lesovik³ , S.V. Klyuev³ , L.S. Sabitov⁴, M.I. Lomov³, S.V. Vavrenyuk⁵, I.A. Vykhodtsev²


¹ Penza State University of Architecture and Construction, Penza, Russian Federation

² Far Eastern Federal University, Vladivostok, Russian Federation

³ V.G. Shukhov Belgorod State Technological University, Belgorod, Russian Federation

⁴ Kazan (Volga region) Federal University, Kazan, Russian Federation

⁵ branch FGBU "TSNIIP Russian Ministry of Construction" DaNIIS, Vladivostok, Russian Federation

 roman44@yandex.ru

Keywords: composites, coatings, appearance, quality, regularities, formation, model

Abstract. The article provides information on the use of fractal dimension in assessing the quality of the appearance of paint coatings. It was established that with an increase in the surface roughness of the coating, a decrease in the appearance quality grade and an increase in the fractal dimension D are observed. A correlation between the fractal dimension and the quality class of the appearance of the coating is established. With an increase in the fractal dimension of the coating surface profile, its brightness decreases and the numerical values of the profile perimeter increase. A model of the coating surface profile length on the fractal dimension D is proposed. The results of evaluating the surface profile of the coatings indicate that with an increase in the surface tension of the paint composition, an increase in the fractal dimension and a lower quality of the appearance of the resulting coating are observed. Numerical values of the index of the fractal dimension of the surface profile of the paint coating are obtained depending on the porosity of the cement substrate. The influence of the method of applying paint on the quality of the appearance of coatings was established.

Funding: The study was supported by the RSF grant No. 22-19-20115, <https://rscf.ru/project/22-19-20115/> (accessed on 18 November 2022) and the Government of the Belgorod Region, Agreement No. 3 of 24 March 2022.

Citation: Loganina, V.I., Fediuk, R.S., Lesovik, V.S., Klyuev, S.V., Sabitov, L.S., Lomov, M.I., Vavrenyuk, S.V., Vykhodtsev, I.A. Application of fractal analysis to assess the quality of the appearance of paint and varnish coatings. Magazine of Civil Engineering. 2024. 17(2). Article no. 12608. DOI: 10.34910/MCE.126.8

1. Introduction

Various types of modern finishing of external concrete walls of buildings are effectively used to improve their architectural expressiveness and performance [1]. A painting of any building structures is one of the most popular types of finishing; it takes up to half of the finishing materials used in the world [2]. The coating for finishing the facade should not only protect the building from external influences, but also have an aesthetic appearance. In addition, the coating must be resistant to precipitation, temperature changes, and ultraviolet radiation. Moreover, it must have long service life and be easy to work and use [3]. The quality of the paintwork is assessed according to several parameters. One of them is the absence of defects. Stains, smudges, shagreen, streaks and scratches: all this can ruin the appearance of the coating.

Waviness and color variability are also not desirable phenomena [4]. An appearance quality class of a paint coating is determined by the presence or absence of defects on its surface [5].

Assessment of paint coating quality can be subjective, as it depends on the opinion of a particular person. There are various methods for assessing the quality of paint and varnish coatings. One of them is visual inspection. Vaspero et al [6] used electron microscopy to study the surface of paintwork. They found that surface quality could be improved by changing the paint composition and application conditions. Zhong et al [7] applied multimodal tomography to study organic paint coatings. They found that this method allowed them to obtain detailed images of the coating's structure and determine its properties. Oliveira and Ferreira [8-9] used electrochemical impedance spectroscopy to study the properties of paint coatings. They found that high-quality systems had lower impedance than defective systems. Quevauviller [10] suggests using certified reference materials to test the quality of paint coatings. Zhou et al [11] developed a mathematical model that describes the release of volatile organic compounds from paint coatings on porous surfaces. Aktas et al [12] systematically investigated different coating methods for marine propellers. They found that certain types of soft paints could protect the surface from cavitation erosion. Tanzim et al [13] created a model that predicts the width of the paint spray when using an electrostatic sprayer.

The method of applying the paint and varnish material and the preparation of the base surface play an important role in ensuring the quality of the appearance of the coating. The correct choice of application method and surface preparation will avoid problems with adhesion, roughness, color uniformity and other defects. Here are some key points to consider when choosing an application method and surface preparation:

1. Type of coating [14]: Before choosing an application method, it is necessary to consider the type of coating. Some coatings require special equipment and skills to apply. For example, powder coatings require a special curing chamber and spray gun, while brush or roller application may not be suitable.
2. Surface size and shape [15]: The size and shape of the surface to be painted also influence the choice of application method. Large flat surfaces can be painted using airless spray or electrostatic spray, while smaller or more complex surfaces may require a brush or roller.
3. Base surface preparation [16]: Base surface preparation includes cleaning, degreasing, sanding and dusting. It is important to ensure that the surface is clean and dry before applying the coating. Poor preparation can lead to poor adhesion of the coating to the surface, the appearance of bubbles and peeling.

According to the Russian standard GOST 9.032-74 classification, modern builders divide the quality of paint coatings into 7 classes, where the first class characterizes coatings without defects, and the seventh one has the maximum number of structural defects.

Scientists must continue to look for new methods to control the quality of paint coatings [17–22]. This will help improve the quality of construction products and make them more competitive in the market. The surface quality of a paint coating can be assessed by its roughness [23]. Surface roughness is determined by the surface profile [24]. The use of fractal physics methods may be promising for assessing the surface profile of paint and varnish coatings [25]. Fractal physics provides more accurate results than traditional roughness measurement methods [26–27].

Takada et al [28] used fractal analysis to study the dispersion of carbon nanotubes in polystyrene. They discovered that ultraviolet radiation can change the properties of nanotubes and affect their dispersion in the polymer. Zivic et al [29] studied the properties of polymer chains attached to the surface of three-dimensional fractal lattices. Li et al [30] developed a model for the fractal fracture of glassy polymers. This model takes into account material damage and hardening. Marquardt et al [31] used fractal analysis to study the surface of blast-cleaned steel. They found that the fractal dimension of a surface influences the adhesion of polymer films to adhesives. Pandey and Chandra [32] studied the effect of thermal degradation of a polymer on its redox-initiated fractal geometry.

Fractal structures play an important role in determining the surface and volumetric properties of materials [33–36]. Fractal geometry is used to comprehensively characterize the pore structure of cement-based materials, allowing the complex pore structure to be quantified and compared and correlated with the macro properties of cement-based materials. In [37–38], it was proven that cementitious materials have fractal properties at certain scales. Using X-ray scattering methods, it was found that the hardening products of cementitious materials can be described by fractal dimensions. Zeng et al [39] offered a comprehensive understanding of the fractal surface features of the porous structure of cement-based materials using massive backscattered electron images.

In [40], the porous structure of cement pastes is described based on the fractal method, which can be used to analyze and predict the durability and strength of cement composites. In [41–42], a connection

was established between the fractal dimension and the process of development of frost-thawing damage to concrete at the microscopic level. It was found in [43] that the fractal dimension can characterize the characteristics of temperature cracks in a low-alkali cement matrix modified with microsilica.

Thus, the surface of paint and varnish coatings quality is determined, among other things, by its roughness (surface profile). Fractal physics can be used to evaluate the surface profile of paint coatings. The successful application of fractal analysis methods in the study of polymers allows us to hope that this approach will be successfully extended to assess the quality of the appearance of coatings. The development of an integral indicator of the surface quality of paint and varnish coatings can be very useful. This will help improve product quality and make it more competitive in the market. The use of fractal dimension can help in assessing the quality of paint and varnish coatings. However, it must be taken into account that the fractal dimension is not the only indicator of the quality of the coating. Other factors such as color, gloss, resistance to external influences, etc. must also be taken into account. For the coating surface profile, the fractal dimension D is in the range $1 < D < 2$ [44–48]. The greater coating roughness, the more curved the coating profile and the greater D value. Thus, the fractal dimension D of the coating profile can serve as a criterion for the quality of its appearance, reflecting the presence of inclusions, stripes, and waviness.

The use of fractal dimension for modeling paint coatings is an underexplored area. This is an interesting direction for this research. The authors of the current article made an attempt to evaluate the possibility of describing the quality of the appearance of coatings using the fractal dimension. To achieve this goal, the following tasks were solved: a correlation was established between the surface roughness of the coating, the appearance quality grade, and the fractal dimension; obtaining numerical values of the index of the fractal dimension of the coating surface profile depending on the porosity of the substrate; assessment of the effect of filling the paint composition on the quality of the appearance of coatings; consideration of the influence of the method of applying the paint composition and the preparation of the base surface on the coatings appearance quality.

2. Materials and Methods

2.1. Materials

Various types of paints were used in the study, as they are widely used in finishing building products and structures. This made it possible to obtain more complete and reliable results. The selected paints have different bases, which provides wider coverage and allows the results of the study to be used in different conditions. The following paint compositions were used in the work: alkyd enamel PF-115 (Yaroslavl paints, Yaroslavl, Russia), oil paint MA-15 (Lakra, Moscow, Russia), nitrocellulose paint NC-132 (Teks, Saint-Petersburg, Russia), acrylate paint Universal (Teks, Saint-Petersburg, Russia), acrylic water-dispersion paint Facade (Belyi dom, Kaluga, Russia), polyvinyl acetate cement (PVAC), polymer-lime, cement-perchlorovinyl (CPCV), and lime paint. The following materials were used for the preparation of colorful compositions:

- white Portland cement (Belgorod cement, Belgorod, Russia);
- colored cements (Yaroslavsky pigment, Yaroslavl, Russia);
- quartz sand (Volsk, Russia) for decorative powder;
- lime – fluff (Penza, Russia);
- lime paste, 50 % (Penza, Russia);
- polyvinyl acetate dispersions (PVAD), grades DF 47/70, and 48/50 (Penza, Russia);
- liquid glass (Penza, Russia);
- water-repellent liquid 136-41 (Penza, Russia).

The substrates were glass, expanded clay concrete M75, cement-sand mortar, and heavyweight concrete. The paint compositions were applied to substrates with different porosities (24 %, 28 % and 32 %) using a brush, pouring and pneumatics in two layers with intermediate drying for 20 minutes.

2.2. Methods

To assess the rheological properties of paints, the Stokes method was used, which allows one to determine the dynamic viscosity of paints. For this, the test liquid is poured into a graduated cylinder, a metal ball of known density ρ_{ball} and radius r is brought to the surface and lowered (without a push). As soon as the movement of the ball becomes uniform, start the stopwatch and determine the time it takes the ball to pass between the given marks. Liquid viscosity was determined by the formula:

$$\mu = \frac{2}{9} gr^2 \frac{(\rho_{ball} - \rho_{paint})t}{l}, \quad (1)$$

where g is gravity acceleration, m/s^2 ; t is time during which the ball passes the distance between the marks A and B, sec; l is distance between the marks A and B, cm; ρ_{ball} , ρ_{paint} are density of the ball and paint, g/cm^3 , respectively.

To determine the conditional viscosity of paint and varnish compositions, a VZ-4 viscometer (K-M, St. Petersburg, Russia) was used. The method is as follows: determine the duration (in seconds) of passing 100 mm of paint through a viscometer nozzle with a diameter of 4 mm.

The stalagmometric method was used to determine surface tension.

To evaluate the paint pouring technique, a method of applying five parallel stripes of paint was used and the degree of spreading was determined by the number of stripes stuck together. The strips were applied by a special device. The degree of spreading was assessed on a ten-point scale from 0 to 9, where 0 is no spreading, and 9 is complete spreading.

The coatings gloss was determined by the photoelectric method on an FB-2 gloss meter (K-M, Saint-Petersburg, Russia) according to the Russian Standard GOST 896-69.

The paint compositions were applied by brush to substrates with a porosity of 30 % in two layers with intermediate drying for 24 hours. The coating profile was determined by an A1 type profilometer-profilograph TR-100 (K-M, Saint-Petersburg, Russia). The length of the coating surface profile was determined using a curvimeter. The fractal dimension of the surface profile of the coatings was estimated using a geometric method. To do this, the image of the curve obtained using a profiler-profilometer was covered with a grid consisting of squares with a side L_1 . Then, the number of squares N , through which the curve $N(L_1)$ passes, was counted. By changing the scale of the grid, each time the number of squares intersecting the curve $N(L_2), N(L_3) \dots N(L_n)$ was counted again. Then, the dependence $N(L)$ was plotted in double logarithmic coordinates, the slope of which was used to determine the fractal dimension. The quality of the substrates was evaluated by the index of total porosity P and surface porosity P_s . Surface porosity was determined by the ratio of the sum of the pore area to the total area of the measured surface. The pore diameter was measured using a measuring magnifier $\times 24$.

Statistical analysis was carried out in order to formulate logical conclusions about the correlation between surface roughness, quality grade and fractal dimension. The reliability and reproducibility of the results was ensured by the fact that 50 measurements were taken on each surface. Statistical indicators were calculated to assess the uniformity of the distribution of roughness indicators along the strike.

3. Results and Discussion

The results of assessing the quality of the appearance of coatings, carried out in accordance with Russian Standard GOST 9.407-2015 and using the fractal dimension of the surface of the coating profile, are given in Table 1.

Table 1. Evaluation of the coating appearance quality.

Type of paint	Coating surface roughness, R_a , μm	Fractal dimension, D	Surface profile perimeter, mm	Coating surface quality grade	Gloss, %
PF-115	0.22	1.17	106	V	70.8
	0.75	1.35	116	VI	67.7
MA-15	0.2	1.075	102	V	83.1
	0.48	1.125	109	VI	78
NC-123	0.2	1.1	105	V	76.9
	0.75	1.36	121	VI	67.7
Universal	0.75	1.3	216	VI	66.2
	1.26	1.42	221	VII	64.2
Facade	0.6	1.25	192	VI	66.2
	1.24	1.7	225	VII	62.2

A correlation was revealed between the roughness of the coating surface, the quality of appearance and the fractal dimension. As the roughness of the coating surface increases, the quality of appearance decreases, and the value of the fractal dimension D increases. The research results indicate that the fractal dimension of the surface profile of a coating based on PF-115 paint with a coating surface roughness of 0.2 microns and an appearance quality class of V is $D = 1.17$, and with a coating surface roughness of 0.75 microns and an external quality class For coating type VI, the fractal dimension is $D = 1.35$. This confirms that the fractal dimension of the coating surface profile depends on the surface roughness and the appearance quality class. Similar patterns are typical for other coatings types. The parameters of gloss and surface profile of the coating also depend on the roughness and quality class of the appearance. As the fractal dimension of the coating surface profile increases, the gloss of the coating decreases.

The correlation between the length L of the coating surface profile on the sample length l and the fractal dimension D can be approximated as:

$$L = lD^{bD}, \quad (2)$$

where l is a base length of measurement; b is a constant depending on surface roughness and appearance quality class. Formula (2) was obtained by the least squares method.

In particular, for the coatings based on paint PF-115 the expression (2) is

$$L = 99.62D^{0.33D}$$

– For paint MA-15 based coating

$$L = 99.08D^{0.63D}$$

– For paint NC based one

$$L = 99.55D^{0.416D}$$

– For acrylic paint based one

$$L = 115.28D^{1.47D}$$

– For water-dispersible façade paint based one

$$L = 131D^{0.645D}$$

The correlation coefficient ranged from 0.93 to 0.95.

The results of the research suggest that for fractal dimension $D = 1-1.09$ the coating appearance quality grade is IV, for $D = 1.1-1.2$ is V, for $D = 1.21-1.4$ is VI, for $D = 1.41-1.99$ is VII. Applying the integral performance index to the coatings appearance such fractal dimensions will let estimate paint coatings quality more objectively. The use of an integral indicator of the quality of the appearance of coatings, such as the fractal dimension, can complement existing indicators and make the assessment of the quality of paint and varnish coatings more objective. The results of calculations in accordance with model (2) are in good agreement with the data given in Table 1.

Research has shown that the quality of the appearance of coatings is determined by the nature of the bottling of the paint. Bottling is considered as a rheological process, which can be described by the following expression:

$$h = \frac{b^2}{8\sigma} f, \quad (3)$$

where h is stroke height; b is width of stroke; f is shift limit stress of the paint; σ is surface tension of the paint. Formula (3) is presented in [38].

Analysis of the data from Table 2, indicate that there is some slowing down of the time of restoration of the structure of paint when applied to the porous surface of the mortar. A slight slowdown in the restoration of the paint structure when applied to a porous surface of the solution has been established. On a glass substrate, the restoration time of the structure of the paint and varnish composition PF-115 is 3 minutes [39–42], and on the cement substrate is 5 minutes [43–44]. The structure of the paint and varnish composition depends on the porosity of the base and the rheological properties of the paint.

Table 2. Dependence of the quality of the appearance of a coating on the rheological properties of paints.

Type of paint	Surface roughness*, R_a , μm	Fractal dimension of the coating surface, D	Surface tension of the paint composition, mJ / m^2	Dynamic viscosity of the paint composition, $\text{Pa} \cdot \text{s}$	Filling the colorful composition**, min.
Alkyd paint (PF-115)	0.61	1.30	19.36	7.89	$\leq 5 / \leq 5$
	0.39	1.120	18.36	6.87	$\leq 5 / \leq 3$
	0.19	1.05	16.68	5.79	$\leq 5 / \leq 3$
	0.79	1.29	17.50	23.70	$\leq 5 / \leq 3$
Oil paint (MA-15)	0.70	1.09	16.94	14.79	$\leq 5 / \leq 3$
	0.45	1.04	16.20	10.37	$\leq 5 / \leq 3$
Nitrocellulose (NC-132)	0.80	1.29	27.11	13.99	$\leq 5 / \leq 3$
	0.59	1.09	24.11	7.40	$\leq 5 / \leq 3$
	0.29	1.07	22.09	6.40	$\leq 5 / \leq 3$
Acryl water dispersed (Façade)	2.99	1.39	37.38	40.05	$\leq 15 / \leq 15$
	2.54	1.26	34.94	30.79	$\leq 15 / \leq 15$
	1.86	1.09	31.90	21.57	$\leq 15 / \leq 15$
Acrylate (Universal)	2.39	1.54	36.12	33.45	$\leq 15 / \leq 15$
	1.78	1.29	33.88	24.29	$\leq 15 / \leq 15$
	1.43	1.09	30.95	15.19	$\leq 15 / \leq 15$

* The coating under study was applied to the glass substrate. Then, under microscope magnification, the roughness of the coating was assessed. Microscopic surface features such as irregularities, pores and inclusions were analyzed to determine the roughness of the coating. This method allows you to obtain accurate and objective data on the roughness of the coating.

** Numerical values of the paint structure recovery time when applied to a solution base are shown on the left, on a glass base – on the right.

The results of assessing the surface profile of coatings show that with an increase in the surface tension of the paint and varnish composition, the quality of the appearance of the coating deteriorates. This may be due to the fact that higher surface tension prevents the paint from spreading evenly on the surface and forming a smooth film. As a result, the coating becomes rougher and less attractive in appearance. So, with the surface tension of the acrylate paint Universal equal to $s = 36.13 \text{ mJ/m}^2$, the surface roughness of the coating is $R_a = 2.4 \mu\text{m}$, and the fractal dimension is $D = 1.53$. Similar patterns are typical for various types of coatings. The roughness and appearance of the coating can depend on various factors such as paint composition, application method and surface preparation.

At the next stage, the probability of coating failure due to the presence of surface defects was assessed. The probability of coating failure can be assessed based on an analysis of surface defects and their effect on the strength and durability of the coating. For this purpose, statistical data analysis methods such as Pareto analysis or cause-and-effect analysis can be used. An assessment of the probability of coating failure based on the safety factor and safety factor can also be used. It was suggested that there is one defect (inclusions, stripes, etc.) on the surface of the coating, which has a random location. Next, it was divided the area of the coating under study into n sections, the area of which is equal to the area of the defect. Possibility of a defect in a certain area during operation is equal to P . As a result, the condition must be observed that in real time $np = \text{const}$. A coating is considered "failed" if more than n_{def} areas are found on its surface, which is determined from the formulas:

$$n_{def} = \frac{S_{def}n}{100}; \quad (4)$$

$$F(c) = \sum_{x=0}^{S_{def}n} \frac{c^x}{x!} e^{-c}, \quad (5)$$

where $c = np = \text{const}$.

It was proven that it is possible to evaluate the kinetics of the concentration of defects on the surface of a coating during its aging. This can help determine when the coating may become more susceptible to

failure due to increased defects. The quality of the appearance of defects can be described using fractal dimension and surface roughness. After the coating had cured, the samples were subjected to various tests, such as freeze-thaw, to test their resistance to various impacts. It was established that the quality of the appearance of the coating can be improved or deteriorated depending on the porosity of the base and the rheological properties of the paint and varnish compositions used. More porous substrates or more viscous paints can result in a rougher, less attractive finish. A coating area of 64 cm² was used for determination of the defect concentration.

It was that cracks appear locally and form near defects on the coating surface. For example, on the coating based on paint MA-15, characterized by a fractal dimension and roughness index of 1.089 and $R_a = 0.23 \mu\text{m}$, respectively, surface cracks appeared, visible to the naked eye, after 5 freeze-thaw cycles, and on a coating with an index of fractal dimension and roughness 1.069 and $R_a = 0.14 \mu\text{m}$, respectively, after 15 test cycles. Other coatings studied are also characterized by similar patterns (Table 3).

Table 3. Coatings appearance quality reducing during freezing–thawing.

Paint coating	Surface roughness*, R_a , μm / Fractal dimension	Number of defects after test cycles/failure possibility, %				
		0	5	10	13	15
Alkyd paint (PF-115)	0.09/1.111	37/17.0	40/42.8	49/99 Coating peeling off	-	-
	0.09/1.09	29/14.9	31/38.43	37/41.9	69/99 Coating peeling off	-
	0.11/1.11	19/13.8	26/35.4	30/40.8	57/47.1	58/53.9
	0.19/1.18	44/16.9	61/99 Coating peeling off	-	-	-
	0.20/1.09	29/16.0	48/199 Coating peeling off	-	-	-
	0.16/1.09	21/13.9 1	47/31.0	55/41.1	60/45.3	64/54.2
	0.27/1.20	53/17.7	68/33.5	79/99 Coating peeling off	-	-
Oil paint (MA-15)	0.24/1.09	30/24.9	59/199 Coating peeling off	-	-	-
	0.20/1.074	21/24.4	24/34.9	27/37.9	29/39.9	34/41.4
	0.16/1.08	9/23.3	16/33.9	19/34.9	20/39.3	27/40.9
	0.28/1.20	29/24.9	71/99 Coating peeling off	-	-	-
	0.19/1.076	22/24.6	50/99 Coating peeling off	-	-	-
	0.18/1.074	11/23.7	17/34.5	20/36.4	24/39.7	30/40.1
	0.29/1.25	33/25.5	81/99 Coating peeling off	-	-	-

Thus, by adjusting the rheological and technological composition of the paint, as well as the physical and mechanical properties of the base and other parameters, it is possible to obtain high-quality coatings with excellent external characteristics.

The porosity of the base certainly affects the quality of the appearance of the resulting coating (Table 4). As the porosity of the substrate increases, the surface roughness of the coating usually also increases. So, for example, the surface roughness of lime coatings increases to 83.4 μm (the porosity of the substrate is 9.7 %); for polymer lime up to 88.1 μm (substrate porosity 12.0 %); for PVAC coatings up to 46.2 μm (substrate porosity 12.7 %). An increase in the porosity of the base usually leads to some deterioration in the quality of the appearance of the resulting coatings.

Table 4. Dependence of the coatings appearance quality on the substrate porosity.

Coating type	Porosity, %	Coating roughness, μm	Coating grade
Lime	0	34.0	V
	5.8	50.6	V
	9.7	83.5	VI
Polymer lime	0	33.4	V
	4.2	41.4	V
	12.0	88.2	VI
PVAC	0	8.3	V
	3.1	20.4	IV
	12.7	58.5	V

Puttying and priming a surface with such porosity helps improve the quality of the appearance of the coating (Table 5).

Table 5. Effect of the substrate surface preparation method on the coatings appearance quality.

Viscosity determined by VZ-4 device, s	Paint application method	Porosity, %	Substrate surface preparation	Coating appearance quality grade according to Russian standard GOST 9.032-74
PVAC Paint				
50	brush	0	padding	VI
30	pneumatic	0	padding	V
50	brush	3.2	padding	VI
50	brush	4.3	padding	VI
50	brush	6	padding	V
50	brush	6	puttying, padding	IV
Lime Paint				
50	brush	0	padding	VI
35	pneumatic	0	padding	V
50	brush	6	padding	VI

The method of applying the paint composition also has a significant impact on the quality of the appearance of the resulting coating. Table 5 presents data about the coatings appearance quality of depending on the method of applying the paint composition for preparing the substrate surface. An analysis of the data given in Table 5 provides that, with an equal porosity of the cement base, the pneumatic application of the paint composition contributes to an increase in the coating class. Thus, in order to obtain a higher coating appearance quality, it is necessary to strive to create a surface porosity of the cement base that does not exceed 5 %.

Statistical processing was done for a more reliable assessment of the distribution of roughness indicators. Information analysis (Table 7) shows that regardless of the paint type, base porosity, there is a heterogeneity in the rough distribution. Thus, when using PF-115 paint on the base with porosity 24 % range \bar{R} is 10.94 μm , and MA-15 paint is 10.12 μm . Swipe between surface roughness R_a of coatings based on paint PF-115 on putty surface is much lower (3.68 μm). For PF-115 paint a coating that is less uniform along the strike is formed when paint is applied to substrate with a porosity of 32 %. The spread of roughness indices $R_a = 11.21 \mu\text{m}$. Regardless of the type of paint composition, a smaller spread of indicators roughness R_a is typical for the surface of all coatings on putty substrate.

Table 7. Coating surface roughness and processing statistics sample information.

Type of paint	Substrate porosity,%	Roughness R_a , μm	RMS deviation σ / data range R
PF-115	24	6.7	2.88/10.94
	28	7.65	1.92/8.61
	32	6.98	3.32/11.61
	The surface is putty	2.6	0.95/3.68
MA-15	24	4.37	2.94/10.12
	28	4.53	2.6/10.31
	32	5.4	5.61/10.1
	The surface is putty	2.8	1.21/4/52

Provided that the surface roughness parameters of the coatings are distributed according to the normal law and taking into account the three-sigma deviations in the tolerance field, you can get the value of the defect level q by expression

$$q = 0.5 - \Phi\left(\frac{ULT - R}{\sigma}\right),$$

where Φ is the Laplace function; σ is standard deviation; ULT is upper limit tolerance; R is the average value of the surface roughness.

It was calculated the defectiveness level of coatings for roughness with surface grades N4 and N5 according to ISO1302 (for roughness class N4, ULT equals $8 \mu\text{m}$, for N5 – $16 \mu\text{m}$). The results of the calculation are given in Table 8.

Table 8. Defect level of coatings.

Type of paint	Substrate porosity,%	Defect level, %, at roughness grade, %,	
		N4	N5
PF-115	24	32.64	0.069
	28	36.84	0.103
	32	38.21	0.33
	The surface is putty	0.001	0.001
MA-15	24	10.93	0.007
	28	12.34	0.012
	32	32.38	3.01
	The surface is putty	0.006	0.001

It was established that coatings based on PF-115 and MA-15 paints, estimated by the N4 roughness grade, have a high defect level (up to 38 %), and by the N5 roughness grade - no more than 0.007–3.01 %. This means that with increasing coating roughness class (i.e. increasing surface roughness), the number of defects on the coating surface increases. Regardless of the type of paint, the porosity of the substrate surface puttying before painting contributes to the formation of coatings with a low level of defects, amounting to 0.001–0.006 %.

So, it is necessary to take into account the porosity of the cement base and select the appropriate type of paint and varnish material to achieve high quality paint coatings on building products and structures.

4. Conclusions

As a result of the conducted study, the following conclusions were drawn.

1. Based on the obtained patterns, recommendations were developed for optimizing the formulations of paints and varnishes to ensure high quality coatings. It was revealed that with an increase in the surface tension of the aqueous paint composition, a lower quality of the appearance of the resulting coating is observed. This may be due to the fact that high surface tension prevents the uniform distribution of pigment and binder particles in the paint and varnish material, which in turn leads to a deterioration in the appearance of the coating.
2. With an increase in the porosity of the substrate, an increase in the roughness of the surface of the coatings is observed. This may be due to the fact that the paint and varnish material fills the pores

of the substrate unevenly, which leads to the formation of irregularities on the surface of the coating. To reduce the roughness of the coating, you can use substrates with less porosity or use special primers to reduce surface porosity.

3. It was established that coatings based on PF-115 and MA-15 paints, estimated by the N4 roughness grade, have a high defect level of (up to 38 %), and by the N5 roughness grade, no more than 0.007–3.01 %. This means that with increasing coating roughness class (i.e. increasing surface roughness), the number of defects on the coating surface increases.
4. Fractal dimension is a quantitative measure of surface roughness and can be used to assess the surface quality of paint and varnish coatings. A correlation was established between the surface roughness of the coating, the quality class of their appearance, and the fractal dimension. This makes it possible to use the fractal dimension as an objective criterion for assessing the surface quality of paint and varnish coatings and determining their appearance class.
5. A model is proposed that allows one to calculate the fractal dimension of a coating surface based on data on the length of the surface profile and other parameters. Numerical values of the index of the fractal dimension of the coating surface profile are obtained depending on the porosity of the substrate. This makes it possible to determine the optimal parameters of paints and varnishes and their application technologies to obtain coatings with the required level of quality.
6. To ensure the quality of paint and varnish coatings of building products and structures, it is necessary to take into account the porosity of the cement base and select the appropriate type of paint and varnish material. The results obtained can be used in various industries to improve the quality of paint and varnish coatings. For example, not only in the construction industry, but also in the automotive industry, furniture production and other areas where paint and varnish coatings are used.

5. Prospects for further development of the topic

Consideration of interdisciplinary approaches can lead to new ideas and solutions in the field of building materials science and the production of paints and varnishes. However, the possible environmental and economic consequences of the use of natural and man-made resources in these processes should be taken into account. More research is needed in this area to determine the effectiveness and safety of such approaches. The algorithm used in the article can be useful in the development of composite finishing coatings for building materials. This can help expand the range of production of building materials and improve a comfortable human environment in architectural design and production of composites.

References

1. Danish, A., Mosaberpanah, M.A., Salim, M.U., Fediuk, R., Rashid, M.F., Waqas, R.M. Reusing marble and granite dust as cement replacement in cementitious composites: A review on sustainability benefits and critical challenges. *Journal of Building Engineering*. 2021. 44, 102600. DOI: 10.1016/j.jobe.2021.102600
2. Guo, M.Z., Maury-Ramirez, A., Poon, C.S. Self-cleaning ability of titanium dioxide clear paint coated architectural mortar and its potential in field application. *Journal of Cleaner Production*. 2016. 112(14). Pp. 3583–3588. DOI: 10.1016/j.jclepro.2015.10.079
3. Hamard, E., Morel, J.C., Salgado, F., Marcom, A., Meunier, N. A procedure to assess the suitability of plaster to protect vernacular earthen architecture. *Journal of Cultural Heritage*. 2013. 14(2). Pp. 109–115. DOI: 10.1016/j.culher.2012.04.005
4. Loganina, V.I., Kisilitsyna, S.N., Mazhitov, Y.B. Development of Sol-Silicate Composition for Decoration of Building Walls. *Case Studies in Construction Materials*. 2018. 9. e00173. DOI: 10.1016/j.cscm.2018.e00173
5. D'Armada, P., Hirst, E. Nano-lime for consolidation of plaster and stone. *Journal of Architectural Conservation*. 2012. 18(1). Pp. 63–80. DOI: 10.1080/13556207.2012.10785104
6. Varepo, L.G., Nagornova, I.V., Trapeznikova, O.V. Application of electron microscopy method for quality control of paint coating surface. *Procedia Engineering*. 2015. 113. Pp. 357–361. DOI: 10.1016/j.proeng.2015.07.283
7. Zhong, X., Burke, M.G., Withers, P.J., Zhang, X., Zhou, X., Burnett, T.L., Liu, Y., Lyon, S.B., Gibbon, S.R. Multi-modal plasma focused ion beam serial section tomography of an organic paint coating. *Ultramicroscopy*. 2019. 197. Pp. 1–10. DOI: 10.1016/j.ultramicro.2018.10.003
8. Oliveira, C.G.; Ferreira, M.G.S. Ranking High-Quality Paint Systems Using EIS. Part I: Intact Coatings. *Corrosion Science*. 2003. 45(1). Pp. 123–138. DOI: 10.1016/S0010-938X(02)00088-4
9. Oliveira, C.; Ferreira, M.G.. Ranking High-Quality Paint Systems Using EIS. Part II: Defective Coatings. *Corrosion Science*. 2003. 45(1). Pp. 139–147. DOI: 10.1016/S0010-938X(02)00089-6
10. Quevauviller, P. Certified reference materials for the quality control of inorganic analyses of manufactured products (glass, polymers, paint coatings). *TrAC Trends in Analytical Chemistry*. 2001. 20(8). Pp. 446–456. DOI: 10.1016/S0165-9936(01)00090-5
11. Zhou, X., Gao, Z., Wang, X., Wang, F. Mathematical model for characterizing the full process of volatile organic compound emissions from paint film coating on porous substrates. *Building and Environment*. 2020. 182. 107062. DOI: 10.1016/j.buildenv.2020.107062
12. Aktas, B., Usta, O., Atlar, M. Systematic investigation of coating application methods and soft paint types to detect cavitation erosion on marine propellers. *Applied Ocean Research*. 2020. 94. 101868. DOI: 10.1016/j.apor.2019.101868

13. Tanzim, F., Kontos, E., White, D. Generating Prediction Model of Fan Width by Optimizing Paint Application Process for Electrostatic Rotary Bell Atomizer. Results in Engineering. 2022. 13. 100302. DOI: 10.1016/j.rineng.2021.100302
14. Kharun, M., Klyuev, S., Koroteev, D., Chiadighikaobi, P.C., Fediuk, R., Olisov, A., Vatin, N., Alfimova, N. Heat treatment of basalt fiber reinforced expanded clay concrete with increased strength for cast-in-situ construction. Fibers. 2020. 8 (11). 0067, Pp. 1 – 16. DOI: 10.3390/fib8110067
15. Loganina, V.I. The influence of surface quality of coatings on their deformation properties. Contemporary Engineering Sciences. 2014. 7. Pp. 1935–1941. DOI: 10.12988/ces.2014.411241
16. Loganina, V.I., Makarova, L.V., Tarasov, R.V. Method of assessment quality protective and decorative coating concrete cement. Case Stud. Case Studies in Construction Materials. 2016. 4. Pp. 81–84. DOI: 10.1016/j.cscm.2016.01.003
17. Wang, L., Jin, M., Wu, Y., Zhou, Y., Tang, S. Hydration, shrinkage, pore structure and fractal dimension of silica fume modified low heat portland cement-based materials. Construction and Building Materials. 2021. 272. DOI: 10.1016/j.conbuildmat.2020.121952
18. Tang, S., Huang, J., Duan, L., Yu, P., Chen, E. A review on fractal footprint of cement-based materials. Powder Technology. 2020. 370. Pp. 237–250. DOI: 10.1016/j.powtec.2020.05.065
19. Li, Y., Zhang, H., Huang, M., Yin, H., Jiang, K., Xiao, K., Tang, S. Influence of different alkali sulfates on the shrinkage, hydration, pore structure, fractal dimension and microstructure of low-heat portland cement, medium-heat portland cement and ordinary portland cement. Fractal and Fractional. 2021. 5(3). 79. DOI: 10.3390/fractalfrac5030079
20. Lü, Q., Qiu, Q., Zheng, J., Wang, J., Zeng, Q. Fractal dimension of concrete incorporating silica fume and its correlations to pore structure, strength and permeability. Construction and Building Materials. 2019. 228. 116986. DOI: 10.1016/j.conbuildmat.2019.116986.
21. Matveeva, O.I., Baishev, N.K., Makarov, A.I., Popov, A.L., Pavlyukova, I.R., Grigoriev, N.A. Enhancing lightweight concrete strength through modified zeolite-alkaline porous aggregate: composition optimization and structural application. Magazine of Civil Engineering. 2024. 17(1). Article no. 12507. DOI: 10.34910/MCE.125.7
22. Wang, L., Luo, R., Zhang, W., Jin, M., Tang, S. Effects of fineness and content of phosphorus slag on cement hydration, permeability, pore structure and fractal dimension of concrete. Fractals. 2021. 29(02). 2140004. DOI: 10.1142/S0218348X21400041
23. Luan, C., Wang, J., Gao, J., Wang, J., Du, P., Zhou, Z., Huang, Y., Du, S. Changes in Fractal Dimension and Durability of Ultra-High Performance Concrete (UHPC) with Silica Fume Content. Archives of Civil and Mechanical Engineering. 2022. 22. 123. DOI: 10.1007/s43452-022-00443-3
24. Usanova, K., Barabanshchikov, Yu.G., Dixit, S. Cementless binder based on high-calcium fly ash with calcium nitrate additive. Magazine of Civil Engineering. 2023. 124(8). Article no. 12405. DOI: 10.34910/MCE.124.5
25. Bessmertnyi, V.S., Lesovik, V.S., Krokhin, V.P. The Reducing Effect of Argon in the Plasma Treatment of High-Melting Nonmetallic Materials (a Review). Glass and Ceramics. 2001. 58. Pp. 362–364. DOI: 10.1023/A:1013963916418
26. Jin, S., Zhang, J., Han, S. Fractal analysis of relation between strength and pore structure of hardened mortar. Construction and Building Materials. 2017. 135. Pp. 1–7. DOI: 10.1016/j.conbuildmat.2016.12.152
27. Neimark, A. A new approach to the determination of the surface fractal dimension of porous solids. Physica A: Statistical Mechanics and its Applications. 1992. 191. Pp. 258–262. DOI: 10.1016/0378-4371(92)90536-Y
28. Takada, T., Ushiomura, R., Fushiki, T. Fractal dimensional analysis on dispersion/aggregation state of MWCNT in poly(4-chloromethyl)styrene: effect of UV-induced polymer-MWCNT chemical bond formation and its influence on electrical conductivity of their composites. International Journal of Polymer Analysis and Characterization. 2020. 25. Pp. 252–261. DOI: 10.1080/1023666X.2020.1783079
29. Živić, I., Elezović-Hadžić, S., Milošević, S. Self-Interacting Polymer Chains Terminally Anchored to Adsorbing Surfaces of Three-Dimensional Fractal Lattices. Physica A: Statistical Mechanics and its Applications. 2018. 490. Pp. 732–744. DOI: 10.1016/j.physa.2017.08.154
30. Li, Y., Sun, X., Zhang, S., Han, S. A fractal crazing constitutive model of glassy polymers considering damage and toughening. Engineering Fracture Mechanics. 2022. 267. 108354. DOI: 10.1016/j.engfracmech.2022.108354
31. Marquardt, T.; Momber, A.W.; Kelm, D. Fractal Dimensions of Blast-Cleaned Steel Surfaces and Their Effects on the Adhesion of Polymeric Foil Systems with Integrated Pressure-Sensitive Adhesives. International Journal of Adhesion and Adhesives. 2022. 118. 103198. DOI: 10.1016/j.ijadhadh.2022.103198
32. Pandey, I., Chandra, A. Effect of Thermal Degradation of Polymer on Redox Initiated Fractal Geometries. Chemical Physics Impact. 2021. 3. 100028. DOI: 10.1016/j.chphi.2021.100028
33. Atangana, A. Fractal-fractional differentiation and integration: connecting fractal calculus and fractional calculus to predict complex system. Chaos, Solitons & Fractals. 2017. 102. Pp. 396–406. DOI: 10.1016/j.chaos.2017.04.027
34. Li, Y., Yang, H., Sun, S. Unveiling the mystery of scale dependence of surface roughness of natural rock joints. Scientific Reports. 2022. 12. 1013. DOI: 10.1038/s41598-022-04935-3
35. Miao, X., Huang, X. A complete contact model of a fractal rough surface. Wear. 2014. 309. Pp. 146–151. DOI: 10.1016/j.wear.2013.10.014
36. Shi, X., Zou, Y. A comparative study on equivalent modeling of rough surfaces contact. Journal of Tribology. 2018. 140. DOI: 10.1115/1.4039231
37. Lesnichenko, E.N., Chernysheva, N.V., Drebezgova, M.Yu., Kovalenko, E.V., Bocharnikov, A.L. Development of a multicomponent gypsum cement binder using the method of mathematical planning of the experiment. Construction Materials and Products. 2022. 5(2). Pp. 5–12. DOI: 10.58224/2618-7183-2022-5-2-5-12
38. Fediuk, R.; Yushin, A. Composite binders for concrete with reduced permeability. IOP Conference Series-Materials Science and Engineering. 2016. 116. 012021. DOI 10.1088/1757-899X/116/1/012021
39. Makhortov, D.S., Zagorodnyuk, L.H., Sumskey, D.A. Binder compositions based on Portland cement and volcanic ash. Construction Materials and Products. 2022. 5(4). Pp. 30–38. DOI: 10.58224/2618-7183-2022-5-4-30-38
40. Fediuk, R., Smoliakov, A., Stoyushko, N. Increase in composite binder activity. IOP Conference Series: Materials Science and Engineering. 2016. 156(1). 012042. DOI: 10.1088/1757-899X/156/1/012042.
41. Amran, M; Abdelgader, HS; Onaizi, AM; Fediuk, R; Ozbakkaloglu, T; Rashid, RSM ; Murali, G. 3D-printable alkali-activated concretes for building applications: A critical review. 2021. 319. 126126. DOI: 10.1016/j.conbuildmat.2021.126126

42. Petrov A.M., Magomedov R.M., Savina S.V. Ecological safety of construction in the concept of sustainable development. Construction Materials and Products. 2023. 6(1). Pp. 5–17. DOI: 10.58224/2618-7183-2023-6-1-5-17
43. Klyuev S.V., Kashapov N.F., Radaykin O.V., Sabitov L.S., Klyuev A.V., Shchekina N.A. Reliability coefficient for fibreconcrete material. Construction Materials and Products. 2022. 5(2). Pp. 51–58. DOI: 10.58224/2618-7183-2022-5-2-51-58
44. Strelkov, Yu.M., Sabitov, L.S., Klyuev, S.V., Klyuev, A.V., Radaykin, O.V., Tokareva, L.A. Technological features of the construction of a demountable foundation for tower structures. Construction Materials and Products. 2022. 5(3). Pp. 17–26. DOI: 10.58224/2618-7183-2022-5-3-17-26

Information about authors:

Valentina Loganina, Doctor of Technical Sciences
ORCID: <https://orcid.org/0000-0001-7532-0074>
E-mail: loganin@mail.ru

Roman Fediuk, Doctor of Technical Sciences
ORCID: <https://orcid.org/0000-0002-2279-1240>
E-mail: roman44@yandex.ru

Valeriy Lesovik, Doctor of Technical Sciences
ORCID: <https://orcid.org/0000-0002-2378-3947>
E-mail: naukavs@mail.ru

Sergey Klyuev, Doctor of Technical Sciences
ORCID: <https://orcid.org/0000-0002-1995-6139>
E-mail: Klyuyev@yandex.ru

Linar Sabitov,
E-mail: sabitov-kgasu@mail.ru

Maksim Lomov,
E-mail: gera21030@yandex.ru

Svetlana Vavrenyuk, Doctor of Technical Sciences
E-mail: trusanova2014@mail.ru

Ivan Vykhodtsev,
E-mail: vykhodtsev.ia@dvfu.ru

Received 28.10.2022. Approved after reviewing 03.03.2023. Accepted 04.03.2023.



Research article

UDC 69.04

DOI: 10.34910/MCE.126.9



Elastic local buckling of trapezoidal plates under linear stress gradients

S. Yehia  , R. Shahin 

Higher Institute of Engineering and Technology, Kafrelsheikh, Egypt

✉ saadyhy81@gmail.com

Keywords: trapezoidal plate, tapered plate, plate buckling, elastic local buckling, stress gradient

Abstract. Steel plates play a pivotal role in the construction of different types of structures used in civil engineering. According to Eurocode 3, plated structures may be designed using three different approaches: the effective width method, the reduced stress method, and the finite element analysis. For the particular case of elements under stress gradients, the effective width method utilises the local buckling coefficient of a plate to calculate the effective cross-sectional area for structural elements. Since the effective width method was developed for uniform web and flange panels, Eurocode 3 and most design codes have no specific provisions for the particular case of non-rectangular panels, stating that they may conservatively be treated as rectangular panels with larger width. With the final objective of improving design rules for tapered members, this paper presented an extensive numerical analysis to evaluate the elastic local buckling behaviour of trapezoidal plates with simply supported end conditions under stress gradients. The study identifies the relative importance of several parameters that influence the local buckling coefficient, such as the tapering ratio of the panel, normalized plate length, and stress ratio. Numerical results are used to propose approximate closed-form expressions that can be used to compute the local buckling coefficient for trapezoidal plates in a direct way. The results show that the proposed formula offers a significant improvement over current Eurocode 3 and most design codes.

Citation: Yehia, S., Shahin, R. Elastic local buckling of trapezoidal plates under linear stress gradients. Magazine of Civil Engineering. 2024. 17(2). Article no. 12609. DOI: 10.34910/MCE.126.9

1. Introduction

Non-uniform members, including trapezoidal steel plates, are widely used in engineering areas such as structural, mechanical, and aeronautical engineering, as shown in Fig. (1). Lee and Morrell [1] affirm that the use of tapered members saved an amount of material compared with rolled plate, and it was first proposed for economic reasons by Amirikian [2]. As it is well known, Eurocode EN-3-1-5 [3] provides three general procedures that can be used when dealing with plate buckling. These procedures are the effective width method, the reduced stress method and finite element analysis. For the case of elements under stress gradients, a reduction factor is utilised for the compressed area in order to calculate the effective width to determine the compression stress in the cross section. Moreover, this reduction factor is a function of the plate aspect ratio and the local buckling coefficient. However, Eurocode 3 only provides a single provision for tapered plates; it suggests that general design rules may be applied by assuming that the panel is rectangular with the maximum width. This means that there are no specific provisions or recommendations for the design of tapered plates in Eurocode 3 beyond this general guidance. Hence, the importance of studying elastic local buckling of tapered plates becomes apparent, which relies on several factors such as plate geometry and boundary conditions to compute the effective width of a slender cross section.



Figure 1. Trapezoidal plates in industrial buildings [4].

Based on the previous researches, the analysis of plate buckling is widely studied in various fields of engineering, such as civil and structural engineering, mechanical engineering, aerospace engineering, marine engineering, etc. It is a vital topic that finds usage in a wide range of structural designs, and other engineering applications, particularly when a lightweight design is the main objective [5]. Plate buckling occurs when a compressive load causes a sudden deflection of the plate, which leads to compressive stress exceeding a critical limit, resulting in the failure of the structure. The failure mode caused by plate buckling is often accompanied by large deflections and sudden structural failure [6, 7]. The origin and analysis of plate buckling are difficult to interpret due to the governing equations being high-order partial differential equations. This makes it challenging to accurately predict and prevent the failure of structures due to plate buckling [8, 9].

On the other hand, the critical local buckling of plates has been extensively studied using a combination of experimental, numerical, and analytical methods in many important investigations. These methods have contributed to identifying the factors affecting buckling failure and developing solutions to prevent it, considering various plate geometries, restraint conditions, loading scenarios, and material properties. A pioneering theoretical study on the buckling of tapered plates under uniform compressive loading was proposed by Pope [10]. Šapalás [11] studied the local tapered web stability under pure bending moment using a theoretical and finite element analysis utilising a COSMOS FEM code. Additionally, he conducted a thorough simulation using a large domain of the second-moment area ratio to calculate a critical load multiplier and investigate the effects of relative slenderness, steel grade, and moment of inertia of beam-ends on the local stability of tapered beams. On the experimental side, one of the initial references to the plate buckling effect on the failure of tapered members was presented by Prawel et al. [12]. Ibrahim et al. [13] conducted an experimental program utilizing three specimens to investigate the axial compressive strength of a prismatic, unstiffened, slender tapered steel web.

Numerical methods have been used with profusion in the past to determine buckling loads of non-rectangular plates, particularly for skew plates [14–16]. Saadatpour et al. [17, 18] make use of Galerkin and Rayleigh-Ritz methods for the analysis of arbitrary quadrilateral plates with arbitrary boundary conditions. Differential quadrature methodology for stability analysis of straight-sided quadrilateral plates has also been employed by Karami and Malekzadeh [19], Civalek [20], and Wang et al. [21]. Eid [22] presented the analysis of a thin tapered plate using the finite difference method. Moreover, he proposed a numerical expression of the thin plates bending under a randomly distributed lateral load. Lkhenazen et al. [23] presented a buckling analysis of an isotropic plate that was subjected to in-plane patch loading. Diez et al. [4] developed a numerical analysis of trapezoidal plates subjected to uniform compression with four different boundary ends to propose a closed formula to calculate the local buckling coefficient for trapezoidal plates. Abu-Hamd [24] developed an approximate empirical formula for tapered plate girders. This formula is based on the numerical results obtained from the FEM of a steel tapered web subjected to shear and moment. Kucukler et al. [25] suggested a simplified stiffness reduction method for the in-plane analysis of the tapered plates by dividing the web member into prismatic elements. Ziemian et al. [26] proposed a numerical technique to investigate lateral buckling of tapered beams, considering the effects of initial stress and load eccentricity. Moreover, Post-local buckling of skew and trapezoidal plates has been studied by Azhari and coworkers [27–29] and by Upadhyay and Shukla [30].

In recent years, the investigation in the field of composite plates has also provided significant results on the buckling behaviour of trapezoidal plates [31–33]. Finally, a new and interesting field of research has recently been proposed by Jing and coworkers [34] with their work on closed-form expressions to determine buckling loads of orthotropic plates.

In the literature, a few numerical results for elastic buckling of trapezoidal plates under stress gradients are available. Since Eurocode 3 directly relates plate ultimate strength with buckling coefficient, the main objective of this paper is to provide an extensive numerical analysis to evaluate the elastic local buckling behaviour of trapezoidal plates with simply supported end conditions under stress gradients. The study identifies the relative importance of several parameters that influence the local buckling coefficient, such as the tapering ratio of the panel, normalized plate length, and stress ratio. Numerical results are used to propose approximate closed-form expressions that can be used to compute the local buckling coefficient for trapezoidal plates in a direct way in order to compute the effective width of a slender cross section. The outcomes show that the Eurocode 3 formulas are more conservative in calculating the ultimate strength of slender trapezoidal plates.

2. Methods

2.1. Problem statement

A trapezoidal plate in a Cartesian coordinate system is given in Fig. 2. The plate has length a , a constant width h at the larger side, and a variable width h_1 at the smaller side with thickness t . The plate is subjected to linearly varying in-plane loading in the longitudinal direction, and all its edges are simply supported in the out-of-plane direction. In other words, there is no lateral edge displacement perpendicular to the plate plane on all four edges.

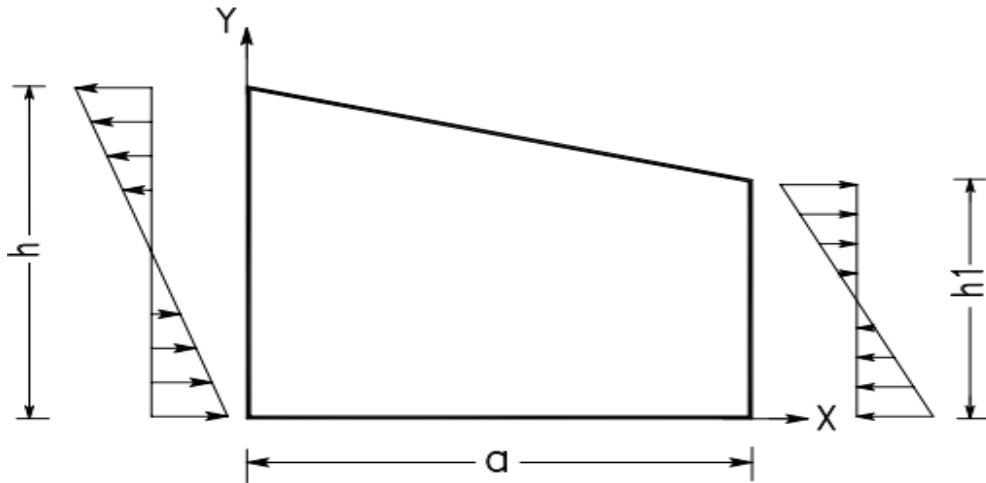


Figure 2. Geometry of a trapezoidal plate in a Cartesian coordinate system.

In the analysis of a trapezoidal plate, a linearly varying stress is applied to the two opposite simply supported edges at $x = 0$ and $x = a$, respectively. The loading conditions are as follows: case (1) has a uniform compression load with $\psi = 1$, case (2) has a trapezoidal load with $\psi = 2/3$, case (3) has a trapezoidal load with $\psi = 1/3$, case (4) has a triangular load with $\psi = 0$, case (5) has a unequal reverse triangular load with $\psi = -1/3$, case (6) has a unequal reverse triangular load with $\psi = -2/3$, and case (7) has a pure bending load with $\psi = -1$. For all compression and bending cases, nodal force is applied and divided according to different ψ ratios. Where ψ is the stress ratio (stress gradients) between minimum and maximum compressive stresses ($\psi = \sigma_2/\sigma_1$) as shown in Fig. 3.

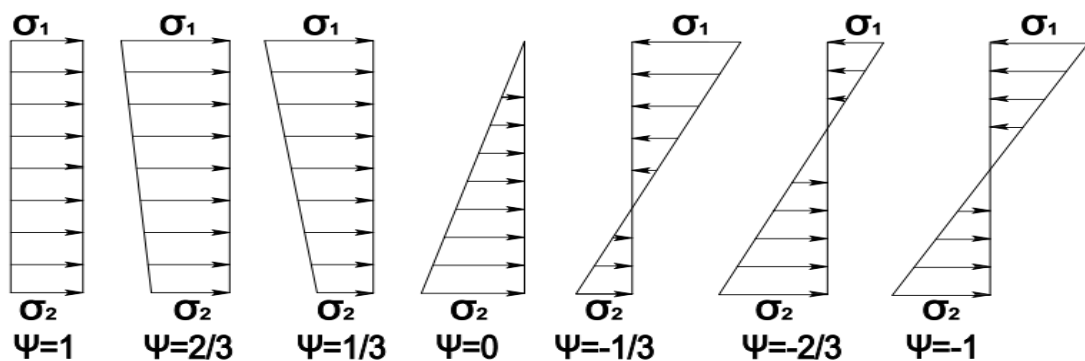


Figure 3. Example of in-plane loading conditions at $x = 0$ and $x = a$.

2.2. Finite element analysis procedure

For all study cases, the following steps were followed to develop predictive models:

1. Choosing the inputs that may affect the critical buckling coefficient;
2. The FE analysis using the ANSYS software [35] is used to execute an eigenvalue analysis to estimate the critical buckling load under normal and bending stresses. The program outputs are verified with well-known theoretical values;
3. The elastic buckling coefficient is determined for each by using Timoshenko's formula [36];
4. Construct the relations between the input variables and the predicted local buckling coefficient;
5. Conducting a regression analysis to generate predictive formulas for design purposes.

2.2.1 Influencing parameters

Based on the literature reviews [4, 37, 38], the fundamental parameters governing the predicted buckling coefficient are identified as the tapering ratio $R = h/h_1$, the normalized plate length ratio ($\alpha = a/h$) the stress ratio between min. and max. compressive stresses ($\psi = \sigma_2/\sigma_1$) and boundary conditions according to Mirambell et al. [39], the influence of the web depth-to-thickness ratio h/t_w is not significant, so the influence of this geometric parameter is ignored in this study. The parameter ranges and increments are shown in Table 1. The tapering ratio R ranges from 1 to 8, the normalized plate length α ranges from 0.25 to 8, and the stress gradients $\psi = \sigma_2/\sigma_1$ equal 1,2/3, 1/3,0, -1/3, -2/3, and -1 for compression and bending cases. The steel is modelled as a linearly elastic-perfectly plastic material with a Poisson ratio $\nu = 0.30$ and a modulus of elasticity $E = 200$ GPa.

Table 1. Different geometric parameter ranges and their increments.

Studied Parameter	Used parameter values for trapezoidal plate	
	Compression and bending cases	
Tapering ratio $R = h/h_1$	1, 1.25,1.5,1.75,2,2.25,2.5,2.75,3,4,5,6,8	
Normalized plate length $\alpha = a/h$	0.25, 0.30,0.35,0.4,0.45,0.5, 0.55, 0.60, 0.65, 0.70, 0.75, 0.80,0.85,0.90,0.95	
	1.00, 1.05, 1.10,1.15,1.20, 1.25,1.30, 1.35,1.40,1.45, 1.50,1.55,1.60,1.65,1.70 1.75,1.80,1.85,1.90,1.95,2.00,2.25,2.50,2.75,3.00,3.25,3.50,3.75,4,6,7,8	
Stress gradients $\psi = \sigma_2/\sigma_1$	1,2/3,1/3,0, -1/3, -2/3, and -1	

2.2.2 Linear buckling analysis

Finite element analysis is performed using ANSYS engineering simulation software [35] with a shell element to calculate the critical buckling load. A four-node shell element (SHELL181), as shown in Fig. 4, is employed to model the tapered plate, which has six degrees of freedom at each node: translations in the x, y, and z directions and rotations about the x, y, and z-axes. In addition, SHELL181 is suitable for modelling thin to moderately thick shell structures, which enables explicit simulation of various buckling deformations. Buckling loads are obtained from eigenvalue analysis. Eigenvalue buckling analysis is also known as linear buckling analysis, where the buckling load can be estimated by using the next equation [40].

$$([K_o] + \lambda[K_\sigma])\{U\} = 0, \quad (1)$$

where K_o and K_σ is the linear stiffness matrix and the geometric stiffness matrix, respectively; λ is the load scaling factor; $\{U\}$ is the lateral displacement vector. From Eq.1, it is clear that the structure's linear stability problem is the eigenvalue problem. By solving the eigenvalue and eigenvector problems, the critical load and buckling mode shape can be determined.

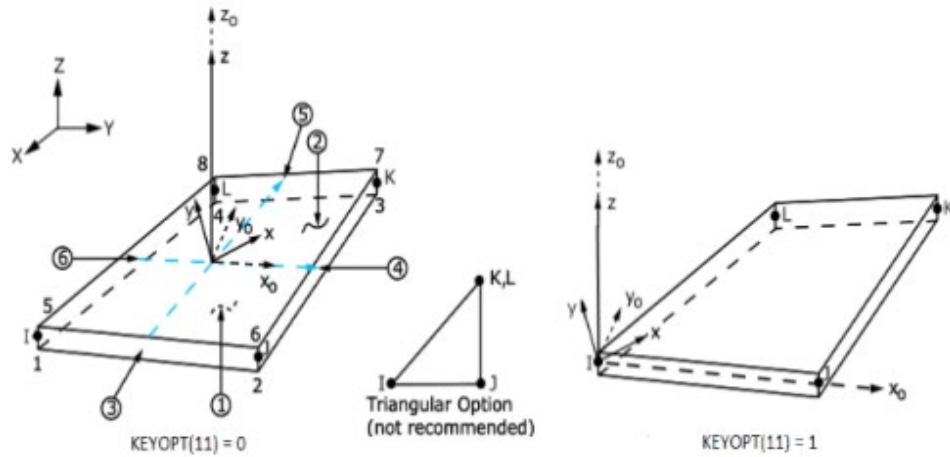


Figure 4. SHELL181 Geometry [41].

2.2.3 Validation of finite element model

To guarantee the finite element model's accuracy, a convergence test on mesh size was carried out employing a reference to the exact theoretical values of the local buckling coefficient for simply supported rectangular plates ($R = 1$) [38]. The mesh size is equal to 25×25 mm for all loading cases. Table 2 provides the percentage error between the FEM and the exact theoretical values of the local buckling coefficient. The normalized plate length ranged between 1 and 5. The last column of the table presents the error percentage, which varies from 0.10 % to 6.14 %. The comparison shows that the proposed boundary condition was well defined, and the results from FEM are reasonable.

Table 2. Numerical and theoretical results of the critical buckling coefficient for tapered web plates with a tapering ratio ($R = 1.00$).

Loading Conditions	Normalized plate length $\alpha = a/h$	Theoretical results Pekoz [38]	FEM results	Error %
Case (1) ($\Psi = 1$)	1	4.00	3.91	2.25
	2	4.00	3.947	1.325
	3	4.00	3.96	1.00
	4	4.00	3.967	0.825
	5	4.00	3.97	0.750
Case (2) ($\Psi = 1/3$)	1	5.925	5.88	0.759
	2	5.925	5.90	0.422
	3	5.925	5.91	0.253
	4	5.925	5.916	0.152
	5	5.925	5.919	0.10
Case (3) ($\Psi = 0$)	1	8.00	7.67	4.125
	2	8.00	7.70	3.75
	3	8.00	7.71	3.625
	4	8.00	7.723	3.465
	5	8.00	7.726	3.425
Case (4) ($\Psi = -1/3$)	1	11.40	10.710	6.00
	2	11.40	10.745	5.70
	3	11.40	10.758	5.63
	4	11.40	10.760	5.63
	5	11.40	10.758	5.63
Case (5) ($\Psi = -2/3$)	1	16.59	16.00	3.55
	2	16.59	15.88	4.28
	3	16.59	15.63	5.78
	4	16.59	15.57	6.14
	5	16.59	15.57	6.14

Loading Conditions	Normalized plate length $\alpha = a/h$	Theoretical results Pekoz [38]	FEM results	Error %
Case (6) ($\Psi = -1$)	1	24.00	25.20	5.00
	2	24.00	23.87	0.54
	3	24.00	23.92	0.33
	4	24.00	23.82	0.75
	5	24.00	23.83	0.70

3. Results and Discussion

By using the validated FE model, the parametric study, which involved more than 4500 FE models, was carried out for compression and bending loading cases to investigate the influence of different parameters on the local buckling coefficient of trapezoidal plates [26]. The lowest deformed mode shapes of a trapezoidal plate for all compression and bending cases with simply supported boundary conditions are shown in Fig. 5.

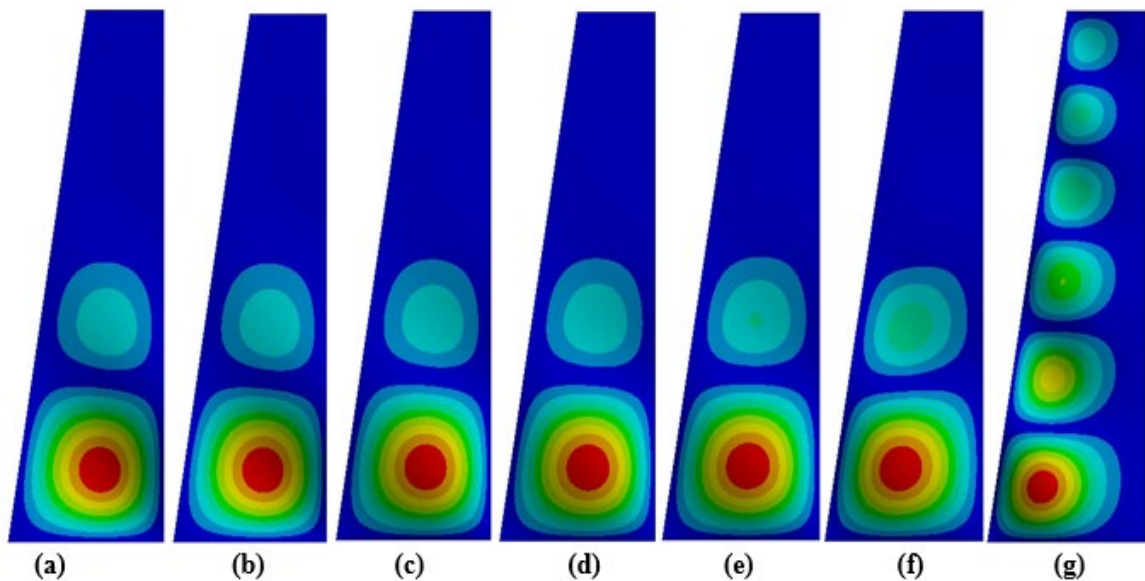


Figure 5. The lowest buckling mode shapes of trapezoidal plates for different loading cases: a) case (1) ($\Psi = 1$) b) case (2) ($\Psi = 2/3$) c) case (3) ($\Psi = 1/3$) d) case (4) ($\Psi = \text{Zero}$) e) case (5) ($\Psi = -1/3$) f) case (6) ($\Psi = -2/3$) g) case (7) ($\Psi = -1$) respectively.

Fig. 6 displays the relationship between the plate buckling coefficient and normalized plate length (α) for several tapering ratios (R) for different loading cases. It can be observed when the normalized plate length (α) is more than 1.00; the K values reduce with increasing (α) and R values. For α less than 1.00, buckling behaviour is exactly the opposite, where k values increase with decrease α and decrease with increase R because the buckling waves are shorter when α values less than 1.00 compared with values more than 1.00. Moreover, for all R values, K declines with increases α up to 5.00, at which point the rate of decrease sharply declines. Typically, the applied stress along the loaded edges of plates ranges from uniform compression case to pure bending moment case. The uniform compression case is considered the most critical loading, and it has the lowest elastic local buckling stress. It can be noted that if the condition $\sigma_1 > 0$ is not satisfied, local buckling will not happen because the plate is subjected to only tension stress [42].

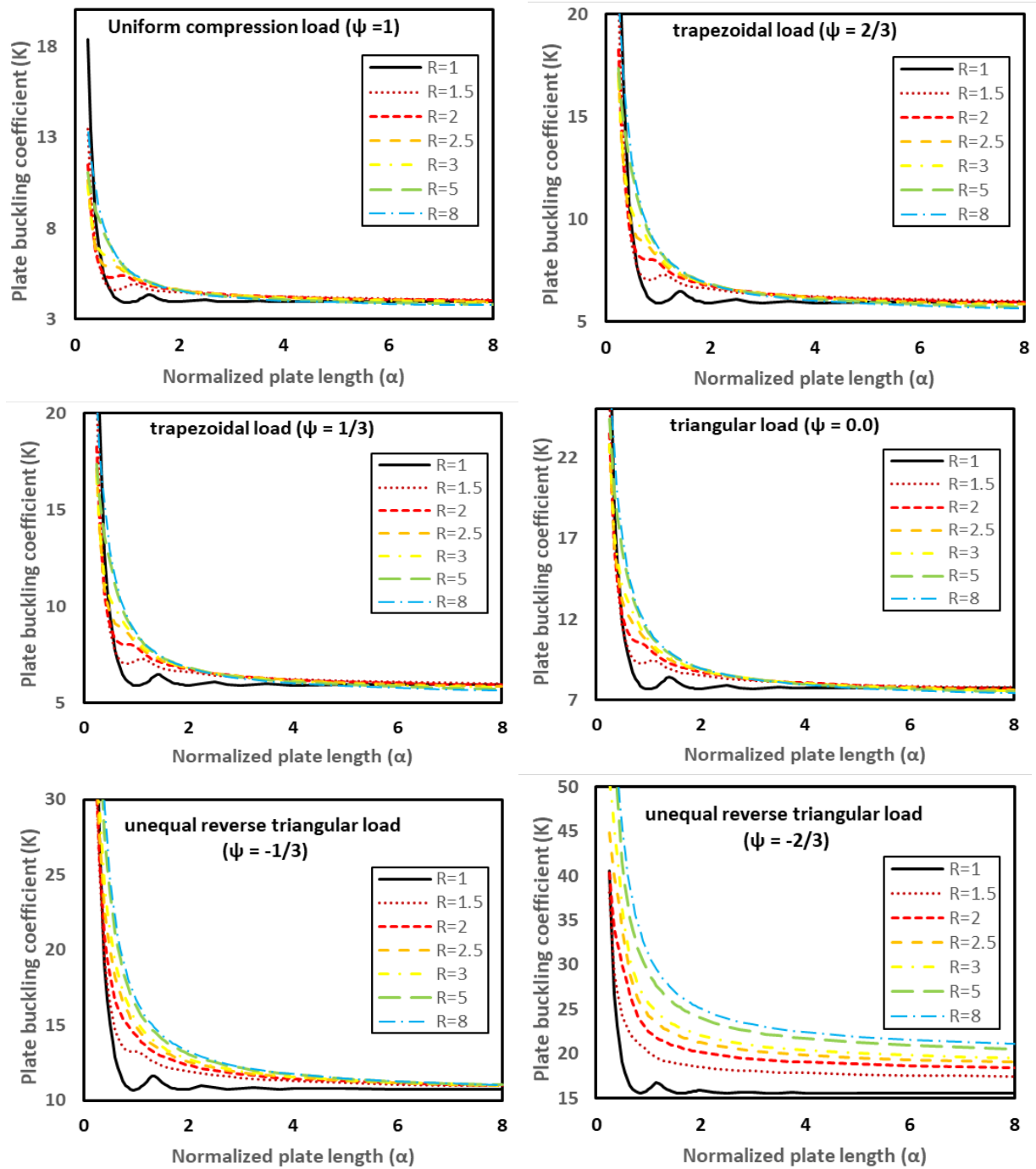


Figure 6. Plate buckling coefficient against normalized plate length (α) for several tapering ratios (R) for case (1) (ψ = 1), case (2) (ψ = 2/3), case (3) (ψ = 1/3), case (4) (ψ = 0), case (5) (ψ = -1/3), and case (6) (ψ = -2/3) respectively.

Fig. 7 presents the relationship between the plate buckling coefficient and normalized plate length (α) for several tapering ratios (R) for the pure bending load (ψ = -1). It can be observed that when the normalized plate length (α) is greater than 2.00, the predicted plate buckling coefficient values for all tapering ratios (R) tend to reach 23.90 for simply supported edges. For the range of α < 2.00 (hatched in Fig. 7), the critical buckling coefficient k values are noticeably lower than expected, especially for higher tapering ratios. Because the interaction with the induced shear stresses developed by additional shear force results from the vertical component of the flange force [43], so, it can be ignoring these deviations because they aren't in the practical application domain of these tapered plates.

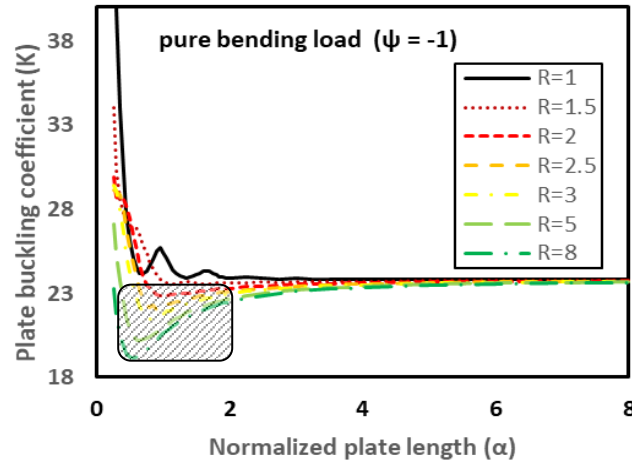


Figure 7. Plate buckling coefficient of pure bending load ($\psi = -1$) against normalized plate length (α) for several tapering ratios (R).

3.1. Proposed formulas for the elastic local buckling coefficients of trapezoidal plates under stress gradients

Regression analysis is employed for the output results to propose a prediction formula to calculate the critical buckling coefficient of trapezoidal plate subjected to compression and bending cases. Regression analysis with MATLAB is performed to estimate the relation between the output (K) and inputs, including stress ratio (ψ), normalized length (α), and tapering ratios (R). Moreover, regression analysis can measure the validity of predicted values with the actual dataset using many tools, such as the coefficient of correlation (R), mean square error (MSE), and standard deviation (SD).

Eqs. (2) to (4) show the elastic local buckling coefficient formulas for trapezoidal plates under stress gradients.

For case (1) [uniform compression load ($\psi = 1.00$)].

$$K_{UC} = 6.31 + \frac{0.87}{\alpha^{1.53}} - \frac{2.81}{R^{0.28}} - \frac{0.29}{\alpha R}, \quad (2)$$

where K_{UC} is the elastic local buckling coefficient of a uniform compression load with $\psi = 1.00$.

For case (2) to case (6) [compression and bending cases ($1.00 < \psi < -1.00$)].

$$K_{CB} = 1 + 1.82K_{UC} - 5.75\psi - 0.82K_{UC}\psi + 4.75\psi^2, \quad (3)$$

where K_{CB} is the elastic local buckling coefficient of a compression and bending cases with $1.00 < \psi < -1.00$.

For case (7) [pure bending load ($\psi = -1.00$)]

$$K_{PB} = 23.90, \quad (4)$$

where, K_{PB} is the elastic local buckling coefficient of a pure bending load with $\psi = -1.00$.

3.2. Validation of Proposed Formulas

The proposed formulas for the elastic buckling coefficient of trapezoidal plates are verified with FE results. Fig. 8 compares the predicted local buckling coefficient from the proposed formula K_{UC} with the actual local buckling coefficient from the FE modeling for a uniform compression load ($\psi = 1.00$). The mean (μ) and standard deviation (σ) for the ratio $K_{FE}/K_{Prop.}$ are 1.00 and 0.09, respectively, where

the mean is the average of two or more numbers. The standard deviation is a statistical parameter that measures the dispersion of a set of numbers from its mean. The standard deviation is defined as:

$$\sigma = \sqrt{\frac{\sum_{i=1}^n (y_i - \bar{y})^2}{n-1}}, \quad (5)$$

where n is the total number of data set, y_i is data point and \bar{y} is the average of the data set.

The coefficient of determination $R^2 = 0.988$ indicates a very strong fit since it is close to 1. In general, good predictions of the elastic buckling coefficient were obtained from the proposed formula.

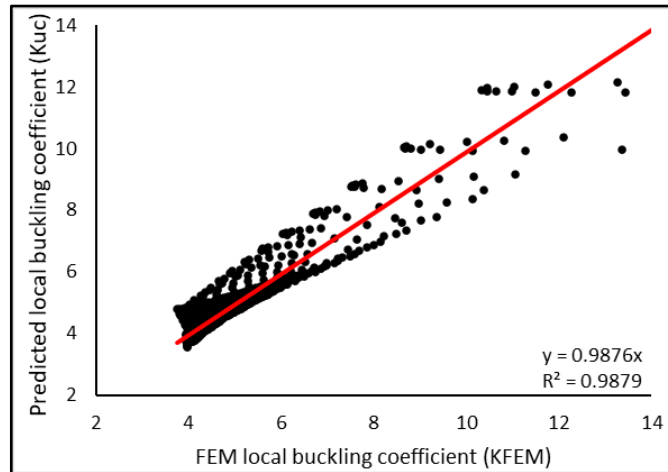


Figure 8. Validating the predicted local buckling coefficient from the proposed formula K_{UC} against the actual local buckling coefficient from the FE modelling for uniform compression load ($\psi = 1.00$).

Fig. 9 presents the comparison between the predicted local buckling coefficient from the proposed formula K_{CB} and the actual local buckling coefficient from the FE modelling for compression and bending cases ($1.00 < \psi < -1.00$). The majority of predicted values for different subsets exhibit a favourable and robust ability to forecast, as they mostly fall within an error range of -20% to $+20\%$, and predictions with an error exceeding 20% tend to fall in the underestimate region, indicating a safer outcome. The mean (μ) and standard deviation (σ) for the ratio K_{FE} / K_{Prop} , are 1.04 and 0.145, respectively. The

coefficient of determination $R^2 = 0.95$ indicates a very strong fit since it is close to 1. In general, good predictions of the elastic buckling coefficient were obtained from the proposed formula.

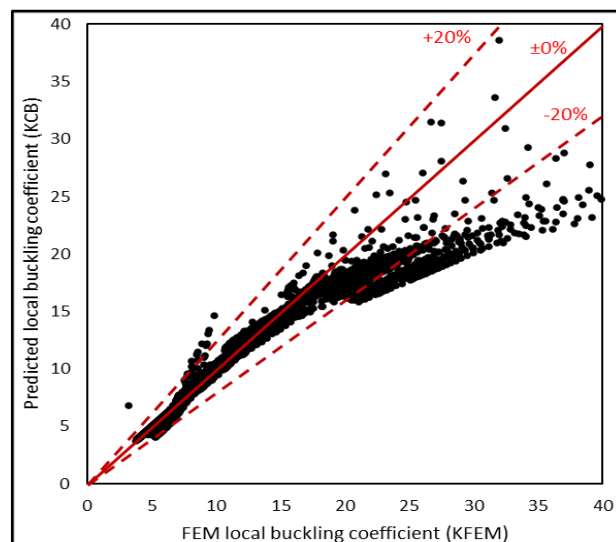


Figure 9. Validating the predicated local buckling coefficient from the proposed formula K_{CB} against the actual local buckling coefficient from the FE modelling for compression and bending cases ($1.00 < \psi < -1.00$).

3.3. Comparison with previous studies

The elastic local buckling coefficient obtained from the proposed formula for a uniform compression load case (Eq. (2)) was compared with the buckling coefficient predicted by Diez et al.[4]. Diez et al. provides the following formulas to estimate the elastic buckling coefficient of trapezoidal plates under a uniform compression load case. The closed-form expression does not give a value for buckling coefficient of trapezoidal plates as a function of R , α , and θ . It provides approximations to minimum and stationary values of buckling coefficient as a function of plate angle θ .

$$\bar{k}_{T_{min}} = 4(1 + \tan \theta); \quad (6)$$

$$\bar{k}_{T_{st}} = 4 + 7.5 \tan \theta, \quad (7)$$

where θ is plate angle, $\bar{k}_{T_{min}}$ is minimum value of buckling coefficient, $\bar{k}_{T_{st}}$ is stationary value of buckling coefficient.

Table 4 displays the comparison between the buckling coefficient obtained from the proposed formula (Eqs.2) and the buckling coefficient obtained from Diez formula for uniform compression load. For all analyses, plate width "h" is equal 1000 mm, plate thickness is equal 10 mm, stress gradients $\psi = 1$, nine values of plate tapering ratio R , and normalized plate length α range from (0.45 to 5). It can be seen that the Diez formula are conservative in calculating the buckling coefficient of trapezoidal plates under uniform compression. The mean value of the $K_{FE} / K_{Prop.}$ ratio is 1.02 with a corresponding coefficient of variation (COV) of 0.07 and the mean value of the K_{FE} / K_{Diez} ratio is 0.75 with a corresponding coefficient of variation (COV) of 0.17. In addition, it should be noted that the Diez formula is not applicable and has limitations to its use, being restricted within a certain range of conditions for normalized plate length α .

Table 4. Comparison of the buckling coefficient obtained from the proposed formula and the Diez formulas for uniform compression load case.

Group	Specimen parameters			Buckling Coefficient (K)			Comparison		
	ψ	R	α	K_{FE}	$K_{Prop.}$	K_{Diez}	$K_{FE} / K_{Prop.}$	K_{FE} / K_{Diez}	
G 1	1.00	1.00	1.00	3.91	4.66	4.00	0.84	0.98	
		1.00	1.05	3.92	4.58	4.00	0.86	0.98	
		1.00	1.10	3.95	4.52	4.00	0.87	0.99	
		1.00	1.15	3.99	4.45	4.00	0.90	1.00	
		1.00	1.20	4.05	4.40	4.00	0.92	1.01	
		1.00	1.25	4.12	4.35	4.00	0.95	1.03	
		1.00	1.30	4.20	4.31	4.00	0.97	1.05	
		1.00	1.35	4.29	4.26	4.00	1.00	1.07	
		1.00	1.40	4.37	4.23	4.00	1.03	1.09	
		1.00	1.45	4.35	4.19	4.00	1.04	1.09	
		1.00	1.50	4.27	4.16	4.00	1.03	1.07	
		-----	-----	-----	-----	-----	-----	-----	-----
		-----	-----	-----	-----	-----	-----	-----	-----
		1.00	3.50	4.02	3.71	4.00	1.08	1.01	
		1.00	3.75	3.98	3.69	4.00	1.08	1.00	
1.00	4.00	3.97	3.68	4.00	1.08	0.99			

Group	Specimen parameters			Buckling Coefficient (K)			Comparison	
	Ψ	R	α	K_{FE}	$K_{Prop.}$	K_{Diez}	$K_{FE} / K_{Prop.}$	K_{FE} / K_{Diez}
		1.00	5.00	3.97	3.63	4.00	1.09	0.99
		1.10	0.90	4.07	4.89	4.35	0.83	0.94
		1.10	0.95	4.06	4.79	4.35	0.85	0.93
		1.10	1.00	4.08	4.71	4.35	0.87	0.94
		1.10	1.05	4.11	4.63	4.35	0.89	0.95
		1.10	1.10	4.16	4.57	4.35	0.91	0.96
		1.10	1.15	4.23	4.51	4.35	0.94	0.97
		1.10	1.20	4.31	4.45	4.35	0.97	0.99
		1.10	1.25	4.39	4.40	4.35	1.00	1.01
		1.10	1.30	4.48	4.36	4.66	1.03	0.96
		1.10	1.35	4.52	4.32	4.66	1.05	0.97
		1.10	1.40	4.48	4.28	4.66	1.05	0.96
		1.10	1.45	4.41	4.25	4.66	1.04	0.95
		1.10	1.50	4.34	4.22	4.66	1.03	0.93
		-----	-----	-----	-----	-----	-----	-----
		-----	-----	-----	-----	-----	-----	-----
		1.10	3.50	4.11	3.78	4.66	1.09	0.88
		1.10	3.75	4.09	3.76	4.66	1.09	0.88
		1.10	4.00	4.09	3.74	4.66	1.09	0.88
		1.10	5.00	4.07	3.70	4.66	1.10	0.87
		1.20	0.80	4.26	5.17	4.71	0.82	0.90
		1.20	0.85	4.22	5.04	4.71	0.84	0.90
		1.20	0.90	4.21	4.93	4.71	0.85	0.89
		1.20	0.95	4.22	4.84	4.71	0.87	0.90
		1.20	1.00	4.26	4.75	4.71	0.90	0.91
		1.20	1.05	4.31	4.68	4.71	0.92	0.92
		1.20	1.10	4.39	4.61	4.71	0.95	0.93
		1.20	1.15	4.47	4.55	5.32	0.98	0.84
		1.20	1.20	4.55	4.50	5.32	1.01	0.86
		1.20	1.25	4.63	4.45	5.32	1.04	0.87
		1.20	1.30	4.64	4.41	5.32	1.05	0.87
		1.20	1.35	4.59	4.37	5.32	1.05	0.86
		1.20	1.40	4.52	4.33	5.32	1.04	0.85
		1.20	1.45	4.46	4.30	5.32	1.04	0.84
		1.20	1.50	4.41	4.27	5.32	1.03	0.83
		-----	-----	-----	-----	-----	-----	-----
		-----	-----	-----	-----	-----	-----	-----
		1.20	3.50	4.17	3.84	5.32	1.09	0.78
		1.20	3.75	4.16	3.82	5.32	1.09	0.78
		1.20	4.00	4.15	3.80	5.32	1.09	0.78
		1.20	5.00	4.12	3.76	5.32	1.10	0.77
		1.37	0.70	4.56	5.54	5.07	0.82	0.90
		1.37	0.75	4.48	5.37	5.07	0.83	0.88
		1.37	0.80	4.44	5.23	5.07	0.85	0.88

Group	Specimen parameters			Buckling Coefficient (K)			Comparison	
	Ψ	R	α	K_{FE}	$K_{Prop.}$	K_{Diez}	$K_{FE} / K_{Prop.}$	K_{FE} / K_{Diez}
	1.37	0.85		4.44	5.10	5.07	0.87	0.88
	1.37	0.90		4.47	4.99	5.07	0.89	0.88
	1.37	0.95		4.52	4.90	5.07	0.92	0.89
	1.37	1.00		4.58	4.82	5.07	0.95	0.90
	1.37	1.05		4.66	4.75	6.01	0.98	0.78
	1.37	1.10		4.74	4.68	6.01	1.01	0.79
	1.37	1.15		4.81	4.62	6.01	1.04	0.80
	1.37	1.20		4.83	4.57	6.01	1.06	0.80
	1.37	1.25		4.79	4.52	6.01	1.06	0.80
	1.37	1.30		4.73	4.48	6.01	1.05	0.79
	1.37	1.35		4.66	4.44	6.01	1.05	0.78
	1.37	1.40		4.61	4.41	6.01	1.05	0.77
	1.37	1.45		4.56	4.38	6.01	1.04	0.76
	1.37	1.50		4.52	4.35	6.01	1.04	0.75
	-----	-----		-----	-----	-----	-----	-----
	-----	-----		-----	-----	-----	-----	-----
	1.37	3.50		4.24	3.93	6.01	1.08	0.70
	1.37	3.75		4.22	3.91	6.01	1.08	0.70
	1.37	4.00		4.20	3.89	6.01	1.08	0.70
	1.37	5.00		4.16	3.85	6.01	1.08	0.69
	1.57	0.65		4.83	5.80	5.46	0.83	0.89
	1.57	0.70		4.75	5.60	5.46	0.85	0.87
	1.57	0.75		4.71	5.43	5.46	0.87	0.86
	1.57	0.80		4.71	5.29	5.46	0.89	0.86
	1.57	0.85		4.75	5.17	5.46	0.92	0.87
	1.57	0.90		4.80	5.06	5.46	0.95	0.88
	1.57	0.95		4.87	4.97	6.73	0.98	0.72
	1.57	1.00		4.95	4.89	6.73	1.01	0.73
	1.57	1.05		5.00	4.82	6.73	1.04	0.74
	1.57	1.10		5.02	4.75	6.73	1.06	0.75
	1.57	1.15		4.99	4.70	6.73	1.06	0.74
	1.57	1.20		4.93	4.65	6.73	1.06	0.73
	1.57	1.25		4.87	4.60	6.73	1.06	0.72
	1.57	1.30		4.80	4.56	6.73	1.05	0.71
	1.57	1.35		4.75	4.52	6.73	1.05	0.71
	1.57	1.40		4.71	4.49	6.73	1.05	0.70
	1.57	1.45		4.67	4.45	6.73	1.05	0.69
	1.57	1.50		4.64	4.42	6.73	1.05	0.69
	-----	-----		-----	-----	-----	-----	-----
	-----	-----		-----	-----	-----	-----	-----
	1.57	3.50		4.27	4.01	6.73	1.06	0.63
	1.57	3.75		4.25	4.00	6.73	1.06	0.63
	1.57	4.00		4.23	3.98	6.73	1.06	0.63
	1.57	5.00		4.17	3.94	6.73	1.06	0.62

Group	Specimen parameters			Buckling Coefficient (K)			Comparison	
	Ψ	R	α	K_{FE}	$K_{Prop.}$	K_{Diez}	$K_{FE} / K_{Prop.}$	K_{FE} / K_{Diez}
	1.87	0.60		5.24	6.11	5.87	0.86	0.89
	1.87	0.65		5.14	5.87	5.87	0.87	0.88
	1.87	0.70		5.11	5.67	5.87	0.90	0.87
	1.87	0.75		5.12	5.51	5.87	0.93	0.87
	1.87	0.80		5.16	5.37	5.87	0.96	0.88
	1.87	0.85		5.22	5.25	7.50	0.99	0.70
	1.87	0.90		5.27	5.15	7.50	1.02	0.70
	1.87	0.95		5.30	5.06	7.50	1.05	0.71
	1.87	1.00		5.29	4.98	7.50	1.06	0.71
	1.87	1.05		5.24	4.91	7.50	1.07	0.70
	1.87	1.10		5.17	4.84	7.50	1.07	0.69
	1.87	1.15		5.10	4.79	7.50	1.06	0.68
	1.87	1.20		5.03	4.74	7.50	1.06	0.67
	1.87	1.25		4.97	4.69	7.50	1.06	0.66
	1.87	1.30		4.91	4.65	7.50	1.06	0.66
	1.87	1.35		4.87	4.62	7.50	1.05	0.65
	1.87	1.40		4.83	4.58	7.50	1.05	0.64
	1.87	1.45		4.80	4.55	7.50	1.05	0.64
	1.87	1.50		4.77	4.52	7.50	1.05	0.64
	-----	-----		-----	-----	-----	-----	-----
	-----	-----		-----	-----	-----	-----	-----
	1.87	3.50		4.28	4.12	7.50	1.04	0.57
	1.87	3.75		4.25	4.11	7.50	1.04	0.57
	1.87	4.00		4.23	4.09	7.50	1.03	0.56
	1.87	5.00		4.16	4.06	7.50	1.02	0.55
	2.37	0.55		5.87	6.50	6.31	0.90	0.93
	2.37	0.60		5.79	6.21	6.31	0.93	0.92
	2.37	0.65		5.76	5.97	6.31	0.96	0.91
	2.37	0.70		5.77	5.78	6.31	1.00	0.91
	2.37	0.75		5.78	5.62	6.31	1.03	0.92
	2.37	0.80		5.78	5.48	8.33	1.06	0.69
	2.37	0.85		5.75	5.36	8.33	1.07	0.69
	2.37	0.90		5.67	5.26	8.33	1.08	0.68
	2.37	0.95		5.58	5.17	8.33	1.08	0.67
	2.37	1.00		5.48	5.10	8.33	1.08	0.66
	2.37	1.05		5.38	5.03	8.33	1.07	0.65
	2.37	1.10		5.30	4.97	8.33	1.07	0.64
	2.37	1.15		5.22	4.91	8.33	1.06	0.63
	2.37	1.20		5.15	4.86	8.33	1.06	0.62
	2.37	1.25		5.10	4.82	8.33	1.06	0.61
	2.37	1.30		5.04	4.78	8.33	1.06	0.61
	2.37	1.35		5.00	4.74	8.33	1.05	0.60
	2.37	1.40		4.96	4.71	8.33	1.05	0.59
	2.37	1.45		4.92	4.68	8.33	1.05	0.59

Group	Specimen parameters			Buckling Coefficient (K)			Comparison	
	Ψ	R	α	K_{FE}	$K_{Prop.}$	K_{Diez}	$K_{FE} / K_{Prop.}$	K_{FE} / K_{Diez}
		2.37	1.50	4.88	4.65	8.33	1.05	0.59
		-----	-----	-----	-----	-----	-----	-----
		-----	-----	-----	-----	-----	-----	-----
		2.37	3.50	4.26	4.27	8.33	1.00	0.51
		2.37	3.75	4.23	4.25	8.33	1.00	0.51
		2.37	4.00	4.20	4.24	8.33	0.99	0.50
		2.37	5.00	4.12	4.20	8.33	0.98	0.49
		3.33	0.35	7.98	8.89	6.80	0.90	1.17
		3.33	0.40	7.49	8.06	6.80	0.93	1.10
		3.33	0.45	7.20	7.45	6.80	0.97	1.06
		3.33	0.50	7.03	6.99	6.80	1.01	1.03
		3.33	0.55	6.91	6.63	6.80	1.04	1.02
		3.33	0.60	6.82	6.35	6.80	1.07	1.00
		3.33	0.65	6.70	6.12	6.80	1.10	0.99
		3.33	0.70	6.55	5.93	9.25	1.10	0.71
		3.33	0.75	6.38	5.77	9.25	1.11	0.69
		3.33	0.80	6.20	5.64	9.25	1.10	0.67
		3.33	0.85	6.04	5.52	9.25	1.09	0.65
		3.33	0.90	5.89	5.42	9.25	1.09	0.64
		3.33	0.95	5.76	5.34	9.25	1.08	0.62
		3.33	1.00	5.64	5.26	9.25	1.07	0.61
		3.33	1.05	5.53	5.19	9.25	1.07	0.60
		3.33	1.10	5.44	5.13	9.25	1.06	0.59
		3.33	1.15	5.36	5.08	9.25	1.05	0.58
		3.33	1.20	5.28	5.03	9.25	1.05	0.57
		3.33	1.25	5.21	4.99	9.25	1.04	0.56
		3.33	1.30	5.15	4.95	9.25	1.04	0.56
		3.33	1.35	5.09	4.92	9.25	1.04	0.55
		3.33	1.40	5.04	4.89	9.25	1.03	0.54
		3.33	1.45	4.99	4.86	9.25	1.03	0.54
		3.33	1.50	4.94	4.83	9.25	1.02	0.53
		-----	-----	-----	-----	-----	-----	-----
		-----	-----	-----	-----	-----	-----	-----
		3.33	3.50	4.21	4.46	9.25	0.95	0.46
		3.33	3.75	4.18	4.44	9.25	0.94	0.45
		3.33	4.00	4.15	4.43	9.25	0.94	0.45
		3.33	5.00	4.05	4.40	9.25	0.92	0.44
		6.20	0.45	9.09	7.68	7.36	1.18	1.23
		6.20	0.50	8.53	7.23	7.36	1.18	1.16
		6.20	0.55	8.04	6.88	7.36	1.17	1.09
		6.20	0.60	7.61	6.60	7.36	1.15	1.03
		6.20	0.65	7.25	6.38	7.36	1.14	0.99
		6.20	0.70	6.94	6.19	7.36	1.12	0.94
		6.20	0.75	6.67	6.04	7.36	1.10	0.91

Group	Specimen parameters			Buckling Coefficient (K)			Comparison	
	Ψ	R	α	K_{FE}	$K_{Prop.}$	K_{Diez}	$K_{FE} / K_{Prop.}$	K_{FE} / K_{Diez}
	6.20	0.80		6.44	5.91	7.36	1.09	0.87
	6.20	0.85		6.24	5.79	7.36	1.08	0.85
	6.20	0.90		6.06	5.70	7.36	1.06	0.82
	6.20	0.95		5.91	5.61	7.36	1.05	0.80
	6.20	1.00		5.77	5.54	7.36	1.04	0.78
	6.20	1.05		5.65	5.48	7.36	1.03	0.77
	6.20	1.10		5.54	5.42	7.36	1.02	0.75
	6.20	1.15		5.44	5.37	7.36	1.01	0.74
	6.20	1.20		5.35	5.32	7.36	1.01	0.73
	6.20	1.25		5.27	5.28	7.36	1.00	0.72
	6.20	1.30		5.20	5.24	7.36	0.99	0.71
	6.20	1.35		5.13	5.21	7.36	0.98	0.70
	6.20	1.40		5.06	5.18	7.36	0.98	0.69
	6.20	1.45		5.01	5.15	7.36	0.97	0.68
	6.20	1.50		4.95	5.12	7.36	0.97	0.67
	-----	-----		-----	-----	-----	-----	-----
	6.20	3.50		4.12	4.77	7.36	0.87	0.56
	6.20	3.75		4.09	4.75	7.36	0.86	0.56
	6.20	4.00		4.05	4.74	7.36	0.85	0.55
	6.20	5.00		3.95	4.71	7.36	0.84	0.54
			Mean				1.02	0.75
			STD				0.07	0.17

3.4. Comparison with design rules

The elastic local buckling coefficient obtained from the proposed formulas was compared with the buckling coefficient predicted by the Eurocode [3]. The EC3 provides the following buckling coefficient formulas, as shown in Table 5 to calculate the ultimate strength of a slender plate of internal compression elements. Eurocode 3 only provides a single provision for tapered plates: it suggests that general design rules may be applied by assuming that the panel is rectangular with the maximum width.

Table 5. Buckling factor formulas for internal compression elements according to Eurocode 3.

Stress gradients ($\Psi = \sigma_2 / \sigma_1$)	Buckling factor K_σ
$\Psi = 1.00$	4.00
$1.00 > \Psi > 0.00$	$8.2 / (1.05 + \Psi)$
$\Psi = 0.00$	7.81
$0.00 > \Psi > -1.00$	$7.81 - 6.29\Psi + 9.78\Psi^2$
$\Psi = -1.00$	23.90

Table 6 displays the comparison between the buckling coefficient obtained from the proposed formulas (Eqs.2 to 4) and the buckling factor formulas from EC3 for internal compression elements. For all analyses, plate width "h" is equal 1000 mm, plate thickness is equal 10 mm, six values of stress gradients Ψ (1;2/3;1/3;0;-2/3;-1/3), five values of plate tapering ratio R (1;2;3;5;8), and eight values of normalized plate length α (1;1.5;2;2.5;3;4;6;8). It can be seen that the Eurocode are conservative in calculating the buckling coefficient of trapezoidal plates under stress gradients to calculate the ultimate strength of slender

plates. The reason is that the EC3 does not take into consideration the normalized plate length and tapering ratio, which have a very significant effect on the buckling coefficient. The mean value of the $K_{FE} / K_{Prop.}$ ratio is 1.04 with a corresponding coefficient of variation (COV) of 0.13 and the mean value of the K_{FE} / K_{EC3} ratio is 1.14 with a corresponding coefficient of variation (COV) of 0.17. The buckling coefficient predicted by EC3 is generally conservative; except for the pure bending case, it was close to that of the FE model prediction.

Table 6. Comparison of the buckling coefficient obtained from the proposed formulas and the EC3 formulas for internal compression elements.

Group	Specimen parameters			Buckling Coefficient (K)			Comparison	
	Ψ	R	α	K_{FE}	$K_{Prop.}$	K_{EC3}	$K_{FE} / K_{Prop.}$	K_{FE} / K_{EC3}
G1	1	1	1	3.91	4.66	4.00	0.84	0.98
			1.5	4.27	4.16	4.00	1.03	1.07
			2	3.95	3.95	4.00	1.00	0.99
			2.5	4.08	3.83	4.00	1.07	1.02
			3	3.96	3.76	4.00	1.05	0.99
			4	3.97	3.68	4.00	1.08	0.99
			6	3.97	3.60	4.00	1.10	0.99
		8	3.98	3.57	4.00	1.11	0.99	
		2	1	5.36	5.01	4.00	1.07	1.34
			1.5	4.81	4.56	4.00	1.06	1.20
			2	4.59	4.37	4.00	1.05	1.15
			2.5	4.44	4.27	4.00	1.04	1.11
			3	4.35	4.21	4.00	1.03	1.09
			4	4.22	4.14	4.00	1.02	1.06
	6		4.10	4.08	4.00	1.01	1.02	
	8	4.03	4.05	4.00	1.00	1.01		
	3	1	1	5.60	5.21	4.00	1.07	1.40
			1.5	4.93	4.78	4.00	1.03	1.23
			2	4.62	4.59	4.00	1.00	1.15
			2.5	4.43	4.50	4.00	0.99	1.11
			3	4.31	4.44	4.00	0.97	1.08
			4	4.16	4.37	4.00	0.95	1.04
			6	4.01	4.32	4.00	0.93	1.00
		8	3.93	4.29	4.00	0.92	0.98	
		5	1	5.75	5.45	4.00	1.05	1.44
			1.5	4.96	5.03	4.00	0.99	1.24
			2	4.59	4.85	4.00	0.95	1.15
			2.5	4.38	4.76	4.00	0.92	1.10
3			4.25	4.70	4.00	0.90	1.06	
4			4.08	4.64	4.00	0.88	1.02	
6	3.92		4.59	4.00	0.85	0.98		
8	3.83	4.56	4.00	0.84	0.96			
8	1	5.79	5.65	4.00	1.03	1.45		
	1.5	4.95	5.23	4.00	0.95	1.24		
	2	4.56	5.06	4.00	0.90	1.14		
	2.5	4.34	4.97	4.00	0.87	1.08		

Group	Specimen parameters			Buckling Coefficient (K)			Comparison	
	Ψ	R	α	K_{FE}	$K_{Prop.}$	K_{EC3}	$K_{FE} / K_{Prop.}$	K_{FE} / K_{EC3}
G2	0.67	1	3	4.20	4.91	4.00	0.85	1.05
			4	4.02	4.85	4.00	0.83	1.01
			6	3.85	4.80	4.00	0.80	0.96
			8	3.77	4.78	4.00	0.79	0.94
		1	1	4.75	4.26	4.77	1.12	1.00
			1.5	5.17	4.72	4.77	1.10	1.09
			2	4.77	4.30	4.77	1.11	1.00
			2.5	4.91	4.47	4.77	1.10	1.03
			3	4.77	4.32	4.77	1.11	1.00
			4	4.78	4.33	4.77	1.10	1.00
			6	4.78	4.34	4.77	1.10	1.00
			8	4.78	4.34	4.77	1.10	1.00
		2	1	6.52	6.10	4.77	1.07	1.37
			1.5	5.96	5.40	4.77	1.10	1.25
			2	5.74	5.12	4.77	1.12	1.20
			2.5	5.58	4.93	4.77	1.13	1.17
			3	5.48	4.81	4.77	1.14	1.15
			4	5.33	4.66	4.77	1.15	1.12
			6	5.18	4.49	4.77	1.15	1.09
			8	5.10	4.41	4.77	1.16	1.07
		3	1	6.91	6.40	4.77	1.08	1.45
			1.5	6.30	5.56	4.77	1.13	1.32
			2	5.99	5.16	4.77	1.16	1.26
			2.5	5.79	4.92	4.77	1.18	1.22
			3	5.65	4.77	4.77	1.19	1.19
			4	5.48	4.58	4.77	1.20	1.15
			6	5.29	4.39	4.77	1.20	1.11
			8	5.18	4.29	4.77	1.21	1.09
5	1	7.23	6.59	4.77	1.10	1.52		
	1.5	6.55	5.59	4.77	1.17	1.37		
	2	6.18	5.12	4.77	1.21	1.30		
	2.5	5.95	4.86	4.77	1.23	1.25		
	3	5.79	4.69	4.77	1.24	1.21		
	4	5.58	4.47	4.77	1.25	1.17		
	6	5.36	4.26	4.77	1.26	1.12		
	8	5.25	4.16	4.77	1.26	1.10		
8	1	7.41	6.65	4.77	1.11	1.55		

Group	Specimen parameters			Buckling Coefficient (K)			Comparison	
	Ψ	R	α	K_{FE}	$K_{Prop.}$	K_{EC3}	$K_{FE} / K_{Prop.}$	K_{FE} / K_{EC3}
G3	0.33	1	1.5	6.68	5.57	4.77	1.20	1.40
			2	6.29	5.08	4.77	1.24	1.32
			2.5	6.04	4.80	4.77	1.26	1.27
			3	5.87	4.62	4.77	1.27	1.23
			4	5.64	4.40	4.77	1.28	1.18
			6	5.41	4.18	4.77	1.29	1.13
			8	5.28	4.07	4.77	1.30	1.11
			2	1	5.88	5.66	5.94	1.04
		1.5		6.38	6.22	5.94	1.03	1.07
		2		5.90	5.72	5.94	1.03	0.99
		2.5		6.07	5.92	5.94	1.03	1.02
		3		5.91	5.74	5.94	1.03	0.99
		4		5.92	5.75	5.94	1.03	1.00
		6		5.92	5.76	5.94	1.03	1.00
		8		5.92	5.76	5.94	1.03	1.00
		3	1	7.87	7.91	5.94	1.00	1.32
			1.5	7.06	7.05	5.94	1.00	1.19
			2	6.73	6.71	5.94	1.00	1.13
			2.5	6.52	6.48	5.94	1.00	1.10
			3	6.38	6.34	5.94	1.01	1.07
			4	6.20	6.15	5.94	1.01	1.04
			6	6.02	5.95	5.94	1.01	1.01
			8	5.92	5.85	5.94	1.01	1.00
		5	1	8.23	8.27	5.94	1.00	1.39
			1.5	7.25	7.24	5.94	1.00	1.22
			2	6.79	6.75	5.94	1.01	1.14
			2.5	6.53	6.47	5.94	1.01	1.10
			3	6.35	6.28	5.94	1.01	1.07
4	6.13		6.05	5.94	1.01	1.03		
6	5.92		5.82	5.94	1.02	1.00		
8	5.80		5.70	5.94	1.02	0.98		
5	1	8.52	8.50	5.94	1.00	1.43		
	1.5	7.36	7.28	5.94	1.01	1.24		
	2	6.82	6.71	5.94	1.02	1.15		
	2.5	6.51	6.39	5.94	1.02	1.10		
	3	6.31	6.18	5.94	1.02	1.06		
4	6.07	5.93	5.94	1.02	1.02			

Group	Specimen parameters			Buckling Coefficient (K)			Comparison	
	Ψ	R	α	K_{FE}	$K_{Prop.}$	K_{EC3}	$K_{FE} / K_{Prop.}$	K_{FE} / K_{EC3}
G4	0		6	5.82	5.67	5.94	1.03	0.98
			8	5.70	5.54	5.94	1.03	0.96
		8	1	8.63	8.57	5.94	1.01	1.45
			1.5	7.37	7.26	5.94	1.02	1.24
			2	6.80	6.66	5.94	1.02	1.14
			2.5	6.47	6.32	5.94	1.02	1.09
			3	6.26	6.11	5.94	1.03	1.05
			4	6.01	5.84	5.94	1.03	1.01
			6	5.75	5.57	5.94	1.03	0.97
			8	5.63	5.44	5.94	1.03	0.95
		1	1	7.68	8.12	7.81	0.95	0.98
			1.5	8.25	8.78	7.81	0.94	1.06
			2	7.70	8.18	7.81	0.94	0.99
			2.5	7.90	8.43	7.81	0.94	1.01
	3		7.72	8.21	7.81	0.94	0.99	
	4		7.72	8.22	7.81	0.94	0.99	
	6		7.73	8.23	7.81	0.94	0.99	
	8		7.73	8.24	7.81	0.94	0.99	
	0	2	1	10.21	10.76	7.81	0.95	1.31
			1.5	9.17	9.76	7.81	0.94	1.17
			2	8.73	9.35	7.81	0.93	1.12
			2.5	8.47	9.09	7.81	0.93	1.08
			3	8.29	8.91	7.81	0.93	1.06
			4	8.06	8.69	7.81	0.93	1.03
			6	7.83	8.46	7.81	0.93	1.00
		8	7.71	8.34	7.81	0.93	0.99	
		3	1	10.73	11.18	7.81	0.96	1.37
			1.5	9.46	9.97	7.81	0.95	1.21
2			8.87	9.40	7.81	0.94	1.14	
2.5			8.53	9.07	7.81	0.94	1.09	
3			8.30	8.85	7.81	0.94	1.06	
4			8.03	8.58	7.81	0.94	1.03	
6	7.75		8.30	7.81	0.93	0.99		
8	7.60		8.16	7.81	0.93	0.97		
5	1	11.19	11.46	7.81	0.98	1.43		
	1.5	9.67	10.02	7.81	0.96	1.24		
	2	8.97	9.35	7.81	0.96	1.15		

Group	Specimen parameters			Buckling Coefficient (K)			Comparison	
	Ψ	R	α	K_{FE}	$K_{Prop.}$	K_{EC3}	$K_{FE} / K_{Prop.}$	K_{FE} / K_{EC3}
G5	-0.33	2	2.5	8.57	8.98	7.81	0.95	1.10
			3	8.31	8.73	7.81	0.95	1.06
			4	7.99	8.43	7.81	0.95	1.02
			6	7.68	8.13	7.81	0.94	0.98
			8	7.52	7.97	7.81	0.94	0.96
		8	1	11.38	11.54	7.81	0.99	1.46
			1.5	9.74	10.00	7.81	0.97	1.25
			2	8.99	9.30	7.81	0.97	1.15
			2.5	8.56	8.90	7.81	0.96	1.10
			3	8.28	8.64	7.81	0.96	1.06
			4	7.95	8.32	7.81	0.95	1.02
			6	7.62	8.01	7.81	0.95	0.98
	1	8	7.45	7.86	7.81	0.95	0.95	
		1	10.71	11.63	10.95	0.92	0.98	
		1.5	11.18	12.39	10.95	0.90	1.02	
		2	10.75	11.70	10.95	0.92	0.98	
		2.5	10.85	11.98	10.95	0.91	0.99	
		3	10.76	11.73	10.95	0.92	0.98	
		4	10.76	11.75	10.95	0.92	0.98	
	0.33	2	6	10.76	11.76	10.95	0.91	0.98
			8	10.75	11.76	10.95	0.91	0.98
			1	14.30	14.66	10.95	0.98	1.31
			1.5	12.92	13.51	10.95	0.96	1.18
			2	12.33	13.04	10.95	0.95	1.13
2.5			11.98	12.74	10.95	0.94	1.09	
3			11.74	12.54	10.95	0.94	1.07	
4			11.44	12.28	10.95	0.93	1.05	
3		6	11.14	12.02	10.95	0.93	1.02	
		8	10.98	11.88	10.95	0.92	1.00	
		1	15.29	15.15	10.95	1.01	1.40	
		1.5	13.53	13.76	10.95	0.98	1.24	
3	2	12.72	13.10	10.95	0.97	1.16		
	2.5	12.25	12.72	10.95	0.96	1.12		
	3	11.95	12.47	10.95	0.96	1.09		
	4	11.57	12.16	10.95	0.95	1.06		
3	6	11.19	11.84	10.95	0.94	1.02		
	8	10.99	11.68	10.95	0.94	1.00		

Group	Specimen parameters			Buckling Coefficient (K)			Comparison	
	Ψ	R	α	K_{FE}	$K_{Prop.}$	K_{EC3}	$K_{FE} / K_{Prop.}$	K_{FE} / K_{EC3}
	5		1	16.23	15.47	10.95	1.05	1.48
			1.5	14.08	13.81	10.95	1.02	1.29
			2	13.08	13.05	10.95	1.00	1.19
			2.5	12.52	12.61	10.95	0.99	1.14
			3	12.15	12.33	10.95	0.99	1.11
			4	11.70	11.98	10.95	0.98	1.07
			6	11.25	11.64	10.95	0.97	1.03
			8	11.03	11.46	10.95	0.96	1.01
	8		1	16.70	15.56	10.95	1.07	1.53
			1.5	14.33	13.79	10.95	1.04	1.31
			2	13.24	12.98	10.95	1.02	1.21
			2.5	12.62	12.52	10.95	1.01	1.15
			3	12.23	12.23	10.95	1.00	1.12
			4	11.74	11.87	10.95	0.99	1.07
			6	11.26	11.51	10.95	0.98	1.03
			8	11.01	11.33	10.95	0.97	1.01
G6	-0.67	1	1	16.00	16.20	16.41	0.99	0.97
			1.5	15.67	17.07	16.41	0.92	0.95
			2	15.88	16.29	16.41	0.97	0.97
			2.5	15.57	16.61	16.41	0.94	0.95
			3	15.64	16.32	16.41	0.96	0.95
			4	15.57	16.34	16.41	0.95	0.95
			6	15.58	16.35	16.41	0.95	0.95
			8	15.57	16.36	16.41	0.95	0.95
	2	1	22.52	19.64	16.41	1.15	1.37	
		1.5	20.89	18.34	16.41	1.14	1.27	
		2	20.15	17.80	16.41	1.13	1.23	
		2.5	19.70	17.46	16.41	1.13	1.20	
		3	19.41	17.24	16.41	1.13	1.18	
		4	19.03	16.95	16.41	1.12	1.16	
		6	18.64	16.65	16.41	1.12	1.14	
		8	18.43	16.49	16.41	1.12	1.12	
3	1	25.67	20.19	16.41	1.27	1.56		
	1.5	23.22	18.62	16.41	1.25	1.41		
	2	22.05	17.88	16.41	1.23	1.34		
	2.5	21.38	17.44	16.41	1.23	1.30		
	3	20.93	17.16	16.41	1.22	1.28		

Group	Specimen parameters			Buckling Coefficient (K)			Comparison	
	Ψ	R	α	K_{FE}	$K_{Prop.}$	K_{EC3}	$K_{FE} / K_{Prop.}$	K_{FE} / K_{EC3}
5			4	20.37	16.80	16.41	1.21	1.24
			6	19.81	16.45	16.41	1.20	1.21
			8	19.51	16.26	16.41	1.20	1.19
			1	29.11	20.55	16.41	1.42	1.77
			1.5	25.62	18.68	16.41	1.37	1.56
			2	23.98	17.81	16.41	1.35	1.46
			2.5	23.05	17.32	16.41	1.33	1.40
			3	22.44	17.00	16.41	1.32	1.37
			4	21.69	16.61	16.41	1.31	1.32
8			6	20.94	16.22	16.41	1.29	1.28
			8	20.55	16.02	16.41	1.28	1.25
			1	31.16	20.65	16.41	1.51	1.90
			1.5	26.99	18.65	16.41	1.45	1.64
			2	25.07	17.74	16.41	1.41	1.53
			2.5	23.97	17.22	16.41	1.39	1.46
			3	23.26	16.88	16.41	1.38	1.42
			4	22.39	16.47	16.41	1.36	1.36
			6	21.53	16.07	16.41	1.34	1.31
		8	21.09	15.87	16.41	1.33	1.28	
		Mean				1.04	1.14	
		COV				0.13	0.17	

4. Conclusions

With the aim of providing technical information that may be used to improve design codes in dealing with tapered structural elements, the buckling behaviour of trapezoidal plates subjected to stress gradients was studied by the finite element method. The critical buckling coefficients were estimated for different compression and bending cases with simply supported boundary conditions, including uniform compression load, trapezoidal compression load, triangle compression load, two unequal reverse triangular load, and pure bending load. More than 650 geometries were analysed for each case, covering tapering ratios from 0.25 to 8, and normalized plate lengths from 1 to 8. The regression analysis was employed to propose approximate closed-form expressions that can be used directly to compute the local buckling coefficient for trapezoidal plates. Based on the findings, the following conclusions and recommendations were reached:

1. Where the load is applied on the shorter edge, the buckling resistance of the tapered plate is directly proportional to the tapering of the web plate because the smaller edge provides a stiffer zone compared to the larger edge.
2. The proposed formulas represent a significant improvement over current Eurocode 3 and most design codes in predicting the critical buckling coefficient under compression and bending stresses and can be used to compute the effective width of a slender cross section.
3. For the pure bending moment case, it is recommended to ignore the decrease in k values for a tapering ratio of less than 2.00.
4. The buckling coefficient predicted by EC3 is generally conservative; except for the pure bending case, it was close to that of the FE model prediction.

References

1. Lee, G.C., Morrell, M.L. Application of AISC design provisions for tapered members. *Engineering Journal*. 1975. 12(1). Pp. 1–13.
2. Amirikian, A. Wedge-Beam Framing. *Transactions of the American Society of Civil Engineers*. 1952. 117 (1). Pp. 596–631. DOI: 10.1061/TACEAT.0006615
3. Eurocode 1993-1-5. Eurocode 3 (EC3): Design of Steel Structures – Part 1-5.
4. Diez, R., Lopez, C., Ibañez, J.R., Serna, M.A. A Numerical Study on Elastic Buckling and Ultimate Strength of Compressed Trapezoidal Plates. *International Journal of Structural Stability and Dynamics*. 2019. 20 (1). DOI: 10.1142/S0219455420500091
5. Al Qablan, H. Applicable Formulas for Shear and Thermal Buckling of Perforated Rectangular Panels. *Advances in Civil Engineering*. 2022. DOI: 10.1155/2022/3790462
6. Taherian, I. Analytical Study on Composite Steel Plate Walls Using a Modified Strip Model, In Proceedings of the 10th International Congress on Civil Engineering, Abriz, Iran, 5–7 May 2015.
7. Dehadray, P.M., Alampally, S., Lokavarapu, B.R. Buckling Analysis of Thin Isotropic Square Plate with Rectangular Cut-Out. *Lecture Notes in Mechanical Engineering*. 2022. Pp. 71–86. DOI: 10.1007/978-981-16-7282-8_6/FIGURES/15
8. Soleymani, A., Esfahani, M.R. Effect of concrete strength and thickness of flat slab on preventing of progressive collapse caused by elimination of an internal column. *Journal of Structural and Construction Engineering*. 2019. 6(1). Pp. 24–40. DOI: 10.22065/JSC.2017.98444.1335
9. Sinha, V., Patel, R., Ghetiya, K., Nair, M., Trivedi, T., Bhaskara Rao, L. Impact of Diamond-Shaped Cut-Out on Buckling Nature of Isotropic Stainless-Steel Plate. *Lecture Notes in Mechanical Engineering*. 2022. Pp. 119–146. DOI: 10.1007/978-981-16-7282-8_10/FIGURES/18
10. Pope, G. The buckling of plates tapered in planform. *Aeronautical Research Council, R. & M. No. 3324*, 1963.
11. Šapalas, V. Local stability of web of tapered beam subjected to pure bending. *Journal of Civil Engineering and Management*. 2010. 16 (2). Pp. 216–221. DOI: 10.3846/JCEM.2009.24
12. Pravel, S.P., Morrell, M.L., Lee, G.C. Bending and buckling strength of tapered structural members. *Welding Research Supplement*. 1974. February. Pp. 75–84.
13. Ibrahim, M.M., El Aghoury, I.M., Ibrahim, S.A.B. Experimental and numerical investigation of axial compressive strength of unstiffened slender tapered-webs. *Journal of Constructional Steel Research*. 2021. 187. Pp. 106921. DOI: 10.1016/J.JCSR.2021.106921
14. York, C.B., Williams, F.W. Buckling analysis of skew plate assemblies: Classical plate theory results incorporating Lagrangian multipliers. *Computers & Structures*. 1995. 56(4). Pp. 625–635. DOI: 10.1016/0045-7949(94)00568-N
15. Wang, C.M., Liew, K.M., Alwis, W.A.M. Buckling of Skew Plates and Corner Condition for Simply Supported Edges. *Journal of Engineering Mechanics*. 1992. 118 (4). Pp. 651–662. DOI: 10.1061/(ASCE)0733-9399(1992)118:4(651)
16. Huyton, P., York, C.B. Buckling of Skew Plates with Continuity or Rotational Edge Restraint. *Journal of Aerospace Engineering*. 2001. 14 (3). Pp. 92–101. DOI: 10.1061/(ASCE)0893-1321(2001)14:3(92)
17. Saadatpour, M.M., Azhari, M., Bradford, M.A. Buckling of arbitrary quadrilateral plates with intermediate supports using the Galerkin method. *Computer Methods in Applied Mechanics and Engineering*. 1998. 164 (3–4). Pp. 297–306. DOI: 10.1016/S0045-7825(98)00030-9
18. Bradford, M.A., Azhari, M., Saadatpour, M.M. Analysis of general quadrilateral orthotropic thick plates with arbitrary boundary conditions by the Rayleigh-Ritz method. *International Journal for Numerical Methods in Engineering*. 2002. 54(7). Pp. 1087–1102. DOI: 10.1002/nme.485.
19. Karami, G., Malekzadeh, P. Static and stability analyses of arbitrary straight-sided quadrilateral thin plates by DQM. *International Journal of Solids and Structures*. 2002. 39 (19). Pp. 4927–4947. DOI: 10.1016/S0020-7683(02)00403-1
20. Civalek, Ö. Application of differential quadrature (DQ) and harmonic differential quadrature (HDQ) for buckling analysis of thin isotropic plates and elastic columns. *Engineering Structures*. 2004. 26(2). Pp. 171–186. DOI: 10.1016/J.ENGSTRUCT.2003.09.005
21. Wang, X., Tan, M., Zhou, Y. Buckling analyses of anisotropic plates and isotropic skew plates by the new version differential quadrature method. *Thin-Walled Structures*. 2003. 41 (1). Pp. 15–29. DOI: 10.1016/S0263-8231(02)00100-3
22. A. Eid. Ausbeulen trapezförmiger Platten. Ph.D., ETH, Zurich, 1957.
23. Ikhenazen, G., Saidani, M., Chelghoum, A. Finite element analysis of linear plates buckling under in-plane patch loading. *Journal of Constructional Steel Research*. 2010. 66 (8–9). Pp. 1112–1117. DOI: 10.1016/J.JCSR.2010.03.006
24. Abu-Hamd, M., El Dib, F.F. Buckling strength of tapered bridge girders under combined shear and bending. *HBRC*. 2016. 12 (2). Pp. 163–174. DOI: 10.1016/J.HBRCJ.2014.11.001
25. Kucukler, M., Gardner, L. Design of laterally restrained web-tapered steel structures through a stiffness reduction method. *Journal of Constructional Steel Research*. 2018. 141. Pp. 63–76. DOI: 10.1016/j.jcsr.2017.11.014
26. Ziemian, R.D. Guide to stability design criteria for metal structures. Hoboken, NJ, USA: John Wiley & Sons, Inc.; 2010. 1078 p.
27. Azhari, M., Shahidi, A.R., Saadatpour, M.M. Post local buckling of skew and trapezoidal plates. *Advances in Structural Engineering*. 2004. 7(1). Pp. 61–70.
28. Jaberzadeh, E., Azhari, M. Elastic and inelastic local buckling of stiffened plates subjected to non-uniform compression using the Galerkin method. *Applied Mathematical Modelling*. 2009. 33 (4). Pp. 1874–1885. DOI: 10.1016/J.APM.2008.03.020
29. Jaberzadeh, E., Azhari, M., Boroomand, B. Inelastic buckling of skew and rhombic thin thickness-tapered plates with and without intermediate supports using the element-free Galerkin method. *Applied Mathematical Modelling*. 2013. 37(10–11). Pp. 6838–6854. DOI: 10.1016/J.APM.2013.01.055
30. Upadhyay, A.K., Shukla, K.K. Post-buckling analysis of skew plates subjected to combined in-plane loadings. *Acta Mechanica*. 2014. 225(10). Pp. 2959–2968. DOI: 10.1007/S00707-014-1205-2/METRICS
31. Jiang, G., Li, F., Zhang, C. Post buckling and nonlinear vibration of composite laminated trapezoidal plates. *Steel and Composite Structures*. 2018. 26 (1). Pp. 17–29.
32. Ashok, S., Pitchaimani, J. Buckling Behavior of Non-Uniformly Heated Tapered Laminated Composite Plates with Ply Drop-Off. *International Journal of Structural Stability*. 2018. 18 (4). DOI: 10.1142/S0219455418500591

33. Kumar, A., Singha, M.K., Tiwari, V. Stability Analysis of Shear Deformable Trapezoidal Composite Plates. *International Journal of Structural Stability and Dynamics*. 2019. 19 (8). DOI: 10.1142/S0219455419710044
34. Jing, Z., Sun, Q., Liang, K., Chen, J. Closed-Form Critical Buckling Load of Simply Supported Orthotropic Plates and Verification. *International Journal of Structural Stability and Dynamics*. 2019. 19(12). DOI:10.1142/S0219455419501578.
35. ANSYS Inc. Ansys Student - Free Software Download. URL: <https://www.ansys.com/academic/students/ansys-student>. (date of access: April 9, 2024).
36. Timoshenko, S.P., Gere, J. M., Prager, W. *Theory of Elastic Stability*, Second Edition. *Journal of Applied Mechanics*. 1962. 29(1). 220. DOI: 10.1115/1.3636481
37. Ibrahim, M.M., El Aghoury, I.M., Ibrahim, S.A.B. Finite element investigation on plate buckling coefficients of tapered steel members web plates. *Structures*. 2020. 28. Pp. 2321–2334. DOI: 10.1016/j.istruc.2020.10.003
38. Pekoz T. Development of a unified approach to the design of cold-formed steel members. *Eighth Int Spec Conf Cold-Formed Steel Struct*. 1986. Pp. 77–84.
39. Mirambell, E., Zárate, A.V. Web buckling of tapered plate girders. *Struct. Build*. 2015. 140(1). Pp. 51–60. DOI: 10.1680/STBU.2000.140.1.51
40. Chen, N.-Z., Soares, C.G., Soares, C.G., Chen, N.Z. *Buckling analysis of stiffened composite panels*. III European Conference on Computational Mechanics. Springer, Netherlands, 2006. DOI: 10.1007/1-4020-5370-3_686
41. SHELL181. Theory Reference. ANSYS Release 19. ANSYS Inc., 2019. URL: https://www.mm.bme.hu/~gyebro/files/ans_help_v182/ans_elem/Hlp_E_SHELL181.html (date of access: April 9, 2024).
42. Gardner, L., Fieber, A., Macorini, L. Formulae for Calculating Elastic Local Buckling Stresses of Full Structural Cross-sections. *Structures*. 2019. 17. Pp. 2–20. DOI: 10.1016/J.ISTRUC.2019.01.012
43. Studer, R.P., Binion, C.D., Davis, D.B. Shear strength of tapered I-shaped steel members. *Journal of Constructional Steel Research*. 2015. 112. Pp. 167–174. DOI: 10.1016/J.JCSR.2015.04.013

Information about authors:

Saad Yehia, PhD

ORCID: <https://orcid.org/0000-0002-3069-6059>

E-mail: saadyhy81@gmail.com

Ramy Shahin, PhD

ORCID: <https://orcid.org/0000-0002-4795-8545>

E-mail: Ramy.shahin@gmail.com

Received 18.06.2023. Approved after reviewing 27.02.2024. Accepted 28.02.2024.



Research article

UDC 624.011.1


DOI: 10.34910/MCE.126.10



Performance of TGk dowel connector plates in wooden structure joints under long-term load

S.A. Isupov 

Vyatka State University, Kirov, Russian Federation

 Deka_1958@mail.ru

Keywords: dowel, TGk metal connector plates, dowel joint, test scheme, deformation diagram, short-term diagram, long-term tests, wood of the dowel hole, isochronous curves.

Abstract. The article is devoted to the study of the bearing capacity and deformation of connections of wooden structures using plates with cylindrical TGk dowels of 5 mm diameter under prolonged load action. The deformation properties of connections of wooden structures are studied to a lesser extent, including in the stage of nonlinear creep under long-term load. The purpose of the research is to confirm the operational strength and rigidity of the compounds under consideration. For the theoretical analysis of the work of connections using metal connector plates under prolonged loading, the provisions of the theory of aging of materials are used. For experimental analysis, long-term tests were carried out on samples of pine beams with dimensions of 80 x 80 x 300 mm. All samples were installed under a constant load with different loading levels. The exposure period of the samples was 730 days. As a result of the performed studies, a conclusion was made about a sufficient degree of strength and rigidity of the connections of wooden structures on the TGk metal connector plates. Isochronous curves of deformation of the wood of the dowel hole and the connections themselves for certain moments of time are obtained. A calculated diagram of the deformation of the wood of the dowel hole $\sigma - \delta$ and calculated diagram $T - \Delta$ connections under prolonged loading is constructed. The results obtained are necessary for practical calculations of composite wooden elements with this type of connections, taking into account the time of action of the load.

Citation: Isupov, S. A. Performance of TGk dowel connector plates in wooden structure joints under long-term load. Magazine of Civil Engineering. 2024. 17(2). Article no. 12610. DOI: 10.34910/MCE.126.10

1. Introduction

Wood belongs to the group of materials with rheonomic properties. The strength and deformation of both the wood itself and its connections depend on the loading rate and the load duration [1–5]. The creep that occurs in this case has a significant effect on the parameters of the stress-strain state of the connections of wooden structures under prolonged load action.

The work of wood under the action of long-term loads can be divided into two areas. The 1st area is characterized by constant attenuation of deformations over time. The 2nd region is characterized by an increase in deformations with increasing speed in time, followed by the destruction of the material. Experimental and theoretical studies of the connections, including composite ones, under the action of long-term loads are given in a number of publications [6–13]. Under prolonged load action on a dowel connection, there is an increase in deformations of the dowel hole wood in time due to wood creep, which leads to redistribution of stresses over time even under constant load on the connection.

When loading a composite element with dowel connections subject to deformation, along with an increase in the deformations of the connections, over time, the deformations of wood itself develop, which together represent the stress-strain state of the composite wooden element at a certain point in time. The most effective way to confirm the operational reliability of new structures during the standard service life is

to conduct long-term tests with the study and confirmation of the operational strength and rigidity of the structure, which is reflected in studies of various wooden structural elements under the influence of long-term loading [14–21].

Vyatka State University developed dowel connectors, which are connecting elements for wooden structures containing a group of cylindrical dowels of increased diameter of 5...8 mm with a more saturated arrangement and fixed on a common base. Connectors of the basic type (Fig. 1), called TGk metal connector plates, were designed mainly for making composite wooden elements of enlarged cross-section from beams and logs. The base of such a connector plate is made from hard materials with a high modulus of elasticity (steel, rigid structural plastics), which is marked by the letter "T". Depending on the end part of the dowel, the plates are divided into types, with "G" marking the dowels sharpened on both sides. Fastening the dowel on the base is performed by welding as marked by letter "k". Therefore, this type of dowel connector plate has the marking of "TGk" [22].

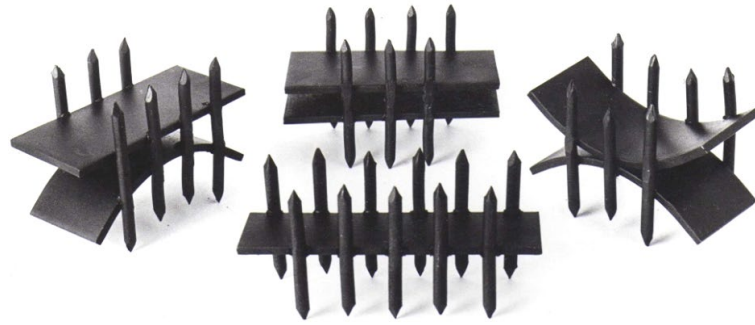


Figure 1. TGk metal connector plates of different types.

At the first stage of studies of compounds on TGk metal connector plates, short-term mechanical characteristics of the wood of the dowel hole and deformation characteristics of the dowel material were determined. The results of experimental and theoretical studies were obtained to determine the bearing capacity and deformability of connections under short-term loading.

The relevance of further studies of compounds is due to the need for experimental and theoretical analysis of the data obtained, taking into account the duration of the load. The purpose of the research is to confirm the operational strength and rigidity of the connections on the TGk metal connector plates, as well as to study the operation of the connections (primarily to obtain quantitative estimates of deformations at design stress levels) under long-term load, which is necessary for practical calculations of composite wooden elements.

To achieve this goal, the following tasks were set:

- to conduct experimental studies of wooden samples with a long-term permanent load;
- to construct isochronous curves of the dowel hole wood deformation and of connections the TGk metal connector plates for certain moments of time;
- to construct a calculated diagram of the dowel hole wood deformation $\sigma - \delta$ and $T - \Delta$ connections under prolonged loading.

2. Methods

To analyze the operation of connectors of wooden structures on TGk metal connector plates under long-term loading, we will use the provisions of the theory of aging of materials as the simplest apparatus for describing long-term processes [23, 24]. Based on this theory, there should be a relationship

$$F(\delta_0 \sigma_0 t T^0) = 0, \quad (1)$$

δ_0 , σ_0 are displacements and stresses under simple loading ; t , T^0 are time and temperature.

The complete displacement will be written as

$$\delta_0 = \delta_{0el} + \delta_{0pl} + \delta_{0pl} + \alpha T^0, \quad (2)$$

δ_{0el} , δ_{0pl} are elastic and plastic displacements; δ_{0pl} , αT^0 are creep displacements and temperature displacements.

In case of non-uniform distribution of stresses, dependence (1) refers to the intensities of strains and stresses and can be written as

$$\delta_i = \delta_i(\sigma_i t T^0). \quad (3)$$

The main hypothesis of the theory of aging is that dependence (3) can be valid both in the stationary mode of loading ($\sigma_0 = \text{const}$, $T^0 = \text{const}$), for which it is easily determined from the experiment, and in the non-stationary mode ($\sigma_0 = \text{var}$, $T^0 = \text{var}$).

The calculation of the connections is based on the creep curves of the wood of the dowel hole, taking into account the fact that the properties of the dowel material (metal) do not change with time. Creep curves are built at different levels of applied stresses – a family of curves is obtained in the coordinates $\sigma - \delta$ (stress – strain). At the moment $\sigma = 0$, the initial displacement corresponds to the instantaneous displacement (elastic or elastic-plastic) as a result of the applied stress. At a certain point in time, for different curves of the family, we will have creep displacements corresponding to the acting stresses, which allows us to construct the dependence

$$\delta = \varphi(\sigma, t). \quad (4)$$

This dependence expresses an isochronous creep curve for a point in time. For the initial value of time $t = 0$, the isochronous curve coincides with the short-term deformation curve. Therefore, for fixed times, you can get a family of isochronous curves in the coordinates $\sigma - \delta$ for the deformation of the wood of the dowel hole, $T - \Delta$ (bearing capacity – deformation of the connection) for deformation of the connections and $M - f$ (bending moment – deflection of a beam of an entire section) for deformation of elements of a composite beam.

After finding isochronous creep curves, the problem is reduced to performing calculations at a certain point in time using known strain diagrams. For dowel connections, after the experimental determination of the family of curves $\sigma - \delta$, the calculation is performed according to the procedure [25]. For the initial time $t = 0$, the calculation completely coincides with the determination of the stress-strain state of dowel connections under short-term loading. For each moment of time, exactly the same calculation is carried out, but the isochronous creep curve for a specific time is taken as the deformation curve.

According to the performed calculations, it is possible to construct creep curves for connections and for deformation of elements of composite beams

$$\Delta = \varphi(T, t), \quad f = \varphi(M, t). \quad (5)$$

Creep curves obtained experimentally allow, in the calculations of a composite element, to correct the modulus of elasticity of wood in bending at a point in time. Using the obtained data, it is possible to perform the calculation of a composite wooden element on pliable bonds for any moment of time.

In order to determine the mechanical characteristics of the wood of the dowel hole and construct a long-term deformation diagram $\sigma_{cr} - \delta$, as well as to study the operation of wood connections on metal connecting plates TGk, experimental studies of samples with a long-term permanent load were carried out. All tests of samples were carried out in accordance with the requirements of [recommendations for testing the connection of wood structures TsNIISK](#).

The whole complex of tests consists of the following stages:

1. preparation of samples, determination of the mechanical characteristics of wood;
2. short-term tests of the control series;
3. long-term testing.

At the first stage, samples were made from four pairs of pine beams with a cross section of 80×80 mm. Length 300 mm – from the condition of the placement of dowels and taking into account the possibility of determining the mechanical characteristics of the wood of the dowel hole. For the manufacture

of samples, pairwise sawing of beams was used, so that each sample consists of the wood of two beams (for analogy with composite beams). Of the total number of samples, 50 % were intended for the control series – short-term tests. When sawing the beams in pairs, the alternate selection of samples was taken into account, so that each working sample subjected to a long-term load, in the accepted sample selection scheme, corresponded to two control samples adjacent in length bar. This makes it possible to evaluate the mechanical characteristics of the working sample by the average value of the characteristics of two control samples. The moisture content of wood for the period of sample preparation was 8...9 %. Samples-cubes 20×20×30 mm in size were sawn out of the working area of all samples, and the compressive strength along the wood fibers was determined in accordance with GOST 16483.10-1973. The average value of the short-term compressive strength of wood $R_z = 46.8$ MPa, which corresponds to the average quality of wood in terms of strength indicators.

At the second stage short-term tests of samples of the control series were carried out. The mechanical characteristics of the dowel hole were determined by testing the samples with a dowel stamp 5 mm in diameter according to the scheme described in [26]. Tests with a dowel stamp were performed on all samples of the control series and on samples of the working series. According to the strength and deformation characteristics, a conclusion was made about the identity of the wood selected for testing. The average value of the short-term strength of the wood of the dowel hole $R_{cr.n} = 36.0$ MPa is taken as the base value for determining the levels of loading of the long-term load. Tests of specimens with TGk dowel plates with a dowel diameter of 5 mm and a length of 60 mm were performed according to symmetrical scheme 1 [27]. As a result the average value of the breaking force per one conditional slice for the given wood was $T = 2.60$ kN.

The third stage of testing is loading and holding samples under a long-term constant load. The test schemes both for determining the mechanical characteristics and for the connections correspond to the schemes for short-term tests of symmetrical connections with the only addition – all wooden elements are sealed in tightly fitting plastic bags in order to reduce the effect of fluctuations in the temperature and humidity conditions of the room on the deformation of the connections over time. A layer of 0.5 mm thick polyethylene film between the dowel plate and the wooden elements does not significantly affect the operation of the connections. The samples were loaded using disk lever installations with a gear ratio of efforts of 12.5. Before loading the samples, each setup was calibrated using a DOR-1 dynamometer of the Tokar system with a stepwise application of the load. All samples were installed under a constant load with different loading steps, shown in Fig. 2.

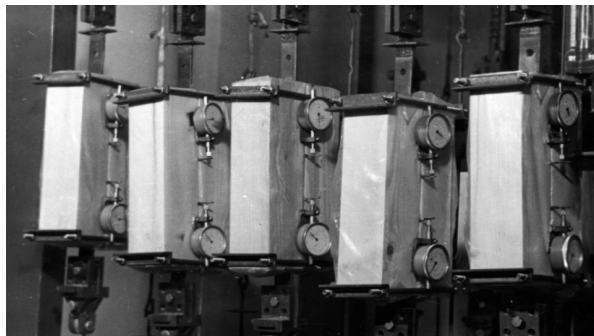


Figure 2. General view of samples during long-term testing.

The loading steps are chosen on the basis of 0.25; 0.5; 0.50; 0.75 of the breaking force for mechanical characteristics and connections, which is 0.67, 1.0; 1.2; 2.0 in fractions of the calculated bearing capacity for the nominal shear of the dowel. For each level of loading, 2 samples are installed, which makes it possible to obtain 4 results. Readings on deformations indicators ICH-10 were taken immediately after loading, then after 1, 3, 12, 24 hours, and subsequently after three, and then seven days. Along with deformation measurements, the temperature and humidity of the air in the laboratory were constantly recorded, as well as the humidity of control samples from wood of the same quality using an electronic moisture meter.

3. Results and Discussion

1. The process of deformation in time of the wood of the dowel hole and connections is shown in Fig. 3. The exposure period of the samples was 730 days. During this period, the deformations of the wood of the dowel hole increased by 5.1...7.7 times, and the deformations of the connections were increased by 2.4...4.8 times, depending on the steps of loading. At the load step $T = 1.0$ kN, the deformations of the connections increased by a factor of 3.5 and amounted to 0.45 mm for two

shear specimens. According to the form of creep curves, one can note an uneven growth of deformations; there are periods of more intense growth of deformations, attenuation, and growth again, especially at higher loading levels. This process can be explained by a change in the relative humidity of the air in the room from 25 to 40 % in winter to 70 to 80 % in summer, although measures were taken to reduce this effect on deformations.

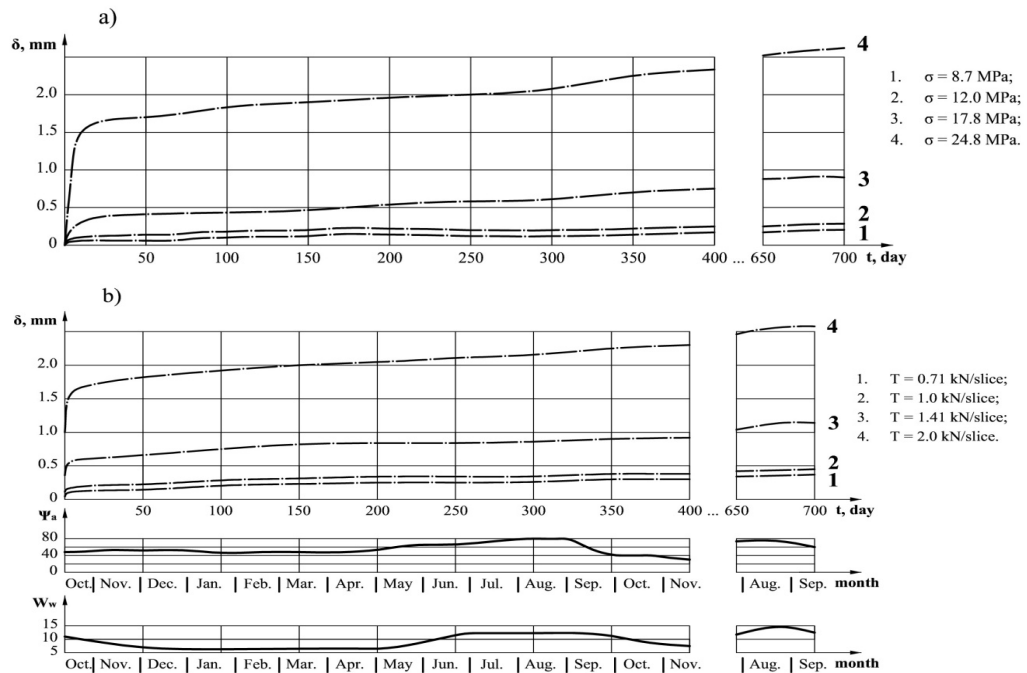


Figure 3. Creep curves a) wood of the dowel hole; b) connections on TGk metal connector plates.

In general, the process of deformation in time of both mechanical characteristics and connections at loading stages up to half the breaking load is damped, regular, and predictable. At higher loading stages, a gradual, undamped process of strain growth is observed, although failure did not occur on any of the specimens.

Prediction of deformations in time can be carried out by applying the well-known Maxwell-Thomson rheological equation [28]

$$\sigma + n\sigma' = E\varepsilon + nH\varepsilon' \quad (6)$$

its solution can be written as

$$\varepsilon(t) = \frac{\sigma}{H} \left(1 + \frac{H-E}{H} e^{-\frac{Et}{Hn}} \right), \quad (7)$$

σ is the magnitude of the voltage (load); H , E , n are rheological coefficients; H is instantaneous elasticity coefficient; E is long-term elasticity coefficient; n is relaxation time factor.

Rheological coefficients H , E , n are determined from experimental creep curves using the technique [29]. The coefficient of instantaneous elasticity H is found from the instantaneous deformation formed immediately after the application of the load

$$H = \frac{\sigma}{\varepsilon_0}. \quad (8)$$

The coefficient of long-term elasticity is determined by the formula

$$E = \frac{\sigma}{\varepsilon_\infty} = \sigma \left(\frac{2\varepsilon_1 - (\varepsilon_0 + \varepsilon_2)}{\varepsilon_1^2 - \varepsilon_0\varepsilon_2} \right), \quad (9)$$

ε_i is deformations at a certain time of observation.

The relaxation time coefficient is determined from the expression

$$\varepsilon(t) = \varepsilon \left(\frac{nH}{E} \right) = \varepsilon_{\infty} - \sigma \left(\frac{H-E}{HE} \right) e^{-1}. \quad (10)$$

The process of predicting deformations in time according to the described method is carried out in the following sequence. Two timings are elected from the condition $t_2 = 2t$, determined by the creep curves of the deformation ε_1 and ε_2 , then the rheological coefficients are determined by formulas (8...10). Substituting them into formula (7) and setting a certain value of σ time, we obtain the necessary deformations at any point.

- Based on the obtained data on the mechanical characteristics of the wood of the dowel hole under a long-term load, the calculations of the connections were performed according to the method [25] for a certain point in time in order to compare the results with experimental data.

To do this, using formula (4), isochronous curves of the deformation of the wood of the dowel hole were constructed for time points 0; 0.8; 24; 73; 200; 411; and 730 days, which are shown in Fig. 4.

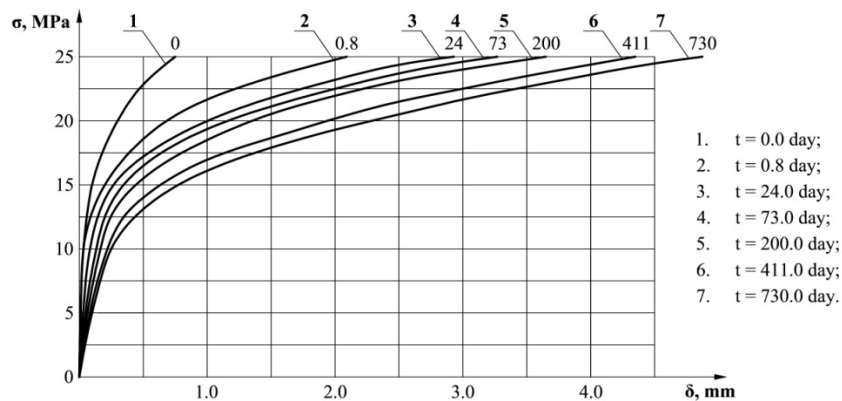


Figure 4. Isochronous curves of deformation of the wood of the dowel hole.

To calculate the connections, we used the previously obtained [26] dowel deformation diagram $M - \chi$ for symmetrical loading. The results of calculations and experimental values of deformations of connections of long-term tests (minimum and maximum values of the four results at individual loading stages) are shown in Table 1.

Table 1. Comparison of calculated and experimental values of connections deformations under long-term loading.

Time, day	Deformations of connections δ (mm) at loading levels T (kN per slice)					
	$T = 0.71$		$T = 1.00$		$T = 1.41$	
	Calculation	Experiment	Calculation	Experiment	Calculation	Experiment
0	0.078	0.062 ... 0.770	0.151	0.112 ... 0.237	0.315	0.267 ... 0.457
24	0.112	0.115 ... 0.137	0.220	0.147 ... 0.292	0.530	0.505 ... 0.865
200	0.181	0.213 ... 0.298	0.315	0.350 ... 0.395	0.768	0.675 ... 1.070
730	0.237	0.258 ... 0.446	0.406	0.420 ... 0.495	1.247	0.800 ... 1.373

The data in the table indicate a good enough convergence of the calculated and experimental results. In most cases, the calculated values of deformations fit into the range of experimental data scatter. The maximum discrepancy from the boundaries of the interval is 8 %.

- For practical calculations of connections on TGk metal connector plates, a design diagram of the deformation of the wood of the dowel hole is required, taking into account the duration of loading and the design resistance to crushing wood crushing of the wood of the dowel hole $R_{cr.n}$.

To construct this diagram, we will use the short-term diagram of the deformation of the wood of the dowel hole with the boundaries of the data scatter, obtained earlier [26], and the isochronous curve in Fig. 3 with a maximum exposure time of 730 days.

After performing calculations on the average values of σ_{cr} with the upper and lower boundaries of the interval with a confidence level of $\alpha = 0.95$, we obtain the calculated long-term diagram of the deformation of the wood of the dowel hole diameter of 5 mm, the values of which are given in Table 2.

Table 2. Estimated diagram of the deformation of the wood of the dowel hole considering the duration of loading.

Value (mm)	Deformations δ (mm) at the level of load $\bar{\sigma}$ (MPa)									
	0.50	0.75	1.00	1.25	1.50	1.75	2.00	2.25	2.50	2.75
δ_{av}	0.08	0.15	0.23	0.38	0.57	0.90	1.45	2.27	3.50	5.30
δ_{min}	0.03	0.07	0.13	0.20	0.30	0.43	0.63	0.93	1.40	2.10
δ_{max}	0.12	0.02	0.35	0.56	0.90	1.50	2.43	3.83	6.80	30.0

Let us determine the calculated resistance of the collapse of the wood of the dowel hole

$$R_{cr.n} = R_{cr.n}^n K_{hom} \frac{m_d}{\gamma_m}, \quad (11)$$

$R_{cr.n}^n$ is normative resistance to crushing of the wood of the dowel hole; K_{hom} is coefficient of wood homogeneity; m_d is coefficient taking into account the duration of the load application; γ_m is coefficient of transition from the confidence level $\alpha = 0.95$ to $\alpha = 0.99$ for the design resistance, $\gamma_m = 1.09$ according to the γ is distribution.

The duration coefficient is determined by the method [recommendations for testing wood structures TsNIISK](#).

$$m_d = (B - Clgt)^{-1}; \quad (12)$$

$$B = \frac{17.1}{17.1 - \lg T}, \quad C = \frac{B-1}{\lg T}, \quad (13)$$

t is time for short-term tests $\rightarrow t = t'/38.2$; T is service life of the structure.

For dowels with a diameter of 5 mm installed in solid wood, we have the standard resistance to crushing of the wood of the dowel hole $R_{cr.n}^n = 28.75$ MPa. $t' = 1667$ sec at $F_{pcs} = 2.8$ cm². $\sigma_{max} = 49.5$ MPa at a load of 0.5 kN per minute – $m_d = 0.54$, which does not contradict long-term tests of the wood of the dowel hole. As a result of calculations according to (11), we obtain the calculated resistance to crushing of the wood of the dowel hole $R_{cr.n} = 13.5$ MPa.

According to the previously obtained [26] dependences $\sigma - \delta$ and $M - \chi$, the calculation of connections on TGk plates with a dowel diameter of 5 mm and 60 mm long was performed to determine the calculated bearing capacity T_n . The calculation results for some load levels are shown in Table 3.

Table 3. Parameters of the stress-strain state of connections under long-term load.

Load, kN	Deformations, mm			Bending moment, kN/cm			Bearing stress, MPa		
	\dot{X}	X_{min} ...	X_{max}	\dot{X}	X_{min} ...	X_{max}	\dot{X}	X_{min} ...	X_{max}
0.50	0.139	0.079 ...	0.181	0.396	0.317 ...	0.440	7.094	6.536 ...	7.859
1.00	0.365	0.247 ...	0.469	0.892	0.759 ...	0.984	12.41	11.41...	13.67
1.50	1.095	0.583 ...	1.774	1.283	1.202 ...	1.296	18.38	18.24 ...	19.42
2.00	4.929	2.179 ...	8.465	1.360	1.308 ...	1.426	26.98	25.35 ...	27.69

The design bearing capacity of the dowel is determined in accordance with the method of limit states from the condition of fulfillment of the inequalities

$$\sigma_{cr.n} \leq R_{cr.n}, \quad M_{n.max} \leq M_t, \quad \delta_n < \delta_{per}. \quad (14)$$

The design resistance to crushing of the wood of the dowel hole is determined by (6) and the design bending moment is determined by the formula

$$M_t = W_y R_n K_c, \quad (15)$$

W_y is moment of resistance of circular section; R_n is design bending resistance of the dowel; K_c is coefficient taking into account the increase in the yield strength due to the constraint of deformations during bending. $K_c = 1.25$, which corresponds to the onset of plastic deformations during tension and bending of class A 240 reinforcing wire.

As a result of calculations according to (15), we have $M_t = 1.0$ kN/cm, at which the diagram of the deformation of the dowel during bending in all cases has a linear character.

Analysis of Table 3 makes it possible, based on the above, to determine the design bearing capacity of the dowel $T_n = 1.0$ kN, at which $M_{max} = 0.984 < M_t = 1.0$ kN/cm; and $\sigma_{cr.max} = 13.67$; $R_{cr.n} = 13.56$ MPa. The obtained value is in good agreement with the results of calculations according to the recommendations for the design and manufacture of wood structures with connections on plates with cylindrical nagels of the TsNIISK-KirPI system.

- To perform calculations of composite beams for a long-acting load, we construct isochronous curves of connections $T - \Delta$ for time points of 0, 24, 200 and 730 days. The construction of curves is based on the calculation of compounds using isochronous curves $\sigma - \delta$ Fig. 3. Isochronous curves of connections at the level of Δ are shown in Fig. 5.

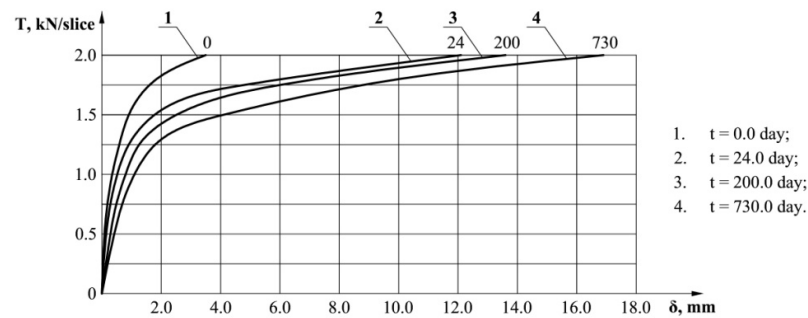


Figure 5. Isochronous deformation curves of connections $T - \Delta$.

In conclusion, in Table 4, we present the calculated deformation diagram $T - \Delta$ for non-symmetrical joints (shear bonds in constituent elements) on TGk metal connector plates with dowels of 5 mm diameter and 60 mm long. The calculated diagram is constructed similarly to the short-term diagram when performing calculations using the dependencies $\sigma - \delta$ according to Fig. 4 and $M - \chi$ (according to the symmetrical and non-symmetrical scheme), as well as taking into account the technological coefficients m_c and m_t [26].

Table 4. Calculation diagram of the deformation of connection under long loading.

Value	Deformations (mm) at the level. T (kN per slice)						
	0.25	0.50	0.75	1.00	1.25	1.50	1.75
δ_{av}	0.22	0.52	0.92	1.48	2.37	4.04	7.38
δ_{min}	0.11	0.31	0.60	0.98	1.49	2.34	3.84
δ_{max}	0.31	0.69	1.20	1.93	3.19	5.87	11.9

4. Conclusion

Based on the results of the research, the following main conclusions can be drawn regarding the long-term strength and rigidity for connections of wooden structures on TGk plates with cylindrical dowels.

- As a result of the tests carried out, a sufficient degree of long-term strength and rigidity of the joints of wooden structures using the TGk metal connector plates was proved.

2. The isochronous curves of the dowel hole wood deformation and of the connections for certain points in time were obtained.
3. When calculating connections using TGk metal connector plates in the range of calculated loads, it is possible to use the predicted creep curves characterizing the base of the dowel hole at any time with rheological coefficients $H = 2700$ MPa, $E = 500$ MPa, $n = 35$.
4. A calculated diagram of the deformation of the wood of the dowel hole $\sigma - \delta$ and connections $T - \Delta$ under long-term load was constructed.
5. The data obtained make it possible to perform calculations of composite wooden elements on this type of connections, considering the duration of the load.

References

1. Naychuk, A.Ya., Pogoreltsev, A.A., Serov, Ye.N. Teoriya i praktika dalneyshego razvitiya derevyannykh konstruksiy. Chast 1. Nagruzki, raschetnyye soprotivleniya i dlitel'naya prochnost drevesiny [Theory and practice of further development of wooden structures. Part 1. Loads, calculated resistances and long-term strength of wood]. Promyshlennoe i grazhdanskoe stroitelstvo. 2018. 6. Pp. 38–44. (rus)
2. Arleninov, D.K., Bekker, D.A. Vliyaniye urovnya napryazheniya na polzuchest drevesiny pri izgibe [Influence of stress level on creep of wood during bending]. Izvestiya VUZov. Lesnoj zhurnal. 2015. 6. Pp. 128–135. (rus)
3. Smorchkov, A.A., Kereb, S.A. Uchet dlitel'nogo nagruzheniya v raschetakh derevyannykh konstruksiy [Accounting for long-term loading in the calculations of wooden structures]. Promyshlennoe i grazhdanskoe stroitelstvo. 2017. 3. Pp. 64–66. (rus)
4. Sekino, N. Korai, N. The evaluation of long-term mechanical properties of wood-based panels by indoor exposure tests. Journal of Wood Science. 2018. 64. Pp. 377–389. DOI: 10.1007/s10086-018-1720-1
5. Huang, Y. Creep behavior of wood under cyclic moisture changes: interaction between load effect and moisture effect. J Wood Sci. 2016. 62. Pp. 392–399. DOI: 10.1007/s10086-016-1565-4
6. Linkov, V.I. Otsenka dlitel'noy prochnosti soyedineniy derevyannykh elementov na naklonnykh metallicheskiykh sterzhnyakh bez primeneniya kleya [Evaluation of the long-term strength of joints of wooden elements on inclined metal rods without the use of glue]. Promyshlennoe i grazhdanskoe stroitelstvo. 2011. 3. Pp. 25–28. (rus)
7. Dmitriyev, P.A. Issledovaniye dlitel'noy nesushchey sposobnosti soyedineniy derevyannykh elementov na stalnykh tsilindricheskikh dowelyakh [Investigation of the long-term bearing capacity of joints of wooden elements on steel cylindrical pins]. Izvestiya VUZov. Stroitelstvo i arhitektura. 1973. 5. Pp. 165–173. (rus)
8. Smirnov, P.N., Pogoreltsev, A.A. Opredeleniye nesushchey sposobnosti dowelnykh soyedineniy na osnovanii standartnykh kharakteristik materialov [Determination of the bearing capacity of dowel joints based on standard characteristics of materials]. Sovremennyye stroitelnye konstrukcii iz metalla i drevesiny. 2013. 17. Pp. 247–253. (rus)
9. Zhuk, V.V., Shchevchuk, V.L., Antiporovich, A.V. Eksperimentalnyye issledovaniye raboty soyedineniy derevyannykh elementov na zhestkikh dowelnykh plastinakh [Experimental study of the operation of joints of wooden elements on rigid dowel plates]. Problemy sovremennogo stroitelstva: materialy mezhdunarodnoy nauchno-tekhnicheskoy konferentsii BNTU [Problems of modern construction: materials of the international scientific and technical conference of BNTU]. Minsk: BNTU, 2019. Pp. 60–65. (rus)
10. Dorn, M., Borst, K., Eberhardsteiner, J. Experiments on dowel-type timber connections. Engineering Structures. 2013. 47. Pp. 67–80. DOI: 10.1016/j.engstruct.2012.09.010
11. Larsson, G., Serrano, E., Gustafsson, P.J., Danielsson, H. Dowel design of the shear plate dowel joint. Engineering Structures. 2020. 209. 110296. DOI: 10.1016/j.engstruct.2020.110296
12. Chiniforush, A.A., Valipour, H.R., Bradford, M.A., Akbarnezhad, A. Long-term behaviour of steel-timber composite (STC) shear connections. Engineering Structures. 2019. 196. 109356. DOI: 10.1016/j.engstruct.2019.109356
13. Yurrita, M., Cabrero, J.M. Experimental analysis of plug shear failure in timber connections with small diameter fasteners loaded parallel-to-grain. Engineering Structures. 2021. 238. 111766. DOI: 10.1016/j.engstruct.2020.111766
14. Ivanov, Yu.M. Dlitelnaya nesushchaya sposobnost derevyannykh konstruksiy [Long-term bearing capacity of wooden structures]. Izvestiya VUZov. Stroitelstvo i arhitektura. 1972. 11. Pp. 6–12. (rus)
15. Sheshukova, N.V. Dlitelnaya prochnost i deformativnost derevyannykh konstruksiy na dowelnykh soyedineniyakh [Long-term strength and deformability of wooden structures on dowel joints]. St. Peterburg: Izd-vo SPbGASU. 2006. 169 p. (rus)
16. Lisitskiy, I.I., Zhadanov, V.I. Dlitelnyye ispytaniya derevyannoy fermy s soyedineniyami elementov na vkleyennykh ploskikh sterzhnyakh [Long-term testing of a wooden truss with connections of elements on glued flat rods]. Izvestiya VUZov. Stroitelstvo. 2020. 1. Pp. 34–45. (rus)
17. Dubois, F., Dopeux, J., Pop, O., Metrope, M. Long-term creep behavior of timber columns: Experimental and numerical protocols. Engineering Structures. 2023. 275. Part B. 115283. DOI: 10.1016/j.engstruct.2022.115283
18. Benkai, S., Weiqing, L., Huifeng, Y. Long-term performance of timber-concrete composite systems with notch-screw connections. Engineering Structures. 2020. 213. 110585. DOI: 10.1016/j.engstruct.2020.110585
19. Zhang, J., Tong, K., Shan, Q., Li, Y. Examining mechanical behavior of steel-bamboo composite I-section column under long-term loading. Journal of Building Engineering. 2022. 45. 103583. DOI: 10.1016/j.jobbe.2021.103583
20. Chiniforush, A.A., Valipour, H.R., Bradford, M.A., Nezhad, A. Experimental and theoretical investigation of long-term performance of steel-timber composite beams. Engineering Structures. 2021. 249. 113314. DOI: 10.1016/j.engstruct.2021.113314
21. Marcos Cesar de Moraes Pereira, Luc Arthur Pascal Sohier, Thierry Descamps, Carlito Caiil Junior. Doweled cross laminated timber: Experimental and analytical study. Construction and Building Materials. 2021. 273. 121820. DOI: 10.1016/j.conbuildmat.2020.121820
22. Isupov, S.A. Experimental substantiation by choosing basic variant of plates with cylindrical dowels. IOP Conference Series. Materials Science and Engineering. 2020. 962. 022047. DOI: 10.1088/1757-899X/962/2/022047

23. Melnikov, B.Ye., Parshin, L.K., Semenov, A.S., Sherstnev, V.A. Soprotivleniye materialov [Resistance of materials]. S-Peterburg: Izd-vo Lan, 2019. 556 p. (rus)
24. Rabotnov, Yu.N. Mekhanika deformiruyemogo tverdogo tela [Mechanics of a Deformable Solid Body]. Moscow: Izd-vo Nauka, 1979. 744 p. (rus)
25. Piskunov, Yu.V., Burov, Ye.V., Zvorygin, A.V. Opredeleniye napryazhenno-deformirovannogo sostoyaniya dowelya v sostave dowlnoy plastiny s uchetom fizicheski nelineynoy raboty materialov [Determination of the stress-strain state of the dowel in the composition of the dowel plate taking into account the physically nonlinear work of materials]. Deponirovannaya statya. Moscow: VNIIS, 1986. 9. 6948. (rus)
26. Isupov, S.A. Mechanical characteristics of materials for joints of wooden structures on TGk dowel plates. AIP Conference Proceedings: II Scientific Conference «Modelling and methods of structural analysis». 2023. 2497. 020024. DOI: 10.1063/5.010602
27. Isupov, S.A. Bearing capacity and deformability of connections of wooden structures on TGk dowel plates. Lecture Notes in Civil Engineering. 2022. 308. Pp. 157–167. Doi.org/10.1007/978-3-031-21120-1_16
28. Rzhantsyn, A.R. Teoriya polzuchesti [Creep Theory]. Moscow: Strojizdat, 1968. 416 p. (rus)
29. Malmeyster, A.K., Tamuzh, V.P., Teters, G.A. Soprotivleniye polimernykh i kompozitnykh materialov [Resistance of polymer and composite materials]. Riga: Izd-vo Zinatne, 1980. 571 p. (rus)

Information about authors:

Sergei Isupov, PhD in Technical Sciences

ORCID: <https://orcid.org/0000-0002-3009-4293>

E-mail: Deka_1958@mail.ru

Received 13.07.2023. Approved after reviewing 27.02.2024. Accepted 28.02.2024.

